

**HYDROPLANING AND SKID RESISTANCE ANALYSIS  
USING NUMERICAL MODELING**

**ONG GHIM PING RAYMOND**

*(B. Eng (Civil) First Class Honours, NUS)*

**A THESIS SUBMITTED  
FOR THE DEGREE OF DOCTOR OF PHILOSOPHY  
DEPARTMENT OF CIVIL ENGINEERING  
NATIONAL UNIVERSITY OF SINGAPORE**

**2006**

## ACKNOWLEDGEMENTS

The author would like to express his utmost appreciation and gratitude to his supervisor, Professor Fwa Tien Fang, for his constant guidance, care, support and encouragement throughout the research. He would also like to extend his gratitude to Dr. Guo Junke, Associate Professor Choo Yoo Sang and Associate Professor Lin Pengzhi, members of his PhD committee for their support and recommendations made to improve the research.

Special thanks are given to the National University of Singapore for providing the research scholarship during the course of research. Thanks are also extended to fellow research mates, Dr. Lee Yang Pin Kelvin, Dr. Liu Wei, Dr. Tan Jun Yew, Dr. Zhu Liying, Ms. Liu Ying, Mr. Wang Yan, Mr. Bagus Hario Setiadji and Mr. Joselito Guevarra for the kind help and friendship.

Gratitude is accorded to Mr. Foo Chee Kiong, Mr. Goh Joon Kiat, Mr. Mohammed Farouk, Mrs. Yap-Chong Wei Leng and Mrs. Yu-Ng Chin Hoe of the Transportation Engineering Laboratory; Mr. Sit Beng Chiat of the Structural Engineering Laboratory; Mr. Yeo Eng Hee, Mr. Wang Junhong and Mr. Zhang Xinhui of the Supercomputing and Visualization Unit of the National University of Singapore Computer Center for their kind assistance and support in the course of research.

Finally, the author would like to express his heartfelt thanks and gratitude to his parents for their tremendous care, utmost support and encouragement given to the author in his work.

# TABLE OF CONTENTS

<b>ACKNOWLEDGEMENTS</b>	<b>i</b>
<b>TABLE OF CONTENTS</b>	<b>ii</b>
<b>SUMMARY</b>	<b>vii</b>
<b>LIST OF TABLES</b>	<b>ix</b>
<b>LIST OF FIGURES</b>	<b>xii</b>
<b>NOMENCLATURE</b>	<b>xvii</b>
<b>CHAPTER 1: INTRODUCTION</b>	<b>1</b>
1.1 Background	1
1.2 Objectives	3
1.3 Organization of Thesis	4
<b>CHAPTER 2: LITERATURE REVIEW</b>	<b>6</b>
2.1 Skid Resistance	6
2.2 Factors Affecting Skid Resistance	7
2.2.1 Pavement Surface Characteristics	8
2.2.1.1 Microtexture	9
2.2.1.2 Macrottexture	9
2.2.2 Presence of Contaminants	10
2.2.3 Vehicle Speed	11
2.3 Friction Testing Methodologies	11
2.3.1 Field Measurements	11
2.3.1.1 Locked-Wheel Methods	12
2.3.1.2 Slip Methods	12
2.3.1.3 Side-Force Methods	13
2.3.2 Laboratory Measurements	14
2.4 Contact Mechanisms for Dry Tire-Pavement Interaction	15
2.4.1 Classical Friction Theories	15
2.4.2 Friction Theories involving Rubber	16
2.4.3 Adhesion	18
2.4.4 Hysteresis	20
2.4.5 Wear	22
2.5 Contact Mechanisms for Wet Tire-Fluid-Pavement Interaction	23
2.5.1 Development of Lubrication Theories	23
2.5.1.1 Hydrodynamic Lubrication	25
2.5.1.2 Elasto-Hydrodynamic Lubrication	26
2.5.1.3 Boundary Lubrication	27
2.5.2 Friction Mechanisms in Tire-Fluid-Pavement Interaction	28
2.5.2.1 Friction Modes in Wet Tire-Fluid-Pavement Interaction	28
2.5.2.2 Mechanism of Tire Sliding on Wet Pavement	29
2.6 Hydroplaning	30
2.6.1 Forms of Hydroplaning	30
2.6.1.1 Dynamic Hydroplaning	30
2.6.1.2 Viscous Hydroplaning	31
2.6.1.3 Reverted-Rubber Hydroplaning	31
2.6.2 Manifestations of Hydroplaning	32
2.7 Modeling of Hydroplaning	33
2.7.1 Experimental/Empirical Approaches in Hydroplaning Studies	34
2.7.1.1 Studies on the Effect of Depth of Fluid on Hydroplaning	34
2.7.1.2 Studies on the Effect of Tire Inflation Pressure on	36

	Hydroplaning	
2.7.1.3	Studies on the Effect of Tire Tread Design on Hydroplaning	37
2.7.1.4	Studies on the Effect of Vertical Load on Hydroplaning	37
2.7.1.5	Studies on the Effect of Tire-Footprint Aspect Ratio on Hydroplaning	38
2.7.1.6	Studies on the Effect of Pavement Surface Texture on Hydroplaning	38
2.7.1.7	Studies on the Effect of Pavement Grooving on Hydroplaning	39
2.7.2	Analytical/Numerical Modeling of Hydroplaning	40
2.8	Modeling of Skid Resistance	43
2.8.1	Experimental/Empirical Approach in Skid Resistance Studies	44
2.8.2	Analytical/Numerical Modeling of Skid Resistance	46
2.9	Summary	48
2.10	Research Needs and Scope of Work	49
<b>CHAPTER 3: DEVELOPMENT OF PNEUMATIC TIRE HYDROPLANING MODEL</b>		<b>64</b>
3.1	Introduction	64
3.2	Fluid Flow Model	64
3.2.1	Fundamental Laws of Fluid Flow	64
3.2.2	Flows in the Turbulent Regime	66
3.2.3	Turbulence Modeling	67
3.3	Hydroplaning Tire Deformation Model	69
3.4	Pavement Surface Model	70
3.5	Concept of Hydroplaning Modeling	71
3.6	Computational Fluid Dynamics in Hydroplaning Simulation	71
3.6.1	Multiphase Modeling and the Volume of Fluid (VOF) Model	72
3.6.1.1	Multiphase Modeling	72
3.6.1.2	Volume of Fluid (VOF) Model	73
3.6.2	Turbulence Modeling using the Standard k- $\epsilon$ Model	75
3.6.3	Wall Functions	75
3.6.3.1	Treatment of Momentum	75
3.6.3.2	Treatment of Turbulence	76
3.6.4	Solver Algorithms	77
3.6.4.1	Segregated Solver	77
3.6.4.2	Pressure Interpolation Scheme	77
3.6.4.3	Pressure-Velocity Coupling	77
3.7	Two-Dimensional Modeling of Browne's Experiment	78
3.7.1	Geometry of Model	78
3.7.2	Boundary Conditions	79
3.7.3	Material Properties	80
3.7.4	Description of Mesh used in the Analysis	80
3.7.5	Simulation Results Based on the Proposed Two-Dimensional Model	81
3.7.6	Mesh Sensitivity Analysis	82
3.7.7	Effect of Boundary Conditions	83
3.7.8	Analysis of Results and Suitability for Hydroplaning Simulation	84
3.8	Three-Dimensional Modeling of Browne's Experiment	84
3.8.1	Geometry of Model and Selection of Boundary Conditions	85
3.8.2	Description of Mesh used for 3-D simulation	85
3.8.3	Simulation Results Based on Proposed 3-D Model	85
3.8.4	Mesh Sensitivity Analysis	86
3.8.5	Effect of Boundary Conditions	87
3.8.6	Analysis of Results and Suitability for Hydroplaning Simulation	88
3.9	Summary	90



**CHAPTER 4: SIMULATION OF HYDROPLANING ON PLANE PAVEMENT SURFACE 115**

4.1	Introduction	115
4.2	Pneumatic Tire Model	115
4.3	Pavement Surface Model	116
4.4	Three-Dimensional Modeling of Hydroplaning	116
4.4.1	Geometry of Model and Selection of Boundary Conditions	116
4.4.2	Description of Mesh used in the Analysis	117
4.4.3	Simulation Results	117
4.4.4	Mesh Sensitivity Analysis	118
4.4.5	Effect of Boundary Conditions	119
4.4.6	Analysis of Results	119
4.4.7	Repeat of Analysis Using NASA Predicted Hydroplaning Speed	121
4.5	Effect of Tire Pressure on Hydroplaning	121
4.5.1	Modeling Methodology	121
4.5.2	Results and Analysis	122
4.6	Effect of Microtexture on Hydroplaning	123
4.6.1	Theoretical Aspects on Incorporating Roughness	124
4.6.2	Modeling Aspects on Incorporating Roughness	126
4.6.3	Results and Analysis	127
4.7	Summary	130

**CHAPTER 5: HYDROPLANING ON PAVEMENT WITH GROOVING 149**

5.1	Introduction	149
5.2	Verification of Simulation Model for Pavement with Pavement Grooving	150
5.2.1	Verification against Experimental Data for Transverse Pavement Grooving	150
5.2.2	Verification against Experimental Data for Longitudinal Pavement Grooving	151
5.3	Simulation of Hydroplaning on Pavement with Pavement Grooving	152
5.3.1	Simulation Results for Transverse Pavement Grooving Designs	152
5.3.2	Simulation Results for Longitudinal Pavement Grooving Designs	153
5.3.3	Comparison between Transverse and Longitudinal Pavement Grooving for Designs A, B and C	154
5.4	Effect of Transverse Groove Dimensions on Hydroplaning	154
5.4.1	Model Parameters Used in Study	154
5.4.2	Results and Analysis	155
5.4.2.1	Effect of Groove Depth on Hydroplaning	155
5.4.2.2	Effect of Groove Width on Hydroplaning	157
5.4.2.3	Effect of Groove Spacing on Hydroplaning	158
5.4.2.4	Relative Effects of Groove Depth, Width and Spacing	159
5.5	Effect of Longitudinal Groove Dimensions on Hydroplaning	160
5.5.1	Model Parameters Used in Study	160
5.5.2	Simulation Results	161
5.5.2.1	Effect of Groove Depth on Hydroplaning	161
5.5.2.2	Effect of Groove Width on Hydroplaning	162
5.5.2.3	Effect of Groove Spacing on Hydroplaning	163
5.5.2.4	Relative Effects of Groove Depth, Width and Spacing	164
5.6	Comparison between Transverse and Longitudinal Pavement Grooving in Hydroplaning Prevention	165
5.7	Summary	167

<b>CHAPTER 6: DESIGN AND EVALUATION OF PAVEMENT GROOVES AGAINST HYDROPLANING</b>	<b>196</b>
6.1 Introduction	196
6.2 Concept of Hydroplaning Risk in Pavement Groove Dimension Design and Evaluation	196
6.2.1 Definition of Hydroplaning Risk	196
6.2.2 Evaluation of Hydroplaning Risk for Given Pavement Groove Design	197
6.2.3 Design of Pavement Groove Dimension based on Hydroplaning Risk	198
6.3 Numerical Example on the Evaluation of Hydroplaning Risk for a given Pavement Groove Design	199
6.3.1 Evaluating Hydroplaning Risks for Transverse Pavement Grooving	200
6.3.2 Evaluating Hydroplaning Risks for Longitudinal Pavement Grooving	201
6.3.3 Comparison of Hydroplaning Risk in Transverse and Longitudinal Pavement Grooving	201
6.4 Numerical Example on Pavement Groove Dimension Design using Hydroplaning Risk Concept	202
6.4.1 Design of Transverse Groove Dimensions	202
6.4.2 Design of Longitudinal Groove Dimensions	204
6.5 Summary	204
 <b>CHAPTER 7: WET TIRE PAVEMENT INTERACTION AND HYDROPLANING MODELING</b>	 <b>210</b>
7.1 Introduction	210
7.2 Finite Element Modeling of Tire-Fluid-Pavement Interaction	211
7.2.1 Overall Concept of Modeling Tire-Fluid-Pavement Interaction	211
7.2.2 Pneumatic Tire Modeling	213
7.2.3 Pavement Surface Modeling	214
7.2.4 Tire-Pavement Contact Modeling	215
7.2.5 Fluid Flow Modeling	216
7.2.6 Fluid-Structure Interaction (FSI) Modeling	218
7.3 Hydroplaning Analysis and Verification of Model	219
7.4 Effect of Footprint Aspect Ratio on Hydroplaning	220
7.5 Effect of Water-Film Thickness on Hydroplaning	221
7.6 Comparing Factors affecting Hydroplaning Speed	223
7.7 Summary	225
 <b>CHAPTER 8: NUMERICAL MODELING OF WET PAVEMENT SKID RESISTANCE</b>	 <b>238</b>
8.1 Introduction	238
8.2 Wet-Pavement Skid Resistance Analysis by Proposed Model	238
8.2.1 Input Parameters	238
8.2.2 Computation of Skid Resistance	240
8.3 Validation of Skid Resistance Prediction	241
8.3.1 Experimental Data and Validation Approach	241
8.3.2 Results of Validation	242
8.4 Analysis of Simulation Results on Mechanisms of Skid Resistance with Vehicle Speed	243
8.4.1 Forces Contributing to Skid Resistance	243
8.4.2 Tire-Fluid-Pavement Interaction	244
8.4.3 Variation of Tire-Pavement Contact Zone	245
8.4.4 Characteristics of SN-Speed Curves	246
8.5 Comparing Factors Affecting Skid Resistance	247

8.5.1	Effect of Wheel Load on Skid Resistance	248
8.5.2	Effect of Tire Inflation Pressure on Skid Resistance	249
8.5.3	Effect of Water-Film Thickness on Skid Resistance	249
8.5.4	Effect of Vehicle Speed on Skid Resistance	250
8.5.5	Comparison of Factors affecting Skid Resistance	251
8.6	Summary	251
<b>CHAPTER 9: CONCLUSIONS AND RECOMMENDATIONS</b>		<b>262</b>
9.1	Conclusions of Research	262
9.1.1	Numerical Modeling of Hydroplaning using Assumed Hydroplaning Tire Profile	262
9.1.1.1	Development of Three-Dimensional Pneumatic Tire Hydroplaning Simulation Model	263
9.1.1.2	Hydroplaning Simulation on Plane Pavement Surfaces	264
9.1.1.3	Hydroplaning on Pavement with Transverse or Longitudinal Pavement Grooving	264
9.1.1.4	Design and Evaluation of Pavement Grooves against Hydroplaning	266
9.1.2	Numerical Modeling of Hydroplaning and Skid Resistance considering Fluid-Structure-Interaction	267
9.1.2.1	Development of Improved Simulation Model for Hydroplaning	267
9.1.2.2	Modeling of Wet-Pavement Skid Resistance	268
9.2	Recommendations for Further Research	269
<b>References</b>		<b>271</b>

## SUMMARY

The occurrences of wet-weather accidents, from the perspective of pavement surface characteristics, can be caused by either poor skid resistance offered from tire-fluid-pavement interaction or hydroplaning. Research since the 1920s had been focusing on two aspects, namely, the measurement and prediction of skid resistance, and the development of strategies to reduce wet-weather accidents. Despite improvements in measurement techniques, the understanding of skid resistance and hydroplaning mechanisms have not improved much over the past decades due to a lack of development in the theoretical, analytical or numerical models that can explain and simulate the mechanisms. This results in the reliance of empirical experimentally-based relationships in skid resistance and hydroplaning speed predictions. This study attempts to develop numerical models to simulate hydroplaning and skid resistance of locked wheels on wet pavements.

The study can be divided into two main stages. This first stage involves hydroplaning simulations using the tire deformation profiles obtained in the experimental hydroplaning studies conducted by the National Aeronautical and Space Administration (NASA). Two- and three-dimensional numerical modeling of hydroplaning are first explored. It is found that three-dimensional model of hydroplaning with the consideration of turbulent flow is necessary to produce numerical results close to experimental results reported in the literature. A three-dimensional numerical hydroplaning simulation model using computational fluid dynamics is presented. The tire pressure-hydroplaning speed relationship predicted by the model is found to be in close agreement with the NASA hydroplaning equation. The effect of pavement microtexture on hydroplaning is studied using the developed model.

Transverse and longitudinal pavement grooving are used on highways and runways to reduce hydroplaning occurrences. The groove dimensions used in practice today are a result of past empirical and experimental studies. The developed numerical simulation model can therefore serve as a tool to understand how transverse and longitudinal pavement grooving

affect hydroplaning from an analytical perspective. The effects of groove dimensions of transverse and longitudinal grooves on hydroplaning are also studied. An analytical procedure for the design of transverse and longitudinal pavement grooving using the numerical simulation model and the concept of hydroplaning risk is proposed to provide a mechanistic-based approach in pavement grooving design.

The second stage of the study involves the relaxation of the hydroplaning tire deformation profile assumption to allow simulations of tire-fluid-pavement interactions at vehicle speeds below the hydroplaning speed. This is needed in order to develop models that can simulate wet skid resistance. The development of a three-dimensional finite element simulation model that is capable of modeling solid mechanics, fluid dynamics, tire-pavement contact and tire-fluid interaction is described. The proposed model is calibrated and validated for the case of a loaded stationary tire under both dry and wet pavement conditions. The model is used to simulate hydroplaning and is found to be able to produce hydroplaning speeds which closely agree with the NASA hydroplaning equation. The model is then applied to simulate the skid resistance of the locked sliding tire for different vehicle speeds. By varying the vehicle speed, the behavior of the tire-pavement contact patch can be studied and compared against observations made in the literature. The effects of water-film thickness, tire inflation pressure and vehicle load on the hydroplaning speed and skid resistance are also studied using the developed numerical simulation model.

## LIST OF TABLES

Table 2.1	Skid-Resistance Measurement Systems	53
Table 2.2	Sources of Load Support using Smooth Surfaces	54
Table 2.3	Sources of Load Support using Rough Surfaces	55
Table 3.1	Summary of current agency practices of measuring surface friction	92
Table 3.2	Summary of boundary conditions used in Browne's experiment	92
Table 3.3	Mass flow rate for air and water through various boundaries based on a turbulent flow model for the proposed 2-D model	92
Table 3.4	Effect of mesh quality on the various parameters under the wheel for the proposed 2-D model	93
Table 3.5	Summary of boundary conditions used in the study of the effect of boundary conditions for the 2-D analysis	93
Table 3.6	Effect of location of boundary conditions on the various parameters under the wheel for the 2-D analyses	93
Table 3.7	Mass flow rate for air and water through various boundaries based on a turbulent flow model for the proposed 3-D model	93
Table 3.8	Effect of mesh quality on the various parameters under the wheel for the proposed 3D model	94
Table 3.9	Summary of boundary conditions used in the study of the effect of boundary conditions for the 3D analysis	94
Table 3.10	Effect of location of boundary conditions on the various parameters under the wheel for the 3D analyses	94
Table 3.11	Summary of simplifying assumptions in hydrodynamics	95
Table 4.1	Summary of boundary conditions used in this study	132
Table 4.2	Mass flow rate for air and water through various boundaries based on a turbulent flow model for the proposed 3-D model	132
Table 4.3	Effect of mesh quality on the various parameters under the wheel for the proposed 3D model	132
Table 4.4	Summary of boundary conditions used in the study of the effect of boundary conditions for the 3D analysis	133
Table 4.5	Effect of location of boundary conditions on the various parameters under the wheel for the 3D analyses	133
Table 4.6	Friction forces and friction coefficient during hydroplaning	134

Table 4.7	Average ground hydrodynamic pressure and recovery factors for different hydroplaning speeds	134
Table 4.8	Equivalent Roughness for New Pipes	135
Table 4.9	Comparison between Predicted and Experimental Friction Coefficients	135
Table 5.1	Description of Various Transversely Grooved Pavement Surfaces tested by Horne and Tanner (1969)	169
Table 5.2	Pavement Grooving Designs Analyzed	169
Table 5.3	Summary of Simulation Results for Grooving Designs Tested	169
Table 5.4	Groove Dimensions Tested	170
Table 5.5	Hydroplaning Speeds and Friction Coefficients of Pavements having Different Transverse Groove Dimensions for Passenger Cars with 186.2 kPa Tire Pressure	171
Table 5.6	Effects of Transverse Groove Depth on Hydroplaning Speed and Friction Coefficient	172
Table 5.7	Effects of Transverse Groove Width on Hydroplaning Speed and Friction Coefficient	173
Table 5.8	Effects of Transverse Groove Spacing on Hydroplaning Speed and Friction Coefficient	174
Table 5.9	Recommended Transverse Tine Dimensions of Various States in U.S.A.	175
Table 5.10	Hydroplaning Speeds for Different Transverse Groove Dimensions and Tire Pressures	176
Table 5.11	Hydroplaning Speeds and Friction Coefficients of Pavements having Different Longitudinal Groove Dimensions for Passenger Cars with 186.2 kPa Tire Pressure	177
Table 5.12	Effects of Longitudinal Groove Depth on Hydroplaning Speed and Friction Coefficient	178
Table 5.13	Effects of Longitudinal Groove Width on Hydroplaning Speed and Friction Coefficient	179
Table 5.14	Effects of Longitudinal Groove Spacing on Hydroplaning Speed and Friction Coefficient	180
Table 5.15	Hydroplaning Speeds for Different Longitudinal Groove Dimensions and Tire Pressures	181
Table 5.16	Findings from Selected Past Research on Transverse and Longitudinal Pavement Grooving	182
Table 6.1	Recommended Longitudinal Groove Dimensions of Various States in U.S.A.	206

Table 6.2	Recommended Guidelines on Surface Texturing Treatments	206
Table 6.3	Hydroplaning Risk for Pavement Grooving Designs A, B and C	206
Table 6.4	Family of Possible Transverse Pavement Grooving Designs based on Selected Level of Hydroplaning Risk	207
Table 6.5	Family of Possible Longitudinal Pavement Grooving Designs based on Selected Level of Hydroplaning Risk	208
Table 7.1	Contact Footprint Dimensions for Different Elastic Moduli of Tire Tread	227
Table 7.2	Comparison of Contact Footprint Dimensions with Experimental Data	227
Table 7.3	Footprint Aspect Ratios for Different Loading Tested	227
Table 7.4	Hydroplaning Speeds for Different Footprint Aspect Ratios Tested	228
Table 7.5	Range of the different Parameters considered in this Study	228
Table 7.6	Regression Relationships between Hydroplaning Speed and Different tested Parameters	229
Table 8.1	Test Conditions for Skid Numbers at Different Vehicle Speeds	253
Table 8.2	Comparison between Experimental and Simulation Results for SN	254
Table 8.3	Factors considered in parametric study of skid resistance for the ASTM E524 tire on plane pavement surface	254
Table 8.4	Comparison of factors affecting skid resistance	255



## LIST OF FIGURES

Figure 2.1	Effect of texture depth on friction and noise	56
Figure 2.2	Influences of water film thickness and vehicle speed on skid resistance	56
Figure 2.3	Differences in locked wheel performance on interchangeable tires on the same wet pavement surface (fine cold asphalt)	57
Figure 2.4	British Pendulum Tester	57
Figure 2.5	Rubber Sliding on a Hard Substrate of Short-ranged and Long ranged Surface Roughness	58
Figure 2.6	Frictional performances of (a) adhesion-producing and (b) hysteresis producing surfaces	58
Figure 2.7	Generalized representation of the coefficient of friction between a steel sphere and rubber as a function of sliding speed	58
Figure 2.8	Schematic of fluid flow between two surfaces and stresses acting on fluid element and velocities in x-z plane	59
Figure 2.9	General iterative procedures for elasto-hydrodynamic lubrication	59
Figure 2.10	Boundary layer lubricated frictional contact	60
Figure 2.11	Hydrodynamic lubricated frictional contact (Partial)	60
Figure 2.12	Tire sliding on wetted pavement surface - three-zone concept	61
Figure 2.13	Longitudinal pavement texture versus transverse pavement texture	62
Figure 2.14	Finite element model of the British pendulum tester developed by Liu et al. (2003)	62
Figure 2.15	Scope of research on thesis	63
Figure 3.1	Tire deformation profile of a hydroplaning tire	96
Figure 3.2	Concept of hydroplaning modeling	96
Figure 3.3	Program structure of FLUENT package	97
Figure 3.4	Overview of the segregated solution method	97
Figure 3.5	Geometry of the proposed three-dimensional model	98
Figure 3.6	Geometry of the proposed two-dimensional model	98
Figure 3.7	Mesh design of the proposed 2D model	99
Figure 3.8	Steady state volume fraction plot for the proposed 2D model	99

Figure 3.9	Zoom-in view of the velocity vector plot near the wheel for the proposed 2D model	100
Figure 3.10	Static pressure contour plot of the 2D model under the moving wheel reference frame	101
Figure 3.11	Ground hydrodynamic pressure distribution under wheel for the proposed 2D model	101
Figure 3.12	Steady state volume fraction plots for the study of the effect of mesh size in the proposed 2D model	102
Figure 3.13	Ground hydrodynamic pressure distribution under wheel for the study of the effect of mesh size in the proposed 2D model	103
Figure 3.14	Effect of mesh quality on the average ground hydrodynamic pressure under the wheel in the proposed 2D model	103
Figure 3.15	Steady state volume fraction plots for the study of the effect of location of boundary conditions in the proposed 2D model	104
Figure 3.16	Comparison between the simulation using the 2D model with the plane of symmetry as pavement model and Browne (1971) experimental results	105
Figure 3.17	Mesh design of the proposed 3D model	105
Figure 3.18	Steady state volume fraction plot along plane of symmetry (centerline of model) for the proposed 3D model	106
Figure 3.19	Zoom-in view of the velocity vector plot near the wheel along plane of symmetry for the proposed 3D model	107
Figure 3.20	Static pressure contour plot of the 3D model under the moving wheel reference frame	108
Figure 3.21	Ground hydrodynamic pressure distribution along the centre-line under wheel for the proposed 3D model	108
Figure 3.22	Ground hydrodynamic pressure distribution along lines under wheel for the proposed 3D model	109
Figure 3.23	Steady state volume fraction plots for the study of the effect of mesh size in the proposed 3D model	110
Figure 3.24	Ground hydrodynamic pressure distribution under the centre-line of the wheel for the study of the effect of mesh size in the proposed 3D model	111
Figure 3.25	Effect of mesh quality on the average ground hydrodynamic pressure under the wheel in the proposed 3D model	111
Figure 3.26	Steady state volume fraction plots along the plane of symmetry for the study of the effect of location of boundary conditions in the proposed 3D model	112

Figure 3.27	Ground hydrodynamic pressure distribution under the hydroplaning wheel from the proposed 3D model	113
Figure 3.28	Comparison between the simulation using the 3D model with the plane of symmetry as pavement model and Browne (1971) experimental results	113
Figure 3.29	Comparison of hydrodynamic pressure distribution under the wheel under turbulent and laminar treatments	114
Figure 4.1	Tire deformation profile of a hydroplaning passenger car pneumatic tire at tire pressure of 186.6 kPa	136
Figure 4.2	Geometry of the proposed 3D hydroplaning model	136
Figure 4.3	Mesh design of the three-dimensional model	137
Figure 4.4	Steady state volume fraction plot along plane of symmetry (centerline of model) for the proposed 3D model	137
Figure 4.5	Zoom-in view of the velocity vector plot near the wheel along plane of symmetry for the proposed 3D model	138
Figure 4.6	Static pressure contour plot of the 3D model under the moving wheel reference frame	139
Figure 4.7	Ground hydrodynamic pressure distribution along the centre-line under wheel for the proposed 3D model	139
Figure 4.8	Ground hydrodynamic pressure distribution along lines under wheel for the proposed 3D model	140
Figure 4.9	Ground hydrodynamic pressure distribution under wheel for the proposed 3D model	140
Figure 4.10	Steady state volume fraction plots for the study of the effect of mesh size in the proposed 3D model	141
Figure 4.11	Ground hydrodynamic pressure distribution under the centre-line of the wheel for the study of the effect of mesh size in the proposed 3D model	142
Figure 4.12	Effect of mesh quality on the average ground hydrodynamic pressure under the wheel in the proposed 3D model	142
Figure 4.13	Steady state volume fraction plots along the plane of symmetry for the study of the effect of location of boundary conditions in the proposed 3D model	143
Figure 4.14	Ground hydrodynamic pressure distribution along lines under wheel in Browne's research	144
Figure 4.15	Ground hydrodynamic pressure distribution along lines under wheel for the proposed 3D model at test speed of 86.7 km/h	144
Figure 4.16	Relationship between tire pressure and hydroplaning speed	145

Figure 4.17	Simplified representation of roughness assuming that sand grain is a perfect sphere	145
Figure 4.18	Geometry of the proposed 3D hydroplaning model to account for microtexture	146
Figure 4.19	Effect of microtexture on the predicted ground hydrodynamic pressure at the NASA hydroplaning speed of 87.5 km/h	146
Figure 4.20	Effect of microtexture on the predicted hydroplaning speed	147
Figure 4.21	Effect of microtexture on the predicted coefficient of friction	147
Figure 4.22	Effect of microtexture on the hydroplaning curves	148
Figure 5.1	Meyer's relationship for experimentally measured data by Horne and Tanner (1969) and predicted points by proposed model	183
Figure 5.2	Meyer's relationship for experimentally measured data by Horne (1969) and predicted points by proposed model for longitudinal pavement grooving	183
Figure 5.3	Ground hydrodynamic pressure distribution under wheel for smooth transversely-grooved pavement of designs A, B and C	184
Figure 5.4	Derived relationship between tire inflation pressure and hydroplaning speed for different transversely grooved pavement surfaces	185
Figure 5.5	Ground hydrodynamic pressure distribution under wheel for smooth transversely-grooved pavement of designs A, B and C	186
Figure 5.6	Derived relationship between tire inflation pressure and hydroplaning speed for different longitudinally grooved pavement surfaces	187
Figure 5.7	Effect of transverse groove depth on hydroplaning as a function of tire pressure	188
Figure 5.8	Effect of transverse groove width on hydroplaning curves for different depths at 15 mm spacing	189
Figure 5.9	Effect of spacing between transverse grooves on hydroplaning curves for different groove depth for groove width of 2 mm	190
Figure 5.10	Frequency distribution of effectiveness indices of different transverse groove dimensions	191
Figure 5.11	Effect of longitudinal groove depth on hydroplaning as a function of tire pressure	192
Figure 5.12	Effect of longitudinal groove width on hydroplaning as a function of tire pressure	193
Figure 5.13	Effect of longitudinal groove center-to-center spacing on hydroplaning as a function of tire pressure	194

Figure 5.14	Frequency distribution of effectiveness indices of different longitudinal groove dimensions	195
Figure 6.1	Wet-speed frequency distribution for a freeway	209
Figure 7.1	Three-dimensional finite element model used in this study	231
Figure 7.2	Overview of simulation procedure	232
Figure 7.3	Tire contact footprints from simulation and experiment for ASTM E-524 tire at 165.5 kPa inflation pressure and 4826 N load	233
Figure 7.4	Convergence analysis of pneumatic tire model	233
Figure 7.5	Convergence analysis of fluid model	234
Figure 7.6	Effect of tire inflation pressure on hydroplaning speed	234
Figure 7.7	Comparison between simulation model and Gallaway model	235
Figure 7.8	Effect of Tire Inflation Pressure, Wheel Load and Water-Film Thickness on Hydroplaning Speed	236
Figure 7.9	Relationship between footprint aspect ratio and wheel load	237
Figure 7.10	Comparison of various factors affecting hydroplaning speed	237
Figure 8.1	Comparison of SN-v relationships between simulation and experiments	256
Figure 8.2	Contributions of traction and fluid drag to skid resistance	257
Figure 8.3	Variations of normal contact and fluid uplift forces with locked-wheel sliding speed	258
Figure 8.4	Changes in tire-pavement contact zone area with sliding wheel speed	258
Figure 8.5	Variations of tire-pavement contact zone with sliding wheel speed	259
Figure 8.6	Effects of tire inflation pressure, wheel load, water-film thickness and vehicle sliding speed on skid number	260
Figure 8.7	Variation of variables in Equation (8.4) with wheel load	261
Figure 8.8	Comparison of various factors affecting skid number	261

## NOMENCLATURE

$BFC$	Braking Force Coefficient
$BPN$	British Pendulum Number
$BSN$	Brake Slip Number
$C_s$	Roughness constant
$d$	Depth of groove
$\underline{\mathbf{d}}$	Nodal displacements
$\mathbf{e}$	Strain tensor
$F$	Frictional force
$F_R$	Total frictional resistance force experienced by the tire
$F_x$	Total frictional resistance force experienced by the tire (i.e. the fluid drag and the sliding contact friction)
$F_s$	Force perpendicular to the plane of test tire
$F_z$	Vertical loading on wheel
$f$	Friction factor
$FAR$	Footprint aspect ratio
$\mathbf{g}$	Gravitation force vector
$h$	Fluid-film thickness
$K_S$	Roughness height
$k$	Turbulence kinetic energy
$L$	Load
$MTD$	Mean texture depth
$N$	Normal force
$\mathbf{n}$	Normal vector
$P$	Wheel load
$P_{av}$	Average ground hydrodynamic pressure
$p_h$	Hydrodynamic pressure

$p_t$	Tire inflation pressure
$PNG$	Percentage-normalized gradient
$Re$	Reynolds number
$SD$	Spin-down
$SFC$	Side-force coefficient
$SN$	Skid number
$SN_0$	Skid number at zero speed
$SN_v$	Skid number at speed $v$ km/h
$s$	Center-to-center spacing between grooves
$TRD$	Tire tread depth
$t$	Time
$t_w$	Water-film thickness
$U$	Vehicle speed
$U^*$	Mean velocity
$\mathbf{U}$	Mean velocity vector
$u$	Velocity in the $x$ -direction
$\mathbf{u}$	Velocity vector
$V$	Vehicle speed
$v$	Velocity in the $y$ -direction
$\mathbf{v}$	Velocity vector
$V_p$	Design hydroplaning speed
$v_p$	Hydroplaning speed
$w$	Width of groove
$w$	Velocity in the $z$ -direction
$\mathbf{w}$	Moving mesh velocity vector
$\alpha$	Hydroplaning risk
$\alpha_{yaw}$	Yaw angle

$\varepsilon$	Turbulence dissipation rate
$\eta$	Dynamic viscosity of fluid
$\theta$	Effective viscosity of fluid
$\lambda$	Second viscosity of fluid
$\kappa$	Von Karman constant (= 0.42)
$\mu$	Coefficient of friction between two surfaces for solid-solid contact
$\mu_t$	Turbulent (eddy) viscosity
$\nu$	Kinematic viscosity of fluid
$\rho$	Density
$\tau$	Stress tensor
$\underline{\tau}$	Nodal stresses
$\tau_w$	Shear stress at wall
$\omega$	Angular velocity



## CHAPTER 1 INTRODUCTION

### 1.1 Background

A major concern in highway and runway operations is the safety of automobiles and aircraft. One of the contributing factors to road and runway incidents is the lack of friction between the tire and pavement, thereby leading to skidding accidents and possibly hydroplaning. Wet skidding accidents figure prominently among traffic accidents (OECD, 1984; Wambold et al. 1986). More than 100 aircraft accidents between 1958 and 1993 occurred due to inadequate pavement skid resistance (Costello, 2000). Benedetto (2002) highlighted some of the fatal incidents due to aircraft hydroplaning on runways from 1971 to 1999, including the incident of a Boeing B727-225 at the JFK airport, New York, U.S.A. in 1975, where there were 115 fatalities out of the 124 passengers onboard. More than a quarter of the wet road accidents in the U.K. are related to skidding conditions (Kennedy et al., 1990). Hosking (1987) reported that an improvement in the average skid resistance level of 10% could result in a 13% reduction in wet skid rates. These studies show the importance of adequate frictional characteristics between the tire and pavement surface and its associated reduction in the risk of hydroplaning occurrences.

Pavement skid resistance has long been recognized as an important factor in traffic safety and has been introduced in design guidelines of highways and runways. For example, the geometric design of highway curves requires information on the coefficient of side friction for the determination of the minimum curve radius in order to prevent vehicle from skidding out of the curve (AASHTO, 2004). Cross slopes have to be designed to provide adequate surface drainage and this is considered a key measure to reduce hydroplaning occurrence (AASHTO, 2004; Wolshon, 2004). The design stopping distances are determined based on assessments of the available pavement skid resistance, while speed limits on highways have to take into consideration operational safety, i.e. skidding and hydroplaning (Lamm et al., 1999).

Research on pavement skid resistance started in the 1920s and since then, it has mostly focused on a few aspects, namely, to measure and predict pavement dry and wet skid resistance accurately, and to develop strategies to reduce wet weather accidents on highway and runways. The term “wet skid resistance” is rather vague, since it depends on various parameters such as the type of contaminant, the depth of fluid, etc. The occurrences of wet weather accidents, from the perspective of pavement surface characteristics, could be attributed to either poor skid resistance offered from the tire-fluid-pavement interaction or hydroplaning. Hydroplaning is a unique situation in wet pavement conditions when the tire is lifted off the pavement surface by hydrodynamic forces and wet skid resistance drops to extremely low or near-zero values (Horne and Joyner, 1965).

Measurement of skid resistance can be broadly classified into direct methods and indirect methods. In the direct methods, some form of skid number or friction factor will be given as output. Techniques such as the locked wheel method (ASTM, 2005a), the slip method (ASTM, 2005j) and the side force method (ASTM, 2005e) result in different types of friction factors being defined, depending on the testing conditions and the intention of conducting the tests. Laboratory techniques such as the portable British Pendulum Tester (ASTM, 2005b) is often employed to measure low speed friction and is commonly used to assess the microtexture of the pavement surface (Giles et al., 1964). The output is the British Pendulum Number (BPN) which is a measure of energy loss in the test, and hence a measure of the skid resistance and friction factor of the surface. Unlike the direct methods, the indirect methods adopt more subtle approaches to deduce the skid resistance of the pavement surface. Indirect methods usually measure and record the texture property of the pavement surface and make use of empirical correlations to deduce the frictional parameters of the pavement surface (Schulze and Beckman, 1962; Horne and Joyner, 1965; Sabey, 1965; Moore, 1966; Shilling, 1969; Williams, 1969). Tests such as the sand/grease patch tests (ASTM, 2005h) and tests using contactless sensors (ASTM, 2005i) often provide a quick measure of the pavement surface characteristics.

Despite improvements in the measurement techniques, the understanding of skid resistance mechanisms have not improved much over the past eighty-odd years as it is hampered by the lack of development in the theoretical, analytical or numerical models that can aptly explain and simulate the skid resistance mechanisms. This therefore results in the reliance (and perhaps over-reliance) of empirical relationships in skid resistance prediction for applications in the field as well as for research in the academia. It is noted that the study of modern friction mechanisms in the field of tribology started only in the 1960s, some forty years after the first studies in skid resistance.

Today, modern theories continue to be hampered by their dependence on experimental data for empirical constants used in the formulation. One important aspect that could not be resolved today is the measurement of the true contact area of a body (especially materials like rubber) on a traveled surface. This is made complicated by the fact that lubrication theories and rubber constitutive modeling result in non-linear partial differential equations where the solutions could not be obtained analytically. Only in the recent decade, with the greatly enhanced computing power can researchers start to look into the issue by solving them numerically. Taking advantage of the computing power available today, it appears feasible to numerically model tire-pavement and tire-fluid-pavement interactions so as to gain a better understanding of the mechanisms of skid resistance and hydroplaning and to offer new perspectives to the skid resistance problem.

## **1.2 Objectives**

The objectives of this research are:

1. To develop a numerical model for hydroplaning of a locked-wheel sliding over smooth plane pavements using an assumed tire deformation profile.
2. To apply the proposed numerical model with an assumed tire deformation profile to study the effect of pavement grooving on hydroplaning
3. To propose a design procedure for pavement groove dimensions in hydroplaning control.

4. To propose an improved numerical model considering coupled tire-fluid-pavement interaction for estimating skid resistance and hydroplaning speed of a locked-wheel sliding over smooth plane pavement.

### **1.3 Organization of Thesis**

*Chapter 1* provides the background of the study of hydroplaning and skid resistance and highlights the need for the current research.

*Chapter 2* reviews the existing literature on the various factors that affect skid resistance, the methods of measuring skid resistance, the contact mechanisms for the dry tire-pavement interaction and the wet tire-fluid-pavement interaction, the concepts of hydroplaning, the various factors that affect hydroplaning, and attempts by past researchers on numerical modeling of skid resistance and hydroplaning.

*Chapter 3* presents the formulation and development of a numerical model that can describe the hydroplaning phenomenon. The suitability of a two dimensional and a three dimensional forms of the model are discussed. Laminar and turbulent flow models are tested and verification of the model made with respect to experiments conducted by past researchers.

*Chapter 4* presents the verification of the model made against the well-known NASA hydroplaning equation. The effect of tire pressure on the hydroplaning speed and the effect of microtexture on the NASA hydroplaning curve are studied and presented.

*Chapter 5* presents the application of the proposed model in studying the effectiveness of transverse and longitudinal pavement grooving against hydroplaning. Verification of the model is made against past reported data. The effect of pavement groove dimensions for both transverse and longitudinal pavement grooving on hydroplaning shall be discussed. A comparison between transverse and longitudinal pavement grooving is made in terms of their effectiveness in hydroplaning control.

*Chapter 6* presents the proposed procedure to design the pavement groove dimensions against hydroplaning for the transverse and longitudinal pavement grooving respectively. The concept of hydroplaning risk is introduced and the design of pavement grooves based on

hydroplaning risk is discussed. A comparison between transverse and longitudinal pavement grooving designs shall also be made.

*Chapter 7* presents the development of a improved wet tire-pavement interaction model and the application of the model in the study of hydroplaning. The formulations and the development of the fluid-structure-interaction numerical model are discussed. Calibration and verification of the model is also discussed. The effects of tire inflation pressure, vehicle loading, tire footprint aspect ratio and water-film thickness on the hydroplaning speed are also studied and presented.

*Chapter 8* presents the application of the improved model in the study of skid resistance. Verification of the model against experimental results is presented. The model is then applied to study the mechanism of wet-pavement skid resistance. The effects of vehicle speed, tire inflation pressure, vehicle loading and water-film thickness on skid resistance are also discussed.

*Chapter 9* summarizes the main conclusions drawn in the current research and provides recommendations and directions for further research.

## CHAPTER 2 LITERATURE REVIEW

This chapter shall present a review of the literature on a few major aspects of this research. Concepts relating to the definitions of friction and skid resistance are first introduced. Factors affecting skid resistance are discussed, particularly the effect of pavement surface texture on skid resistance. Different field and laboratory skid resistance measurement techniques are also described. Friction mechanisms related to dry tire-pavement interaction and wet tire-fluid-pavement interaction respectively are introduced, with emphasis on the concepts relating to the hydroplaning phenomenon. Factors affecting the occurrence of hydroplaning and the strategies used in practice to reduce hydroplaning occurrences are reviewed. Last but not least, past experimental and analytical/numerical works in the research area of skid resistance and hydroplaning are presented in the chapter.

### 2.1 Skid Resistance

Skid resistance is defined as the force developed when a tire that is prevented from rotating slides on the pavement surface (Highway Research Board, 1972). It is often thought of as a pavement property and is the antonym of slipperiness. This term does not have a precise meaning and is used to describe the pavement surface in a general way.

Friction force is the resistance measured or experienced when one body in contact with another is being moved or is to be moved. It is dependent on the contact area and is thus not suited for describing the character of the contact pairing (Highway Research Board, 1972). In mechanics, the coefficient  $\mu$  is used and is defined as:

$$\mu = \frac{F}{L} \quad (2.1)$$

where  $F$  is the frictional resistance to motion in the plane of interface and  $L$  is the load perpendicular to the interface. The coefficient of friction is a useful term when all the conditions can be precisely defined. However, most of these conditions are difficult to describe and measure in practice for the cases of a rolling, slipping or sliding tire, especially when water

is present at the interface. In this case, the preferred term, in lieu of the coefficient of friction, is the friction factor  $f$  and is defined as:

$$f = \frac{F_R}{P} \quad (2.2)$$

where  $F_R$  is the total frictional resistance force experienced by the tire (i.e. the fluid drag and the sliding contact friction) and  $P$  is the vehicle wheel load.

It is incorrect to say that a pavement has a certain friction factor (or coefficient of friction), because friction always involve two contacting bodies. It is even imprecise to say that a particular tire on a given pavement surface produces certain friction factor, unless the sliding (or rolling) speed, the tire inflation pressure, load, temperature, water film thickness and other details can be accurately specified. To overcome the resulting communication problem, standards have been developed that prescribe all variables that influence the friction factor.

One example of such a standard is the ASTM Method E 274-97 (ASTM, 2005a). Measurements made in accordance to it are reported as skid numbers ( $SN$ ) defined as:

$$SN = 100f = 100 \frac{F_R}{P} \quad (2.3)$$

in which  $F_R$  is obtained in a strictly defined manner by sliding a locked, standardized tire, (i.e. the ASTM standard rib tire as stated in ASTM E 501-94 (ASTM, 2005d) or the ASTM standard smooth tire as stated in ASTM E 524-88 (ASTM, 2005f)) at a constant speed of 65km/h (40 mph) on an artificially wetted pavement. The term skid number should not be used with other skid resistance measurements except those made at the same test speed and test tires in accordance to ASTM E 274-97.

## 2.2 Factors Affecting Skid Resistance

The skid resistance of a pavement can be affected by many factors. They can be broadly classified into four categories:

- (a) those related to pavement surface characteristics, such as pavement material type, and pavement surface texture in the form of microtexture and macrotexture;

- (b) those related to the tire, such as tire rubber material type, tread design, and tire inflation pressure;
- (c) those related to the presence of contaminants that interfere with the tire-pavement interaction, such as presence of water, water film thickness, presence of loose particles like grit, sand and silt, presence of oils; and
- (d) those related to the operating conditions, such as pavement surface temperature, and vehicle speed.

The four groups as stated above constitute the major components of the tire-fluid-pavement interaction in a very general sense. A thorough understanding of the interaction of these components would allow researchers to better understand the process of skid resistance development and the occurrence of hydroplaning. The next few sub-sections shall discuss how these parameters affect skid resistance.

### **2.2.1 Pavement Surface Characteristics**

Pavement surface texture is the “roughness” that, in a bituminous surface, is most significantly influenced by the sizes and gradation of the aggregate and in Portland cement surface by the finishing method (e.g. burlap drag, brush finish etc). Texture not only affects the development of the necessary frictional forces under both dry and wet pavement conditions, but also influences the nature and area of contacts with the tire by projecting through water films. The tire-pavement interaction (under dry condition) and the tire-fluid-pavement interaction (under wet condition) are heavily dependent on pavement surface texture. Pavement surface texture can be broadly classified into microtexture, macrotexture, megatexture and unevenness (ISO/CD13473, 1994). Microtexture and macrotexture are considered important for skid resistance and tire-pavement friction while unevenness is associated with road roughness and rider comfort. Megatexture generally results in vibration in tire walls but not in vehicle suspension (Wu and Nagi, 1995). Although it is a continuum between macrotexture and unevenness, it has not been generally separated or measured (Wu



and Nagi, 1995). Figure 2.1 illustrates the specific influence of each texture category on tire-pavement interaction.

### **2.2.1.1 Microtexture**

Microtexture is a surface texture irregularity which is measured at the micro-scale of harshness and the scale of irregularities from 0.005 to 0.3mm. The lower limit of this range represents the smaller size of surface irregularities that affects wet friction (Forster, 1990). The definition of the range of microtexture is often controversial (Forster, 1990; PIARC, 1995; ASTM, 2005g). For example, ASTM 867-02a (ASTM, 2005g) states that pavement microtexture is deviations of a pavement surface from the true planar surface with characteristic dimensions of wavelength and amplitude less than 0.5 mm. This definition is the same as that stated in the ISO/CD 13473 where microtexture refers to the peak-to-peak amplitudes varying in the range of 0.001 to 0.5 mm (ISO/CD, 1994). This research adopts the definition of microtexture as stated in the ASTM E 867-02a and the ISO/CD 13473.

Microtexture plays a fundamental role in the skid resistance behavior by locally deforming or even penetrating into the soft rubber material of the tire. A harsh pavement surface has an average microtexture depth of 0.05 mm. It is known to be a function of aggregate particles mineralogy for given conditions of weather effect, traffic action and pavement age (Kokkalis and Panagouli, 1998). On a wet pavement surface, microtexture governs the adhesion component because it controls the intimacy of contact between the rubber and the pavement surface by breaking through the thin water film that remains even after the bulk of the water is displaced. The manner in which microtexture is effective is complex because it affects the molecular and electrical interaction between the contacting surfaces (Kummer, 1966).

### **2.2.1.2 Macrottexture**

Macrottexture is a surface texture irregularity which is measured in millimeters and is usually visible to the eye. Similar to microtexture, there are various definitions of macrottexture

in terms of the range of texture depth. Researchers such as Kokkalis and Panagouli (1998) define macrotexture as irregularities between 0.3 mm and 5.0 mm. ASTM 867-02a (ASTM, 2005g) states that pavement macrotexture is deviations of a pavement surface from the true planar surface with characteristic dimensions of wavelength and amplitude from 0.5 mm to those that can no longer affect tire-pavement interaction. ISO/CD 13473 (1994) adopts a slightly different definition which states that pavement macrotexture is the deviations of a pavement surface with characteristic dimensions of 0.5 mm to 50 mm.

A pavement surface can be considered rough if the average depth of macrotexture is more than 1.0 mm. The harsh asperities of the aggregate are able to penetrate a thin film of water on pavement surface and offer irregularities that help dispel the water between the pavement and tire tread. Inadequate macrotexture can be caused by poor construction, worn aggregates, embedded aggregates or surface bleeding. It leads to dramatically decreased skid resistance, thus increasing accident risk (Kokkalis and Panagouli, 1998).

The macrotexture of asphalt pavement surfaces is mainly attributed to aggregate size, shape, angularity, spacing, and distribution of coarse aggregates (bigger than 2.0 mm). The principle function of pavement macrotexture is to provide, together with tire tread, escape channels for rainwater, which would otherwise be trapped in the tire-pavement contact patch. Deep macrotexture means that the pavement surface has a large void area, which is capable of draining excess water from the tire-pavement contact region. Friction between tire and wet pavement decreases with increasing speed, but deep macrotexture is helpful to lessen the gradient of such decline (Highway Research Board, 1972).

### **2.2.2 Presence of Contaminants**

Under normal operating circumstances, dry friction between the tire and pavement never poses a serious safety problem. However, a serious loss in friction can occur once contaminants such as water from rainfall or oils from fuel leakage are present on a pavement surface. These contaminants act as lubricating agents which cause a loss in friction and the braking ability of the automobiles and aircraft. The presence of such contaminants under

certain operating conditions (i.e. vehicle speed, tire pressure etc.) can lead to the occurrence of hydroplaning.

### 2.2.3 Vehicle Speed

The influence of vehicle or aircraft speed on skid resistance is highly dependent upon the properties of the tire and the pavement surface. Figure 2.2 shows that an increase in vehicle speed causes a decrease in the dry skid resistance for dry pavement. This decrease is gradual as compared to the wet skid resistance which decreases dramatically with increasing speed. The wet skid resistance is also related to other factors such as water film thickness, tire tread pattern and depth, and pavement surface properties. Figure 2.3 highlights the effect of vehicle speed on friction factor for different tires using locked wheel trailer method as stated in ASTM E 274-97 (ASTM, 2005a). This highlights the variability of the skid resistance measured under the influence of different rubber materials for the tires, and the trend of decreasing friction with increasing speed for wetted pavements.

## 2.3 Friction Testing Methodologies

### 2.3.1 Field Measurements

The methods for measuring skid resistance in the field vary widely but can be classified into three groups:

- a) the locked wheel method, producing a skid number ( $SN$ ) as a function of the test speed;
- b) the slip method, producing brake slip numbers ( $BSN$ ) as a function of percent slip and test speed; and
- c) the side-force method, producing side-force coefficients ( $SFC$ ) as a function of yaw angle and test speed.

Standard test procedures for these methods have been developed. For wet-pavement traction evaluation, these procedures have supplanted braked-vehicle tests, such as the ASTM

Method for Stopping Distance on Paved Surfaces Using a Passenger Vehicle Equipped With Full-Scale Tires (ASTM, 2005a) and the ASTM Method for Measurement of Skid Resistance on Paved Surfaces Using a Passenger Vehicle Diagonal Braking Technique (ASTM, 2005e). These braked-vehicle methods are not commonly used for highway evaluations because of the potential interference with traffic and the difficulties of maintaining constant, repeatable, test-vehicle characteristics. The diagonal braking test has seen limited use on runways and has been replaced by slip tests for runway friction. The following measurement methods have been used in practice: diagonal braked vehicle (Horne, 1977), Skiddometer (Zoeppritz, 1977), front locked wheel car (Albert and Walker, 1966), towed trailer (Lander and Williams, 1968), SCRIM (Hosking and Woodford, 1976) and Mu-Meter (Sugg, 1972). A summary of the current practices in skid resistance measurement is shown in Table 2.1 (Henry, 1986; Henry, 2000).

#### **2.3.1.1 Locked Wheel Methods**

The locked-wheel methods provide a coefficient of friction for a standard set of test conditions, which is reported either as a coefficient or as a skid number ( $SN_v$ ) given by Equation (2.3). This method is widely used in the United States chiefly due to its simplicity and its ability to clearly define and control most of the operational variables of the test. The disadvantage of the locked-wheel method for pavement evaluation is that it does not provide a continuous measurement. When the test wheel is intermittently locked for measurement, low friction areas may be overlooked. In addition, in some cases, the test speed must be reduced, such as locations of low radius of curvature, T-intersections, and congested traffic areas. In order to compare these surfaces with tangent surfaces, a correction for speed must be applied. As such, additional measurements are needed, such as texture, or the test must be performed at several speeds to establish the speed dependency of the friction measurement.

#### **2.3.1.2 Slip Methods**

Slip methods produce brake slip numbers ( $BSN$ ), defined as:

$$BSN(v, \% slip) = 100 \frac{F}{N} \quad (2.4)$$

$$\% slip = 100 \left( \frac{v - r\omega}{v} \right) \quad (2.5)$$

where  $v$  is the test speed,  $F$  is the friction force,  $N$  is the normal (vertical) load on the test tire,  $r$  is the effective rolling radius of the tire, and  $\omega$  is the angular velocity of the tire.

Constant-slip devices have the advantage that they can be operated continuously without creating flat spots on the tire. Slip tests, in which the friction forces are recorded during the brake application from the free-rolling condition to the locked-wheel condition, are used in two ways. The peak friction force divided by the vertical load on the test tire provides the peak braking force coefficient. The peak braking force coefficient is highly dependent upon the tire characteristics and is therefore useful for evaluating tires and for determining the performance of anti-lock brake systems. The friction force can be measured as the rotational speed of the tire is reduced to zero. It is then evaluated at various levels of slip to provide a brake slip number for those levels of slip. For example, the Penn State Road friction tester is routinely used in this mode with the friction force evaluated at 25%, 50%, 75% and 100% (locked-wheel) slip levels.

### 2.3.1.3 Side-Force Methods

The side-force coefficient ( $SFC$ ) is the ratio of the force perpendicular to the plane of the rotating tire to the vertical load on the tire when the plane of the tire is maintained at a fixed angle with respect to the forward velocity vector, as shown in Equation (2.6).

$$SFC(v, \alpha_{yaw}) = 100 \frac{F_s}{N} \quad (2.6)$$

where  $v$  is the test speed,  $\alpha_{yaw}$  is the angle between the plane of the test tire and the forward velocity vector (yaw angle),  $N$  is the normal (vertical) load on the test tire, and  $F_s$  is the force perpendicular to the plane of the test tire.

Some systems are capable of operating in a combined slip and side-force mode, but these measurements are usually conducted for research purposes only. The two most popular side-force measurement systems are the Side-Force Coefficient Road Inventory Machine (SCRIM) and the Mu-Meter. The Mu-Meter was developed for runway friction determination. The SCRIM was developed for highway evaluation and has gained popularity in Europe and the British Commonwealth of Nations. Its ability to perform continuous measurements with a narrow test tire, which requires relatively low water flow, is a particularly attractive feature.

### **2.3.2 Laboratory Measurements**

The British Pendulum Tester, developed by the British Road Research Laboratory (1960), is one of the simplest and cheapest instruments used in the measurement of friction characteristics of pavement surfaces in the field as well as in the laboratory. This apparatus measures the frictional resistance between a spring-loaded rubber slider that is mounted on the end of a pendulum arm and the road surface as specified by ASTM standard E303-93 (ASTM 2005b), as shown in Figure 2.4. The widespread use of the British Pendulum Test is probably attributable to two aspects of its design. First, the BPN is directly related to energy loss which is a fundamental physical quantity. Second, the initial velocity between the slider and the surface takes place at velocities of the order of 3 m/s, which is considerably higher than the velocity reached by other small-scale friction testers and is relevant to studies of skid initiation and to the design of anti-locking braking systems (Keith and Cunningham, 1998).

The British Pendulum Tester measures low-speed friction and is commonly used to assess the microtexture of pavement surfaces. At low speeds the adhesion component of friction is dominant. It is primarily a function of the microtexture of the contact surface. The ability of this instrument to aid in the identification of high-risk pavement surfaces has been referred to in several publications (Road Research Laboratory; 1960, Giles et al., 1964; Sabey, 1965). However, the tester has some limitations. Its main limitations in road use are:

- a) its unreliable behavior on coarse rough surfacing (i.e. with chippings larger than 12 mm) (Salt, 1977);

- b) the small area of pavement tested;
- c) the difficulty of carrying out tests in heavily trafficked sites; and
- d) its low measurement speed.

Friction value falls with speed on the majority of surfaces, and typically at different rates for different types of surface. It follows that the pendulum, which by its nature is able to give only one value for one surface in a given condition, cannot indicate the whole of the friction versus speed relationship, or any possible change in order of merit of surfaces with speed. Studies by the Transport and Road Research Laboratory (Giles et al., 1964) have indicated that there is a reasonable correlation between the pendulum measurements and *SFC* at 30 mph but that the correlation is poor at high speeds.

## **2.4 Contact Mechanisms for Dry Tire-Pavement Interaction**

### **2.4.1 Classical Friction Theories**

Many of the basic laws of friction, such as the proportionality of normal force and limiting friction force, are thought to be developed by da Vinci (1452-1519) in the late 15<sup>th</sup> century. Da Vinci introduced for the first time the concept of the coefficient of friction  $\mu$  as the ratio of the frictional resistance to the weight (MacCurdy, 1938). It is noted that the term “force” was not explicitly mentioned until Newton (1642-1727) resolved the situation 200 years later with the publication of the *Principia* which forms the basis of modern sliding friction theories.

Amontons (1699) proposed that surfaces are covered by small spheres and the coefficient of friction is a result of the contact angle between each contacting surfaces of the spheres. Friction is predominately a result of the work done to lift one surface over the roughness of the other, or from the deforming or the wearing of the other surface. His work contributed the first and second laws of friction (commonly known as the Amontons-Coulomb laws) which are:

1. Friction force is proportional to load; and
2. Coefficient of friction is independent of apparent contact area.

Coulomb (1785) later expanded Amontons' findings and found that:

3. Static coefficient of friction is greater than kinetic coefficient of friction.
4. The coefficient of friction is independent of sliding speed.
5. The coefficient of friction is material dependent.

It is noted that these classical laws have survived years without significant amendments until recent times. In fact most of the laws are now found to be incorrect (Moore, 1975). The first law is correct except at high pressure when the actual contact area approaches the apparent contact area in magnitude. However, the remaining laws must be severely qualified. The second law appears to be valid only for materials possessing a definite yield point (such as metals) and does not apply to elastic and visco-elastic materials. The third law does not apply to visco-elastic material. The fourth law is invalid for all materials, though the extent of violation is not as severe in metals as compared to elastomers where visco-elastic properties are dominant. The fifth law is more of an observation rather than a mathematical definition.

Coulomb (1785) also proposed a theory of friction after considering the works by Amontons (1699) on asperity interactions and that by Desaguliers (1734) on cohesion. This is shown in Equation (2.7) for the case of frictional resistance to sliding on horizontal surfaces.

$$F = A + \mu N \quad (2.7)$$

where  $F$  is the friction force,  $A$  is the force attributed to adhesive or cohesive effects, and  $\mu N$  refers to the deformation or ploughing action. He noted that although the cohesive forces are not zero, its contribution to friction could be neglected in practice. Even though Equation (2.7) is found to be defective as stated in the earlier paragraphs and could not explain the abnormally low friction and high load bearing forces found in lubricated surfaces, it is still useful to understand the dry surface contact mechanism from a macroscopic point of view. In fact, modern contact mechanism modeling still employs the Coulomb's laws of friction.

#### **2.4.2 Friction Theories Involving Rubber**

It is noted that rubber does not normally obey the laws of frictions and the coefficient of friction becomes a variable numerical parameter, depending on the real contact area, normal



load, velocity and other factors (Brown, 1996). Rubber friction has been investigated as early as in the 1950s. Gough (1958a, 1958b) described the general characteristics of the friction of rubber and pointed out that the force of friction initially rose rapidly with sliding velocity in the region of creep relative to the counter face, reached a maximum and then fell as the sliding velocity increased. Recognizing that rubber was a visco-elastic material, the study by William et al. (1955) on the relaxation of polymers proved particularly useful in representing friction data at different temperatures and speeds on a single curve. At this stage, the futility of quoting the coefficient of friction of rubber without specifying the conditions was appreciated, recognizing that the range of  $\mu$  could vary from slightly above zero to larger than 3.

Two mechanisms of rubber friction had initially been proposed under non-abrasive conditions: adhesion and deformation. Moore and Geyer (1972) in their review paper of adhesion friction noted that friction force generated between sliding bodies can be written as:

$$F = F_{adh} + F_{def} \quad (2.8)$$

where  $F$  is the frictional force,  $F_{adh}$  is the adhesion term and  $F_{def}$  is the deformation term. The adhesion term can be viewed as a surface effect and may be regarded as occurring to a depth on either surfaces which do not exceed molecular dimensions (i.e. Angstroms units); whereas the deformation term can be classified as a bulk phenomenon having its ultimate effect on the sliding interface.

Veith (1986) further refined the definition to include abrasion or wear through the wear term  $F_{wear}$ :

$$F = F_{adh} + F_{def} + F_{wear} \quad (2.9)$$

For rough and textured hard surfaces, the deformation term is usually dominant, while for smooth surfaces the adhesion term is usually dominant. The wear term depends on the surface texture and the unique conditions that produce the abrasion loss. All three terms are affected in the presence of lubricants.

The true or actual contact area (as distinct from the apparent area) between rubber and a hard counter-surface is also important. The larger this area the greater is the friction. Contact

area depends on surface texture. Rough surfaces have reduced contact areas compared to smooth surfaces and this effect, acting alone, will reduce friction. However, for rubbers that have an appreciable deformation term, an increase in texture will increase the deformation loss and the resulting friction component. The net effect of increased texture is dependent on operational conditions such as sliding velocity, temperature, the presence of lubricants and on the hardness or elastic modulus as well as loss modulus of rubber. Elastic modulus is important for its influence on the true contact area especially on textured surfaces where the draping of the rubber over the asperities is important. Low modulus or hardness yields increased contact area (Veith, 1996).

### **2.4.3 Adhesion**

The adhesion component can be attributed to a bonding of exposed surface atoms between sliding members, the breaking of which requires work. The energy lost in breaking the adhesive bonds is assumed to be not fully compensated for the energy made in re-making them, the difference being mainly exhibited as heat within the rubber. It is this dissipation process that creates difficulties in all adhesion theories of rubber (Veith, 1986).

Adhesion theories can be broadly classified as molecular or macroscopic (Moore and Geyer, 1972). Both views share a common idea that bonds are formed at the sliding interface, strained and then broken but differ in their approaches. The former typically assumed that adhesion between rubber and the hard solids under dry conditions arose mainly of the van der Waals forces and using the Eyring rate theory would show a maximum friction coefficient at a certain speed (Bartenev, 1954; Bowden and Tabor, 1964). However these fail at very low speeds where vanishing friction is predicted when rubber possesses a static coefficient of friction. Macroscopic theories, on the other hand, are based on phenomenological theory which assumes that rubber adhered to the track in domains containing a number of bonds with each domain being able to sustain a small but finite force (Savkoor, 1965). This approach ensures the existence of static friction. Kummer (1966) further attempted to reconcile these views of the adhesion friction into a unified theory where adhesion is attributed to the electrostatic

attraction between the rubber and track. It is noted in these theories that implicitly, a nominally flat sliding surface is assumed. Practical surfaces (such as pavement), however, exhibit microtexture and macrotexture effects as shown in Figure 2.5 and these in turn determine the actual contact area when elastomers is draped over the surface under the action of an applied load.

Pavement researchers believe that microtexture governs the adhesion component (Priyantha and Gary, 1995). On wet pavements and specimens, the adhesion component attributed by frictional force is governed by microtexture in such a manner that intimate contact remains by breaking through the thin water film even after the bulk of water has been displaced. The manner in which microtexture is effective is complex because it affects the molecular and electric interaction between the contacting surfaces (Kummer, 1966; Highway Research Board, 1972).

The influence of speed on the adhesion component of friction is illustrated as shown in Figure 2.6 which compared the frictional performances of two types of surfaces and classified them as (a) adhesion-producing and (b) hysteresis-producing (Kummer and Meyer, 1966). The relative contributions of the adhesion and deformation component of friction change with microtexture and macrotexture of the surface. In the low speed range, the microtexture ensures physical penetration of the interface squeeze-film so that good adhesion is obtained. However, the mechanism of the draping of the elastomers about the individual asperities of the surface is time dependent so that slower speeds permit a greater draping effect and thus ensure a distinctly higher adhesion. In both types of surfaces, the adhesion component is dominant at low speeds (Moore, 1969; Moore, 1972).

Studies by Roberts (1992) and Persson (1998) also showed that the adhesion component is reduced when particles or water film are present at the contact surface. Similarly, the adhesion component can disappear if the surface is completely covered by a lubricant (Highway Research Board, 1972). A theoretical explanation on friction in tire-pavement interaction is offered by Moore, (1972). In the dry case, since the interfacial area has a maximum value, the mechanism of molecular-kinetic bonding is most widespread. However,

upon wetting, the interfacial film of fluid is spread uniformly and this effectively suppresses the electrical roughness of the surface, thereby reducing the adhesion component to a very low value. If the road surface has a high macrotecture, the voids in the asperities can act as reservoirs for the fluid under the wet condition and the pressure distribution at each asperity summit promotes local drainage. There is therefore a greater probability of suitable conditions existing for some adhesion under wet condition for a pavement with some macrotecture as compared to the completely smooth case. This probability would be greatly enhanced if a distinct microtexture at the asperity peaks is also provided. This explains why there is a combined effect of micro- and macrotecture in minimizing the decrease in coefficient of adhesion below the dry value, even though there is still a reduction.

#### **2.4.4 Hysteresis**

Hysteresis is the deformation component of friction which occurs in the case of elastomers when the sliding elastomers “flow” over the rigid asperities of the base and conform to their contours. This is a characteristic feature of frictional behavior of visco-elastic bodies on rigid surfaces. It refers to the internal energy losses that may occur in a body subjected to cyclic stress variation. Hysteresis theories may be divided into three types: elastic and visco-elastic theories; single and multiple element models; and force and energy concepts (Moore and Geyer, 1974).

Early concepts of hysteresis applied elastic theory to the rolling of spheres and cylinders on an elastomeric plane surface (Greenwood and Tabor, 1958) and it was conjectured that a small fraction of the input elastic energy to the deformed elastomers must be dissipated in the form of hysteric friction. This theory is at best applicable to low-speeds sliding and is thus of little significance to practical tire-pavement interaction. Kummer (1966) proposed a unified theory of friction using semi-empirical and generalized equations by analogy. This theory, however, has a severely limited speed range within which it is valid. Hegmon (1969) proposed a relaxation theory of hysteresis based on an energy method of analysis and a simple Maxwell model of visco-elastic behavior. The original work is found to be erroneous, because

of the use of the Kummer's concept and certain assumptions made in the derivations (Moore and Geyer, 1974).

The most significant theory on hysteric friction is due to Yandell (1971) who offered a complex network of spring and dashpot elements or mechano-lattice analogy to explain the frictional resistance of rubber slipping on an irregular lubricated surface. The analysis permits large deformations and any value of Poisson ratio, rigidity or damping factor. Through the use of this model, the contribution of hysteric friction due to microtexture and macrotexture can be identified by the superposition principle. Furthermore it is maintained that in the case of a road surface, there is a multiplicity of superimposed scales of texture, and the resultant hysteric friction force is made up of a large number of friction-speed curves with each having a peak at a different speed (Holla and Yandell, 1976). For a given speed of operation of a vehicle, the total friction force due to hysteresis is a superposition of the contributions from different scales of texture on the road asperities. Even though Yandell indicated that both microtexture and macrotexture affect hysteresis friction, it is believed that the magnitude is controlled by the macrotexture on the pavement surface (Priyantha and Gary, 1995) and the deformation component of friction can disappear on a perfectly smooth surface (Highway Research Board, 1972).

On a skid-resistant pavement the contribution of the deformation component to the total friction is usually small. But when the pavement is slippery it may represent an appreciable percentage of the total. The hysteresis contribution usually is fairly independent of speed in the range in which highway tires are likely to slide. Unlike the adhesive friction component which tends to decrease with speed, the deformation component gains in importance at higher speeds as shown in Figure 2.7 (Moore, 1969). At high speeds, macrotexture is needed to maintain surface-pavement contact in the presence of water film (Shulze and Beckman 1962, Highway Research Board, 1972).

### 2.4.5 Wear

The wear component of friction is attributed to the loss of material from one (or both) surface during the sliding contact that generates the frictional work (Veith, 1986). Moore (1972) identified three distinct mechanisms of rubber wear which are dependent on the nature of the surface texture, namely:

- a) Abrasive wear- A sharp texture in the base surface causes abrasion and tearing of the sliding elastomers.
- b) Fatigue wear- If the base surface has blunt rather than sharp projections, the surface of the elastomers undergoes cyclic deformation and failure eventually occurs as a result of fatigue.
- c) Roll formation- On smooth surfaces, a new mechanism of wear specific to highly elastic materials causes roll formation at the sliding interface and eventual tearing of the rolled fragment.

It is observed that abrasion and fatigue wear occur on rough surfaces, whereas roll formation is characteristic of smooth surfaces having a high coefficient of friction (Reznikovskii and Brodskii, 1967). Abrasion and roll wear are usually very severe, but fatigue wear is relatively mild. In general, all three forms of wear co-exist simultaneously.

Although scientific literature on tread wear versus pavement texture is sparse, a significant contribution was made by Lowne (1970). The tread wear of passenger car tires was measured on a series of test pavements at the Transportation and Road Research Laboratory in the U.K. The tests showed that microtexture is the controlling pavement characteristic in determining the influence of pavement texture on tread wear. Macrottexture played a minor role, with increased macrottexture giving increased wear. Wear rate increases with an increase in temperature or an increase in speed, even though the coefficient of friction decreases with increased temperature or speed. A relatively large amount of rubber is lost at the sliding interface when melting occurs, resulting in a high wear rate.

The presence of lubricants in general reduces the friction of rubber tires to varying degrees. It depends on the type of polymer used and the lubricant involved. Increasing velocity

in the presence of water causes the wear rate to decrease. For sufficiently high velocities, typically more than 1 m/s, the wear rate decreases to a level lower than that obtained under dry condition. This appears to be caused by the hydrodynamic lubricating effect of water since it is accompanied by a decline in friction coefficients to extremely low values (Stachowiak and Batchelor, 2005).

## **2.5 Contact Mechanisms for Wet Tire-Fluid-Pavement Interaction**

The prior section discusses the mechanisms involved in the interaction between a dry tire and a pavement. However, several questions are left unanswered. These theories fail to explain why the coefficient of friction decreases dramatically when the surface is lubricated and also why in the case of hydroplaning, the presence of a thin film of fluid could result in forces large enough to lift the tire from the pavement surface. This section shall explain the classical development of the lubrication theories and the various concepts of lubrication involving rubber, in particular tire-fluid-pavement interaction.

### **2.5.1 Development of Lubrication Theories**

Modern lubrication theories are developed based on Reynolds' hydrodynamic theory of lubrication (Reynolds, 1886) for incompressible fluid. The assumption of incompressible fluid is unnecessary assumption and the effects of compressibility are included in subsequent developments. Reynolds' theory establishes a relationship between the geometry of surfaces, the relative sliding velocity, the property of the fluid and the magnitude of the normal load. Reynolds equation can be derived either from the Navier-Stokes Equations of fluid motion and the continuity equation or from the principles of mass conservation and the laws of viscous flow (Pinkus and Sternlicht, 1961; Cameron, 1976; Gross et al., 1980, Hamrock, 1994; Frene et al., 1997; Szeri, 1998; Bhushan, 1999; Khonsari and Booser, 2001).

Figure 2.8 shows the schematic of fluid flow between two surfaces and stresses acting on a fluid element and the velocities in the x-z plane. Some assumptions are made to derive the

generalized Reynolds equation for the case of slow viscous flow where pressure and viscous terms are predominant. They are:

- a. Surfaces are smooth.
- b. Fluid is Newtonian and laminar.
- c. Inertia forces resulting from acceleration of the liquids and body forces are small compared with the surface (viscous shear) forces and may be neglected.
- d. Surface tension effects are negligible.
- e. Fluid film thickness is small compared to other dimensions.
- f. Pressure, density and viscosity are constant across the film.
- g. No-slip boundary conditions are obeyed at the wall.
- h. Compared with velocity gradients  $\partial u/\partial z$  and  $\partial v/\partial z$ , all the other velocity gradients are negligible since  $u$  and  $v$  are much greater than  $w$  and  $z$  is of a much smaller dimension than  $x$  and  $y$ .

Based on these assumptions, the generalized Reynolds equation is derived as in Equation (2.10) (Bhushan, 1999).

$$\begin{aligned} \frac{\partial}{\partial x} \left( \frac{\rho h^3}{12\eta} \frac{\partial p}{\partial x} \right) + \frac{\partial}{\partial y} \left( \frac{\rho h^3}{12\eta} \frac{\partial p}{\partial y} \right) = \frac{\partial}{\partial x} \left[ \frac{\rho h (u_a + u_b)}{2} \right] + \frac{\partial}{\partial y} \left[ \frac{\rho h (v_a + v_b)}{2} \right] \\ + \rho \left[ (w_a + w_b) - u_a \frac{\partial h}{\partial x} - v_a \frac{\partial h}{\partial y} \right] + h \frac{\partial \rho}{\partial t} \end{aligned} \quad (2.10)$$

where  $u_a, v_a$  are velocity components of the upper surface;  $u_b, v_b$  are velocity components of the lower surface along the  $x$  and  $y$  axes respectively;  $h$  is the fluid film thickness;  $\rho$  is the density of the fluid,  $\eta$  is the dynamic viscosity of the fluid and  $t$  is the time. This provides a general relationship between the film thickness and the fluid pressure. There is no general closed form solution to this equation. Boundary conditions and other simplifications are required to solve the Reynolds equations by numerical methods (Bhushan, 2002). This also gives rise to various form of lubrication such as hydrodynamic lubrication and elasto-hydrodynamic lubrication. Only boundary lubrication could not be attributed to the Reynolds equation.



### 2.5.1.1 Hydrodynamic Lubrication

The generalized Reynolds equation is the basis of hydrodynamic lubrication and it consists of three terms of which load support is contributed, namely the wedge term, the stretch term and the squeeze film term as shown in Equations (2.11) to (2.13) respectively.

$$\text{Wedge term} = 6h(u_a - u_b) \frac{\partial \rho}{\partial x} + 6\rho(u_a - u_b) \frac{\partial h}{\partial x} + 6h(v_a - v_b) \frac{\partial \rho}{\partial y} + 6\rho(v_a - v_b) \frac{\partial h}{\partial y} \quad (2.11)$$

$$\text{Stretch term} = 6\rho h \frac{\partial}{\partial x} (u_a - u_b) + 6\rho h \frac{\partial}{\partial y} (v_a - v_b) \quad (2.12)$$

$$\text{Squeeze film term} = 12 \frac{\partial(\rho h)}{\partial t} \quad (2.13)$$

where  $u_a$ ,  $v_a$  are velocity components of the upper surface;  $u_b$ ,  $v_b$  are velocity components of the lower surface along the  $x$  and  $y$  axes respectively;  $h$  is the fluid film thickness;  $\rho$  is the density of the fluid,  $\eta$  is the dynamic viscosity of the fluid and  $t$  is the time. Of these three terms, the wedge term appears to be the most important in hydroplaning studies due to the facts that there will always be consistent film thickness variations along the  $x$  and  $y$ -axis and the possibilities of the absence of squeeze motion and negligence of the stretch term (Moore, 1975). This is shown in Equation (2.11) where the first and third terms are due to density variations and the second and last terms are due to changes in  $h$  with increasing  $x$ .

It is noted that hydrodynamic lubrication is subjected to the effects of surface roughness. For smooth surfaces, load support due to hydrodynamic lubrication is due to pressure generation from the wedge, stretch and squeeze terms as shown in Table 2.2 (Moore, 1975). For example, a sliding tire over a smooth pavement surface will exhibit a stretch term (due to relative velocity variations) and wedge terms (due to film thickness variations). The introduction of surface roughness causes an additional of at least four contributions to load support on a macroscopic scale, namely directional effect, macro-elasto-hydrodynamic effects, cavitation effects, and viscosity effects as shown in Table 2.3 (Moore, 1975). The directional effect gives rise to changes in positive and negative pressure increments which affects the net load support. One example is the pavement wear at approaches to traffic signals or speed

reducing obstacles. In such situation, the predominant braking mode of the vehicle and the tire behavior will eventually cause a small positive directional effect. This will be especially useful in wet weathers where a small negative load support is produced, assuming a locked wheel braking action. This would thus increase traction and the hydroplaning speed. The macro-elasto-hydrodynamic effect is in essence elasto-hydrodynamic lubrication and is discussed in the next sub-section. If the asperities are flexible, then the generation of pressure would distort the asperities creating an increase or decrease of load support depending on the directional effect. Cavitation effects destroy the contribution to pressure to negative load support since the liquid could only sustain a modest state of tension before bubble formation. Viscosity effect occurs due to the fact that viscosity varies with temperature and pressure. It is noted that viscosity is sensitive to temperature change (extremely so for lubricating oils). It can be shown that the pressure dependence of the viscosity produces an additional load support, though minute, and the temperature sensitivity has an opposite effect.

### **2.5.1.2 Elasto-hydrodynamic Lubrication**

Elasto-hydrodynamic lubrication is the study of situations in which elastic deformation of the surrounding solids play a significant role in the hydrodynamic lubrication process. Two significant effects which occur in elasto-hydrodynamic lubrication but are not accounted for in the classical theory are the (a) influence of high pressure on the viscosity of the liquid lubricants and (b) substantial local deformation of the elastic solids. These will drastically change the geometry of the lubricating film and affects the pressure distribution. In essence, the hydrodynamic pressure generation must match the elastic pressure in the contacting solids. One such application is the tire sliding or rolling on wet roads.

The elasto-hydrodynamic problem involves an iterative procedure to establish a compatibility between the hydrodynamic pressure generated in the lubrication films which separates the bodies (elastic-elastic or elastic-rigid) in relative motion and the elastic pressures developed between the bodies as a result of the virtual contact. The general iterative procedure

is illustrated in Figure 2.9. A film thickness distribution is first assumed, inserted into Reynolds equation to generate the pressure and the pressure distribution is inserted into the elastic equation to obtain the displacements until both the displacement predicted by the elastic theory and the film thickness distribution matches.

The elasto-hydrodynamic lubrication makes use of the elastic theory and Reynolds equation. In cases involving polymers as a sliding surface (such as tires), in order to account for both the elastic effects and hysteresis effects, the use of visco-elastic theory is more appropriate with the Reynolds equation to model the visco-elastic-hydrodynamic lubrication effect (Moore, 1975).

### **2.5.1.3 Boundary Lubrication**

Fully hydrodynamic lubrication presupposes that the presence of fluid completely separates two surfaces. Since the solid parts do not touch, there can be no wear and the viscosity of the fluid determines the coefficient of friction. This occurs when the “film” is of molecules thick, where the Reynolds equation breaks down. The film is formed normally by physical absorption of the fluid, chemical absorption or chemical reaction (Bhushan, 2002).

Moore (1975) showed that for boundary lubrication of elastomers under low speed, if the hysteresis effects are ignored, the frictional force of an elastomers moving over a thin interfacial film can be effectively modeled by the simple adhesion theory. In this case, the coefficient of friction in the boundary lubrication would be approximately the same as the dry coefficient of friction.

For metallic surfaces, the introduction of boundary lubrication would render the coefficient of friction to be considerably less than the dry coefficient of friction but the situation is not clear in the situation of elastomers in the event of high travel speed. This is due to the fact that the magnitude of the hysteresis component of the dry and wet friction coefficients becomes uncertain especially when both are appreciable at higher speeds and the dry coefficient of friction would be subjected to a higher operating temperature. This is further

complicated by the fact that hydrodynamic lubrication will start to occur and leads to a reduction in the coefficient of friction.

## 2.5.2 Friction Mechanisms in Tire-Water-Pavement Interaction

Veith (1983) developed a simple tire wet traction model based on two sources of information: (1) the basic lubricated rubber friction modes as developed from the lubrication theories described in Section 2.5.1, and (2) a simplified picture of the mechanics of water-tire interaction on a wet surface. It was proposed that there were three types of friction modes, namely the boundary lubrication, elasto-hydrodynamic lubrication and mixed lubrication mode (a transition regime from elasto-hydrodynamic lubrication to boundary lubrication).

### 2.5.2.1 Friction Modes in Wet Tire-Pavement Interaction

Lubricated friction as proposed by Veith (1983) is basically of two types, as illustrated in Figures 2.10 and 2.11. Boundary layer friction occurs when the bodies are in relatively intimate asperity contact with a film of lubricant only of a few molecular layers thick separating the asperities. As shown in Figure 2.10, this mode occurs only under low velocity conditions,  $V_1$  and produces a fairly large frictional force,  $F_1$ .

The opposite situation is shown in Figure 2.11. Here the velocity,  $V_2$  is high and if rubber is the upper surface, two phenomena can be investigated. First, an elastic indentation of the rubber develops due to lubricant accumulating at the leading edge of the upper body. The inertia and viscosity-induced retardation of lubricant displacement caused the attendant indentation. Second, this accumulation generates an upward pressure  $P_2$  which accounts for a drastic reduction in friction force  $F_2$ . The latter situation is actually the occurrence of elasto-hydrodynamic lubrication as described in Section 2.5.1.2. With higher velocity, the entire body would be in the full hydrodynamic lubrication regime, which means completely no boundary-type contacts. The full separation leads to the normal force to be borne by fluid pressure with very low frictional force and this condition is known as hydroplaning. These phenomena and the associated theory had also been discussed previously by Hersy (1966) and Dowson (1969).

These two modes are representative of the extreme bounds of the velocity, the former occurring under low velocity conditions and the latter occurring at high velocity condition. Apart from these two modes, there is another intermediate velocity situation, which is also shown in Figure 2.11. The left side of the upper body in the figure illustrates boundary friction contact. The situation depicted in this figure had been defined as a mixed lubrication mode: partial boundary. At intermediate velocities, mixed lubrication mode governs.

### **2.5.2.2 Mechanism of Tire Sliding on Wet Pavement**

The lubrication mode concept clarifies the three-zone concept proposed by Gough (1959) and Moore (1966) later carried the concept further to cover the case of a locked sliding tire. The three zones are illustrated in Figure 2.12. This conceptual model has been useful to understand the effect of water and travel speed on skid resistance and hydroplaning. The zones are described as follows:

#### Zone A: Sinkage, or Squeeze-Film Zone

Under wet condition, the forward part of the contact area under dry condition would float on a thin film of water. It is formed due to the displacement inertia of the intercepted water film. This corresponds to the extreme situation previously described, namely the elasto-hydrodynamic lubrication. The frictional force developed is strongly dependent on the bulk properties of the lubricant, mainly the viscosity and velocity gradient in the lubricant film.

Hydroplaning occurs when the total hydrodynamic lift force acting on the tire equals the sum of the weight of the tire plus the downward vertical loading upon it (Browne, 1975). As either speed or water film thickness increases, the fully developed Zone A would replace both Zone B and Zone C and the tire would eventually appear as skidding on the film of water.

#### Zone B: Draping/ Transition Zone

The draping zone begins when the tire elements, having penetrated the squeeze film, start to drape over the major asperities of the surface and make contact with the lesser asperities. A mixed lubrication regime exists, which is called a partial boundary. Partial

dynamic hydroplaning may occur at ordinary speeds, when the uplift forces are not great enough to develop a full dynamic hydroplaning (Balmer and Gallaway, 1983).

#### Zone C: Actual contact, or Traction Zone

This is the region where the tire elements, after draping, having attained a vertical equilibrium position on the surface. In this position, boundary-layer lubrication becomes dominant and results in an intimate contact between the tire and pavement. The length of this region depends on vehicle velocity. The frictional force is a function of the properties of the contacting solids and of the lubricant at their common interface.

## **2.6 Hydroplaning**

### **2.6.1 Forms of Hydroplaning**

There are three main types of hydroplaning, namely dynamic hydroplaning, viscous hydroplaning and reverted-rubber hydroplaning. The following sub-sections shall describe briefly each form of hydroplaning.

#### **2.6.2.1 Dynamic Hydroplaning**

Dynamic hydroplaning occurs during driving on a puddle or flooded pavement when the inertial forces in the fluid film are sufficient to completely separate the vehicle tires from the pavement surface (Horne and Dreher, 1963; Browne, 1975). For this situation to exist, the amount of fluid encountered by the tire must exceed the combined drainage capacity of the tread pattern and the pavement macrotexture. In addition, the vehicle velocity must be sufficiently high so that the inertial force developed in the fluid film is comparable to the tire inflation pressure. This causes the tire surface to buckle, thereby produces a large region of fluid capable to support the loaded tire. In terms of the skid resistance mechanisms highlighted in the previous section, dynamic hydroplaning is said to occur when zone C and Zone B disappears and the bulk water penetrates the entire footprint (Zone A). This creates a situation where the vehicle experiences low (or near-zero) coefficient of friction and the uplift force in the fluid film is sufficiently large to cause a loss of contact between the tire and the pavement.

Most hydroplaning researchers simply refer hydroplaning to dynamic hydroplaning as it is the most common form encountered on highways and runways.

### **2.6.2.2 Viscous Hydroplaning**

Viscous hydroplaning occurs only on surfaces where there is very little microtexture. A thin film of fluid remains between tire and pavement since there is insufficient pavement microtexture to cause its breakdown. Viscous hydroplaning can occur at any speed and with any fluid film depth. Therefore sufficient microtexture on pavement surfaces is helpful to prevent viscous hydroplaning. This could occur even if the pavement is moist and only Zone C in the wet skid resistance mechanism is present.

### **2.6.2.3 Reverted-Rubber Hydroplaning**

Reverted rubber hydroplaning only occurs when large vehicles such as trucks or aircraft lock their wheels when moving at high speeds on wet pavements with high macrotexture but little microtexture. Heat built up in the tread rubber upon sliding on the pavement causes the rubber to revert and melt. The tire then slides along on a cushion of molten rubber, water and steam (Horne et al., 1969). As such this form of hydroplaning not only includes the wet traction mechanisms, but also involves the wear mechanism of rubber under high operating temperatures.

Reverted rubber hydroplaning is limited to aircraft using high tire inflation pressure. This phenomenon is not observed for ground vehicles with low tire pressure of less than 165 kPa when the wheels are locked. Reverted rubber hydroplaning develops only when prolonged wheel lockups occur. Thus, the avoidance of reverted rubber hydroplaning involves improving the pilot braking procedure and the locked-wheel protection circuits of the aircraft antiskid braking systems (Horne et al., 1976).

## 2.6.2 Manifestations of Hydroplaning

Eight types of phenomena or manifestations which indicate when a tire is hydroplaning have been identified in research conducted by Horne and Dreher (1963). They are:

a) Detachment of tire footprint. It was shown in hydroplaning studies made with the NASA Langley landing load trucks (Horne and Leland, 1962) that as the ground speed increases, a wedge of fluid progressively penetrates the tire-ground contact region and a hydrodynamic pressure is developed between the tire and ground. The resulting hydrodynamic lift tends to detach the tire footprint from the runway surface.

b) Changes in ground hydrodynamic pressure. Tire hydroplaning speed is defined as the ground speed at which the hydrodynamic lift acting on the tires becomes equal to the weight of the vehicle, i.e. the average hydrodynamic pressure in the tire footprint region is equal to the tire pressure. Up till today, there is still no accurate measurement of the ground hydrodynamic pressure on the tire surface. Nevertheless, inferences are now widely made based on the ground hydrodynamic pressure with the aid of pressure gage under the centre-line of the tire path. This technique showed that (1) the ground hydrodynamic pressure develops ahead of the initial tire-ground contact point due to the action of the tire bow wave; (2) the peak ground hydrodynamic pressure is considerably higher than the tire pressure for the 85-knot ground speed signature; and (3) near negligible ground hydrodynamic pressure is observed at the rear of the wheel. It is noted that the first point indicates the involvement of fluid dynamics of fluid flow around an obstacle. The second point indicates the existence of tire buckling. The third point is not understood and could not be explained even till today.

c) Spin-down or stopping of wheel rotation. It is noted that free-rolling tires slow down or stop rotating under hydroplaning. This can be explained due to the moment created from the ground hydrodynamic pressure distribution that is opposite to the rotation.



- d) Suppression of tire bow-wave or spray. It is shown that a large bow-wave forms in front of the tire for all ground speeds below hydroplaning speed and it reduces with increasing speed until at some high speed beyond hydroplaning speed, the bow-wave disappears (Horne and Leland, 1962; Sommers et al., 1962).
- e) Scouring action of escaping fluid in tire-ground footprint region. The escaping fluid under the action of high hydrodynamic pressure tends to clean the runway surface in the tire path (Horne and Leland, 1962).
- f) Peaking of fluid displacement drag. It was shown experimentally that fluid displacement drag reaches a maximum at a ground speed near the tire hydroplaning speed and speeds above the critical hydroplaning speed results in appreciable reductions in drag (Sommers et al., 1962). This is attributed to tires being lifted off the pavement surface resulting in less fluid being displaced.
- g) Loss in braking traction. It is noted that for pavement surface that is flooded with slush or water to depths large enough to initiate tire hydroplaning, the braking traction loss are catastrophic at speeds near or in excess of the hydroplaning speed.
- h) Loss in directional stability. It is noted that there is a loss in directional stability during hydroplaning in studies conducted by the Federal Aviation Administration (Sommers et al., 1962). This loss is noted to be serious for aircrafts when landing or taking off in the presence of high cross winds.

## **2.7 Modeling of Hydroplaning**

Hydroplaning modeling to date can be broadly classified into two main categories: experimental and analytical/numerical approaches. The former involves conducting experiments and derives qualitative or empirical relationships to relate the hydroplaning speed with different measurable parameters, while the latter involve the use of friction and lubrication theories to deriving the hydroplaning speed analytically or numerically. The following sub-sections shall describe the research development in these two categories.

### 2.7.1 Experimental/Empirical Approach in Hydroplaning Studies

Numerous experimental investigations of dynamic hydroplaning have been conducted in an attempt to increase the knowledge of the phenomenon and to determine ways to reduce the frequency of occurrence. Experimental studies have been done with much success (Horne and Dreher, 1963; Horne and Joyner, 1965; Yeager and Tuttle, 1972). Insight into these experiments led to the use of pavement grooving (Mosher, 1969) and air-jets (Horne and Joyner, 1965) to reduce the occurrence of dynamic hydroplaning. In particular, the experimental approach has allowed researchers to understand how different factors can affect hydroplaning, be it qualitatively or quantitatively in the form of empirical models. The major findings from the different experimental studies are summarized in the following subsections:

#### 2.7.1.1 Studies on the Effect of Depth of Fluid on Hydroplaning

Dynamic hydroplaning could not occur below certain minimum fluid depth on a pavement surface. However, this minimum fluid depth is difficult to define due to the large effects of other parameters such as the tire tread depth and the macro- and microtexture of the pavement surface. For tires with comparatively smooth belt surface and smooth tread, hydroplaning occurs at fluid depths as low as 0.02 in. (0.508 mm) to 0.09 in. (2.286 mm) (Harrin, 1958; Harrin, 1960). For full scale aircraft tires on a relatively smooth test track flooded with water, the fluid depth varied from 0.1 in. (2.54 mm) to 0.4 in. (10.16 mm) (average depth approximates 0.3 in. or 7.62 mm)(Horne and Leland, 1962).

Agrawal and Henry (1977) performed experiments on locked sliding tires on pavement with water film thickness less than 2.4 mm (0.095 in.). Using the 18 data points obtained from the experiments, the hydroplaning speed is determined by Equation (2.14).

$$v_p = 33.7 + 5.28(t_w)^{-0.5} \quad (2.14)$$

where  $v_p$  is the hydroplaning speed in mph and  $t_w$  is the water film thickness in inch.

Gallaway et al. (1979) also performed experiments using the spin-down technique for rolling tires using 1038 data points with variations in spin-down, tire pressure, tread depths,

water-film thickness and mean texture depth of the pavement surface. They developed a regression relationship as shown in Equation (2.15).

$$v_p = (SD)^{0.04} (p)^{0.3} (TRD + 1)^{0.06} A \quad (2.15)$$

where A is the greater of  $\left[ \frac{10.409}{t_w^{0.06}} + 3.507 \right]$  or  $\left[ \frac{28.952}{t_w^{0.06}} - 7.817 \right] (MTD)^{0.14}$  and  $v_p$  is the hydroplaning speed in mph,  $SD$  is the spin-down in %,  $t_w$  is the water-film thickness in inch,  $MTD$  is the mean texture depth in inch,  $TRD$  is the tire tread depth in 1/32 inch.

For a smooth ASTM tire with 165.5 kPa (24 psi) inflation pressure and assuming that hydroplaning occurs at 90% spindown, Equation (2.15) can be further simplified to give Equation (2.16).

$$v_p = 3.09A \quad (2.16)$$

where A is the greater of  $\left[ \frac{10.409}{t_w^{0.06}} + 3.507 \right]$  or  $\left[ \frac{28.952}{t_w^{0.06}} - 7.817 \right] (MTD)^{0.14}$ .

These empirical hydroplaning speed models to relate the hydroplaning speed and the water film thickness are further refined by Huebner et al. (1986). Huebner et al. (1986) proposed the use of Equation (2.17), which is a modification of Equation (2.14), for water-film thickness below 2.4 mm and the use of Equation (2.16) for water-film thickness above 2.4 mm.

$$v_p = 26.04(t_w)^{-0.259} \quad (2.17)$$

These models predict the hydroplaning speed based on the water film thickness above the mean texture depth MTD as determined from the sand patch test or micro profile measurements. However, Anderson et al. (1998) noted that these models are empirical in nature but nevertheless they represent the state of the art at that time and are used in the design of pavements for surface drainage.

### 2.7.1.2 Studies on the Effect of Tire Inflation Pressure on Hydroplaning

Tire inflation pressure appears to be the most important single parameter that determines the hydroplaning speed (Horne and Dreher, 1963). Research with the Langley landing loads tracks involving bogie and nose-gear studies indicated the well known NASA hydroplaning equation as shown in Equation (2.18).

$$v_p = 6.36\sqrt{p_t} \quad (2.18)$$

where the  $p_t$  is the tire inflation pressure in kPa and  $v_p$  is the hydroplaning speed in km/h, or alternatively,

$$v_p = 9\sqrt{p_t} \quad (2.19)$$

where  $p_t$  is the tire inflation pressure in psi and  $v_p$  is the hydroplaning speed in knots. The hydroplaning speeds obtained are valid for smooth and closed pattern tread tires which do not provide escape paths for the tires, and for rib tread tires on fluid covered runways where the fluid depth exceeds the groove depths in the tread of the tires.

The above equation is derived from dimensional analyses (Horne and Leland, 1962) and based on three main assumptions:

- a) The ratio of the uplift force to the nominal footprint contact area can be approximated by the tire inflation pressure. This assumption is reasonable if there is complete separation between the tire and the pavement by the fluid as in the case of dynamic hydroplaning. This indicates that the equation can only be used for dynamic hydroplaning.
- b) Runway fluids have densities approaching that of water. This assumption implies that the hydroplaning speed would not be valid if the fluid is slush or is contaminated with lubricating oils. This means that there should be a density effect of the fluid on the hydroplaning speed.
- c) Based on hydroplaning experiments conducted by Horne and Leland (1962), in order to fit the calculated and experimental hydroplaning speeds, a recovery factor (defined as  $P_{av}/0.5\rho U^2$ , where  $P_{av}$  is the average ground hydrodynamic pressure,  $\rho$

is the density of the fluid and  $U$  is the vehicle speed) of 0.7 has to be assumed. It is this assumption that led to the empirical nature of the NASA hydroplaning equation, since the experimental hydroplaning speed is largely dependent on other factors such as pavement surface parameters, tire parameters, temperature etc.

### **2.7.1.3 Studies on the Effect of Tire Tread Design on Hydroplaning**

Experimental studies have found that tire tread design has two effects on hydroplaning speed (Horne and Dreher, 1963). First, adequate tread designs, such as circumferential ribs, tend to require higher ground speeds for hydroplaning than smooth tread tires (Harrin, 1958; Horne and Leland, 1962). Second, good tread designs tend to increase the minimum fluid depth required for hydroplaning. The loss in braking traction due to partial hydroplaning effects is considerably less for rib-tread tires than for smooth-tread tires even when the fluid depth on the pavement surface is greater than the tread groove depth. Sipe systems are also used to enhance the tread grooves dispersal functions by channeling water into the tread grooves and their design create pressure surges along the edge. This makes the tire more effective on wet surfaces (Michelin, 2001). This is of a key concern of tire engineers and numerical research today is geared towards developing tire tread designs to delay hydroplaning and to improve traction (Williams and Evans, 1983; Zmindak and Grajciar, 1997; Okano and Koishi, 2000; Michelin, 2001).

### **2.7.1.4 Studies on the Effect of Vertical Load on Hydroplaning**

It has been found that increasing the vertical load has only a small effect on the tire hydroplaning speed (Horne and Dreher, 1963). This is because the tire acts as an elastic body and changes in vertical load on the tire will produce a corresponding change in the tire footprint area such that the tire inflation pressure remains approximately constant. It is noted that increasing the aircraft tire from zero load to maximum static load only increase the tire inflation pressure by 3% to 4% and the hydroplaning speed by less than 2%.

### 2.7.1.5 Studies on the Effect of Tire-Footprint Aspect Ratio on Hydroplaning

Horne et al. (1986) studied the effect of tire aspect ratio on the dynamic hydroplaning speed and proposed the following relationship based on curve-fitting approach on the experimental data conducted on truck tires.

$$v_p = 23.3 p_t^{0.21} \left( \frac{1.4}{FAR} \right)^{0.5} \quad (2.20)$$

where  $v_p$  is the hydroplaning speed in mph,  $p_t$  is the tire inflation pressure in psi and  $FAR$  is the tire footprint aspect ratio (width divided by length). This equation is based on limited test results for use of ground vehicles with pneumatic tires that exhibit a large range of tire footprint aspect ratio for different inflation pressure and vertical loads. It is explained that the NASA hydroplaning equation is valid for aircraft tires, since the aircraft-tire footprint aspect ratio appears to be nearly constant through the normal aircraft operating load and inflation pressure range.

Horne et al. (1986) also found that hydroplaning speed is also dependent on the tire footprint aspect ratio based on experiments conducted on ASTM E501 (ribbed) tires (ASTM 2005d), ASTM E524 (smooth) tires (ASTM 2005f), and worn truck tires traveling on flooded pavement surface:

$$v_p = 51.80 - 17.15 FAR + 0.72 p_t \quad (2.21)$$

where  $FAR$  is the footprint aspect ratio (defined as the width of the footprint divided by its length) and  $p_t$  is the tire inflation pressure in psi.

### 2.7.1.6 Studies on the Effect of Pavement Surface Texture on Hydroplaning

Balmer and Gallaway (1983) suggested that pavements with coarse surface texture or finish could improve wet traction and reduce hydroplaning occurrences. Figure 2.13 shows that the skid numbers on wet PCC pavements are higher for transverse textures than for longitudinal textures and is more pronounced for higher speeds. It was suggested that transverse macrotexture contributed more to the hysteresis friction to tires as compared to longitudinal macrotexture and this frictional component increases with speed. In comparison

with the longitudinal texture, transverse texture, aligned with the direction of cross slope, provides (1) a better surface drainage of the pavement as a whole; (2) more effective water expulsion between the tire and the pavement because of shorter relief passageways; and (3) less forward motion of water that produces the water wedge to cause hydroplaning.

Studies conducted by Horne and Dreher (1963) also noted that “a rough or open textured surface required a greater depth of fluid for hydroplaning to occur because of more paths for the trapped water to escape”. In this case, no differentiation was made between macrotexture and microtexture. Horne (1977) stated that pavement with a good microtexture is a major mean to combat viscous hydroplaning and pavement with good macrotexture can delay hydroplaning.

#### **2.7.1.7 Studies on the Effect of Pavement Grooving on Hydroplaning**

It has been shown experimentally that transverse pavement grooving (with respect to vehicle motion) can substantially increase the water depth required for hydroplaning to occur. Tests conducted by Yager (1969) on aircraft tires showed that transverse runway grooves provide (1) substantially increased aircraft braking capability and directional control, (2) improved runway surface water drainage, and (3) more rapid wheel spin-up rates. They also reduce tire wear and the susceptibility to dynamic hydroplaning and reverted rubber hydroplaning. These findings are consistent with other research focused on aircraft hydroplaning and runway skid resistance (Shilling, 1969; Pelloli, 1977) and thus lead to the use of transverse grooving in runways as a measure to combat hydroplaning (FAA, 1997).

While transverse grooving is widely accepted in alleviating hydroplaning and skid resistance problems on runways, the use of longitudinal grooving or transverse grooving on highways is often controversial. The use of transverse grooving exhibits significant improvement in traction control and reduction in hydroplaning occurrences as expected in the runways. However, the use of longitudinal grooving showed little or no improvement in traction but was found to cause reductions in hydroplaning occurrences (Horne, 1969; Caltrans, 1978; FHWA, 1978; FHWA, 1980; ACI, 1988; PTI, 1988). Longitudinal grooving is

often favored by highway agencies as only one lane at a time needs to be closed during maintenance, unlike transverse grooving where the whole road section have to be closed, thereby posing extreme traffic problems (Highway Research Board, 1972; FHWA, 1978; PTI, 1988).

### **2.7.2 Analytical/Numerical Modeling of Hydroplaning**

It is noted that the experimental and empirical approach in hydroplaning studies has yielded valuable information on the various parameters that can affect hydroplaning and helps in the formulation of strategies to reduce hydroplaning occurrences. However, the qualitative and empirical models have done little in advancing pavement researchers' understanding on the mechanisms involved in hydroplaning. Thus researchers have also looked into the problem from an analytical and numerical perspective since the 1960s.

The first analytical treatment of the hydroplaning problem was proposed by Moore (1967) in his discussion of the theory of viscous hydroplaning. In this analysis, a rubber sliding on a two-dimensional smooth sinusoidal asperity separated by a thin fluid film is modeled. A one-dimensional Reynolds equation solution was obtained in which inlet, central and outlet regions for the fluid film were treated separately. Correlation was obtained with expected values for load capacity, friction level and minimum clearance by the inclusion of many empirical constants in the formulation. The main weaknesses of the method are that many assumptions on the nature of the problem had to be made; there are limitations due to a two-dimensional asperity and a lack of consideration of side flow. This theory is thus strictly limited to the viscous hydroplaning situation.

Subsequent works in the theoretical and numerical modeling in the next two decades were sponsored by NASA. Martin (1966) considered the two-dimensional irrotational flow problems of rigid curved surfaces of arbitrary shape planning on an incompressible viscid fluid. Potential flow theory was employed and conformal mapping techniques were used to obtain the solution. A recovery factor of 0.8 was obtained as compared to 0.644 for NASA. However, when the proper approximations were added to his theory so that the results could be



applied to finite aspect-ratio surfaces, the lift coefficient dropped considerably below that of NASA (Browne, 1971). This is due to the fact that side flow and viscosity were totally neglected in his analysis, resulting in no formation of bow-wave, and the fact that no variation in gap in the direction perpendicular to the flow was incorporated.

Eshel (1967) considered the total dynamic hydroplaning using a three-region approach. Different simplifying assumptions were made to the nature of the flow in each region. The solutions obtained were coupled at the regional boundaries. Simple models of tire flexibility were coupled to the system to allow an elasto-hydrodynamic system. However, the model failed to consider the side flow in the inlet region under the wheel. Furthermore, the treatment of the problem as a two-dimensional problem is inappropriate. The assumption of a laminar parabolic velocity profile is not accurate as Browne (1971) has shown the flow to be turbulent.

Tsakonas et al. (1968) took a purely inviscid approach using the hydrofoil theory to solve the problem of a flat rigid surface of small aspect ratio in extremely shallow water. The only case for which a solution was obtained was for a plane flat rigid plate of low aspect ratio under which the pressure distribution of the pavement was a step function equal to the inflation pressure. However, this method is not appropriate because (1) the lift coefficient was small compared to experimentally measured values such as those by NASA; (2) the use of the inviscid theory is invalid for hydroplaning; and (3) the real tire deformation profile is never planar.

Browne (1971) proposed a two-dimensional treatment for a three-dimensional tire deformation model for hydroplaning, making use of the Navier-Stokes equations. In his model, inviscid, laminar and turbulent models were explored, and side flow was considered. The later parts of his work made use of solely the laminar flow model in the hydroplaning simulation. However this method is not entirely appropriate since (1) the flow in the hydroplaning situation is turbulent (Schlichting, 1960); (2) the recovery factors of 0.56 in his model is low compared to the NASA experimentally measured values of about 0.644; (3) the model

verification made use of a plane of symmetry in his experimental works and yet uses a laminar flow and pavement surface in his numerical verification.

Browne and Whicker (1983) extended the analysis to include tire deformation by considering the interaction of the fluid flow module and the tire deformation module in the interactive procedure. This is one of the first numerical models of dynamic hydroplaning. However, as explained in the preceding paragraph, the fluid flow model is plagued with the inability to model the NASA hydroplaning relationship.

Recent advances in computational fluid dynamics have prompted researchers to re-look into the problem of hydroplaning. Researchers began to analyze the problem of hydroplaning using two-phase flow. Groger and Weis (1996) proposed a simple mathematical two-phase model to describe the shape of the free-surface of the water around an automobile tire. Water was assumed to be incompressible and fully turbulent. The Navier-Stokes equations were solved using the finite-volume method (FVM). However, the model did not consider the effects of tire deformation during hydroplaning. Similarly, the research done by Aksenov and Dyadkin (1996) also neglected the effect of the tire deformation profile during hydroplaning.

The development of technology in fluid structure simulation has led to the use of commercial computer packages to model hydroplaning. Zmindar and Gradjar (1997) employed the ADINA fluid structure interaction package to simulate the aquaplaning of a tire using the finite element method (FEM). Although the idea was rather innovative, the flow was assumed to be laminar and there was no verification with any experimental data or the NASA equation. Okano and Koishi (2000) made use of MSC.DYTRAN to simulate hydroplaning through fluid-structure interaction. However this study suffered a drawback in that the fluid flow was modeled using the potential flow theory. It is noted that recent research in this field is propelled by the tire industry whose main aim is to produce better tire tread design. No attention is being paid to the pavement surface characteristics and its influence to hydroplaning.

Andren and Jolkin (2003) made use of Reynolds equation without consideration of the stretch term and coupled it with ABAQUS finite element package for the tire deformation

profile in an attempt to model viscous hydroplaning. Smooth surfaces were assumed, i.e. zero microtexture depth. The analyses gave results that are rather incomprehensible since it showed that hydroplaning could not occur in speed from 0 to 200 km/h and the speed had to be increased to  $1.6 \times 10^3$  m/s (5760 km/h) for the first full film regime to occur. Such findings could be due to a few problems. First, neglecting the asperities in micro-scale would cause the wedge effect developed by the film in micro-scale to be ignored and since viscous hydroplaning is a phenomenon associated with the microtexture of a plane surface, the assumption of a smooth surface is inappropriate. Second, the use of water as a lubricant could also cause complications. One would expect viscous hydroplaning to occur when the surface is slippery and this phenomenon tends to be associated with oil contaminated surface, rather than water. Unlike water whose density and viscosity are relatively stable at room temperature, oils have density and viscosity which vary with pressure even at room temperature. This would result in viscous hydroplaning at much lower speeds since the uplift force capable of separating the tire and asperity could be achieved when there is a thin film (of the order of micron and nanometers) of oil. Last, the problem is likely to be too large to be handled computationally since the actual dimensions of the tire differ from the film by at least three orders.

## **2.8 Modeling of Skid Resistance**

Similar to hydroplaning modeling, the modeling of skid resistance to date can also be broadly classified into two main categories: experimental and numerical approaches. The former involves conducting experiments and deriving qualitative or empirical relationships to relate the skid resistance with different measurable parameters, while the latter involves the use of finite element method in the study of skid resistance. The following sub-sections shall describe the research developments in these two categories.

### 2.8.1 Experimental/Empirical Approach in Skid Resistance Studies

As mentioned in Section 2.2, there have been numerous experimental works in skid resistance in the past. These experimental works have led pavement researchers to recognize and understand through empirical relationships the different factors that can affect skid resistance as described in Section 2.2. In terms of the development of empirical models, most pavement researchers are concerned on developing models that describe the variation of skid resistance with vehicle speed. This is due to the fact that accidents typically occur as a result of low skid resistance or hydroplaning, particularly during high speed travel in wet weather (OECD, 1984; Wambold et al. 1986).

The magnitude of wet tire-pavement friction (in terms of  $SN$ , as defined in Equation (2.3)) at a given vehicle speed is found to be related to the pavement surface microtexture, and the rate of decrease of the friction (in terms of  $SN$ ) with vehicle speed to be a function of pavement surface macrotexture, as reported by Henry (1986), based on correlation analysis of extensive experimental data. Meyer (1991) proposed the following relationship between skid resistance and vehicle speed,

$$SN_v = SN_0 e^{-(PNG/100)v} \quad (2.22)$$

$$PNG = 100 \left( \frac{d(SN_v)/dv}{SN_v} \right) \quad (2.23)$$

where  $SN_v$  is the skid number at vehicle speed  $v$ ,  $SN_0$  is a fictitious skid number at zero vehicle speed, and PNG is the percentage normalized gradient of the  $SN$  versus  $v$  curve.

The zero-speed intercept ( $SN_0$ ), which is an indication of friction at low speeds, is found to be very well correlated with the microtexture height and thus is seen as a microtexture parameter. It is found to be very well correlated with the British Pendulum Number ( $BPN$ ) which is obtained from ASTM E 303-93 (ASTM, 2005b).  $BPN$  is frequently used as a surrogate microtexture parameter.  $SN_0$  is related to  $BPN$  by Equation (2.24) (Henry and Meyer, 1983).

$$SN_0 = 1.32(BPN) - 34.9 \quad (r = 0.95) \quad (2.24)$$

The percentage normalized gradient (*PNG*) determines the rate at which the skid number decreases with speed and this is found to be related to macrotexture by a non-linear relationship (Henry and Meyer, 1983). An alternative measure of macrotexture is the mean texture depth (*MTD*) in mm obtained from the sand patch test using ASTM E 965-96 (ASTM, 2005h) and the *PNG* can be predicted by Equation (2.25).

$$PNG = 0.45(MTD)^{-0.47} \quad (r = 0.96) \quad (2.25)$$

It is noted that the coefficients in the relationships proposed in Equations (2.24) and (2.25) are based on a limited number of observations and, unless the pavement is relatively free from contamination, the texture measurements may not adequately account for contamination at the interface. However, the general form of these relationships appears to be valid (Henry et al., 1983).

Kulakowski and Meyer (1989) proposed an alternative relationship for skid number *SN* at any speed *v*:

$$SN = SN_0 e^{-\left(\frac{v}{v_0}\right)} \quad (2.26)$$

where  $v_0$  is a speed constant that replaces *PNG*. Direct calculation of  $v_0$  and  $SN_0$  can be done if ribbed tire testing is carried out at two speeds  $v_1$  and  $v_2$ , by solving Equation (2.27).

$$v_0 = \frac{v_2 - v_1}{\ln\left(\frac{SN_{v_1}}{SN_{v_2}}\right)} \quad (2.27)$$

It is noted that these equations are attempts to understand the observations through a regression approach based on experimental data. In fact, most pavement research undertaken today is still based on such techniques. Although they serve well in providing practitioners with quick ideas on the factors that affect skid resistance, they do not provide researchers with scientific explanations to the effect of the various operating conditions (such as the presence of contaminants, water depth etc.), pavement surface characteristics, and tire characteristics.

## 2.8.2 Analytical/Numerical Modeling of Skid Resistance

The finite element method is probably one of the most popular numerical simulation methods to analyze pneumatic tires in contact with pavement. The modeling of frictional effects is one of the important aspects of tire analysis and many in-house coding efforts have been made by the tire industry. The early codes, NOSAP (Bathe and Wilson, 1973), ADINA (Bathe, 1976) and AGGIE (Haisler, 1977) were all developed to simulate three-dimensional solid elements, loading of non-conservative forces and realistic constitutive laws for rubber properties. However, none possessed the whole functions to model the general tire behavior. Recent developments in finite element simulations allow a relatively detailed analysis of the tire-pavement contact. Commercial software such as ABAQUS (ABAQUS Inc., 2003), ADINA (ADINA R&D Inc., 2005a and 2005b), MSC.Marc (MSC. Software Corporation, 2003a) and MSC.Nastran (MSC. Software Corporation, 2003b), have been developed and are used in tire analyses.

Tire analyses on the part of tire engineers and researchers typically focus on the design of the tire materials. Finite element models developed by Tanner (1996), Davis (1997), Johnson et al. (1999) and Han (2003) typically focus on the simulation of dry tire-pavement interaction of rolling and sliding tires on smooth pavement surfaces and the response of tire structure due to tire-pavement frictional interaction. These simulations focus on the design and modeling of the pneumatic tire and the selection of materials for the manufacture of the tire. There is a lack of studies in the areas of skid resistance development mechanism and tire-pavement interaction from the perspective of pavement surface characteristics.

In order to provide a better understanding of the skid resistance of road pavement materials, a three-dimensional finite element model was developed by Liu et al. (2003) to simulate the British Pendulum Test. The model was a simplified representation of the British Pendulum Tester as shown in Figure 2.14. The essential geometric properties (including mass and centre of gravity) were identical to those of the actual tester. It comprises several beam elements as well as a spring element to provide the loading mechanism. During the analysis, the rubber slider will slide along the test surface, and the kinetic energy loss during the event

can be determined and expressed in terms of the pendulum measurements for comparison with experimental measurements. Besides the constant parameter values representing the characteristics of the tester, a friction parameter is the only necessary input to the computer model which can be determined based on laboratory measurements. The results computed by the finite element model showed very good agreement with laboratory measured test data. The model could be used to determine not only the skid resistance value of the test surface, but also other contact information which cannot be easily measured by laboratory tests.

Studies by Lee (2004) revealed that the model could not be used to analyze complex surface textures with non-symmetric patterns as it suffered excessive distortion when tested on these surfaces. Hence there is a need for a more robust model in order to be used on more realistic texture patterns. A curved slider design was proposed through analyses from finite element modelling to improve the reliability of the British Pendulum tester for coarse, rough surfaces.

Liu (2004) made use of the model proposed by Liu et al. (2003) and Lee (2004) to study patterns of macrotecture which are difficult to fabricate in the laboratory using the finite element modeling of the British Pendulum Tester, thereby providing a more accurate evaluation of skid resistance as compared to the laboratory test. A model for moist skid resistance is proposed through the use of multi-textured surface. However, it was found that (1) the British Pendulum Tester produced increasing friction with an increase in water depth for smooth and aggregate surfaces, which contradicted field locked-wheel measurements; and (2) the pendulum re-bounced upon contact with edges in the test surface, indicating that there is a discrepancy in friction mechanisms in the British Pendulum Tester and the actual tire-pavement interaction. Furthermore, the model proposed offered little improvement in knowledge to the friction mechanisms in the event of a moist or wet situation, since fundamental lubrication theories were not considered.

## 2.9 Summary

It is noted that the skid resistance of the pavement is highly variable and factors affecting skid resistance can be broadly classified into four categories: pavement surface characteristics (microtexture and macrotexture), tire related parameters (such as tire inflation pressure, rubber material and tread design), presence of contaminants (such as water and oils) and the operating conditions (such as climate, temperature and speed). These four groups constitute the major components of the tire-fluid-pavement interaction, the understanding of which would allow researchers to better understand the process of skid resistance development and the occurrence of hydroplaning.

A brief introduction to the various techniques used in measuring friction is given. Field measurement techniques such as the locked wheel method, the slip method, the side force method and laboratory techniques such as the portable British Pendulum Tester are being described.

The contact mechanisms for dry tire-pavement interaction are then introduced. Classical friction laws such as the Coulomb law are discussed, and its validity in tire-pavement friction mechanism questioned. Modern dry friction concepts used primarily in the field of tribology are discussed and these offer an insight into the adhesion, hysteresis (deformation), and wear mechanisms for elastomers. Theoretical explanations on friction in the tire-pavement interaction for dry and wet (at extremely low speed) conditions are offered using the adhesion, hysteresis and wear concepts. An understanding of the contact mechanisms involved in wet tire-fluid-pavement, especially at low and high speeds is essential since the dry friction mechanisms could not explain the phenomenon of extremely low coefficient of friction in wet or lubricated surfaces. Classical lubrication concepts such as the Reynolds equation are therefore introduced and the four different forms of lubrication theories, namely hydrodynamic, elasto-hydrodynamic and boundary lubrication are discussed. Various theories using these concepts to explain the complex tire-fluid-pavement interaction for the locked sliding tire have been also been discussed.



The phenomenon of hydroplaning is next discussed and the various manifestations of the hydroplaning phenomenon are given. There are three forms of hydroplaning, namely dynamic hydroplaning, viscous hydroplaning and reverted rubber hydroplaning. Of the three types of hydroplaning, dynamic hydroplaning is of the main concern to pavement and tire researchers because it is the most easily triggered mechanism considering the operating conditions of vehicles on highways and aircraft on runways.

Two main approaches in hydroplaning modeling are discussed, namely the experimental/empirical approach and the analytical/numerical approach. The models reviewed invariably highlight the infancy of the state of hydroplaning model development. Modeling with turbulence flow (which should be the case during hydroplaning) proposed by researchers so far had neglected even the effect of tire deformation profile, not to mention the elasto-hydrodynamic portion of the problem. Similarly, numerical models that attempt to provide for fluid-structure coupling are not extended to turbulence modeling. In fact most commercial software still relies on the simplistic potential flow theory for the fluid flow modules or at most laminar flow models. These highlight the current difficulties in producing suitable models for hydroplaning and wet skid resistance due to the intrinsic complexity of the problem.

Last, skid resistance models are discussed and they can be classified into experimental/empirical models or numerical simulation models. Numerical skid resistance models are found to be adequate for dry conditions but poor in wet skid resistance predictions. This is primarily due to the assumption of the Coulomb law which is only valid in the case of dry friction and a plausible model for boundary lubrication, and the negligence of hydrodynamic effects of the friction mechanism.

## **2.10 Research Needs and Scope of Work**

Based on the extensive literature review provided in this chapter, it is noted that although numerous experiments had been conducted to understand the phenomenon of hydroplaning and the prediction of skid resistance, the analytical and numerical aspect of it is

still very much in its infancy stage. Several areas have been identified as possible areas of research.

1. To identify skid resistance and hydroplaning mechanisms that could adequately explain the development of skid resistance and hydroplaning in tire-fluid-pavement interaction. A true appreciation of the various test methods in obtaining the coefficient of friction could never be achieved without understanding the underlying mechanisms of skid resistance under different testing conditions.
2. To propose a numerical model that could model hydroplaning by using the turbulent flow model and taking into consideration the tire deformation profile. This is needed as it is noted that currently numerical modeling of hydroplaning using turbulent fluid flow model does not take into account the changes in tire deformation profile.
3. To re-assess the validity of the NASA hydroplaning equation. This equation is widely adopted by aircraft engineers, tire engineers and pavement researchers due to its simplicity. However, other factors that are known to affect hydroplaning are not reflected in this equation. It is therefore necessary to assess factors such as microtexture, macrotexture, pavement grooving, water-film thickness, load etc. from an analytical and numerical point of view.
4. To assess the validity of current pavement engineering techniques used to improve skid resistance and reduce the risk of hydroplaning. Examples include pavement grooving, and surface treatment to improve microtexture or macrotexture. Current understanding of the effects of such measures is purely based on past experience and experimental evidence. There exists a need to model these effects and to explain them on an analytical or theoretical basis.
5. To propose a numerical model that could model hydroplaning and wet skidding and predict the skid resistance under these situations by using the turbulent flow model and taking into consideration coupled fluid-structure interaction. This is considered as a natural extension in the modeling of elasto-hydrodynamic

lubrication. Current models taking into account fluid-structure interaction only make use of potential flow theory of laminar flow model, which does not correctly represent the conditions at incipient hydroplaning.

The primary objective of this research is to develop numerical models that could simulate hydroplaning and skid resistance. The research would adopt a two-stage approach as shown in Figure 2.15 and the relevant chapters of each topic covered in this thesis are shown in Figure 2.15. The first stage would involve simulating the hydroplaning phenomenon numerically by assuming a hydroplaning tire profile while the second stage would relax the assumed hydroplaning tire profile assumption to develop a more generic model to simulate both hydroplaning and skid resistance. These models are applied to study major issues of concern to pavement researchers, such as the effect of different pavement-related, operational, loading and environmental parameters on hydroplaning and skid resistance, and the use of pavement grooving in hydroplaning prevention.

The scope of the work planned for this research can be stated as follows:

Stage I: Numerical Modeling of Hydroplaning using Computational Fluid Dynamics and Using the NASA Hydroplaning Tire Profile

1. To develop a numerical model for hydroplaning assuming a fixed tire deformation profile and to verify it with experimental results reported by past researchers. Two-dimensional and three-dimensional forms of the model will be assessed for their suitability.
2. To apply the proposed numerical model to study the effects of tire pressure on hydroplaning and to verify the NASA hydroplaning equation.
3. To apply the proposed numerical model to study the effects of microtexture on hydroplaning and to study the validity of NASA hydroplaning equation in this context.
4. To apply the proposed numerical model to assess the effectiveness of transverse and longitudinal pavement grooving in reducing the risk of hydroplaning.

5. To apply the proposed numerical model to develop a procedure for the design of transverse and longitudinal pavement grooving against hydroplaning.

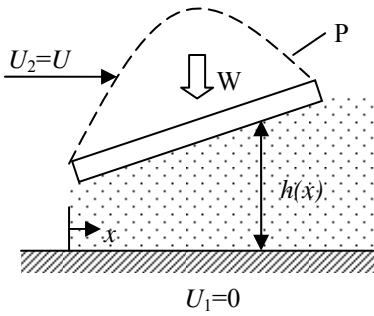
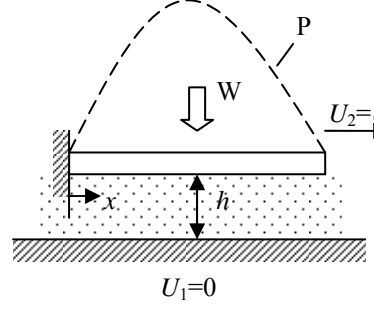
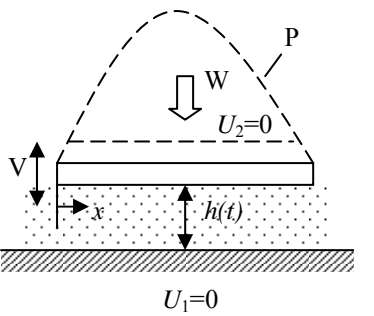
Stage II: Numerical Modeling of Hydroplaning and Skid Resistance using Fluid-Structure-Interaction (Solid Mechanics and Computational Fluid Dynamics) and relaxing the NASA Hydroplaning Tire Profile Assumption

1. To develop an improved numerical model for the prediction of skid resistance and hydroplaning speed with the consideration of fluid-structure interaction and to verify it with experimental results reported in past research and the NASA hydroplaning equation.
2. To apply the improved numerical model in hydroplaning simulation and to study the effects of tire pressure, water-film thickness, footprint aspect ratio and wheel load on hydroplaning.
3. To apply the improved numerical model in wet-pavement skid resistance simulation and to study the effects of vehicle speed, tire pressure, water-film thickness and wheel load on skid resistance.

**Table 2.1 Skid resistance measurement systems updated based on Henry (1986) (Henry, 2000)**

<b>Locked-Wheel Methods</b>	<b>Test Tire</b>		<b>Water Depth (nominal), mm</b>	<b>Country</b>
Skid resistance trailer (ASTM E 274)	Ribbed (ASTM E 501) Blank (ASTM E 524)		0.5	United States, Canada, Taiwan
Stuttgarter Reibungsmesser SRM	PIARC (ribbed)		1	Germany
Skiddometer BV8	165-R15 (ribbed)		0.5	Switzerland
Polish SRT-3	Patterned		0.5	Poland
Japanese Skid Tester	165-SR13		0.5	Japan
<b>Slip Methods</b>	<b>% Slip</b>	<b>Test Tire</b>	<b>Water Depth, mm</b>	<b>Country</b>
Skiddometer BV 11	15	VTI 4.00-8	0.5	Sweden, Slovakia
Skiddometer BV 12	0-50	Passenger car type	0.5	Sweden (VTI)
Saab Friction Tester (RST)	15	VTI 4.00-8	0.5	Sweden
DWW Trailer	86	165-R15 (PIARC smooth)	0.5	Netherlands
Griptester	14.5	Griptester	0.5	Scotland, Canada
<b>Side Force Methods</b>	<b>Low Angle, degree</b>	<b>Test Tire</b>	<b>Water Depth (nominal), mm</b>	<b>Country</b>
Side-force coefficient road inventory machine (SCRIM)	20	3.00-20 (smooth)	0.5-1	United Kingdom, Australia, Belgium, France, Ireland, Italy, Spain
Mu meter	7.5	Special	External	United Kingdom United States (FAA), Norway
<b>Locked-Wheel Methods</b>	<b>Low Angle, degree</b>	<b>Test Tire</b>	<b>Water Depth (nominal), mm</b>	<b>Country</b>
Stradograph	12	PIARC 165-R15 (smooth)	0.2	Denmark
Finnish	8	Nokia 165 SR15 (smooth)	1.1	Finland
<b>Multifunction Systems</b>	<b>Methods</b>			<b>Country</b>
Stradograph	Locked-wheel, slip (0 to 15%), side force (0 to 15°), locked-wheel side force			Belgium, France
Penn State road friction Tester	Locked-wheel, transient slip (0 to 100%), side force (0 to 12°), locked-wheel side force			United States (Penn State)
Mobile tire traction dynamometer (MTTD)	Locked-wheel, slip (0 to 100%), side force (0 to 25°)			United States (U.S. DOT)
Skid resistance measuring machine	Locked-wheel, slip (0 to 100%), side force (0 to 45°)			Japan
Skiddometer BV 8	Locked-wheel, slip (14%)			Switzerland

Table 2.2 Sources of load support using smooth surfaces

Description of system*	Schematic representation	Hydrodynamic equation
1. <i>Plane, smooth, rigid, inclined surfaces.</i> No vertical motion.		<i>Wedge term:</i> $\frac{d}{dx} \left( h^3 \frac{dp}{dx} \right) = 6\mu U \frac{dh}{dx}$
2. <i>Plane, smooth, parallel surfaces.</i> Lower surface rigid and fixed. Upper surface flexible and held at one end.		<i>Stretch term:</i> $\frac{d}{dx} \left( h^3 \frac{dp}{dx} \right) = 6h\mu \frac{dU}{dx}$
3. <i>Plane, smooth, parallel, rigid surfaces.</i> No side motion, lower surface fixed. Upper surface reciprocates vertically.		<i>Squeeze term:</i> $\frac{d}{dx} \left( h^3 \frac{dp}{dx} \right) = 12\mu V$

\* Incompressible, iso-viscous liquid. Two-dimensional models.

Table 2.3 Sources of load support using rough surfaces

Classification of support mechanism	Remarks	Schematic representation
1. <i>Directional effect</i>	Directional parameter negative. <i>Rigid, parallel</i> surfaces, lower surface fixed.	
2. <i>Macro-elasto-hydrodynamic</i>	Upper surface <i>plane, smooth</i> and <i>rigid</i> . Lower surface <i>flexible</i> with sinusoidal or symmetrical roughness. Elasto-hydrodynamic distortion produces net load support.	
3. <i>Cavitation</i>	<i>Rigid, parallel</i> surfaces. Upper surface <i>smooth</i> , lower has sinusoidal roughness. Cavitation destroys negative pressure, giving net load support.	
4. <i>Viscosity effects</i>	For sinusoidal roughness in lower surfaces (same conditions as 3 above), pressure effect increases viscosity and load support, temperature has opposite effect.	<p>In all cases:</p> $W \equiv \sum p_+ \delta A - \sum p_- \delta A$

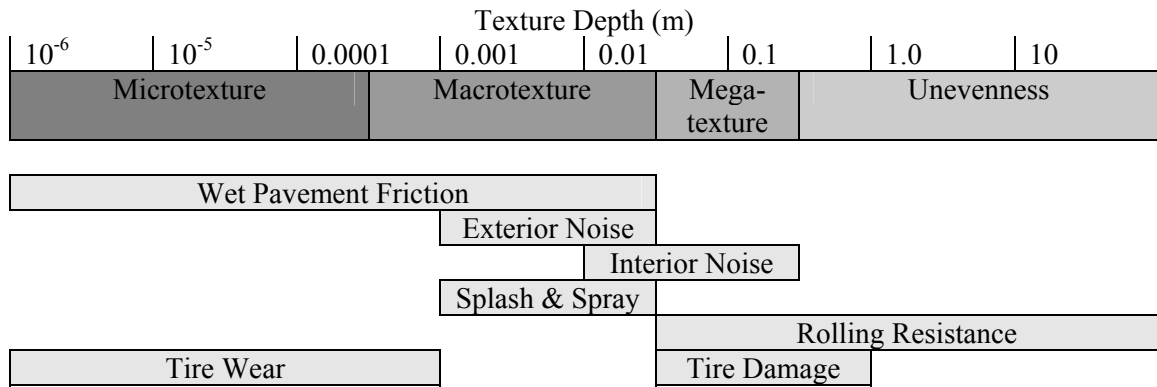


Figure 2.1 Effect of texture depth on friction and noise (PIARC, 1987)

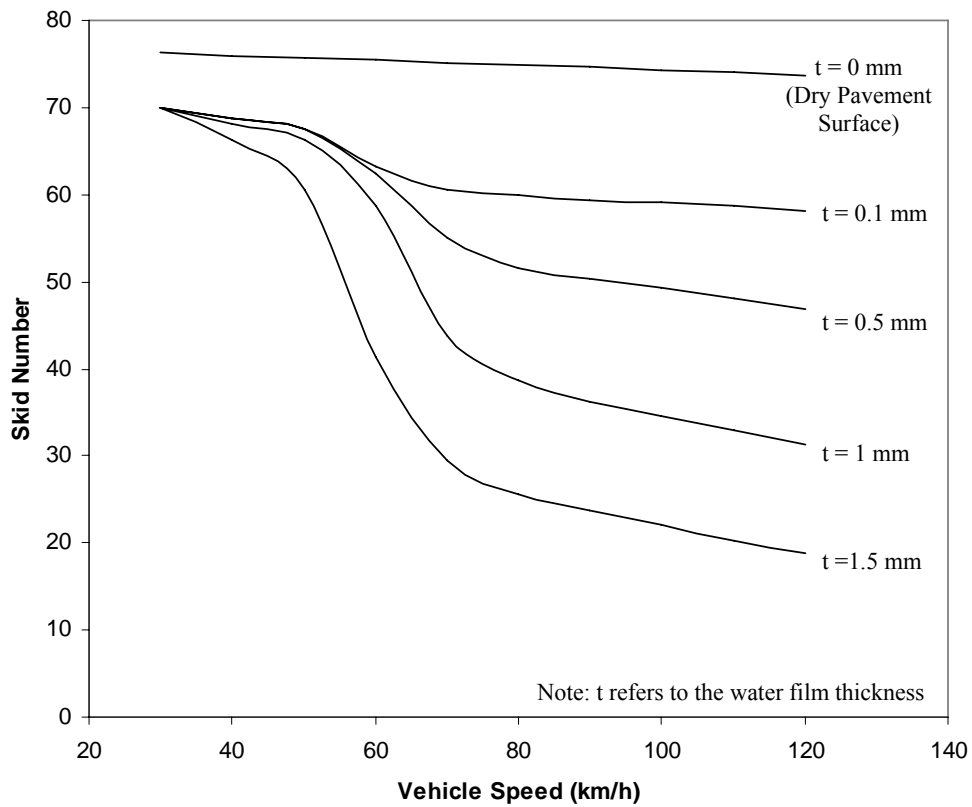
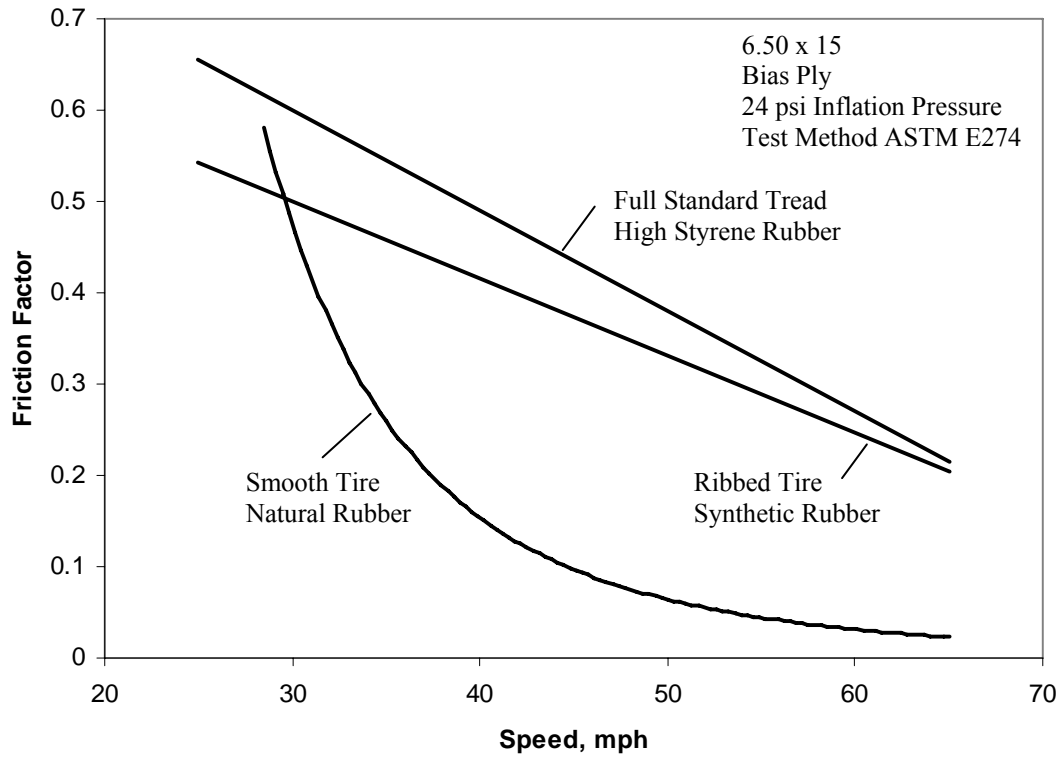
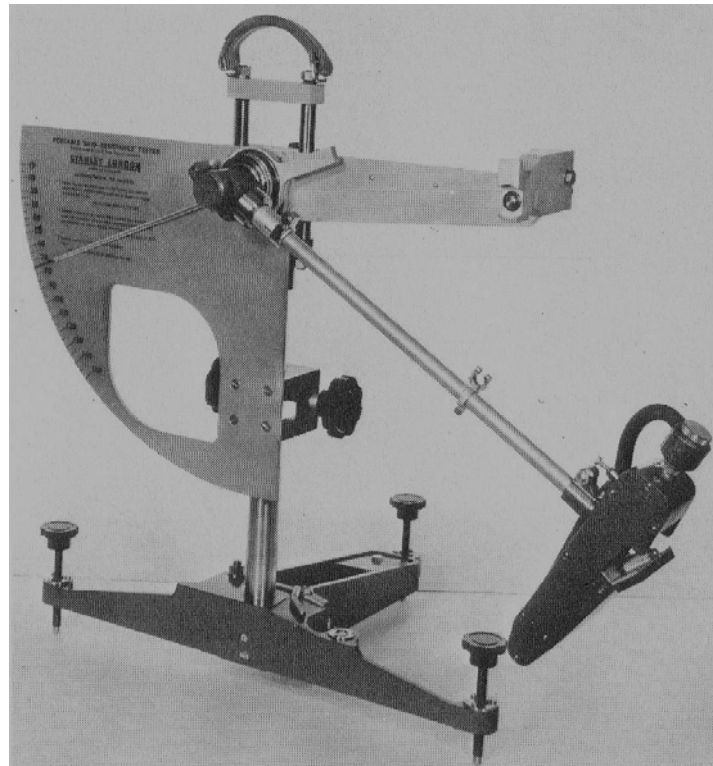


Figure 2.2 Influences of water film thickness and vehicle speed on skid resistance (Benedetto, 2002)





**Figure 2.3** Differences in locked wheel performance on interchangeable tires on the same wet pavement surface (fine cold asphalt) (Maycock, 1965)



**Figure 2.4** British Pendulum Tester (Giles et al., 1964)



Figure 2.5 Rubber Sliding on a Hard Substrate of Short-ranged and Long ranged Surface Roughness (Persson, 1998)

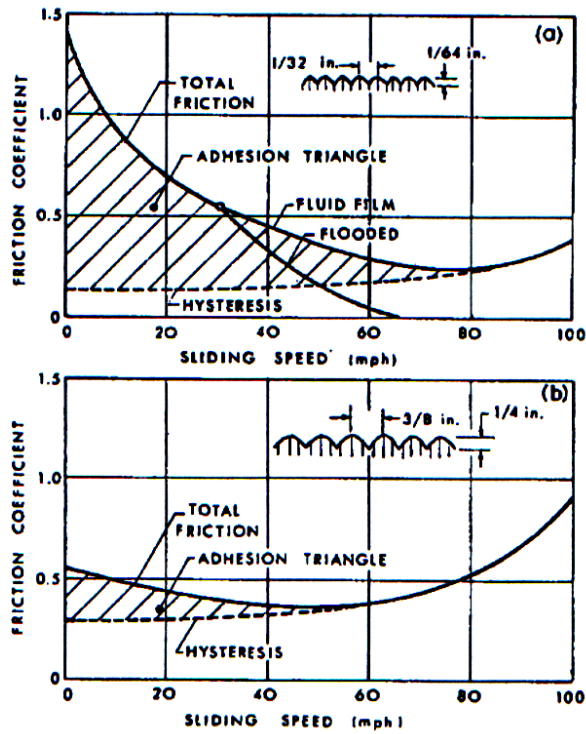


Figure 2.6 Frictional performances of (a) adhesion-producing and (b) hysteresis producing surfaces (Kummer and Meyer, 1966)

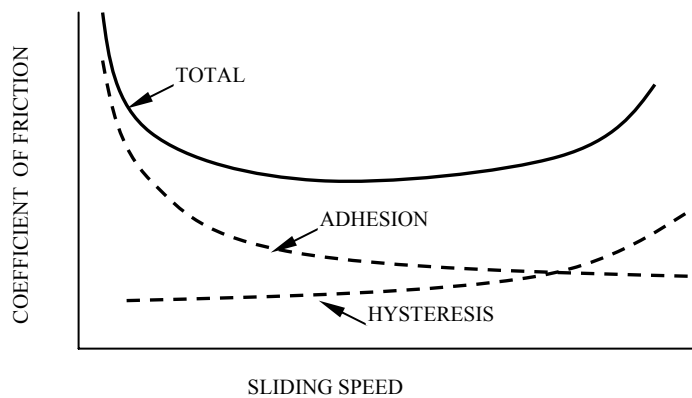


Figure 2.7 Generalized representation of the coefficient of friction between a steel sphere and rubber as a function of sliding speed (Highway Research Board, 1972)

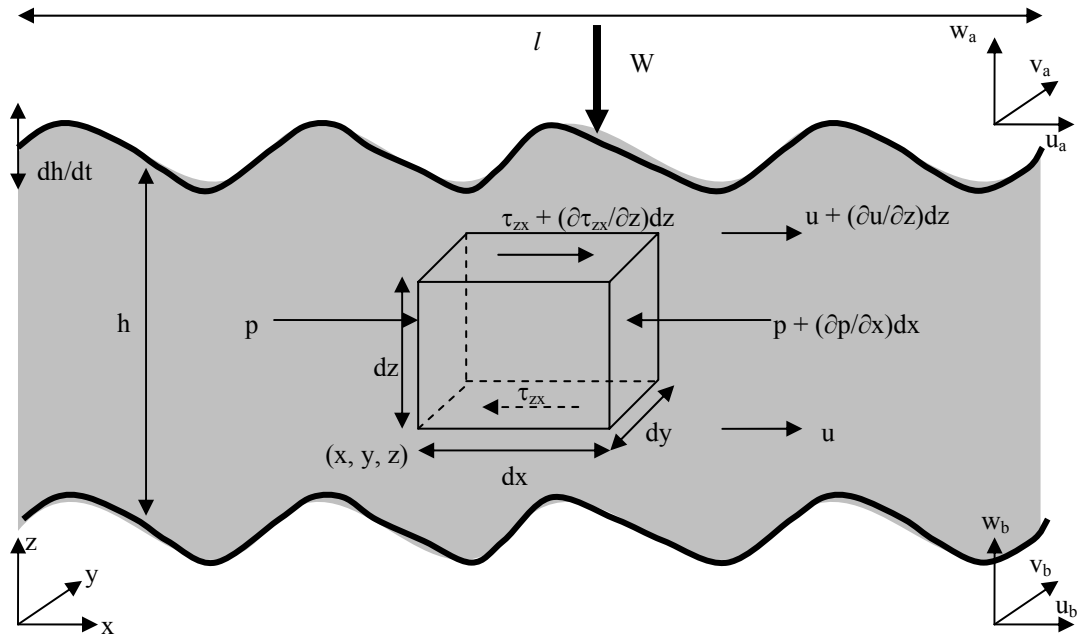


Figure 2.8 Schematic of fluid flow between two surfaces and stresses acting on fluid element and velocities in x-z plane

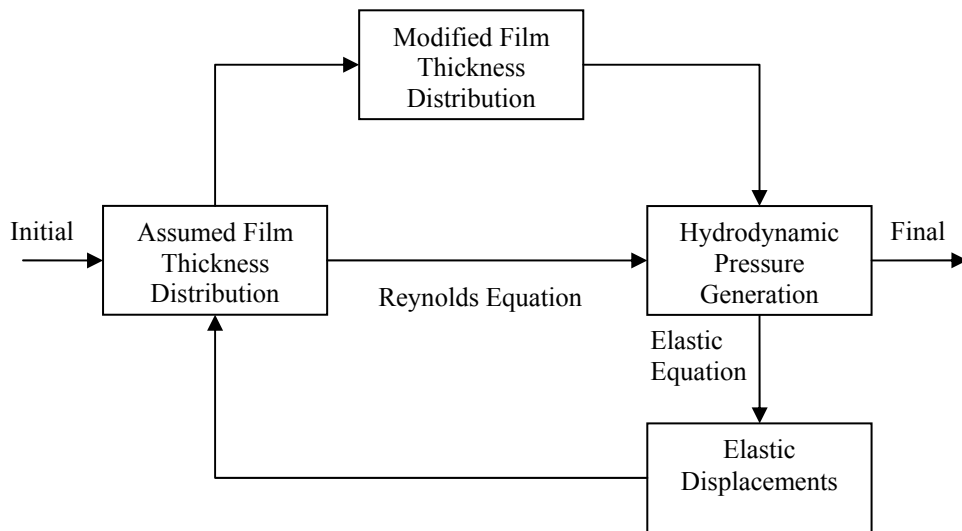


Figure 2.9 General iterative procedures for elasto-hydrodynamic lubrication

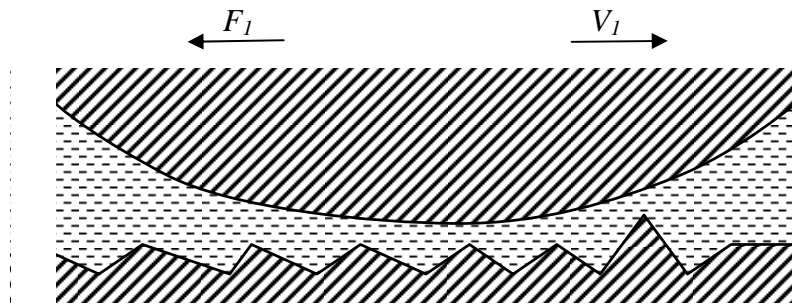


Figure 2.10 Boundary layer lubricated frictional contact

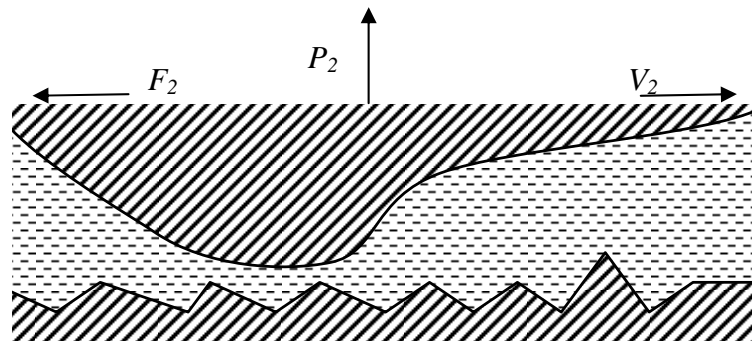
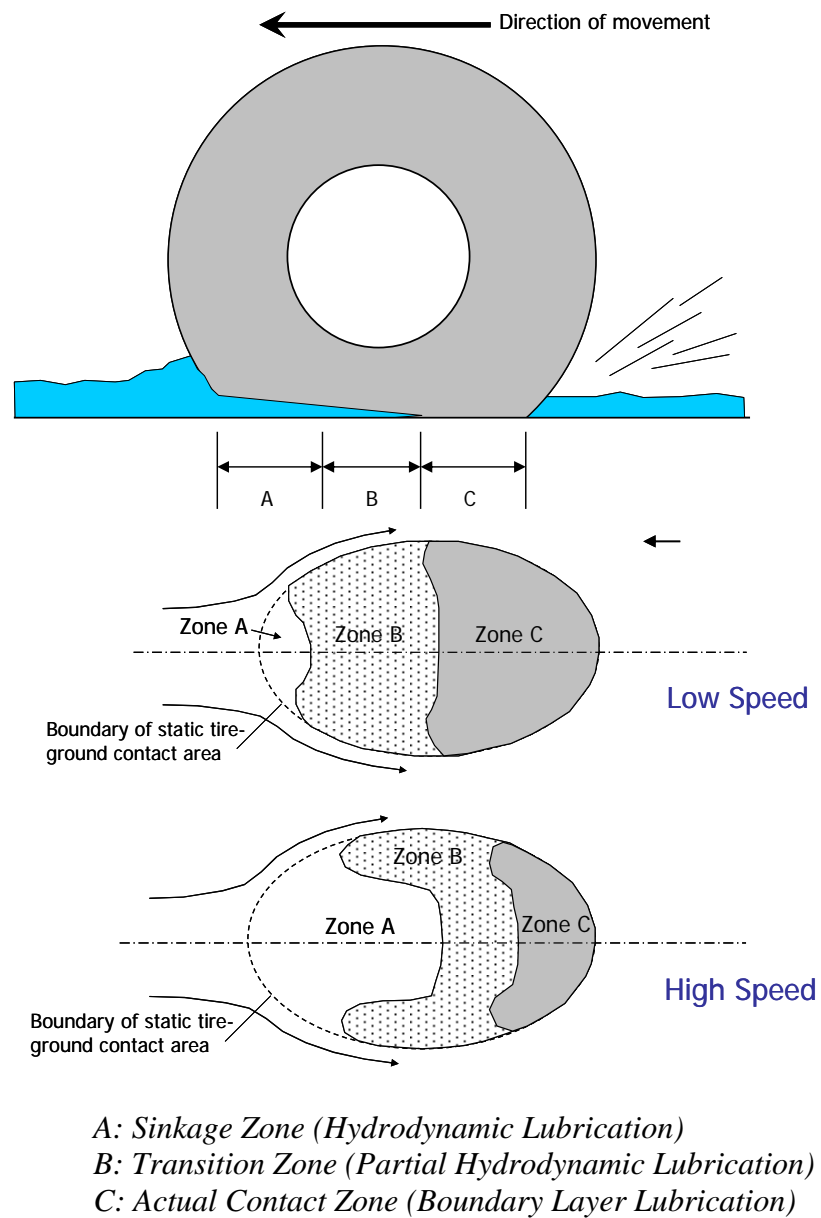


Figure 2.11 Hydrodynamic lubricated frictional contact (Partial)



**Figure 2.12** Tire sliding on wetted pavement surface - three-zone concept (Moore 1966)

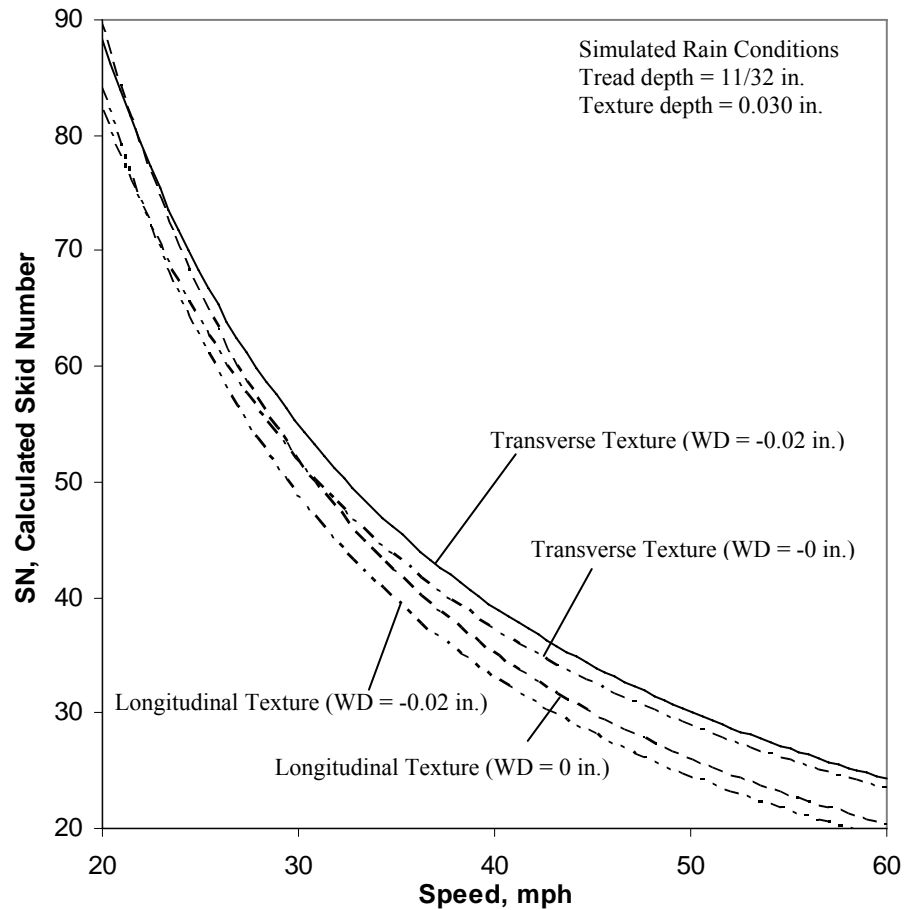


Figure 2.13 Longitudinal pavement texture versus transverse pavement texture (Balmer and Galloway, 1983)

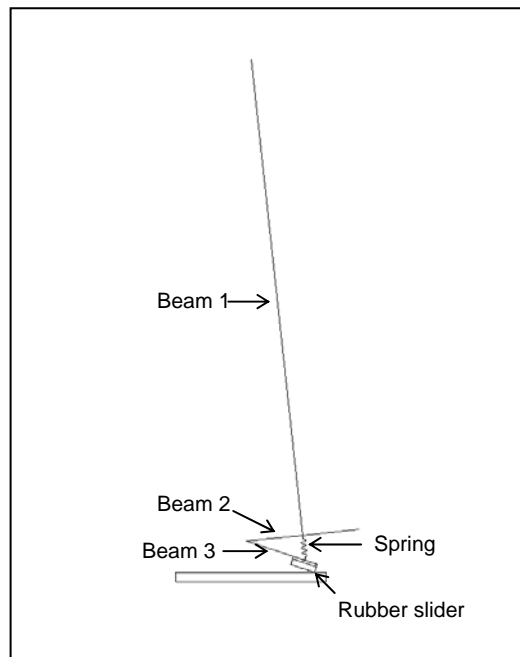


Figure 2.14 Finite element model of the British pendulum tester developed by Liu et al. (2003)

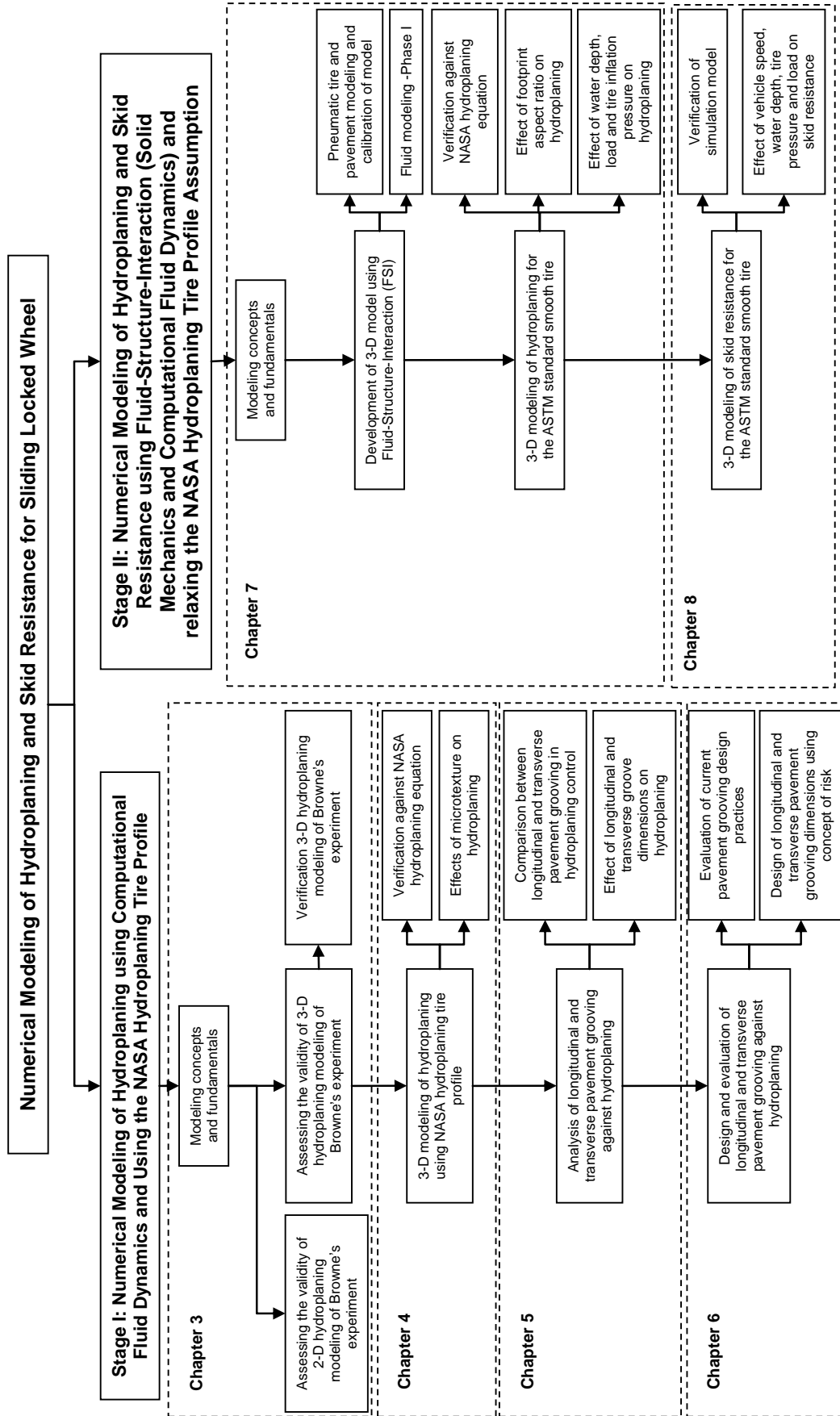


Figure 2.15 Scope of Research in Thesis

## **CHAPTER 3      DEVELOPMENT OF PNEUMATIC TIRE HYDROPLANING MODEL**

### **3.1      Introduction**

From the overview of the scope of research as shown in Figure 2.15 of Chapter 2, there is a need to ascertain the fundamental theories that should be used to describe hydroplaning. These theories must be able to produce simulation results that can fit closely to experimental data. One also has to consider whether the hydroplaning problem should be modeled two-dimensionally (which is simpler) or three-dimensionally (which is more realistic). Such considerations have to be taken care of before proceeding to the simulation of a hydroplaning tire. This chapter therefore presents the fundamentals leading to the development of a numerical model that simulates pneumatic tire hydroplaning, using an assumed tire deformation profile. A two-dimensional finite-volume approach was first adopted by Browne (1971) in the simulation of the hydroplaning. A turbulent viscous flow model was employed but was found to produce results not matching the well-known NASA hydroplaning equation. In the present research, a fresh approach is proposed to apply the fundamentals of computational fluid dynamics (CFD) to develop a numerical model for the analysis of hydroplaning. The model will be validated against experimental data reported in the literature.

### **3.2      Fluid Flow Model**

#### **3.2.1      Fundamental Laws of Fluid Flow**

The fundamental equations of fluid dynamics are based on the universal laws of conservation, namely the conservation of mass, the conservation of momentum and the conservation of energy. The equation that results from the conservation of mass (known as the continuity equation) is shown in Equation (3.1) in Cartesian notation or equivalently in Equation (3.2) in vector notation. The notations  $\rho$ ,  $u$ ,  $v$ ,  $w$  and  $t$  represent the density, x-velocity, y-velocity, z-velocity and time respectively.



$$\frac{\partial \rho}{\partial t} + \frac{\partial(\rho u)}{\partial x} + \frac{\partial(\rho v)}{\partial y} + \frac{\partial(\rho w)}{\partial z} = 0 \quad (3.1)$$

$$\frac{\partial \rho}{\partial t} + \nabla \cdot (\rho \mathbf{u}) = 0 \quad (3.2)$$

This equation can be derived by considering the infinitesimally small control volume fixed in space. Alternatively, the continuity equation can be expressed in its integral form as shown in Equation (3.3) by considering flow through the control surface  $S$  in and out of a finite control volume  $V$  fixed in space.

$$\frac{\partial}{\partial t} \iiint_V \rho dV + \iint_S \rho \mathbf{u} \cdot d\mathbf{S} = 0 \quad (3.3)$$

The momentum equations are shown in Equations (3.4a) to (3.4c) in non-conservation form. The forces considered include body forces  $f$  and the surface forces (which include pressure on the surface by surrounding elements  $p$  and the shear and normal stresses on surface by friction  $\tau$ ) of an infinitesimally small moving fluid element.

$$\rho \frac{Du}{Dt} = -\frac{\partial p}{\partial x} + \frac{\partial \tau_{xx}}{\partial x} + \frac{\partial \tau_{yx}}{\partial y} + \frac{\partial \tau_{zx}}{\partial z} + \rho f_x \quad (3.4a)$$

$$\rho \frac{Dv}{Dt} = -\frac{\partial p}{\partial y} + \frac{\partial \tau_{xy}}{\partial x} + \frac{\partial \tau_{yy}}{\partial y} + \frac{\partial \tau_{zy}}{\partial z} + \rho f_y \quad (3.4b)$$

$$\rho \frac{Dw}{Dt} = -\frac{\partial p}{\partial z} + \frac{\partial \tau_{xz}}{\partial x} + \frac{\partial \tau_{yz}}{\partial y} + \frac{\partial \tau_{zz}}{\partial z} + \rho f_z \quad (3.4c)$$

These equations are also known as the Navier-Stokes Equations. Viscous effects for Newtonian fluids can be incorporated into the momentum equations to give Equations (3.5a) to (3.5c). The notation  $\eta$  represents the first or dynamic viscosity that relates stresses to linear deformations, and  $\lambda$  represents the second viscosity that relates stresses to volumetric deformations.

$$\rho \frac{Du}{Dt} = -\frac{\partial p}{\partial x} + \frac{\partial}{\partial x} \left[ 2\eta \frac{\partial u}{\partial x} + \lambda \text{div} \mathbf{u} \right] + \frac{\partial}{\partial y} \left[ \eta \left( \frac{\partial u}{\partial y} + \frac{\partial v}{\partial x} \right) \right] + \frac{\partial}{\partial z} \left[ \eta \left( \frac{\partial u}{\partial z} + \frac{\partial w}{\partial x} \right) \right] + S_{Mx} \quad (3.5a)$$

$$\rho \frac{Dv}{Dt} = -\frac{\partial p}{\partial y} + \frac{\partial}{\partial x} \left[ \eta \left( \frac{\partial u}{\partial y} + \frac{\partial v}{\partial x} \right) \right] + \frac{\partial}{\partial y} \left[ 2\eta \frac{\partial v}{\partial y} + \lambda \text{div} \mathbf{u} \right] + \frac{\partial}{\partial z} \left[ \eta \left( \frac{\partial v}{\partial z} + \frac{\partial w}{\partial y} \right) \right] + S_{My} \quad (3.5b)$$

$$\rho \frac{Dw}{Dt} = -\frac{\partial p}{\partial z} + \frac{\partial}{\partial x} \left[ \eta \left( \frac{\partial u}{\partial z} + \frac{\partial w}{\partial x} \right) \right] + \frac{\partial}{\partial y} \left[ \eta \left( \frac{\partial v}{\partial z} + \frac{\partial w}{\partial y} \right) \right] + \frac{\partial}{\partial z} \left[ 2\eta \frac{\partial w}{\partial z} + \lambda \text{div} \mathbf{u} \right] + S_{Mz} \quad (3.5c)$$

These can also be re-written to give Equations (3.6a) to (3.6c) that are useful in the development of the finite volume method.

$$\frac{\partial(\rho u)}{\partial t} + \nabla \cdot (\rho u \mathbf{u}) = -\frac{\partial p}{\partial x} + \nabla \cdot (\eta \nabla u) + S_{Mx} \quad (3.6a)$$

$$\frac{\partial(\rho v)}{\partial t} + \nabla \cdot (\rho v \mathbf{u}) = -\frac{\partial p}{\partial y} + \nabla \cdot (\eta \nabla v) + S_{My} \quad (3.6b)$$

$$\frac{\partial(\rho w)}{\partial t} + \nabla \cdot (\rho w \mathbf{u}) = -\frac{\partial p}{\partial z} + \nabla \cdot (\eta \nabla w) + S_{Mz} \quad (3.6c)$$

where  $S_{Mx}$ ,  $S_{My}$  and  $S_{Mz}$  are the source terms (such as source term due to gravity) in the x, y and z direction respectively.

It is noted that the Navier-Stokes equations presented in Equations (3.6a) to (3.6c) are non-linear, second order partial differential equations. They are not amenable to exact mathematical solutions except in a few instances such as the Couette flow and the Poiseuille flow. This leads to the use of numerical methods to solve Equations (3.2) and (3.6), which are referred to as the complete set of Navier-Stokes equations in computational fluid dynamics (CFD). It is noted that the Navier Stokes equations apply to both laminar and turbulent fluid flows, but for turbulent flow each velocity component fluctuates randomly with time and this added complication makes an analytical solution intractable.

### 3.2.2 Flows in the Turbulent Regime

The flow experienced in hydroplaning is largely turbulent in nature (Schlichting, 1960; Wallace, 1964). This means that any mathematical formulation of hydroplaning has to take into account the turbulent nature of fluid flow. Turbulent fluid motion can be viewed as “an irregular condition of flow in which the various quantities show a random variation with time and space coordinates so that statistically distinct average values can be discerned” (Hinze, 1975). Thus, the Navier-Stokes equations in the prior sub-section can be re-formulated using Equations (3.7), (3.8) and (3.9) to obtain the Reynolds averaged Navier-Stokes equation.

Equation (3.7) defines the mean  $\Phi$  of flow property  $\varphi$  and Equation (3.8) states that the time-average of the fluctuating component is by definition zero. Equation (3.9) states the definition of a time-dependent flow property  $\varphi(t)$ .

$$\Phi = \frac{1}{\Delta t} \int_0^{\Delta t} \varphi(t) dt \quad (3.7)$$

$$\overline{\varphi'} = \frac{1}{\Delta t} \int_0^{\Delta t} \varphi'(t) dt \equiv 0 \quad (3.8)$$

$$\varphi(t) = \Phi + \varphi'(t) \quad (3.9)$$

Using the above stated definitions, the time-averaged Navier-Stokes equations for a large Reynolds number flow can be obtained as shown in Equations (3.10).

$$\frac{\partial(\rho u)}{\partial t} + \nabla \cdot (\rho u \mathbf{u}) = -\frac{\partial p}{\partial x} + \nabla \cdot (\eta \nabla u) + \left[ -\frac{\partial(\overline{\rho u' u'})}{\partial x} - \frac{\partial(\overline{\rho u' v'})}{\partial y} - \frac{\partial(\overline{\rho u' w'})}{\partial z} \right] + S_{Mx} \quad (3.10a)$$

$$\frac{\partial(\rho v)}{\partial t} + \nabla \cdot (\rho v \mathbf{u}) = -\frac{\partial p}{\partial y} + \nabla \cdot (\eta \nabla v) + \left[ -\frac{\partial(\overline{\rho u' u' v'})}{\partial x} - \frac{\partial(\overline{\rho v' v'})}{\partial y} - \frac{\partial(\overline{\rho v' w'})}{\partial z} \right] + S_{My} \quad (3.10b)$$

$$\frac{\partial(\rho w)}{\partial t} + \nabla \cdot (\rho w \mathbf{u}) = -\frac{\partial p}{\partial z} + \nabla \cdot (\eta \nabla w) + \left[ -\frac{\partial(\overline{\rho u' u' w'})}{\partial x} - \frac{\partial(\overline{\rho v' v' w'})}{\partial y} - \frac{\partial(\overline{\rho w' w'})}{\partial z} \right] + S_{Mz} \quad (3.10c)$$

where  $S_{Mx}$ ,  $S_{My}$  and  $S_{Mz}$  are the source terms (such as source term due to gravity) in the x, y and z direction respectively.

The extra turbulent stresses in the above equation are termed as Reynolds stresses. The only unknowns in the complete set of Navier-Stokes equations are  $p$ ,  $u$ ,  $v$  and  $w$ . With the consideration of turbulence, the performance of the time-averaging operation on the momentum equations allows the state of flow in the instantaneous fluctuations to be removed. Since there are six unknown Reynolds stresses, it is necessary to make closing assumptions to the Reynolds equations through turbulence modeling.

### 3.2.3 Turbulence Modeling

A turbulence model is a computational procedure needed to close the system of continuity and momentum equations. For most engineering applications, it is unnecessary to

resolve the details of turbulence fluctuations. Only the effect of turbulence on the mean flow is sought. In particular, expressions for the Reynolds stresses and the turbulent scalar transport terms in Equation (3.10) are needed. Therefore, researchers have over the past three decades developed different models ranging from the simplest zero-equation model to the well-known  $k$ - $\varepsilon$  model which is a two-equation model to the complex Reynolds Stress Model.

In cases where the effect of convection and diffusion of turbulence properties are not negligible, as in the case of tire-pavement interaction where bow waves and fluid separation are expected to occur, the dynamics of turbulence had to be considered. As such two-equation models, such as the  $k$ - $\varepsilon$  model, are required to analyze the mechanisms that affect the turbulent kinetic energy. The semi-empirical standard  $k$ - $\varepsilon$  model (Launder and Spalding, 1974) has two model equations: one for the turbulent kinetic energy  $k$  and another for the viscous dissipation  $\varepsilon$  as shown in Equation (3.11).

$$\frac{\partial(\rho k)}{\partial t} + \nabla \cdot (\rho k \mathbf{U}) = \nabla \cdot \left[ \frac{\mu_t}{\sigma_k} \nabla k \right] + 2\mu_t E_{ij} \cdot E_{ij} - \rho \varepsilon \quad (3.11a)$$

$$\frac{\partial(\rho \varepsilon)}{\partial t} + \nabla \cdot (\rho \varepsilon \mathbf{U}) = \nabla \cdot \left[ \frac{\mu_t}{\sigma_\varepsilon} \nabla \varepsilon \right] + C_{1\varepsilon} \frac{\varepsilon}{k} 2\mu_t E_{ij} \cdot E_{ij} - C_{2\varepsilon} \rho \frac{\varepsilon^2}{k} \quad (3.11b)$$

Also the eddy viscosity is defined as follows:

$$\mu_t = \rho C_\mu \frac{k^2}{\varepsilon} \quad (3.12)$$

These equations contain 5 unknowns  $C_\mu$ ,  $\sigma_k$ ,  $\sigma_\varepsilon$ ,  $C_{1\varepsilon}$  and  $C_{2\varepsilon}$ . The standard  $k$ - $\varepsilon$  model employs values for the constants that are arrived at by comprehensive data fitting for a wide range of turbulent flows:

$$C_\mu = 0.09; \sigma_k = 1.00; \sigma_\varepsilon = 1.30; C_{1\varepsilon} = 1.44; C_{2\varepsilon} = 1.92 \quad (3.13)$$

The standard  $k$ - $\varepsilon$  model given above is not appropriate for use in the viscous sub-layer because the damping effect associated with solid boundaries has not been included in the model. Closure can be achieved with the use of the standard model by assuming that the law of wall holds in the inner region, and either using wall functions of the form described by Launder and Spalding (1974) or using a traditional damped mixing length algebraic model and

matching with the two-equation model by neglecting the convection and diffusion of  $k$  and  $\varepsilon$  as shown in Tannehill et al. (1997).

The advantages of the  $k$ - $\varepsilon$  model is that it is the simplest turbulence model for which only initial and/or boundary conditions need to be supplied. It also has excellent performance for many industrial flows and is currently the most well-established and widely validated turbulence model. On the other hand, it is more expensive to implement compared to the zero-equation and one-equation models since there is a need to include the pair of equations shown in Equations (3.11) in the complete set of Navier-Stokes equations.

### **3.3 Hydroplaning Tire Deformation Model**

The prior section covered the theoretical aspects of the fluid flow portion of the hydroplaning problem. It is noted that the solutions to the Navier-Stokes equations are dependent on the choice of the boundary conditions and the initial conditions. Hence the correct representation of the deformation of the tire is a significant factor in the analysis. An ideal model must incorporate the effects of interaction between the tire, the fluid and the pavement characteristics.

Since the consideration of the three-component interaction is a highly complex problem, this study as undertaken a two stage approach as described in Section 2.10. The first part of the analysis involves the use of a fixed hydroplaning tire profile. This will essentially simplify the problem, but at the same time limits the model to simulate only hydroplaning. The first part of the analysis also lays the foundations for the fluid dynamics model which has to be used in the complete model considering the tire, fluid and pavement interaction. The second part of the analysis involves the relaxation of this assumption by considering the ability of the tire to deform with varying vehicle speed. This means a more complex solution methodology utilizing the idea of fluid-structure-interaction but also suggest the versatility of the model to simulate both hydroplaning and skid resistance at different vehicle speed.

This chapter thus starts from the assumption of a fixed hydroplaning tire profile as shown in Figure 3.1. This profile is used by Browne (1971) in his experiments and numerical

modeling on hydroplaning of pneumatic tires which is modeled from the hydroplaning profiles obtained from the NASA experiments conducted by Horne and Joyner (1965). It is noted that the hydroplaning profile can be divided into three regions, namely the entry regions where bow wave is expected to form, the main hydroplaning region, and a land region where the tire-pavement gap is less than a millimeter thick. This profile is coherent with the three-zone concept proposed by Veith (1983) where hydrodynamic lubrication (water wedge), mixed hydrodynamic lubrication and boundary layer lubrication corresponds to the three main regions respectively.

### **3.4 Pavement Surface Model**

Apart from tire and pavement contaminants (e.g. fluid), the pavement surface is third key element of modeling hydroplaning and skid resistance on a pavement. However the consideration of a real pavement surface is a rather complex task and past researchers (Martin, 1966; Eshel, 1967; Tsakonas et al., 1968; Browne, 1971; Okano and Koishi, 2000) have mostly chosen to ignore the asperities and macrotexture of the pavement surface. Another reason is that the pioneering experimental work on runway of the hydroplaning phenomena done by Horne and Dreher (1963) was performed on a glass surface. It is noted that substantial hydroplaning research has also been conducted by the tire industry in the design of tire, including tire tread pattern design. However the engineering properties and characteristics of pavement surface are not adequately addressed in their analyses. On the other hand, pavement engineers and researchers are required to provide pavement designs that would reduce the risk of hydroplaning adequately even for the worst tire design. In this study, a smooth plane pavement surface is first assumed to verify the proposed model. The term “smooth” means that the average roughness height of the micro-texture is taken to be zero and the term “plane” refers to a plane surface without any pavement grooving and any form of inclination or slope.

### 3.5 Concept of Hydroplaning Modeling

The modeling of hydroplaning of a locked wheel on a smooth pavement surface in the first phase of this research involves modeling the fluid by means of appropriate governing equations and defining a hydroplaning profile which is obtained from past experimental studies. The simulation of a locked wheel is of practical significance as most commonly-used skid resistance measuring devices operate on the locked wheel concept as shown in Table 3.1 (Henry, 2000). In a stationary observer frame of reference, the hydroplaning phenomenon can be simulated by a locked wheel moving at a speed of  $U$  m/s sliding on a smooth pavement flooded with water as shown in Figure 3.2a. In a moving wheel frame of reference, the problem can be modeled as a jet comprising of a layer of air and a layer of water, and a smooth plane pavement surface all moving at a speed of  $-U$  m/s towards the wheel as shown in Figure 3.2b using a steady-state analysis. In this study, water is used as the contaminant and the temperature is assumed to be 20°C. Hydroplaning is assumed to occur when the average ground hydrodynamic pressure is equivalent to the tire pressure of the wheel, i.e. when the vehicle's load is equal to the hydrodynamic lift force. This definition is the same as that adopted by other researchers such as Horne and Joyner (1965) and Browne (1971).

### 3.6 Computational Fluid Dynamics in Hydroplaning Simulation

The Navier-Stokes equations for the hydroplaning problem are generally not solvable by simple mathematical manipulations, due to the complexity of the second-order non-linear Navier-Stokes equations and the consideration of multiphase flow. The problem is usually solved numerically. The numerical solution of fluid dynamics problems falls into the field of computational fluid dynamics (CFD). The CFD software FLUENT (FLUENT Inc., 2005) is used in the present research as it offers various algorithms that are suitable for modeling fluid flow and heat transfer in complex geometries. The FLUENT package consists of FLUENT 6.2, the solver; prePDF, the pre-processor for modeling non-premixed combustion in FLUENT; GAMBIT, the pre-processor for geometry modeling and mesh generation; TGrid, an additional pre-processor that can generate volume meshes from existing boundary meshes. Figure 3.3

shows the organizational structure of these components. In this study, only the software GAMBIT and FLUENT in the FLUENT package are used. FLUENT utilizes the finite volume method in solving the Navier-Stokes equations.

In order to model the tire hydroplaning problem, a few important algorithms have to be selected in the FLUENT 6.2 solver. They include a multiphase model (in this case the volume-of-fluid (VOF) model), an algorithm for turbulence modeling, the correction algorithms for the promotion of convergence and stability, and the segregated/implicit/explicit solvers. The functions of these algorithms or models are described in the following subsections.

### **3.6.1 Multiphase Modeling and the Volume of Fluid (VOF) Model**

#### **3.6.1.1 Multiphase Modeling**

The proposed hydroplaning model is essentially one that simulates a free surface flow with moving boundaries. In this case, the free surface is an air-water boundary. This makes the computation more complex as the location of the free surface must be computed as part of the solution and the free surface is not known in advance. Location of the free surface must therefore be identified iteratively in the computations. This increases the complexity of the problem greatly. Methods used to determine the shape of the surface can generally be divided into the following two categories (Ferziger and Peric, 2002):

- Interface tracking methods: These are methods which treat the free-surface as a sharp interface. In this case, boundary fitted grids are used and they advanced each time the free surface is moved.
- Interface capturing methods: These are methods which do not define the interface as a sharp boundary. The computation is performed on a fixed grid, which extends beyond the free surface. The shape of the free surface is determined by computing the fraction of each near-interface cell that is partially filled. This can be done by introducing mass-less particles at the free surface at the initial time and following their motion. This is called the marker and cell or MAC scheme that was first



proposed by Harlow and Welsh (1965). Alternatively, one can solve the transport equation for the fraction of a cell occupied by the liquid phase (Hirt and Nicholls, 1981; Fluent Inc., 2005).

### 3.6.1.2 Volume of Fluid (VOF) Model

The FLUENT software package includes the VOF model which can model two or more immiscible fluids by solving a single set of momentum equations and tracking the volume fraction of each of the fluids throughout the domain. Even though it is useful in the prediction of jet break-up (similar to the proposed model) and the steady and transient tracking of any liquid-gas interface, it has some limitations. Only segregated solvers can be used and the coupled solvers cannot be used. The large eddy simulation turbulence model and the second-order implicit time-stepping formulation cannot be used with the VOF model offered by FLUENT version 6.2 (Fluent Inc., 2005).

In general, the VOF model is applied to time-dependent problems. It can also be applied to steady-state problems if the solution is independent of the initial conditions and there are distinct inflow boundaries for each flow. The hydroplaning problem can be modeled as a steady-state problem and there are distinct boundaries for velocity inlets for air and water. Researchers have been using a steady-state analysis for smooth tire-smooth pavement interaction to some degree of success since the 1960s (Martin, 1966; Eshel, 1967; Tsakonas et al., 1968; Browne, 1971).

The VOF model relies on the fact that two or more fluids are not interpenetrating. For each additional phase in the model, a variable which is the volume fraction of the phase in the computational cell is introduced. In each control volume, the volume fraction of all phases must sum to unity. The variables and the properties of a given cell are either purely representative of one of the phases, or representative of a mixture of phases, depending on the volume fraction values. In other words, if the  $q$ th fluid's volume fraction in the cell is denoted by  $\alpha_q$ , then the following three conditions are possible:

- $\alpha_q = 0$ : the cell is empty (of the  $q$ th fluid).

- $\alpha_q = 1$ : the cell is full (of the  $q$ th fluid).
- $0 < \alpha_q < 1$ : the cell contains an interface between the  $q$ th fluid and one or more other fluids.

Based on the local value of  $\alpha_q$ , the appropriate properties and variables will be assigned to each control volume within the domain.

The tracking of the interface between the phases can be accomplished by the solution of the continuity equation for the volume fraction of one or more of the phases. For the  $q$ th phase, the equation used in FLUENT is shown in Equation (3.14) (Fluent Inc., 2005).

$$\frac{\partial \alpha_q}{\partial t} + \mathbf{u} \cdot \nabla \alpha_q = 0 \quad (3.14)$$

The primary phase volume fraction can be computed based on the constraint shown in Equation (3.15).

$$\sum_{q=1}^n \alpha_q = 1 \quad (3.15)$$

A single momentum equation is solved throughout the domain and the resulting velocity field is shared among the phases. The momentum equation as shown in Equation (3.16) is dependent on the volume fractions of all phases through the use of density  $\rho$  and viscosity  $\eta$ .

$$\frac{\partial}{\partial t}(\rho \mathbf{u}) + \nabla \cdot (\rho \mathbf{u} \mathbf{u}) = -\nabla p + \nabla [\eta (\nabla \mathbf{u} + \nabla \mathbf{u}^T)] + \rho \mathbf{g} + \mathbf{F} \quad (3.16)$$

where  $\mathbf{F}$  is the force vector due to external sources (which is zero in this model since no external sources are specified). For additional scalars such as the turbulence quantities, a single set of transport equations is solved and the quantities are shared by the phases throughout the field.

A steady-state with implicit interpolation scheme is used in FLUENT (Fluent Inc., 2005). In the implicit interpolation scheme, the standard finite difference interpolation schemes are used to obtain the face fluxes for all the cells, including those near the interface.

$$\frac{\alpha_q^{n+1} - \alpha_q^n}{\Delta t} V + \sum_f (U_f^{n+1} U_{q,f}^{n+1}) = 0 \quad (3.17)$$

Since this equation requires the volume fraction values at the current time step, a standard scalar transport equation is solved iteratively for each of the secondary phase volume fractions at each time step. This scheme can be used for both time-dependent and steady-state calculations.

### 3.6.2 Turbulence Modeling using the Standard k-ε Model

FLUENT uses a form similar to that of Equations (3.11) for the transport equations for turbulent kinetic energy  $k$  and dissipation rate  $\varepsilon$  as shown in Equations (3.18) (Fluent Inc., 2005).

$$\frac{\partial(\rho k)}{\partial t} + \frac{\partial}{\partial x_i}(\rho k u_i) = \frac{\partial}{\partial x_j} \left[ \left( \eta + \frac{\mu_t}{\sigma_k} \right) \frac{\partial k}{\partial x_j} \right] + G_k + G_b - \rho \varepsilon - Y_M + S_k \quad (3.18a)$$

$$\frac{\partial(\rho \varepsilon)}{\partial t} + \frac{\partial}{\partial x_i}(\rho \varepsilon u_i) = \frac{\partial}{\partial x_j} \left[ \left( \eta + \frac{\mu_t}{\sigma_\varepsilon} \right) \frac{\partial \varepsilon}{\partial x_j} \right] + C_{1\varepsilon} \frac{\varepsilon}{k} (G_k + C_{3\varepsilon} G_b) - C_{2\varepsilon} \rho \frac{\varepsilon^2}{k} + S_\varepsilon \quad (3.18b)$$

In these equations,  $G_k$  represents the generation of turbulent kinetic energy due to the mean velocity gradients;  $G_b$  represents the generation of turbulent kinetic energy due to buoyancy;  $Y_M$  represents the contribution of the fluctuating dilation in compressible turbulence to the overall dissipation rate;  $C_{\mu}$ ,  $\sigma_k$ ,  $\sigma_\varepsilon$ ,  $C_{1\varepsilon}$  and  $C_{2\varepsilon}$  are the model constants as shown in Equation (3.17); and  $S_k$  and  $S_\varepsilon$  are the source terms.

### 3.6.3 Wall Functions

In the simulation of hydroplaning, the standard wall functions supplied by FLUENT is used. They are based on the proposal of Launder and Spalding (1974) and have been widely used for industrial flows. This allows the transition of turbulent flow to laminar flow in the boundary layer near the wall.

#### 3.6.3.1 Treatment of Momentum

The law of the wall for the mean velocity  $U^*$  is defined as follows,

$$U^* = \frac{1}{\kappa} \ln(Ey^*) \quad (3.19)$$

$$U^* \equiv \frac{U_P C_\mu^{1/4} k_P^{1/2}}{\tau_w / \rho} \quad (3.20)$$

$$y^* \equiv \frac{\rho C_\mu^{1/4} k_P^{1/2} y_P}{\eta} \quad (3.21)$$

where  $\kappa$  is the von Karman constant ( $= 0.42$ );  $E$  is an empirical constant ( $= 9.793$ );  $U_P$  is the mean velocity at point P;  $k_P$  is the turbulence energy at point P;  $y_P$  is the distance from point p to the wall and  $\mu$  is the dynamic viscosity of the fluid. The logarithmic law is known to be valid for  $y^* > 30$  to  $60$ . In FLUENT, the log-law is employed when  $y^* > 11.225$ . For  $y^* < 11.225$ , the laminar stress-strain relationship is employed as shown in Equation (3.22).

$$U^* = y^* \quad (3.22)$$

### 3.6.3.2 Treatment of Turbulence

In the  $k$ - $\varepsilon$  model, the  $k$  equation is solved in the whole domain including the wall-adjacent cells. The boundary condition for the  $k$  imposed at the wall is

$$\frac{\partial k}{\partial n} = 0 \quad (3.23)$$

where  $n$  is the local coordinate normal to the wall.

The production of kinetic energy,  $G_k$  and its dissipation rate  $\varepsilon$  at the wall-adjacent cells, which are the source terms in the  $k$ -equation, are computed on the basis of local equilibrium hypothesis. Under this assumption, the production of  $k$  and its dissipation rate are assumed to be equal in the wall-adjacent control volume. Thus the production of  $k$  is computed from:

$$G_k \approx \tau_w \frac{\partial U}{\partial y} = \tau_w \frac{\tau_w}{k \rho C_\mu^{1/4} k_P^{1/2} y_P} \quad (3.24)$$

and  $\varepsilon$  is computed from the  $\varepsilon$ -equation using Equation (3.25).

$$\varepsilon_P = \frac{C_\mu^{1/4} k_P^{1/2}}{\kappa y_P} \quad (3.25)$$

### **3.6.4 Solver Algorithms**

#### **3.6.4.1 Segregated Solver**

The solution of the integral governing equations for the conservation of mass, momentum, energy and other scalars such as the turbulence quantities are solved using the segregated solver provided by FLUENT. Using this approach, the governing equations are solved sequentially. As the governing equations are non-linear and coupled, several iterations of the solution loop must be performed before a converged solution is obtained. The steps within each iteration are shown in Figure 3.4. In the segregated solver method, each discrete governing equation is linearized implicitly with respect to the equation's dependent variable. This will result in a system of linear equations for each cell in the domain. A point implicit (Gauss-Seidel) linear equation solver is used in conjunction with an algebraic multi-grid (AMG) method to solve the resultant scalar system of equations in each cell.

#### **3.6.4.2 Pressure Interpolation Scheme**

The so-called PRESTO! (Pressure Staggering Option) pressure interpolation scheme is used to compute the face values of pressure from the cell values. This scheme makes use of the discrete continuity balance for a staggered control volume about the face to compute the face pressure. This procedure is similar in concept with the staggered grid schemes used with structured meshes (Patankar, 1980).

#### **3.6.4.3 Pressure-Velocity Coupling**

For the pressure-velocity coupling, the so-called Pressure-Implicit with Splitting of Operators (PISO) pressure-velocity coupling scheme is used. The PISO scheme, part of SIMPLE (Semi-Implicit Method for Pressure-Linked Equations) family of algorithms, is based on the higher degree of the approximate relation between the corrections for pressure and velocity. One of the limitations of the SIMPLE and SIMPLEC (SIMPLE-Consistent) algorithms is that new velocities and corresponding fluxes do not satisfy the momentum

balance after the pressure correction equation is solved. As a result the calculations must be repeated until the balance is satisfied. To improve the efficiency of the calculation, the PISO algorithm performs two additional corrections, namely the neighbor correction and the skewness correction. The main idea of the PISO algorithm is to move the repeated calculations required by SIMPLE and SIMPLEC inside the solution stage of the pressure correction equations (Issa, 1986).

After one or more additional PISO loops, the corrected velocities satisfy the continuity and momentum equations more closely. This is known as the neighbor-correction step. Although the PISO algorithm takes more CPU time per solver iteration, the number of iterations for convergence is dramatically decreased for convergence, especially for transient problems. For mesh with some degree of skewness, the approximate relationship between the correction of mass flux at the cell face and the difference of the pressure corrections at the adjacent cells is very rough. Since the components of the pressure-correction gradient is not known in advance, an iterative process similar to the PISO neighbor correction is necessary (Ferziger and Peric, 2002). After the initial solution of the pressure-correction equation, the pressure-correction gradient is re-calculated and used to update the mass flux corrections. This process is known as the skewness correction and it significantly reduces the convergence difficulties associated with highly distorted meshes.

### **3.7 Two-Dimensional Modeling of Browne's Experiment**

Based on the hydroplaning profile shown in Figure 3.1 and the solver algorithms described in the prior sections, it is first sought if a two-dimensional approach of a typical hydroplaning region is representative of the entire hydroplaning phenomenon.

#### **3.7.1 Geometry of Model**

The geometry of the three-dimensional model, which the proposed two-dimensional form is based on, is as shown in Figure 3.5. The tire deformation model shown in the bottom

of the figure is based on the experimental model used by Browne (1971) for numerical verification of his two-dimensional model.

Studies conducted by Dreher and Horne (1966) indicated that when the ground speed increases above the critical hydroplaning speed, the angle between the bow wave and runway decreased progressively until at some high ground speed, the bow wave completely disappeared. However in this study, the emphasis is on incipient hydroplaning and not on speeds exceeding the critical hydroplaning speed. Thus, the formation of bow wave is expected. Therefore, it is necessary that the model must include the ability of surface tracking of the free surface of water and the formation of bow wave. In order to do so, a two-phase flow comprising a layer of air jet and a layer of water jet has to be considered. This is indicated in Figure 3.2(b) and Figure 3.5, in which air and water each has its own inlets and outlets for.

A two-dimensional model is also analyzed in this study. In this model, the centre-line profile of the hydroplaning region is used and is shown in Figure 3.6. This model has a geometry that is essentially a simplification of the proposed three-dimensional model.

### **3.7.2 Boundary Conditions**

As shown in Figure 3.6, the upstream boundary conditions consist of a pair of inlets, namely a velocity inlet of 5.08 mm (0.2 in.) thick for water and a velocity inlet of 50.8 mm (2 in.) thick of air. The choice of the water film thickness is based on the experimental and numerical conditions used by Browne (1971). In this case, a uniform velocity profile is used. The pavement surface is modeled as a moving wall. The speed of the air, water and the pavement surface are kept as 15.3 m/s (34.4 mph) in order to be consistent with Browne's work. The assumption of a moving wall to model the pavement surface is different from the experimental conditions assumed by Browne (1971) that the pavement surface is replaced by an imaginary plane symmetrical about the center-line. This is because in his experiment, he had fabricated two plates and directed a jet of 10.16 mm (0.4 in.) towards the plates separated by a gap of 0.254 mm (0.01 in.). Hence in the verification of the model, the choice of a pavement surface as a wall and that of a line of symmetry has to be tested as a check to the

experimental results. Furthermore, his numerical model's assumptions of a moving wall and a laminar flow model are also tested. The inlet is placed at a distance of 100 mm away from the leading edge of the wheel (approximately 40 times the thickness of the hydroplaning region, or 400 times the smallest film thickness) so as to allow for any possible formation of bow wave.

The side edges and the trailing edge are modeled as pressure outlets with the pressure set as 0 kPa (i.e. atmospheric pressure). These are consistent with measurements made by prior experimental research by Horne and Joyner (1965) and the boundary conditions used in the numerical research by Browne (1971). Similarly, the top boundary is set as a pressure outlet at atmospheric pressure and the top boundary is placed at a distance of 25.4 mm (or one time the thickness of plate, or 100 times the smallest film thickness). It is noted that the side edge pressure outlet is not used in the two-dimensional model, but has to be used and tested in the three-dimensional model. For the boundary conditions, there is a need to conduct simulations on the effect of the boundary distance from the wheel model to test if there is any convergence in the ground hydrodynamic pressure. It is noted that the centre line of the wheel can be treated as a plane of symmetry. A summary of the boundary conditions used by Browne and this study is shown in Table 3.2.

### **3.7.3 Material Properties**

The properties of water and air at 20°C are used in this study. The density, dynamic viscosity and kinematic viscosity of water at 20°C are 998.2 kg/m<sup>3</sup>, 1.002 x 10<sup>-3</sup> Ns/m<sup>2</sup> and 1.004 x 10<sup>-6</sup> m<sup>2</sup>/s respectively (Chemical Rubber Company, 1988). The density, dynamic viscosity and kinematic viscosity of air at standard atmospheric pressure and 20°C are 1.204 kg/m<sup>3</sup>, 1.82 x 10<sup>-5</sup> Ns/m<sup>2</sup> and 1.51 x 10<sup>-5</sup> m<sup>2</sup>/s respectively (Blevins, 1984).

### **3.7.4 Description of Mesh used in the Analysis**

As explained in the earlier sections, the pre-processor GAMBIT is used to generate the meshes for the fluids. In the simulation using the two-dimensional hydroplaning model,



quadrilateral mesh elements are used to depict each finite volume. Since the finite volume method is employed in the analysis, only 4-node quadrilateral mesh elements are allowed.

FLUENT (2005) recommends the use of at least 5 mesh elements for channel and pipe flows. In the simulation in this research, ten 4-node quadrilateral mesh elements are used for the smallest channel in the model, i.e. the hydroplaning region. The optimal number of mesh elements needed to give a converged solution can be tested through a mesh sensitivity analysis. Figure 3.7 shows the mesh set-up of the two-dimensional hydroplaning model. There are 14,375 elements in the model.

### 3.7.5 Simulation Results Based on the Proposed Two-Dimensional Model

The simulation is performed on SUN BLADE 1000 workstations which have single 900MHz UltraSPARC-III processor and 1 or 2 G-bytes memory each. The fluid models used in the analysis include the usual Navier-Stokes equations, the  $k-\varepsilon$  turbulence model and the VOF multiphase model as described in the earlier parts of the chapter.

Based on the specified geometry, boundary conditions and initial conditions, the steady-state volume fraction plot is shown in Figure 3.8. It is observed that a bow-wave is formed, which is expected and is observed in experiments conducted by Browne (1971). Figure 3.9(a) and Figure 3.9(b) show the velocity vectors under the wheel in the moving reference frame (i.e. the model) and the stationary observer reference frame (i.e. the reality) respectively.

Figure 3.10 indicates the contours of the hydrodynamic pressure in the model and it is seen that the pressure near the boundaries are at near zero pressure (i.e. atmospheric pressure), thereby indicating the suitability of the choice of the boundary conditions. This will be further verified in the later parts of this sub-section.

Table 3.3 shows the inflow and outflow properties of the two fluids used in the study, namely air and water using the laminar model setup. It is noted that some recirculation will occur and this is mainly due to the formation of the bow-wave and this forces the air to go into recirculation. Also, the conservation of mass is obeyed as 99.97% of the air and 99.73% of the

water is conserved. The slightly lower level of mass conservation for water is due to the fact that in the solution scheme of the VOF method, air is used as a primary phase for computational convergence and water is used as a secondary phase. In this case it is noted that 98.83% of the water is lost as splash.

The ground hydrodynamic pressure distribution is shown in Figure 3.11 and the average ground hydrodynamic pressure under the hydroplaning wheel is found to be 121.1 kPa. This value ought to be equivalent to the tire pressure of the wheel. But at this point, the obtained average ground hydrodynamic pressure serves to act as a verification of the model in terms of mesh quality and the choice of the boundary conditions. The aptness of the model in simulating hydroplaning will be further discussed in the later parts of the section.

### **3.7.6 Mesh Sensitivity Analysis**

In order to ensure that the solution obtained is numerically accurate, grid independence tests have to be conducted. Various finite volume mesh sizes were examined to obtain the optimal mesh quality to be used. In this study, the mesh design in the hydroplaning region is of utmost importance since it is the thinnest flow channel expected in the model. As such, the number of finite volume cells in the depth of the hydroplaning region is a key aspect in mesh design. Four different mesh designs are tested and the steady-state volume fraction plot is shown in Figure 3.12. The aspect ratio (maximum edge length divided by minimum edge length) of the different mesh designs are kept constant at 7.5 for each of the four cases tested. It can be seen that the plots show similar fluid behaviors with the exception of the use of coarse mesh (i.e. the mesh using 5 quadrilateral mesh elements within the smallest hydroplaning channel). A key indicator of mesh convergence is the average ground hydrodynamic pressure as this parameter is used in the definition of hydroplaning. Figure 3.13 shows the ground hydrodynamic pressure distribution under the wheel for the various meshes and it can be observed that there are little variations among the various pressure profiles except for the one with 5 mesh elements, thereby indicating grid independence. Figure 3.14 and Table 3.4 show the effect of the mesh design on the average ground hydrodynamic pressure. It can be

seen that using 10 mesh elements within the hydroplaning regions is sufficient to render a relatively accurate solution to ensure grid independence and thus this mesh design is used in subsequent two-dimensional analyses.

### 3.7.7 Effect of Boundary Conditions

The effect of the boundary conditions has to be studied to ensure that the distances of the boundaries, especially the locations of the velocity inlets and the pressure outlets are sufficiently far away to ensure numerical accuracy of the model in terms of the key indicator of hydroplaning, i.e. the average ground hydrodynamic pressure under the wheel. The boundary locations of the various models tested are shown in Table 3.5. The choice of the locations is based on the consideration of the aptness of the location of the boundaries and the computational efficiency of the analysis. Model A is essentially a modification of the model used by Browne (1971). The choice of these boundary conditions are justified through prior experimental and numerical research as explained in the earlier sections of the chapter. The computational constraint is perhaps the sole consideration in the testing of the effects of the boundary conditions. This is because the two-dimensional model proposed would be used in the three-dimensional form of the proposed model. The number of mesh elements of the three-dimensional form of model B and D easily exceeds one million mesh elements while that of models C and E easily exceeds two-million mesh elements. The current computational capabilities of the workstations even with the use of 16 parallel processors, would find the three-dimensional forms of models C and E computationally demanding to solve.

The steady-state volume fraction plots of the various models are shown in Figure 3.15 and it can be seen that the plots exhibit similar fluid behaviors. Table 3.6 shows the effect of the location of the boundary conditions on the average ground hydrodynamic pressure. It can be seen that the average ground hydrodynamic pressure are similar with an error of less than 1%, thereby indicating that the effect of the locations of the boundary conditions considered are insignificant. This indicates that the proposed model with the boundary conditions used in the prior sections is adequate to achieve the intended numerical accuracy.

### 3.7.8 Analysis of Results and Suitability for Hydroplaning Simulation

From the ground hydrodynamic pressure distribution shown in Figure 3.11, the average ground hydrodynamic pressure under the hydroplaning wheel and the tire inflation pressure are both found to be 121.1 kPa. The ratio of tire pressure to  $0.5\rho U^2$  is found to be 1.027 which is much larger than the expected NASA hydroplaning equation value of 0.644. This means that the proposed two-dimensional model using a turbulent flow model assumption is not an adequate model in simulating hydroplaning. Furthermore, the model shows that 98.83% of the water is lost as splash. This is a reflection of the inadequacy of the model because one important component of outflow, the in-plane and out-of-plane outflows are not modeled. This has resulted in an excessively high hydrodynamic pressure being developed under the wheel and an extremely high percentage of splashes. Browne (1971) indicated in his model that close to 6% of the water would pass through the imprint and approximately 55% lost as splash. The proposed two-dimensional model predicts that hydroplaning would occur at a speed of 68.6 km/h (42.8 mph) compared to 87.3 km/h (54.4 mph) predicted by the NASA hydroplaning equation. The two-dimensional model is overly conservative in the prediction of hydroplaning speed.

To further substantiate the point, the model is re-run using the plane of symmetry as the pavement surface model. It is noted that the experimental data points for the hydrodynamic pressure do not fit well to the ground hydrodynamic pressure profile obtained from the simulation as shown in Figure 3.16. In fact, this model would over-predict the pressure. The average ground hydrodynamic pressure is 103.0 kPa, yielding a ratio of tire pressure to  $0.5\rho U^2$  of 0.87. This is still considerably larger than Browne's value of 0.56, showing the inappropriateness of the two-dimensional model.

### 3.8 Three-Dimensional Modeling of Browne's Experiment

The prior section shows that the two-dimensional model is inadequate to simulate hydroplaning accurately. This section presents the development of a three-dimensional model

to simulate hydroplaning based on the actual three-dimensional geometry introduced in Section 3.3.

### **3.8.1 Geometry of Model and Selection of Boundary Conditions**

This proposed three-dimensional model uses the tire deformation profile shown in Figure 3.1 which is based on Browne's (1971) experiment and a geometry shown in Figure 3.5. The boundary conditions and the initial conditions adopted are as described in Section 3.7.2 for the two-dimensional model.

### **3.8.2 Description of Mesh used for 3-D simulation**

The pre-processor GAMBIT is used to generate the finite volume mesh for the fluids. In the simulation using the three-dimensional hydroplaning model, hexahedral and wedge elements are used to depict each finite volume. Since the finite volume method is employed in the analysis, only 6-node wedge elements and 8-node hexahedral elements are allowed. FLUENT (Fluent Inc., 2005) recommends the use of at least 5 mesh elements for channel and pipe flows and in this simulation, ten 8-nodes hexahedral elements are used for the smallest channel in the model, i.e. the hydroplaning region. The optimal number of mesh elements needed to give a converged solution can be tested through a mesh sensitivity analysis. Figure 3.17 shows the mesh design of the three-dimensional hydroplaning model. There are 394,900 mesh elements in the proposed model.

### **3.8.3 Simulation Results Based on Proposed 3-D Model**

The simulation is performed either on the 3 or 8 parallel CPUs available in the COMPAQ GS320 alpha server, which is configured with 22 EV67 731 MHz Alpha 21264 CPUs and 11 GB of memory. The computational time needed for the simulation ranges from 36 CPU-hours for a 0.5 million elements model to 150 CPU-hours for a 1.7 million elements model, thereby warranting the need for parallel processing. The fluid models used in the analysis include the Navier-Stokes equations, the  $k-\varepsilon$  turbulence model and the VOF

multiphase model. Based on the specified geometry, boundary conditions and initial conditions, the steady-state phase plot along the plane of symmetry is shown in Figure 3.18. It is observed that a bow-wave is formed, which is expected and is observed in experiments conducted by Browne (1971). Figure 3.19 shows the velocity vectors under the wheel in the moving reference frame (i.e. the model) and the stationary observer reference frame (i.e. the reality). It is observed that the velocities near the wheel are near-zero, indicating that in the actual reference frame, there is a thin film of lubricant under the hydroplaning wheel moving at near the vehicle speed along with the sliding wheel.

Table 3.7 shows the inflow and outflow properties of the two fluids used in the study, namely air and water using the laminar model setup. Also, the conservation of mass is obeyed as 99.93% of the air and 99.60% of the water is conserved. In this case, 25.28% of the water is lost as splash.

Figure 3.20 indicates the contours of the hydrodynamic pressure in the model and it is seen that pressure near the boundaries are at near zero pressure (i.e. atmospheric pressure), thereby indicating the suitability of the choice of the boundary conditions. This will be further verified in the latter parts of this sub-section. The ground hydrodynamic pressure distribution under the centre-line of the wheel is shown in Figure 3.21 and selected profiles along lines in the wheel direction are shown in Figure 3.22. The average ground hydrodynamic pressure under the hydroplaning wheel is found to be 72.5 kPa. This value would serve to act as a verification of the model in terms of mesh quality and the choice of the boundary conditions. This is smaller than the average ground hydrodynamic pressure of 121.1 kPa obtained from the two-dimensional analyses, as shown in Figure 3.11. This is expected since the two-dimensional analyses ignore the side flow of the water impinging on the wheel as opposed to the three-dimensional analyses of fluid flow shown in this section.

### **3.8.4 Mesh Sensitivity Analysis**

In order to ensure that the solution obtained is numerically accurate, grid independence tests have been conducted. Different mesh densities were examined to obtain the optimal mesh

design. The number of hexahedral elements in the width of the hydroplaning region is a key aspect of mesh design. Five different mesh designs are tested and the steady-state volume fraction plot is shown in Figure 3.23. The aspect ratio (maximum edge length divided by minimum edge length) of the different mesh designs are kept constant at 7.5 for each of the four cases tested. It can be seen that the plots exhibit similar fluid behaviors. A key indicator of mesh convergence is the average ground hydrodynamic pressure as this parameter is used in the definition of hydroplaning. Figure 3.24 shows the ground hydrodynamic pressure distribution along the centre line under the wheel for the various mesh designs and it can be observed that there are little variations between the various pressure profiles except for the mesh with 5 elements, thereby indicating grid independence for the for designs with 10 or more elements. Figure 3.25 and Table 3.8 show the effect of the mesh design on the average ground hydrodynamic pressure. It can be seen that using 10 mesh elements within the hydroplaning regions is sufficient to render a relatively accurate solution and thus this mesh design is used in subsequent three-dimensional analyses in this research.

### **3.8.5 Effect of Boundary Conditions**

Similar to that performed in the two-dimensional analyses, the effect of the boundary conditions has to be studied to ensure that the distances of the boundaries, especially the locations of the velocity inlets and the pressure outlets, are sufficiently far away to ensure numerical accuracy of the model in terms of the key indicator of hydroplaning, i.e. the average ground hydrodynamic pressure under the wheel. The boundary locations of the various models tested are shown in Table 3.9. The choice of the locations is based on the consideration of the aptness of the location of the boundaries and the computational efficiency of the analysis. Models A to E are essentially the three-dimensional form of the two-dimensional models highlighted in the prior analyses. Model F is added to test the effect of varying the location of the pressure outlet from the side of the hydroplaning wheel.

The steady-state volume fraction plots of the various models are shown in Figure 3.26 and it can be seen that the plots show similar fluid behaviors. Table 3.10 shows the effect of

the location of the boundary conditions on the average ground hydrodynamic pressure. It can be seen that the average ground hydrodynamic pressure are similar with an error of less than 2%, thereby indicating that the effect of the locations of the boundary conditions considered are insignificant. This indicates that the proposed model with the boundary conditions used in the prior sections is adequate to achieve the intended numerical accuracy.

### **3.8.6 Analysis of Results and Suitability for Hydroplaning Simulation**

Modeling after Browne's (1971) experimental set-up, the ground hydrodynamic pressure distributions obtained from the simulations are shown in Figure 3.21 and Figure 3.22 and the average ground hydrodynamic pressure under the hydroplaning wheel is found to be 72.5 kPa. This value should theoretically be equal to the tire inflation pressure in order for hydroplaning to occur. The average ground hydrodynamic pressure is therefore used to evaluate the ratio of tire pressure to  $0.5\rho U^2$ . This ratio is found to be 0.620 which is close to the expected NASA hydroplaning equation value of 0.644 with a percentage difference of 3.7%. This difference is acceptable, considering the fact that the NASA hydroplaning equation is empirically derived from a wide variety of tires operating on flooded pavements (Horne and Joyner, 1965). This means that the proposed three-dimensional model using a turbulent flow model is an acceptable model in simulating hydroplaning. Furthermore, the model shows that 95% of the water is lost either as side-flow or splash and will not leave through the trailing edge of the wheel. This corresponds to Browne's numerical research which claimed that approximately 94% of the water will not leave through the trailing edge of the wheel. Comparing the hydroplaning profile with experimental data from past research (Horne and Dreher, 1963; Horne and Joyner, 1965; and Browne, 1971) indicates that the hydrodynamic pressure profile obtained from the simulations (as shown in Figure 3.27) is similar to those works. These evidences highlight the appropriateness of the model in hydroplaning simulation.

It is noted that the proposed model is not entirely consistent with the experimental model used in Browne's research (Browne, 1971) as highlighted in Table 3.2. In order to assess the validity of the model, it is sought if using a plane of symmetry as the boundary



condition for the pavement surface (as modeled in Browne's experiment and subsequently used in his numerical studies) would yield compatible results to Browne's experimental data. In this case, the model is re-run using the plane of symmetry as the pavement surface model. It is noted that the experimental data points for the hydrodynamic pressure fit rather well to the ground hydrodynamic pressure profile obtained from the simulation as shown in Figure 3.28. The average ground hydrodynamic pressure is 67.0 kPa, yielding a ratio of tire pressure to  $0.5\rho U^2$  of 0.57. This corresponds extremely well with Browne's value of 0.56, showing the appropriateness of the model and the fundamental governing equations behind the hydroplaning theory. However, this also highlights that Browne's research could not accurately predict hydroplaning primarily because of a different choice in the boundary conditions and flow model.

Another option to be considered is the use of laminar flow model instead of the turbulence flow model. This is because of the fact that hydrodynamic lubrication theory invariably makes use of Reynolds assumptions as shown in Table 3.11. It is noted that laminar flow is one of the many critical assumptions made and may not be valid under the hydroplaning condition. The assumptions made are appropriate for viscous hydroplaning which is essentially a low speed phenomenon. However, no research has been conducted to assess the validity of this assumption in the case of hydroplaning under the high speed scenario. It is highlighted here that Reynolds lubrication equation is in fact a special case of the set of Navier-Stokes equations and can be derived from the Navier-Stokes equations by using the Reynolds assumptions. As such, simulations using the 3D model are run using the laminar flow assumption to assess the suitability in hydroplaning simulation. The ground hydrodynamic pressure profile along the centerline of the wheel is shown in Figure 3.30. The average ground hydrodynamic pressure is 67.0 kPa, yielding a ratio of tire pressure to  $0.5\rho U^2$  of 0.57, which is close to Browne's value of 0.56. This highlights that using a laminar model such as the one proposed by Browne is inappropriate. This value, as compared to the proposed 3-D model using the turbulent flow model, provides a poor approximation to the ratio predicted by the NASA hydroplaning equation. Such observations are expected since flows are

likely to be turbulent and the assumption in the classical hydrodynamic theory is likely to be invalid. As such modifications have to be made to consider the effects of turbulence (Stachowiak and Batchelor, 2001). Since the simulation considers the full set of Navier-Stokes equations of which the lubrication theory is a special situation, it is deemed that the proposed 3-D model is theoretically sound in hydroplaning simulation. This is supported in the current study through evidences in the experimental and numerical verification as highlighted in this chapter.

### **3.9 Summary**

This chapter has provided the major considerations in the development of a pneumatic tire hydroplaning model to simulate hydroplaning of a locked wheel using an assumed tire deformation profile.

The first part of the chapter lays the theoretical foundations for the simulation of hydroplaning. Three main models are considered, namely the fluid flow model, the tire deformation model and the pavement surface model. For the fluid flow model, the complete set of Navier-Stokes equations is applied with the consideration of turbulence. Turbulence is modeled using the standard k-e model developed by Launder and Spalding (1974). For the hydroplaning tire deformation model, a hydroplaning profile used by Browne (1971) in his experiments and numerical modeling on hydroplaning of pneumatic tires is considered. For the pavement surface model, it is assumed that the pavement surface is a smooth plane surface.

The second part of the chapter highlights the numerical modeling concept of the hydroplaning phenomenon. The hydroplaning phenomenon of a locked wheel over a flooded smooth pavement is studied. Water is used as a contaminant. Hydroplaning is assumed to occur when the average ground hydrodynamic pressure is equal to the tire pressure of the wheel. The CFD package FLUENT is used to simulate the hydroplaning phenomenon by means of the finite volume method.

The third part of the chapter discusses the possibility of two-dimensional modeling of the hydroplaning phenomena through the consideration of the experimental tire deformation

model used in Browne's (1971) works. Grid independence tests are conducted and the effect of boundary locations is examined. It is found that the proposed two-dimensional model using a turbulent flow model assumption is a poor model in simulating hydroplaning. This is because one important component of outflow, the in-plane and out-of-plane outflows are not modeled, thus resulting in an excessively high hydrodynamic pressure under the wheel and an extremely high percentage of splash. The two-dimensional model also results in an over-conservative prediction of hydroplaning speed which is very much lower than that predicted by the NASA hydroplaning equation.

The last part of the chapter discusses the possibility of three-dimensional modeling of the hydroplaning phenomenon through the consideration of the experimental model used in Browne's (1971) works, knowing that side outflows have to be considered. Grid independence tests are conducted and the effect of boundary locations is examined. It is found that the proposed 3-D model could adequately model hydroplaning and it gives a ratio of tire pressure to  $0.5\rho U^2$  of 0.620 which is close to the predicted NASA hydroplaning value of 0.644. Furthermore the shapes of the computed ground hydrodynamic profiles are closely consistent with data reported by Horne and Dreher (1963), Horne and Joyner (1965) and Browne (1971). Therefore, the proposed three-dimensional model is suitable for the simulation of hydroplaning.

**Table 3.1: Summary of current agency practices of measuring surface friction (Henry, 2000)**

Surface Friction Measurement Method	Number of Responding Agencies
<b>United States and Puerto Rico</b>	
Locked-wheel trailer (exclusive use of ASTM ribbed tire)	20 State Highway Agencies and Puerto Rico
Locked-wheel trailer (exclusive use of ASTM smooth tire)	5 States
Locked-wheel trailer (use of both ASTM ribbed and smooth tire)	7 States
Fixed slip device	1 State (Arizona)
Do not measure surface friction	2 States
<b>Foreign Agencies</b>	
Locked wheel method	4 agencies
Side force or variable slip methods	17 agencies

**Table 3.2: Summary of boundary conditions used in Browne's experiment (Browne, 1971) and in this study**

	Browne's numerical model	Proposed numerical model in this study
Lead edge of footprint	Velocity U, pressure based on Bernoulli's equation to simulate bow-wave/splash, assumed parabolic velocity profile.	Evaluated from Navier-Stokes equations based on boundary conditions of velocity inlet of velocity U for both air and water at pressure 0 kPa with a uniform velocity profile.
Side edge of footprint	Pressure outlet of 0 kPa.	Pressure outlet of 0 kPa.
Midline of footprint	Plane of symmetry.	Plane of symmetry.
Trailing edge of footprint	Pressure outlet of 0 kPa	Pressure outlet of 0 kPa
Pavement surface	Plane of symmetry for experimental and numerical simulation, effects of gravity ignored. Moving wall of velocity U for laminar model in later parts of his work.	Moving wall of velocity U for experimental and numerical simulation, effects of gravity considered.
Tire Profile	Assumed tire deformation profile from experiments conducted by Horne and Joyner (1965)	Assumed tire deformation profile from experiments conducted by Horne and Joyner (1965)

**Table 3.3: Mass flow rate for air and water through various boundaries based on a turbulent flow model for the proposed 2-D model**

Boundary Conditions	Mass Flow Rate for Fluid (kg/s/m)	
	Air	Water
Velocity Inlet – Air	0.8605	0
Velocity Inlet – Water	0	77.9137
Pressure Outlet– Air	-0.3674	0
Pressure Outlet – Water	0	-1.1210
Top Pressure Outlet	-0.5429	-77.0039
Sum (Percentage conserved)	-0.0003 (99.97%)	-0.2112 (99.73%)

**Table 3.4: Effect of mesh quality on the various parameters under the wheel for the proposed 2-D model**

Number of mesh elements in the smallest channel	Number of mesh elements in the model	$F_Y$ (N)	$F_X$ (N)	Average ground hydrodynamic pressure (kPa)	%
5	1,255	31,427.0	996.7	127.8	-
10	14,375	28,530.1	993.4	121.1	5.2
15	30,750	28,494.0	992.1	121.0	0.1
20	59,750	28,436.6	990.2	120.9	0.1

**Table 3.5: Summary of boundary conditions used in the study of the effect of boundary conditions for the 2-D analysis**

Boundary condition locations	Model				
	A	B	C	D	E
Distance of velocity inlets from lead edge of footprint, X1 (mm)	100 (20 <i>t</i> )	100 (20 <i>t</i> )	500 (100 <i>t</i> )	100 (20 <i>t</i> )	100 (20 <i>t</i> )
Distance of pressure outlet from trailing edge of footprint, X2 (mm)	0 (0 <i>t</i> )	0 (0 <i>t</i> )	0 (0 <i>t</i> )	100 (20 <i>t</i> )	500 (100 <i>t</i> )
Distance of pressure outlet from top of tire model, X3 (mm)	25 (5 <i>t</i> )	50 (10 <i>t</i> )	50 (10 <i>t</i> )	50 (10 <i>t</i> )	50 (10 <i>t</i> )

Note:  $t$  is the water film thickness used in the study and is equal to 5.08 mm (0.2 in.)

**Table 3.6: Effect of location of boundary conditions on the various parameters under the wheel for the 2-D analyses**

Model	Number of mesh elements in model	$F_Y$ (N)	$F_X$ (N)	Average ground hydrodynamic pressure (kPa)
A	14,375	28,530.1	993.4	121.1
B	31,125	28,539.0	999.2	121.1
C	36,375	28,406.3	994.8	120.5
D	42,125	28,283.7	998.5	120.0
E	86,125	28,278.9	1000.5	120.0

**Table 3.7: Mass flow rate for air and water through various boundaries based on a turbulent flow model for the proposed 3-D model**

Boundary Conditions	Mass Flow Rate for Fluid (kg/s)	
	Air	Water
Velocity Inlet – Air	0.05485	0
Velocity Inlet – Water	0	4.9385
Pressure Outlet– Air	-0.01256	0
Pressure Outlet – Water	0	-0.2227
Top Pressure Outlet	-0.04207	-1.2484
Side Pressure Outlet	-0.00018	-3.4477
Sum (Percentage conserved)	0.00004 (99.93%)	0.0197 (99.60%)

**Table 3.8: Effect of mesh quality on the various parameters under the wheel for the proposed 3D model**

Number of mesh elements in the smallest channel	Number of mesh elements in the model	$F_Y$ (N)	$F_X$ (N)	Average ground hydrodynamic pressure (kPa)	% improved
5	12,287	948.3	29.3	70.0	-
8	94,585	945.5	29.0	71.8	2.6
10	394,900	949.2	29.1	72.5	1.0
15	1,004,330	946.8	29.8	72.6	0.1
20	1,805,400	947.2	29.6	72.6	0.0

**Table 3.9: Summary of boundary conditions used in the study of the effect of boundary conditions for the 3D analysis**

Boundary condition locations	Model					
	A	B	C	D	E	F
Distance of velocity inlets from lead edge of footprint, X1 (mm)	100 (20 <i>t</i> )	100 (20 <i>t</i> )	500 (100 <i>t</i> )	100 (20 <i>t</i> )	100 (20 <i>t</i> )	100 (20 <i>t</i> )
Distance of pressure outlet from trailing edge of footprint, X2 (mm)	0 (0 <i>t</i> )	0 (0 <i>t</i> )	0 (0 <i>t</i> )	100 (20 <i>t</i> )	500 (100 <i>t</i> )	0 (100 <i>t</i> )
Distance of pressure outlet from top of tire model, X3 (mm)	25 (5 <i>t</i> )	50 (10 <i>t</i> )	50 (10 <i>t</i> )	50 (10 <i>t</i> )	50 (10 <i>t</i> )	25 (10 <i>t</i> )
Distance of pressure outlet from side of tire model, X4 (mm)	0 (0 <i>t</i> )	0 (0 <i>t</i> )	0 (0 <i>t</i> )	0 (0 <i>t</i> )	0 (0 <i>t</i> )	100 (20 <i>t</i> )

Note:  $t$  is the water film thickness used in the study and is equal to 5.08 mm (0.2 in.)

**Table 3.10: Effect of location of boundary conditions on the various parameters under the wheel for the 3D analyses**

Model	Number of mesh elements in model	$F_Y$ (N)	$F_X$ (excluding the front portion) (N)	Average ground hydrodynamic pressure (kPa)
A	394,900	949.2	29.1	72.5
B	619,990	948.6	29.1	72.5
C	1,039,900	964.7	30.6	73.6
D	559,900	945.7	29.1	72.3
E	1,672,500	965.3	30.6	73.6
F	1,054,300	962.5	30.2	73.4

**Table 3.11: Summary of simplifying assumptions in hydrodynamics (Stachowiak and Batchelor, 2001)**

	Assumption	Comments
1	Body forces are neglected.	Always valid, since there is no extra outside fields of forces acting on the fluids with an exception in magneto-hydrodynamic fluids and their applications.
2	Pressure is constant through the film.	Always valid, since the thickness of the film is in the range of several mm. There might be some exceptions though with elastic fluids.
3	No slip at the boundaries.	Always valid, since the velocity of the oil layer adjacent to the boundary is the same as that of the boundary.
4	Lubricant behaves like a Newtonian fluid.	Usually valid with certain exceptions, e.g. polymeric oils.
5	Flow is laminar.	Usually valid, except large bearings, e.g. turbines
6	Fluid inertia is neglected.	Valid for low bearing speeds or high loads. Inertia effects are included for more exact analysis.
7	Fluid density is constant.	Usually valid for fluids where there is not much thermal expansion. Not valid for gases.
8	Viscosity is constant throughout the generated fluid film.	Crude assumption, but necessary to simplify calculations, although this is not true. Viscosity is not constant throughout the film.

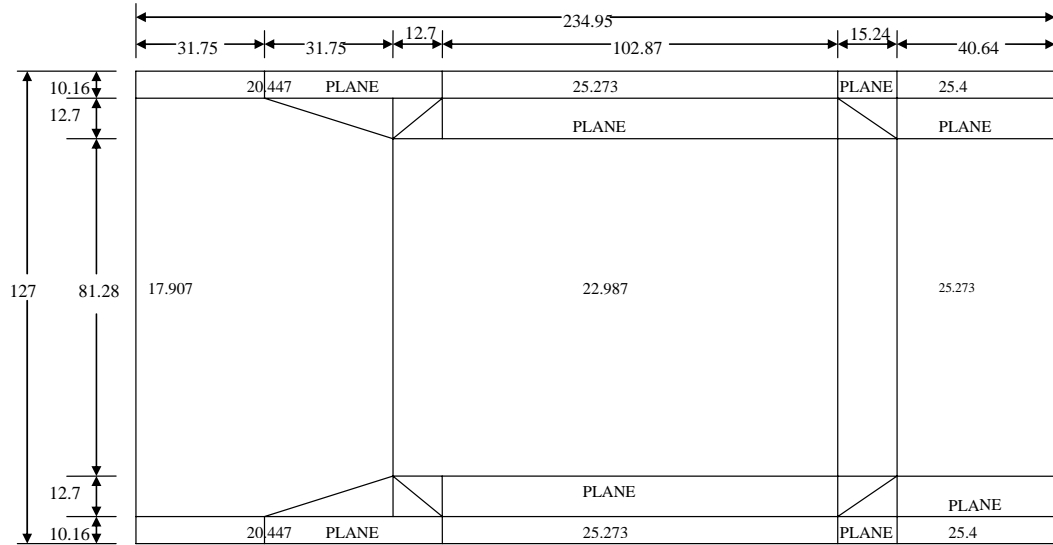
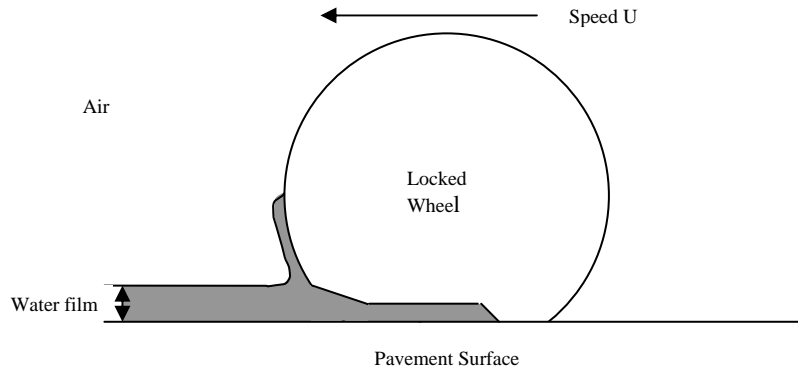
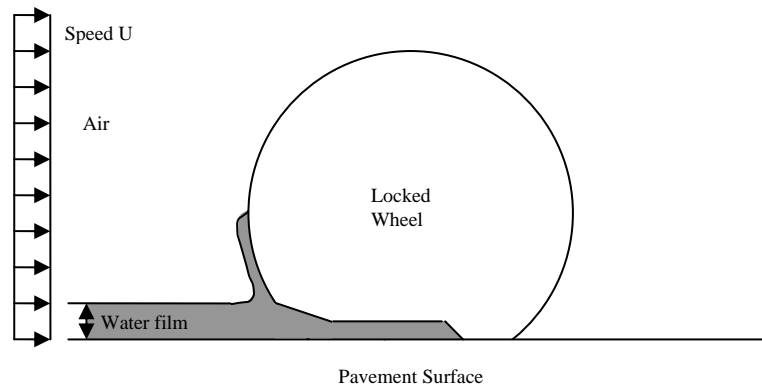


**Figure 3.1: Tire deformation profile of a hydroplaning tire (Browne, 1971). (Dimensions are shown in mm)**



**(a) Stationary observer frame of reference**



**(b) Moving wheel frame of reference**

**Figure 3.2: Concept of hydroplaning modeling**



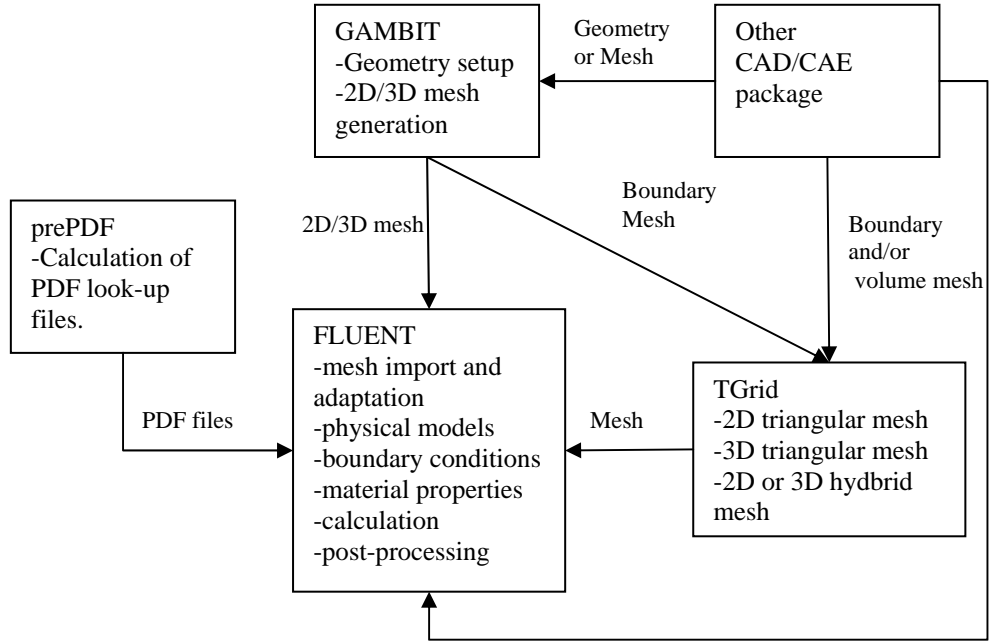


Figure 3.3: Program structure of FLUENT package (Fluent Inc., 2005)

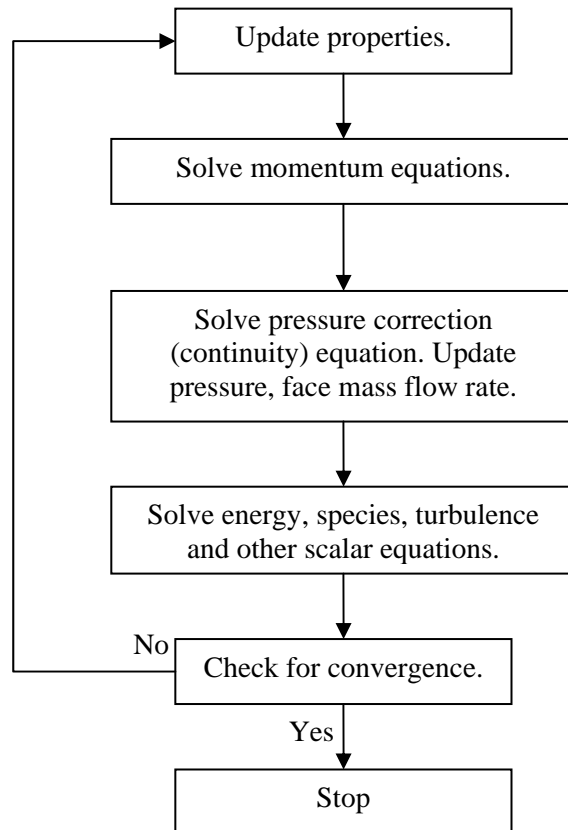


Figure 3.4: Overview of the segregated solution method (Fluent Inc., 2005)

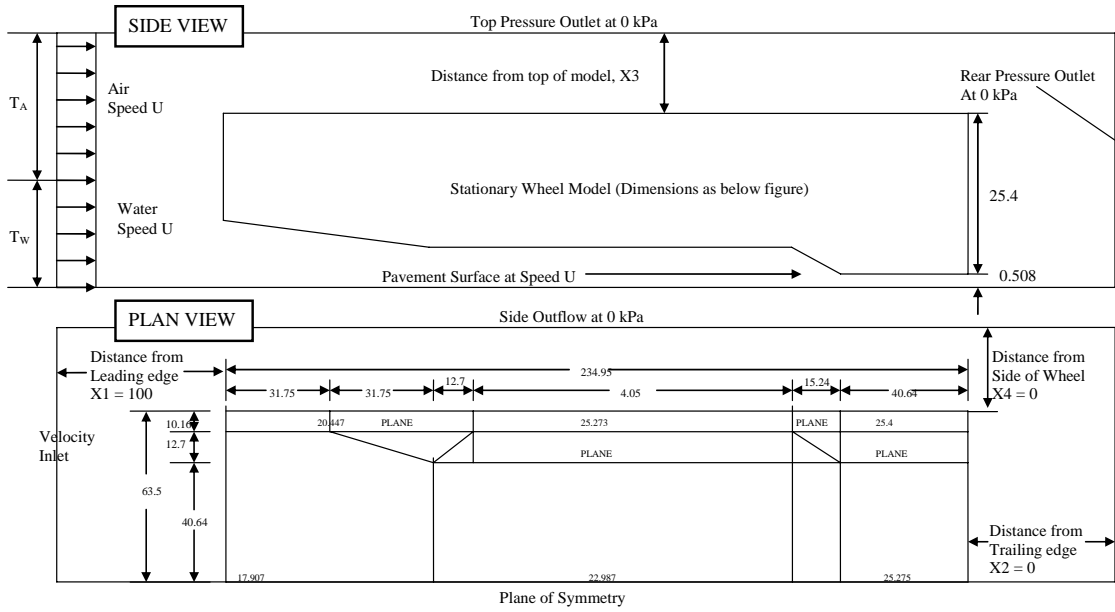


Figure 3.5: Geometry of the proposed three-dimensional model (Dimensions are in mm.)

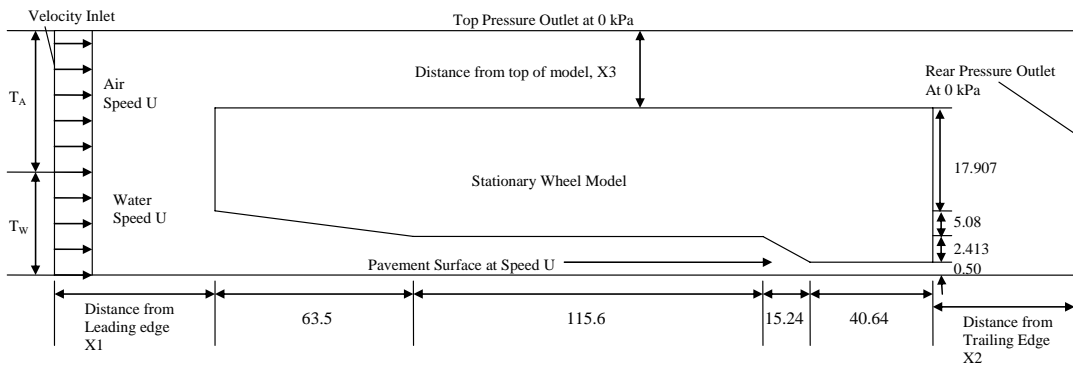


Figure 3.6: Geometry of the proposed two-dimensional model (Dimensions are in mm.)

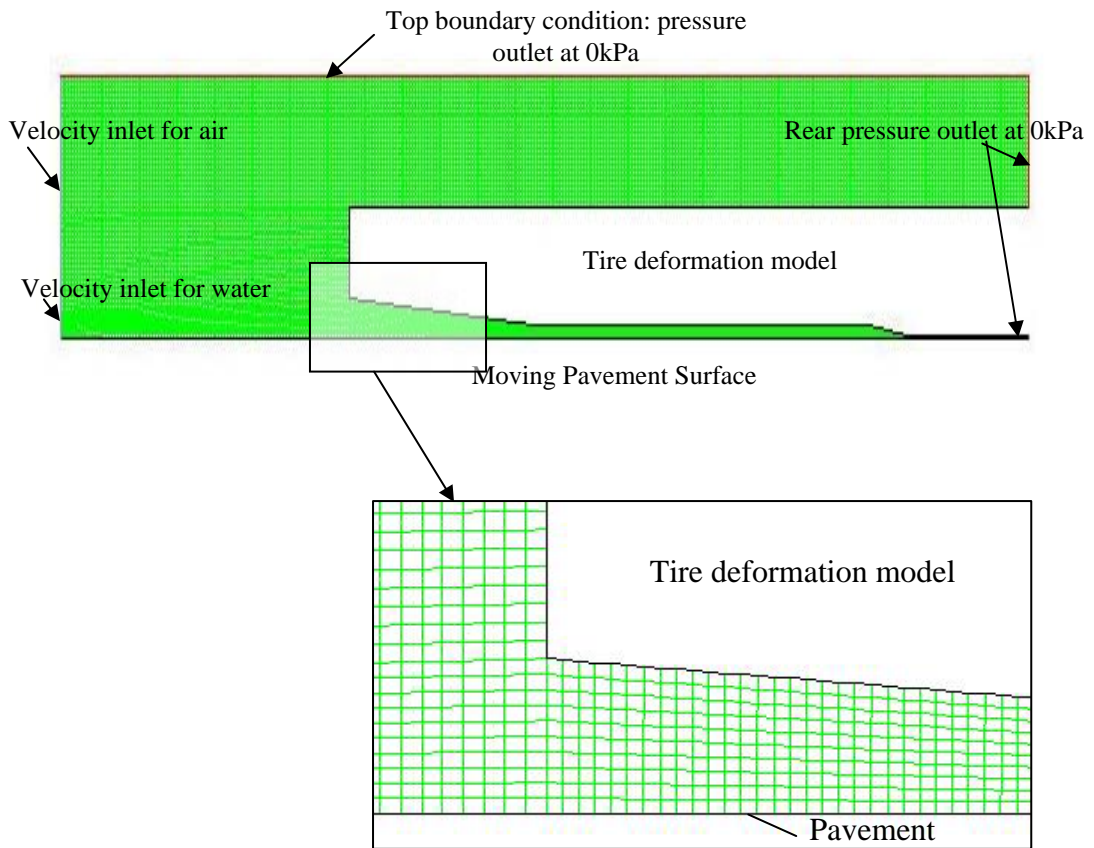


Figure 3.7: Mesh design of the proposed 2D model

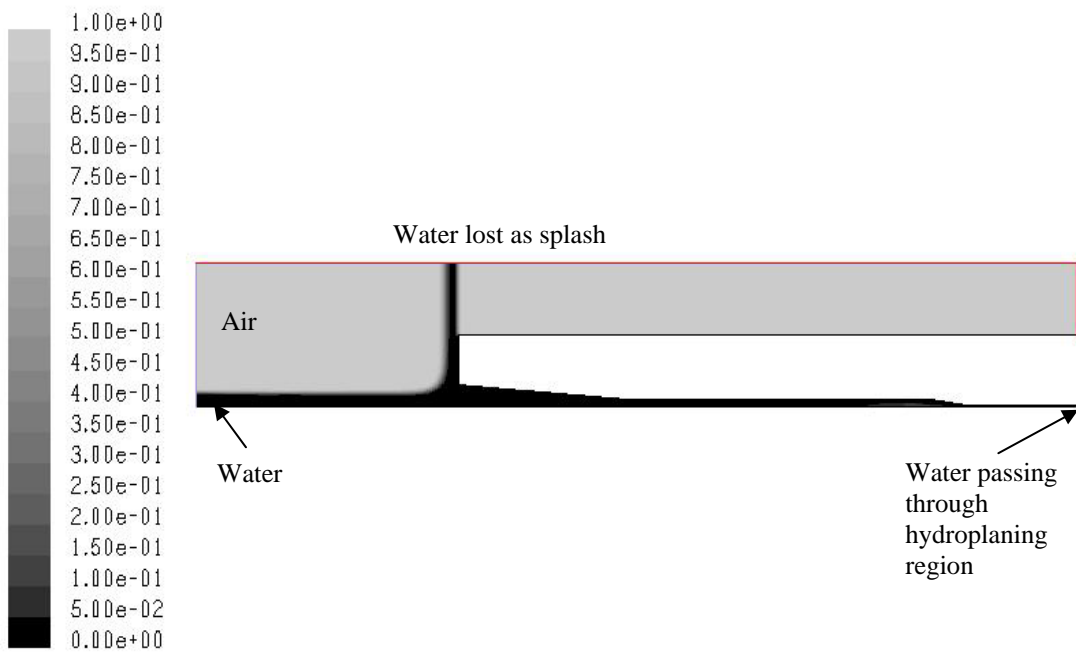
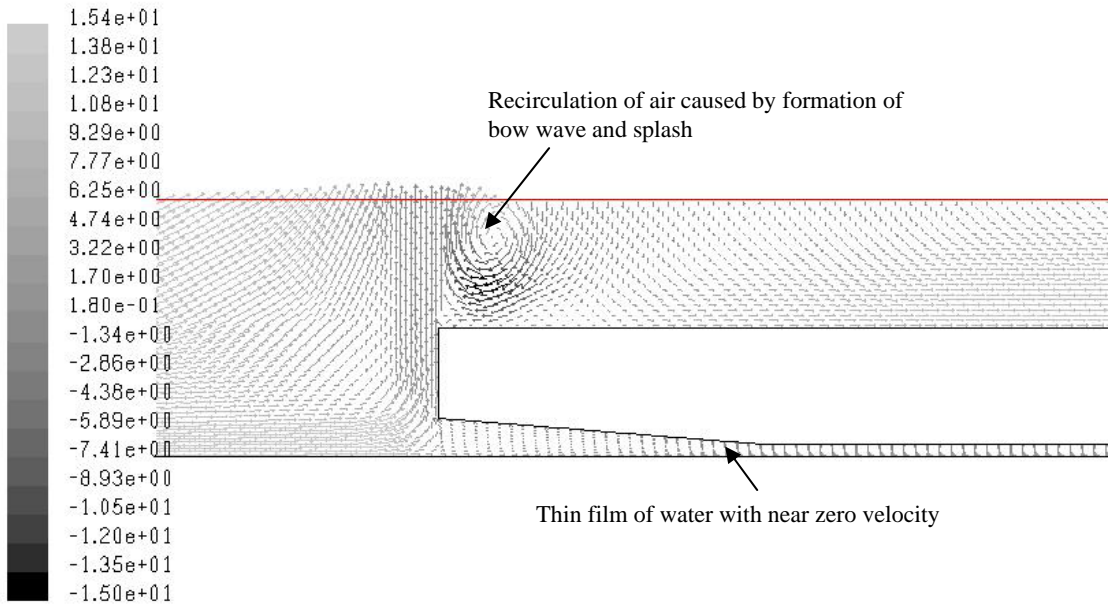


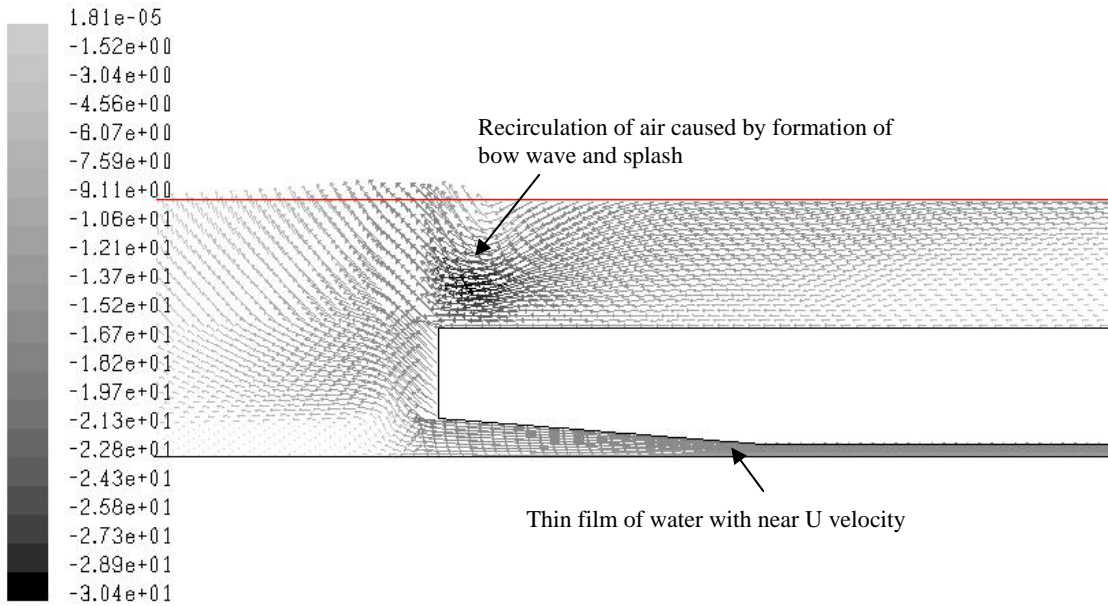
Figure 3.8: Steady state volume fraction plot for the proposed 2D model

Color scale by x-velocity (m/s)



(a) Moving wheel reference frame

Color scale by x-velocity (m/s)



(b) Stationary Observer reference frame

**Figure 3.9: Zoom-in view of the velocity vector plot near the wheel for the proposed 2D model**

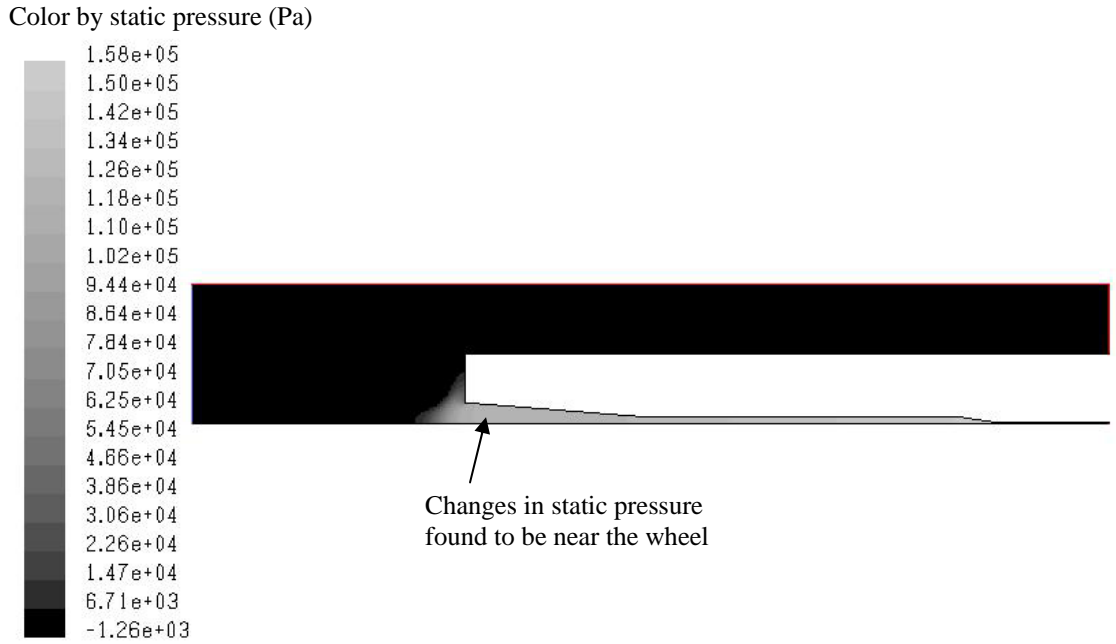


Figure 3.10: Static pressure contour plot of the 2D model under the moving wheel reference frame

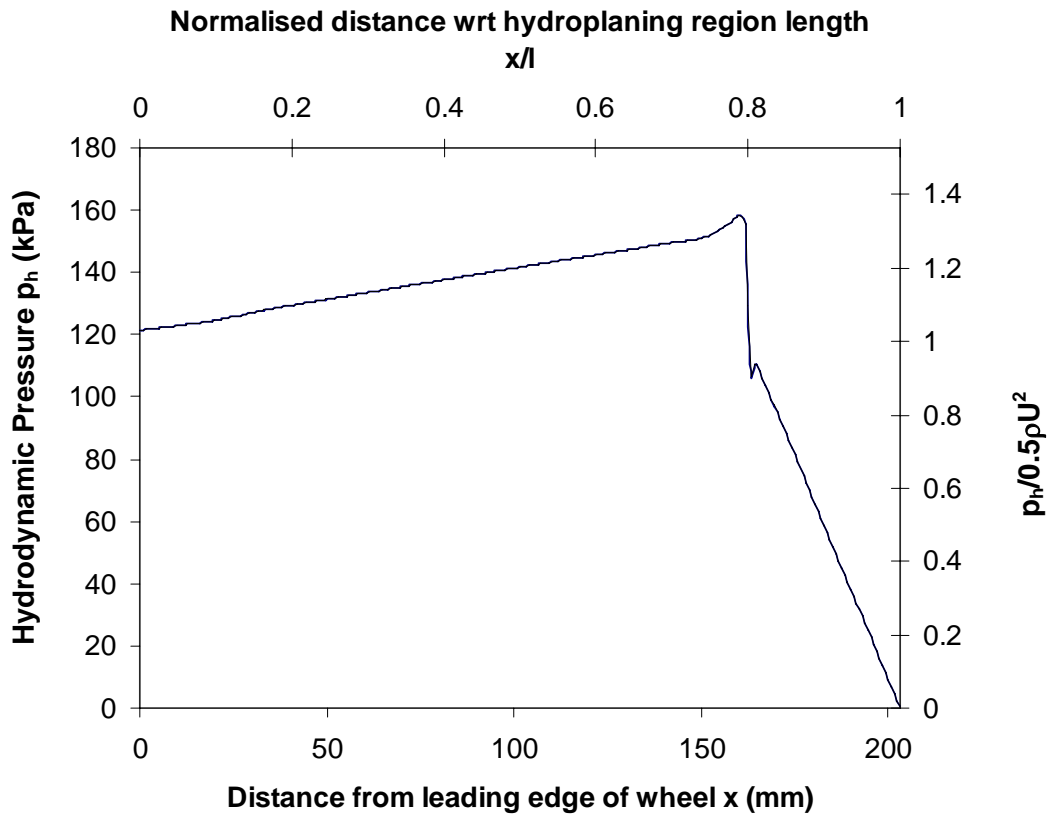
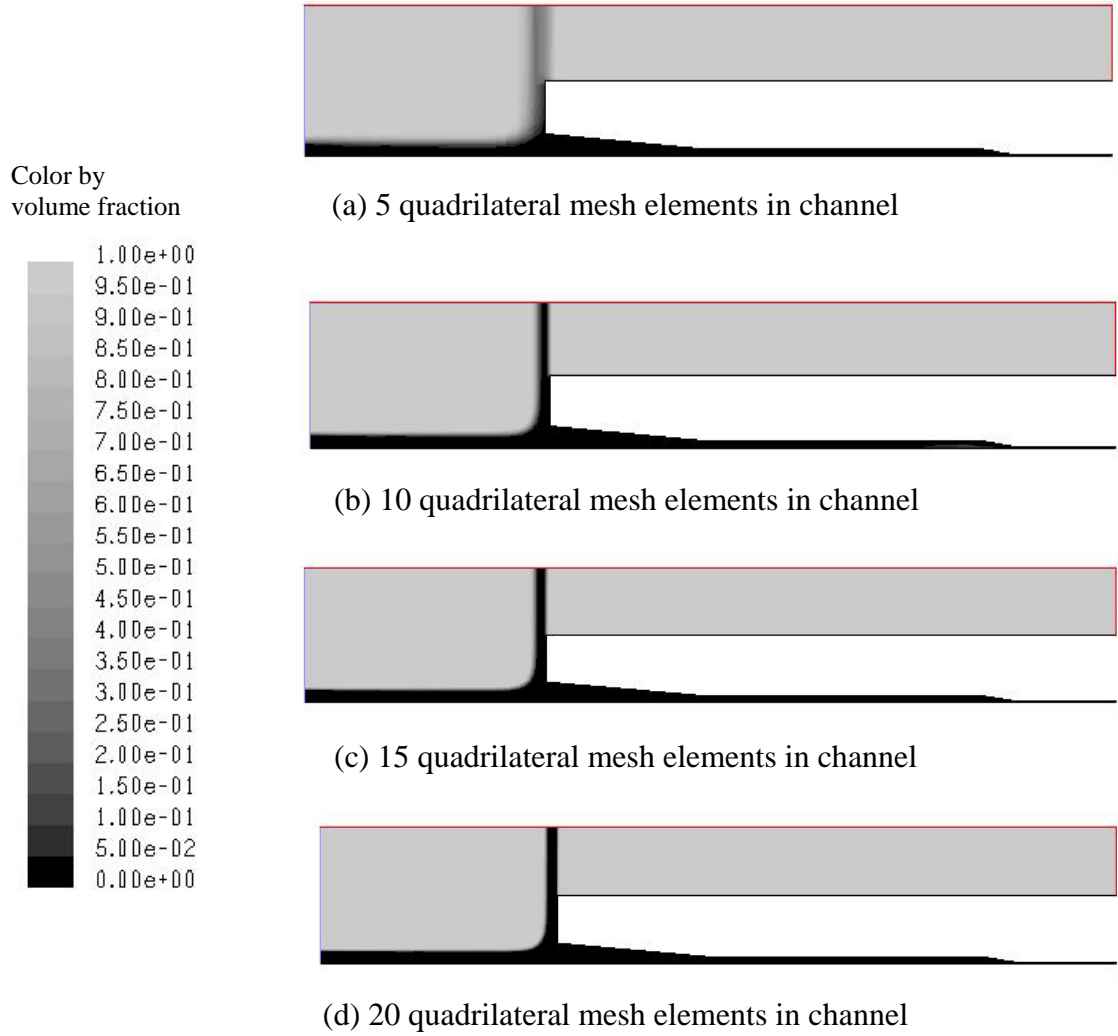


Figure 3.11: Ground hydrodynamic pressure distribution under wheel for the proposed 2D model



**Figure 3.12: Steady state volume fraction plots for the study of the effect of mesh size in the proposed 2D model**

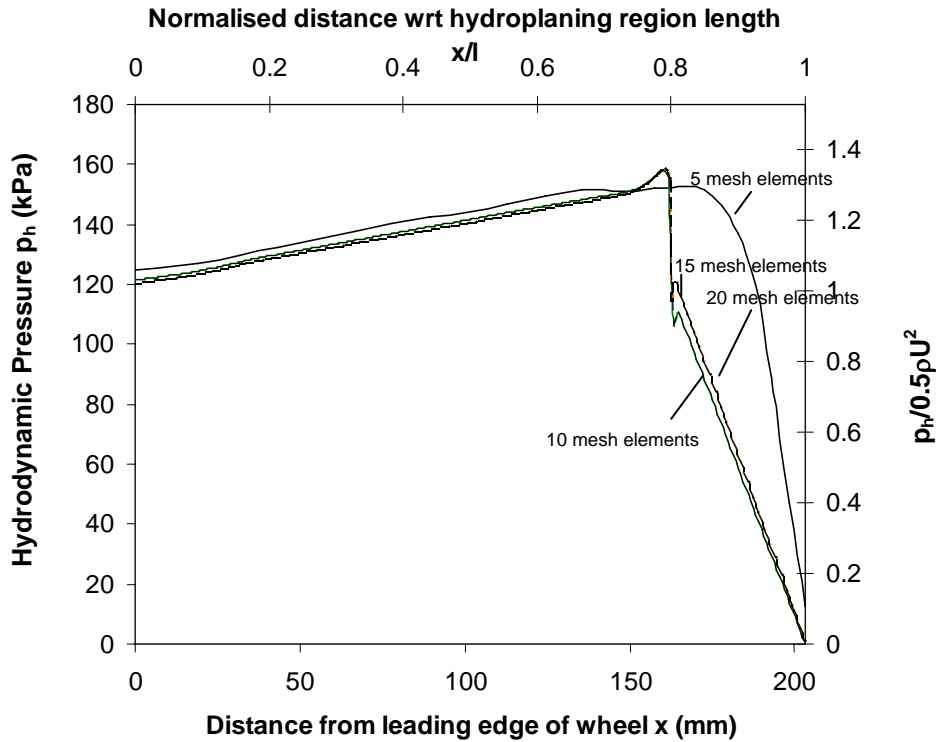


Figure 3.13: Ground hydrodynamic pressure distribution under wheel for the study of the effect of mesh size in the proposed 2D model

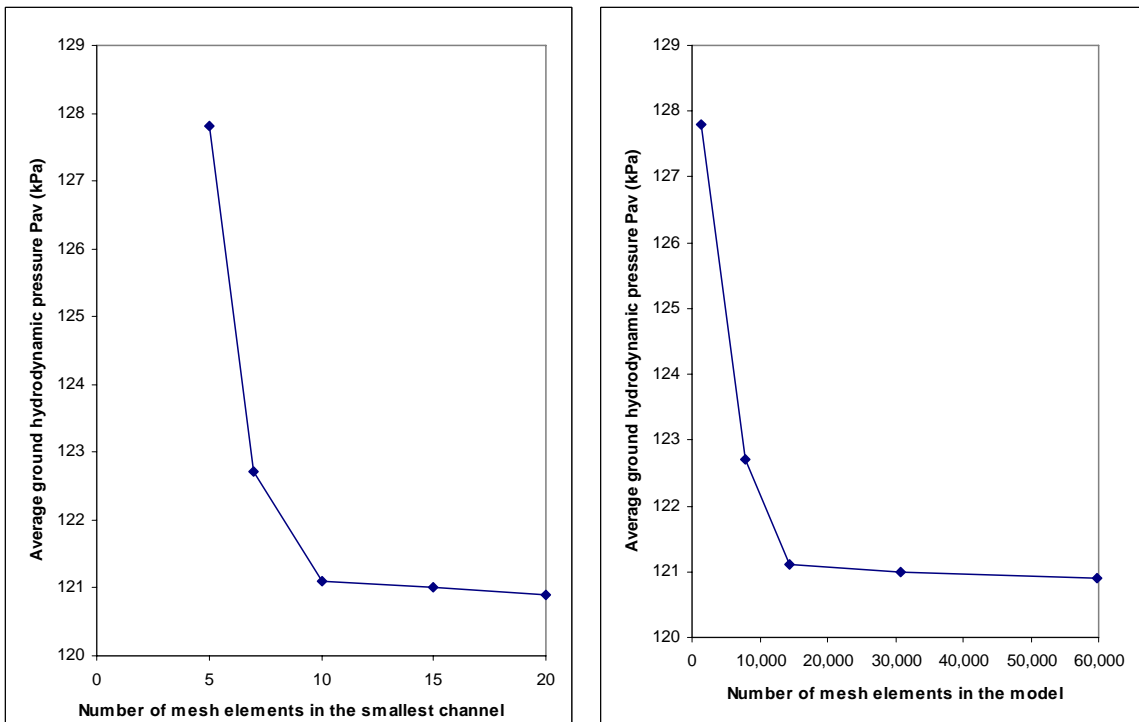


Figure 3.14: Effect of mesh quality on the average ground hydrodynamic pressure under the wheel in the proposed 2D model (left: in terms of number of elements in channel, right: in terms of number of elements in model)

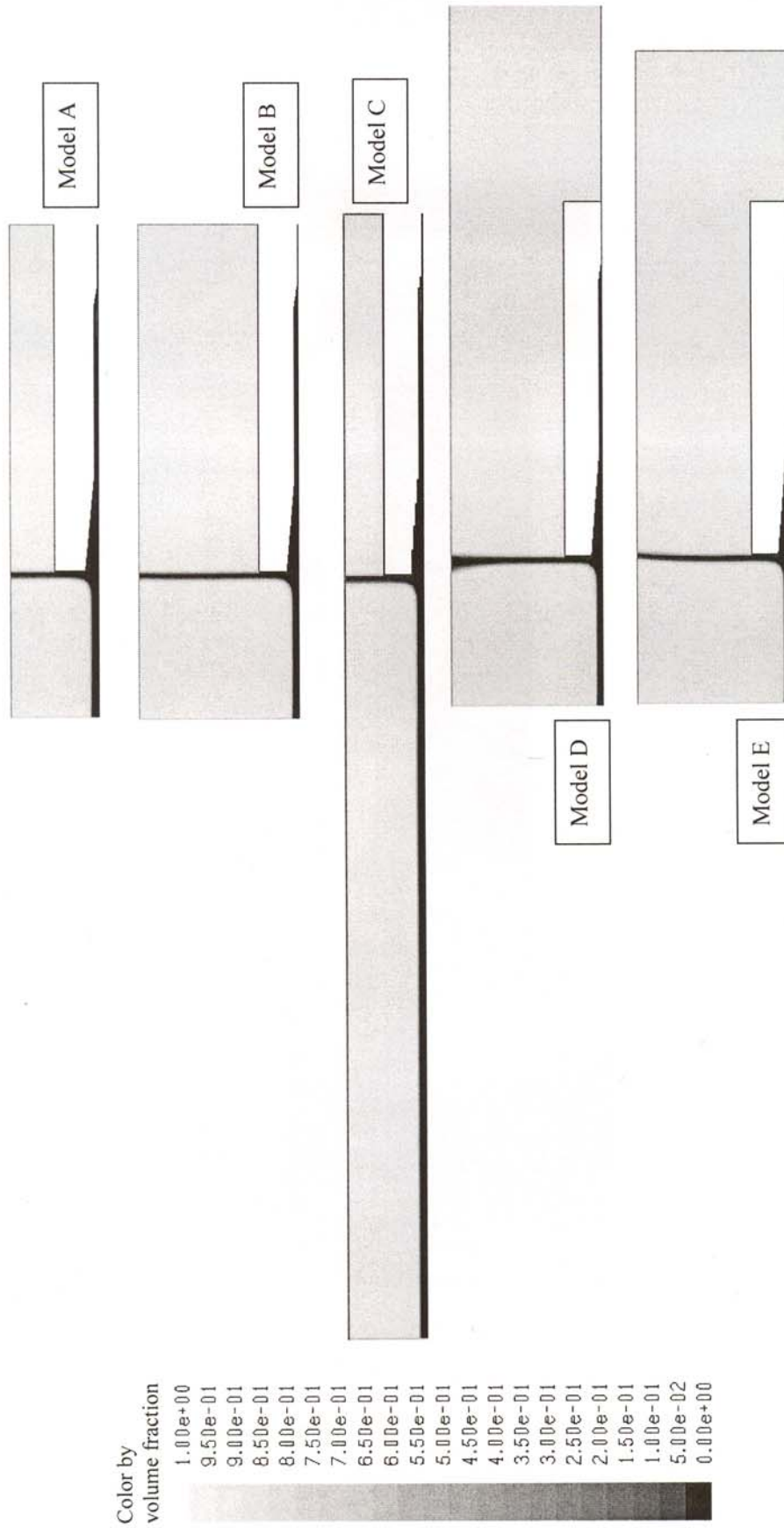


Figure 3.15: Steady state volume fraction plots for the study of the effect of location of boundary conditions in the proposed 2D model



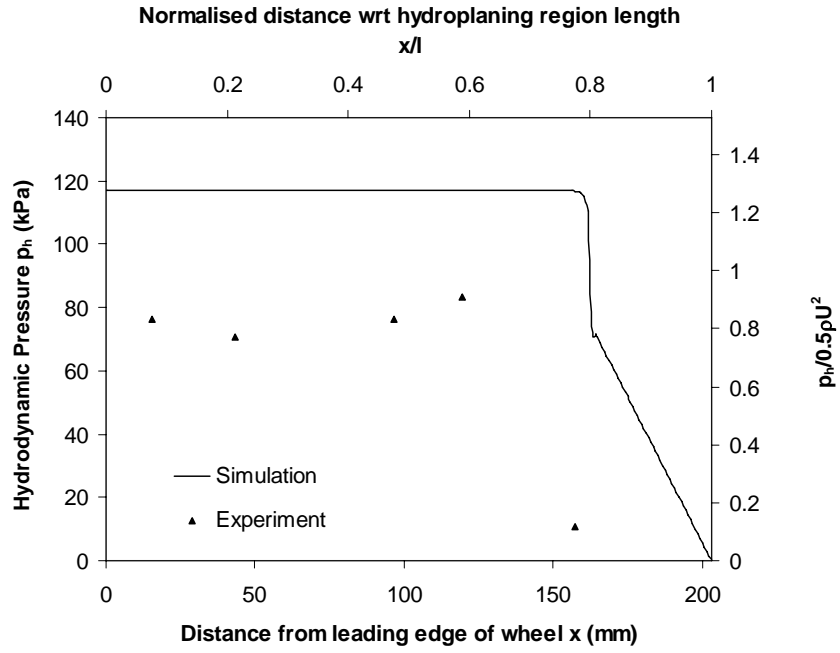


Figure 3.16: Comparison between the simulation using the 2D model with the plane of symmetry as pavement model and Browne (1971) experimental results

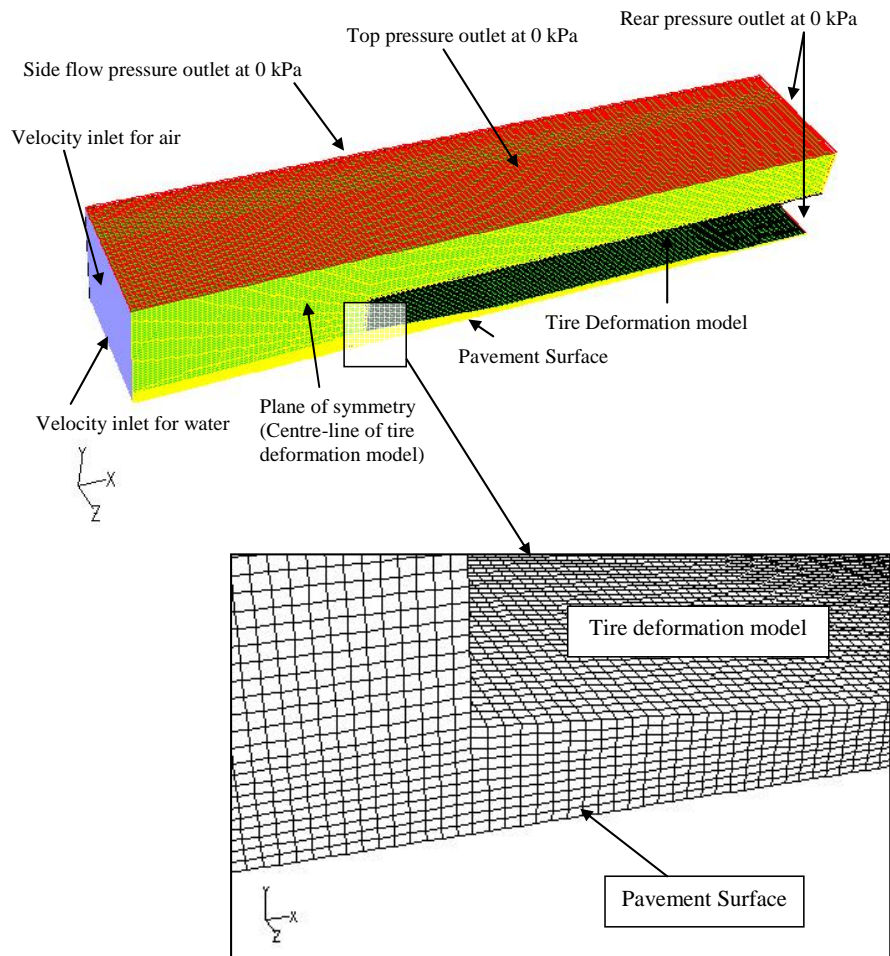
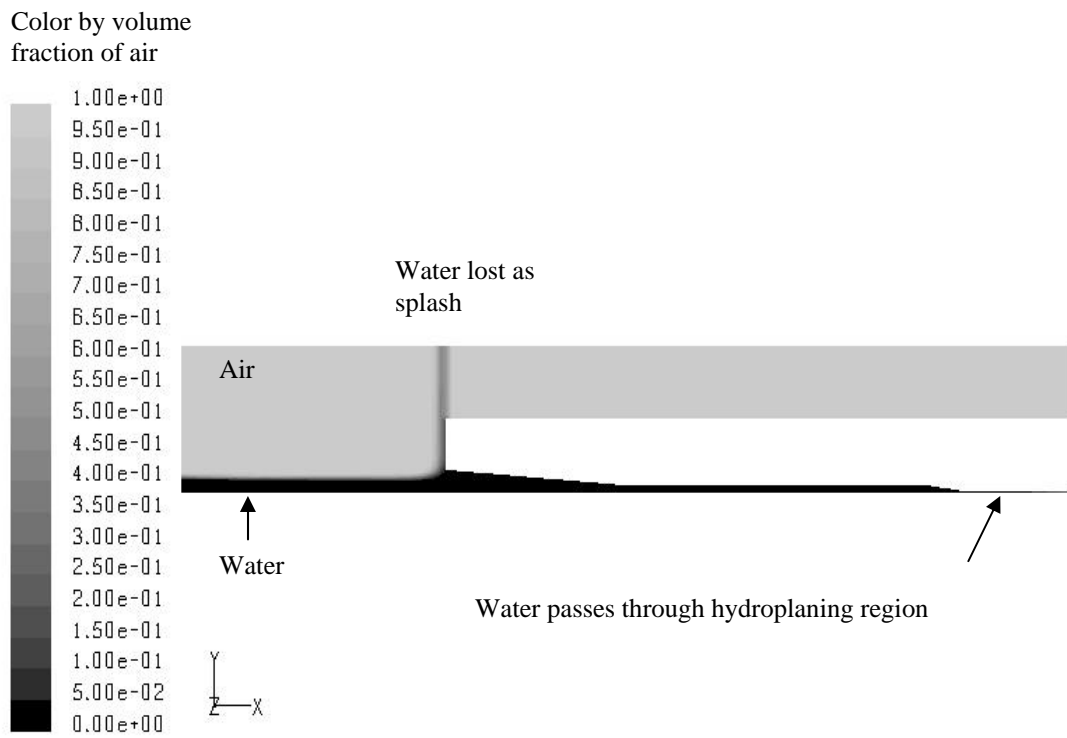
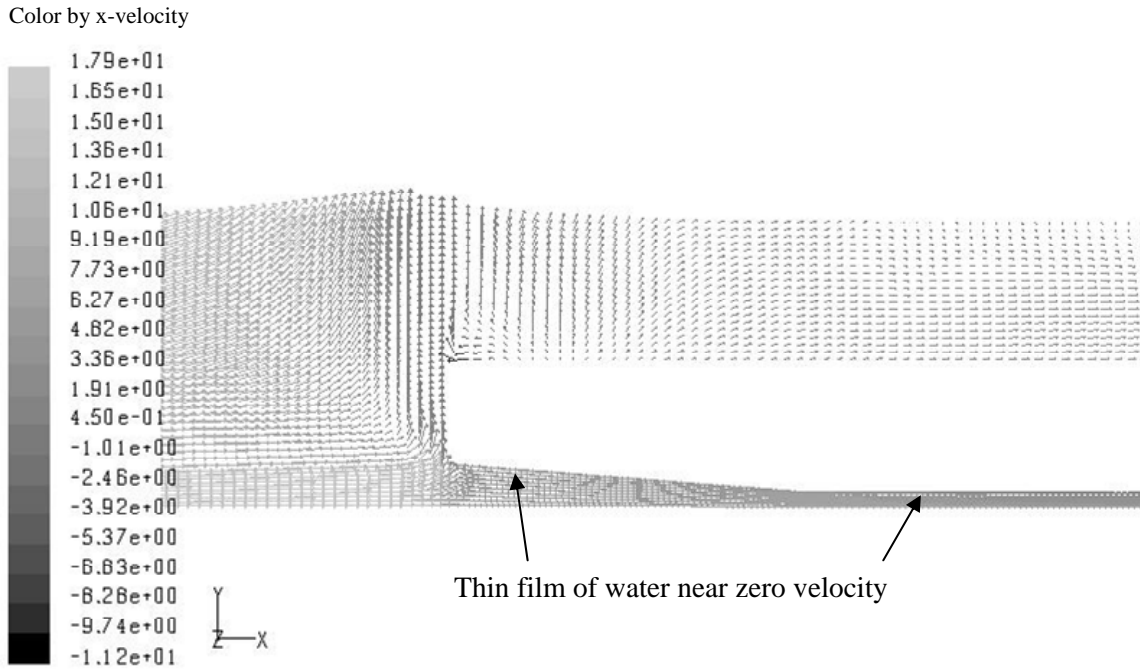


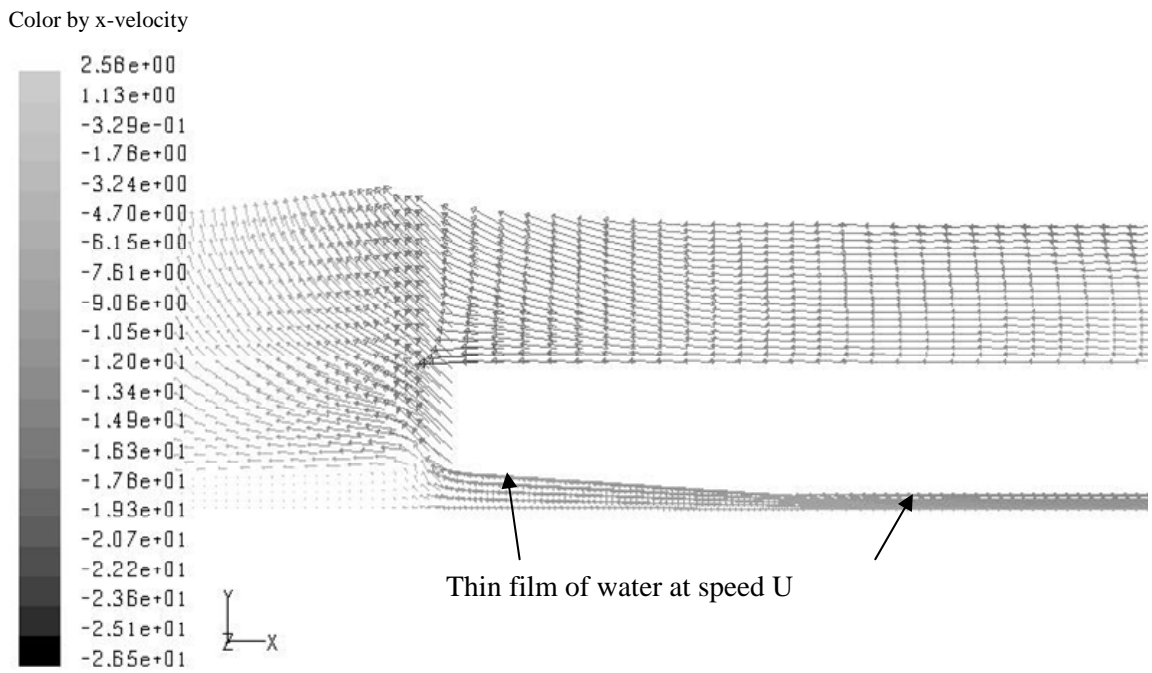
Figure 3.17: Mesh design of the proposed 3D model



**Figure 3.18: Steady state volume fraction plot along plane of symmetry (centerline of model) for the proposed 3D model**



(a) Moving wheel reference frame



(b) Stationary observer reference frame

**Figure 3.19: Zoom-in view of the velocity vector plot near the wheel along plane of symmetry for the proposed 3D model**

Color by static pressure (Pa)

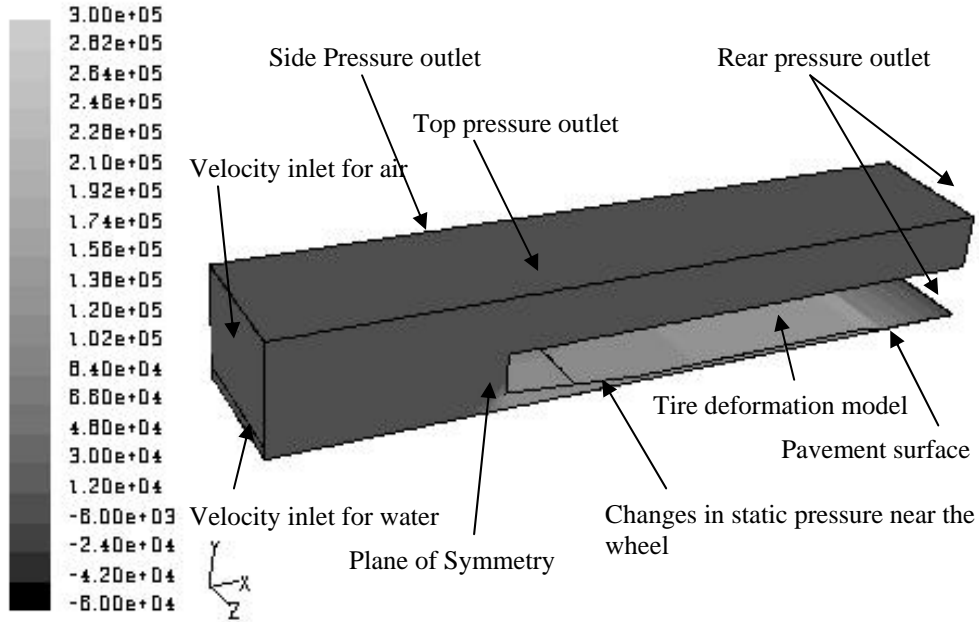


Figure 3.20: Static pressure contour plot of the 3D model under the moving wheel reference frame

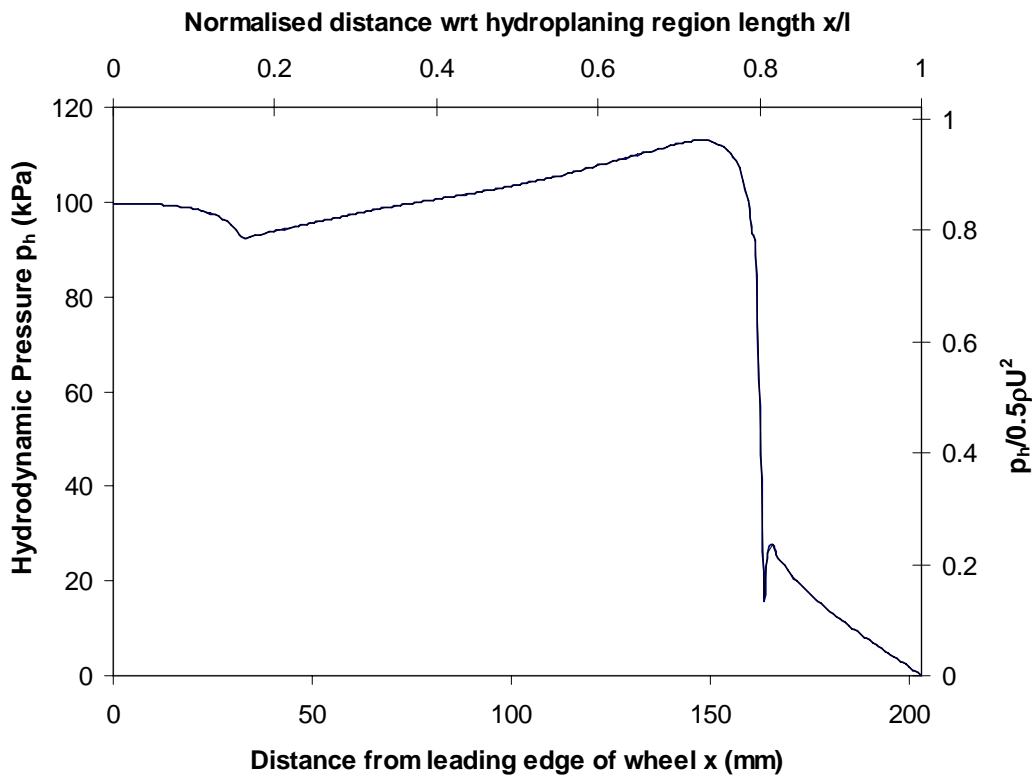


Figure 3.21: Ground hydrodynamic pressure distribution along the centre-line under wheel for the proposed 3D model

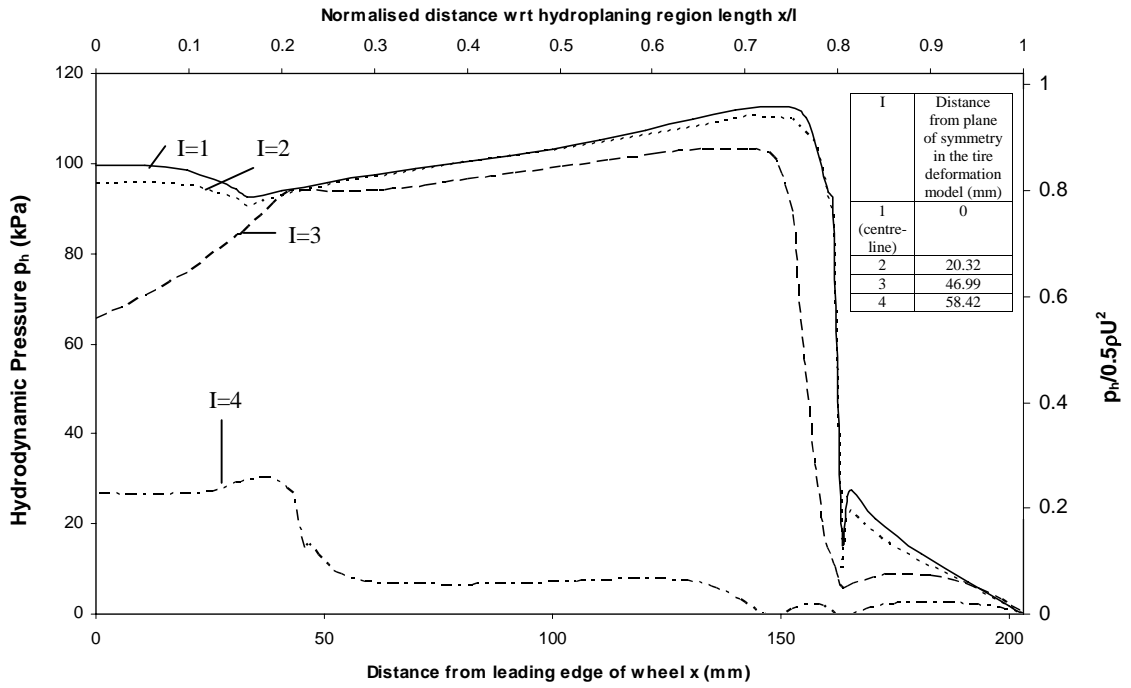
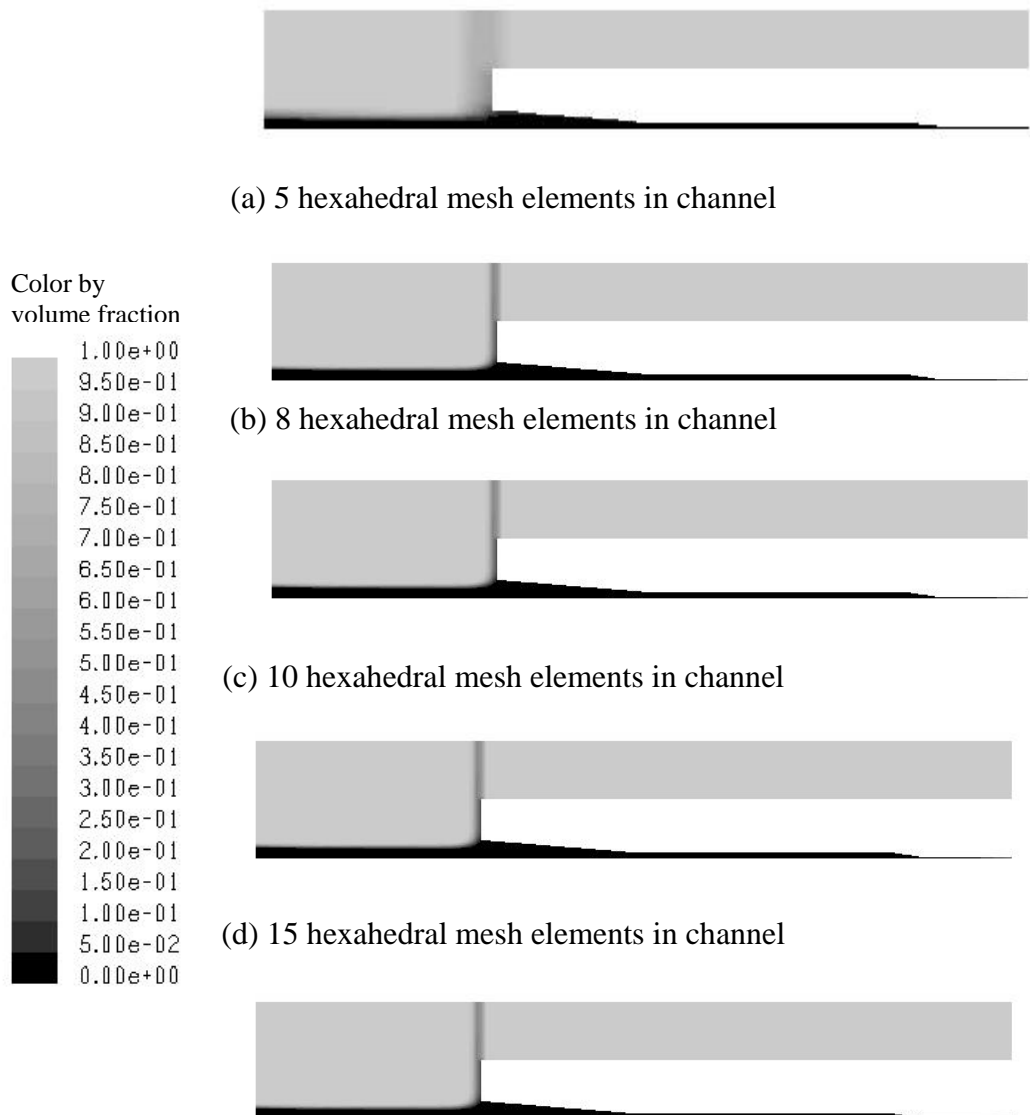


Figure 3.22: Ground hydrodynamic pressure distribution along lines under wheel for the proposed 3D model



**Figure 3.23: Steady state volume fraction plots for the study of the effect of mesh size in the proposed 3D model**

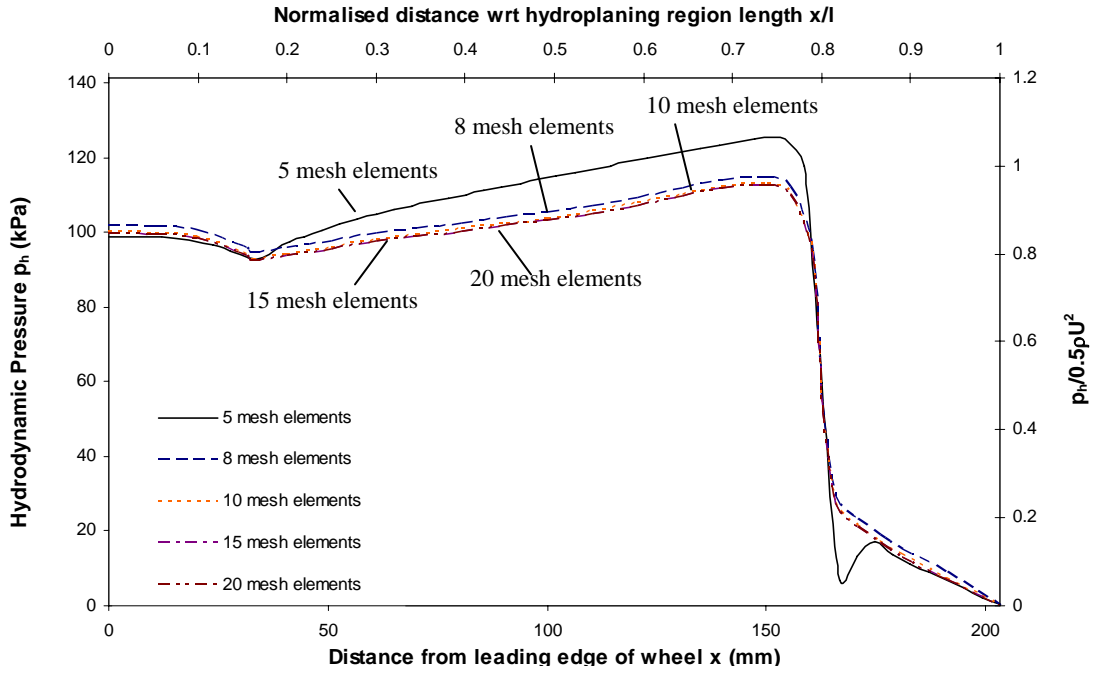


Figure 3.24: Ground hydrodynamic pressure distribution under the centre-line of the wheel for the study of the effect of mesh size in the proposed 3D model

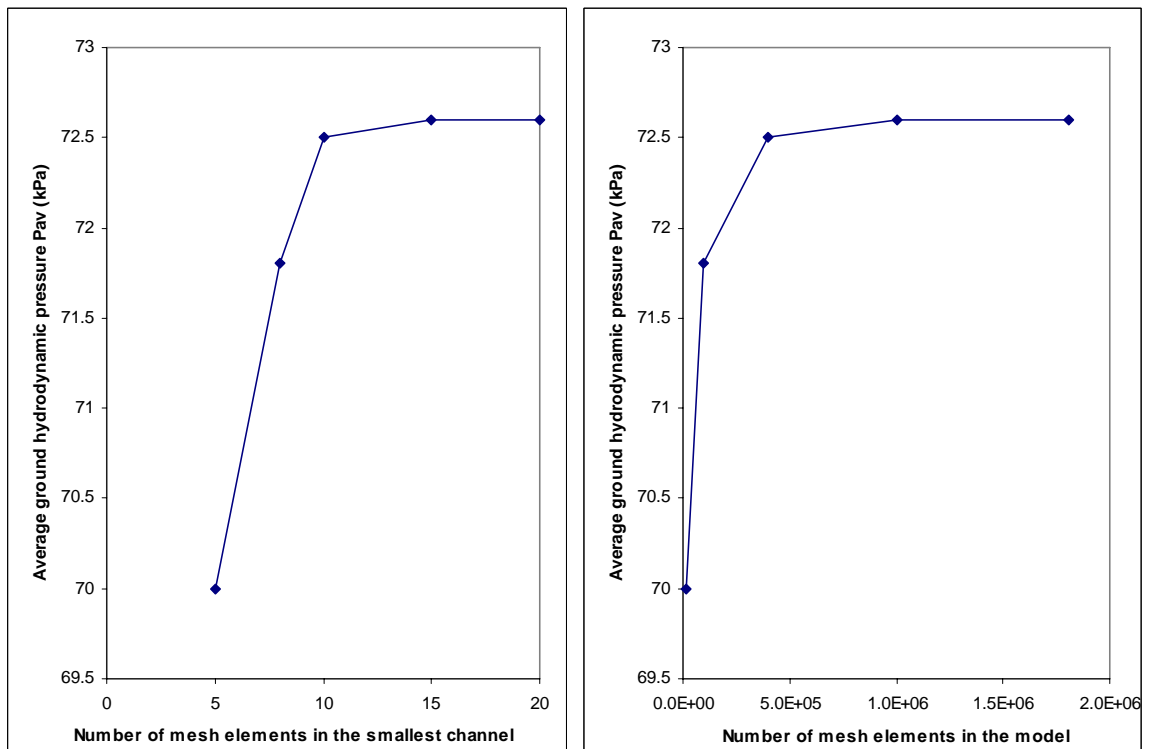


Figure 3.25: Effect of mesh quality on the average ground hydrodynamic pressure under the wheel in the proposed 3D model (left: in terms of number of elements in channel, right: in terms of number of elements in model)

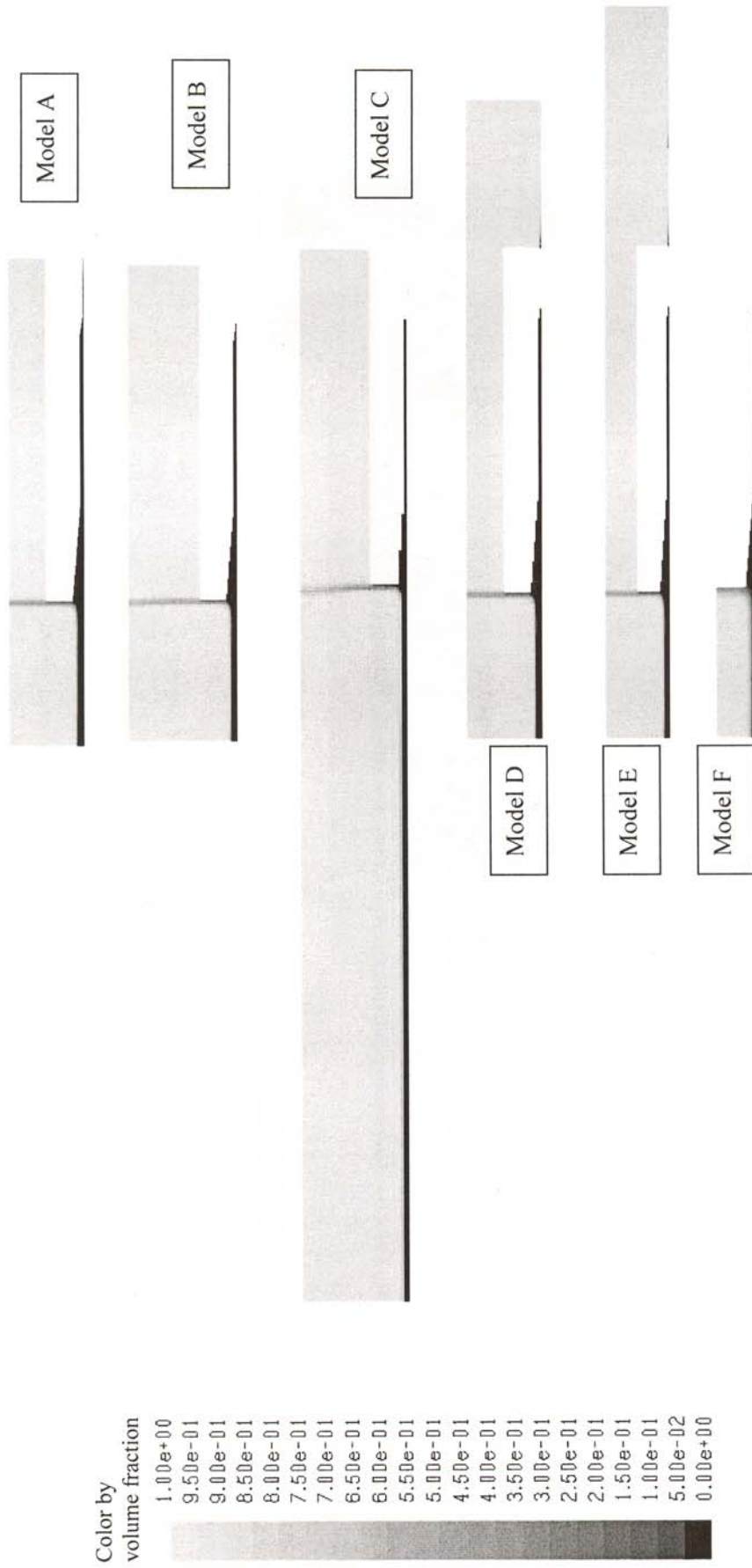


Figure 3.26: Steady state volume fraction plots along the plane of symmetry for the study of the effect of location of boundary conditions in the proposed 3D model



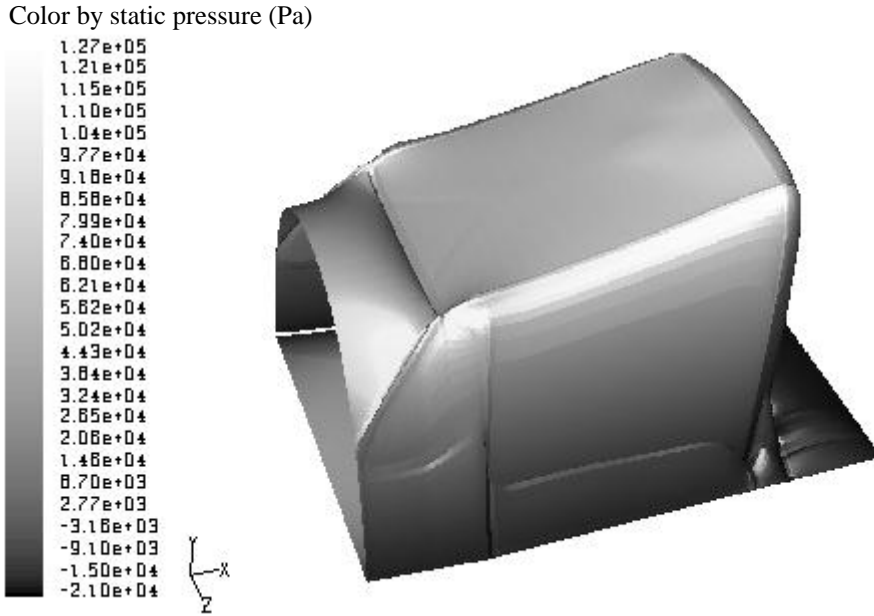


Figure 3.27: Ground hydrodynamic pressure distribution under the hydroplaning wheel from the proposed 3D model

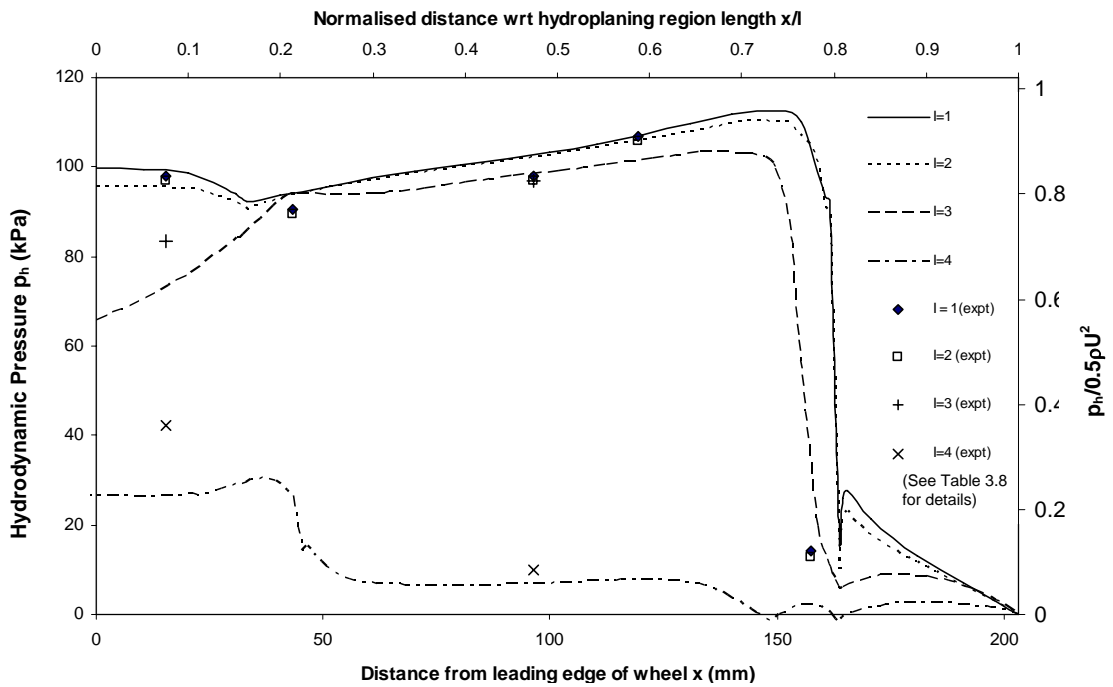


Figure 3.28: Comparison between the simulation using the 3D model with the plane of symmetry as pavement model and Browne (1971) experimental results

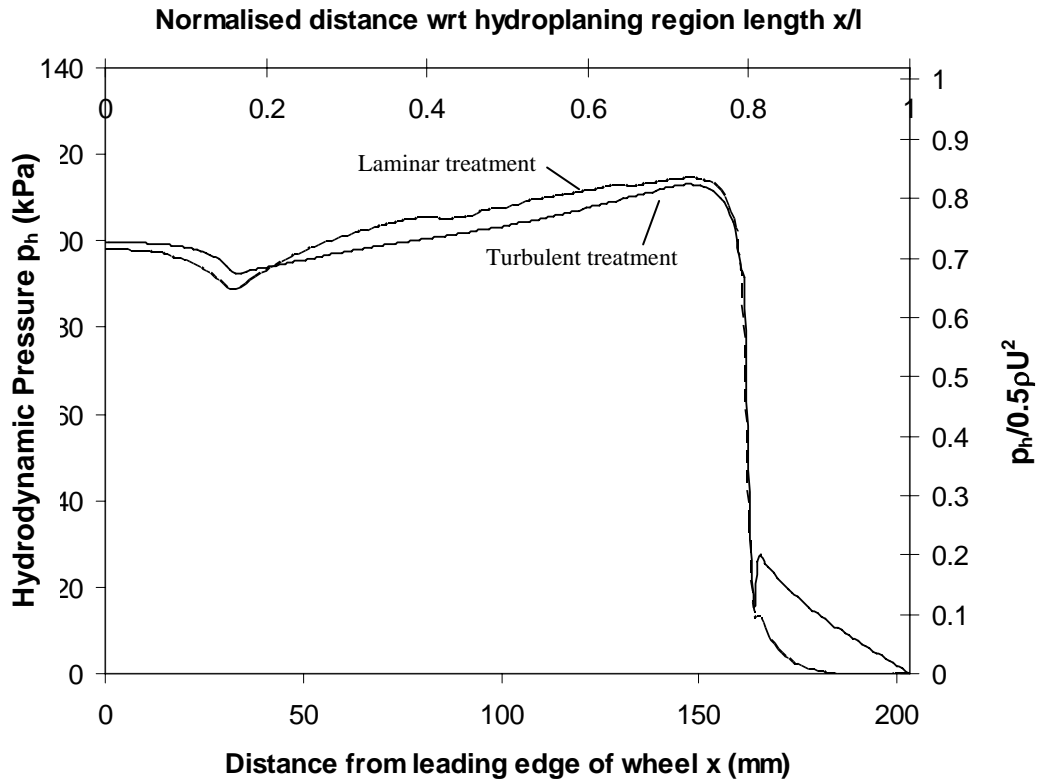


Figure 3.29: Comparison of hydrodynamic pressure distribution under the wheel under turbulent and laminar treatments

## **CHAPTER 4      SIMULATION OF HYDROPLANING ON PLANE PAVEMENT SURFACE**

### **4.1      Introduction**

It is highlighted in the previous chapter that in order to simulate hydroplaning, the choice of the fluid model, pavement surface model and tire deformation model is important. It has been found that turbulence has to be considered to improve the simulation to more closely match the recovery factor of 0.644 given by both the experimental data and the NASA hydroplaning equation. However, the NASA experiment covered only the case of aircraft tires sliding on a smooth surface flooded with a water depth of 7.62 mm. This chapter provides another tire deformation model based on that of a passenger car tire during hydroplaning with the aim to study the hydroplaning phenomenon in greater depth.

As highlighted in Figure 2.15 in Chapter 2, a study would be conducted in this chapter to verify the NASA hydroplaning equation under the effects of different tire pressures. Also analyzed is the effect of microtexture on hydroplaning from the theoretical and numerical points of view, with the aim to confirm experimental findings of prior studies in the past decades.

### **4.2      Pneumatic Tire Model**

The pneumatic tire model used in this chapter is shown in Figure 4.1. This model is essentially based on the profiles captured in the experiments conducted by Horne and Joyner (1965) and is used in the numerical research conducted by Browne (1971). This profile is obtained based on a pneumatic tire with a tire pressure of 186.6 kPa (27 psi) sliding at a speed of 96.5 km/h (60 mph) on a submerged glass plane surface with a water film thickness of 7.62 mm (0.3 in.). It is noted that in the experiment, hydroplaning had already occurred and the testing speed was slightly above the hydroplaning speed. The hydroplaning profile can be divided into three regions, namely the entry region where a bow wave is expected to form, the

main hydroplaning region, and a land region where the tire-pavement gap is less than a millimeter thick. This profile is consistent with the three-zone concept proposed by Veith (1983) who identified three zones as characterized by hydrodynamic lubrication (water wedge), mixed hydrodynamic lubrication and boundary layer lubrication respectively.

### **4.3 Pavement Surface Model**

In this study, a smooth plane pavement surface is first examined to verify the proposed finite volume model. The term “smooth”, as explained in the previous chapter, means that the average roughness height of the microtexture is taken to be zero and the term “plane” refers to a plane surface without any pavement grooving or any form of inclination or slope.

### **4.4 Three-Dimensional Modeling of Hydroplaning**

It has been shown in Section 3.7 of Chapter 3 that a two-dimensional model is inapt to model hydroplaning and thus the three-dimensional model of the hydroplaning profile shown in Figure 4.1 is used in the hydroplaning simulation. This section describes the main features of the 3D model and its verification.

#### **4.4.1 Geometry of Model and Selection of Boundary Conditions**

This proposed three-dimensional model has geometry as depicted in Figure 4.2. The boundary conditions and the initial conditions adopted, as summarized in Table 4.1, are similar to those as described in Chapter 3. As shown in Figure 4.2, the upstream boundary conditions consists of a pair of inlets, namely a velocity inlet of 7.62 mm (0.3 in.) thick for water and a velocity inlet of 76.2 mm (3 in.) thick of air. A uniform velocity profile is used. The pavement surface is modeled as a moving smooth plane wall with no microtexture. The speed of air, water and the pavement surface are kept as 96.5 km/h (60 mph) in order to be consistent with Horne and Joyner’s (1965) experiments. The inlet is placed at a distance of 100 mm away from the leading edge of the wheel (approximately 40 times the thickness of the hydroplaning region,

or 400 times the smallest film thickness, whichever is larger) so as to allow for any possible formation of bow wave.

The side edges and the trailing edge of the model are modeled as pressure outlets with the pressure set as 0 kPa (i.e. atmospheric pressure). The top boundary is set as a pressure outlet at atmospheric pressure and is placed at a distance of 25.4 mm (equal one time the thickness of plate, or 100 times the smallest film thickness, whichever is larger). On the boundary conditions, there is a need to conduct simulations on the effect of the distance of the boundaries from the wheel model to test if there is any convergence in the ground hydrodynamic pressure. It is noted that the centre-line of the wheel can be treated as a plane of symmetry.

#### **4.4.2 Description of Mesh used in the Analysis**

The pre-processor GAMBIT is used to generate the finite volume mesh for the fluids (Fluent Inc., 2004). In this simulation, ten 8-node hexahedral elements are used for the smallest channel in the model, i.e. the hydroplaning region. The optimal number of mesh elements needed to give a sufficiently accurate solution can be tested through a mesh sensitivity analysis. Figure 4.3 shows the mesh design of the three-dimensional hydroplaning model. There are altogether 463,300 mesh elements in the proposed model.

#### **4.4.3 Simulation Results**

The simulation is performed either on the 3 or 8 parallel CPUs (depending on availability) of the COMPAQ GS320 alpha server, which is configured with 22 EV67 731 MHz Alpha 21264 CPUs and 11 GB of memory. The computational time needed for the simulation ranges from 36 CPU-hours for a 0.5 million elements model to 150 CPU-hours for a 1.7 million elements model. Based on the specified geometry, boundary conditions and initial conditions, the steady-state phase plot along the plane of symmetry is shown in Figure 4.4. It is observed that a bow-wave forms at the front of the wheel and the splash is observed as shown in this figure.

Figure 4.5 shows the velocity vectors under the wheel in the moving reference frame (i.e. the model) and the stationary observer reference frame (i.e. the reality). It is observed that the velocities near the wheel are near-zero in Figure 4.5(a). This means that in the actual reference frame under the hydroplaning wheel, there is a thin film of lubricant moving at near the vehicle speed along with the sliding wheel as shown in Figure 4.5(b).

Figure 4.6 indicates the contours of the hydrodynamic pressure in the model and it is seen that pressure near the boundaries are at near zero pressure (i.e. atmospheric pressure), thereby indicating the suitability of the choice of the boundary conditions. This will be further verified in the later parts of this sub-section.

Table 4.2 shows the inflow and outflow properties of the two fluids in the system, namely air and water using the turbulent model setup. Also, the conservation of mass is obeyed as 99.97% of the air and 99.95% of the water is conserved. 73.0% of the water is lost as splash.

The ground hydrodynamic pressure distribution under the centre-line of the wheel is shown in Figure 4.7 and selected profiles along lines in the wheel direction are shown in Figure 4.8. The locations of the planes labeled as  $I = 1$ ,  $I = 2$ ,  $I = 3$  and  $I = 4$  are shown in the table in Figure 4.8. The ground hydrodynamic pressure distribution under the entire hydroplaning wheel is shown in Figure 4.9. The average ground hydrodynamic pressure under the hydroplaning wheel is found to be 228.5 kPa. This ground hydrodynamic pressure exceeds the tire pressure of 186.6 kPa, implying that hydroplaning has already occurred and is indeed the case.

#### 4.4.4 Mesh Sensitivity Analysis

In order to ensure that the solution obtained is numerically accurate, grid independence tests were conducted. Different mesh densities were examined to obtain the optimal mesh design. The number of hexahedral elements in the width of the hydroplaning region is a key aspect of mesh design. Four different mesh designs were tested and the steady-state volume fraction plot is shown in Figure 4.10. The aspect ratio (maximum edge length divided by minimum edge length) of the different mesh designs are kept constant at 7.5 for each of the

four cases tested. It can be seen that the plots exhibit similar fluid behaviors. A key indicator of mesh convergence is the average ground hydrodynamic pressure as this parameter is used in the definition of hydroplaning. Figure 4.11 shows the ground hydrodynamic pressure distribution along the centre line under the wheel for the various mesh designs and it can be observed that there are little variations between the various pressure profiles, thereby indicating grid independency except for the coarsest mesh (i.e. 5 hexahedral cells in the smallest channel). Figure 4.12 and Table 4.3 shows the effect of the mesh design on the average ground hydrodynamic pressure. It can be seen that using 10 mesh elements within the hydroplaning regions is sufficient to render a relatively accurate solution and thus this mesh design is used in the subsequent three-dimensional analyses.

#### **4.4.5 Effect of Boundary Conditions**

The effect of boundary conditions has to be studied to ensure that the distances of the boundaries, especially the locations of the velocity inlets and the pressure outlets, are sufficiently far away to ensure numerical accuracy of the model in terms of the key indicator of hydroplaning, i.e. the average ground hydrodynamic pressure under the wheel. The boundary locations of the various models tested are shown in Table 4.4. The choice of the locations includes the consideration of the aptness of the locations of the boundaries and the computational efficiency of the analysis.

The steady-state volume fraction plots of the various models are shown in Figure 4.13 and it can be seen that the plots show similar fluid behaviors. Table 4.5 shows the effect of the location of the boundary conditions on the average ground hydrodynamic pressure. It can be seen that the average ground hydrodynamic pressure are similar with an error of less than 2%, thereby suggesting that the effect of the locations of the boundary conditions considered are insignificant. This shows that the proposed model with the boundary conditions used in the prior sections is adequate to achieve the intended numerical accuracy.

#### 4.4.6 Analysis of Results

Comparisons of the proposed model with the numerical research conducted by Browne (1971), and the experimental results from existing literature are presented in this section. Some discrepancies are expected as it is noted in the previous chapter that (i) the boundary conditions used by Browne's analysis for the pavement surface is inappropriate, and (ii) the proposed model provides a much better recovery factor that is closer to the NASA's recovery factor of 0.644 as compared to Browne's.

Figure 4.8 and Figure 4.14 show the ground hydrodynamic pressure distributions for various locations along the wheel for the main hydroplaning region for the proposed model and Browne's (1971) model respectively. The general trends of results obtained with the two models are similar. It is noted that Browne's solution shows some regions with excessively high negative hydrodynamic pressure. Compared with experimental results from various tests done by researchers (Horne and Leland, 1962; Horne and Joyner, 1965; Yeager and Tuttle, 1972), excessively high negative hydrodynamic pressures such as that along line I = 4 were not detected and typically, negative hydrodynamic pressures were not found in the main hydroplaning region. Although regions of negative hydrodynamic pressure is not shown in the cut-off planes, they do exist in the proposed model, and in this configuration, the maximum negative hydrodynamic pressure is -38.9 kPa.

The average ground hydrodynamic pressure under the hydroplaning wheel is found to be 228.5 kPa. The average ground hydrodynamic pressure is therefore used to evaluate the recovery factor (i.e. ratio of tire pressure to  $0.5\rho U^2$ ). This factor is found to be 0.636 which is close to the expected NASA hydroplaning value of 0.644 with a percentage difference of 1.2%. This, compared to the value of 0.56 obtained by Browne, provides a much better modeling of the hydroplaning phenomenon and offers credibility to the NASA hydroplaning equation. It implies that if the point of analysis is that of incipient hydroplaning, the expected tire pressure predicted by the proposed model is equal to that proposed by NASA which is experimentally based. Conversely, if it is known that the tire pressure is 186.6 kPa (which is the case), the model predicts that hydroplaning has already occurred since the uplift force is greater than the



weight of the vehicle (i.e. the average ground hydrodynamic pressure predicted by the model exceeds the tire pressure). This suggests that hydroplaning has already occurred, as noted by Horne and Joyner (1965).

#### **4.4.7 Repeat of Analysis Using NASA Predicted Hydroplaning Speed**

The simulations conducted in the preceding section were based on the experimental speed of 96.5 km/h (60 mph). The analyses are repeated using the NASA predicted hydroplaning speed of 87.5 km/h (54.4 mph) in order to verify that the model could closely simulate hydroplaning. In this case the velocities of the air, water and pavement are fixed at the NASA predicted hydroplaning speed of 87.5 km/h. The resulting ground hydrodynamic pressure obtained from the simulation analysis is 184.6 kPa. Figure 4.15 shows the selected ground hydrodynamic pressure profiles along lines in the wheel direction. The tire pressure of the passenger car tire used in this simulation is 186.6 kPa. The computed ground hydrodynamic pressure differs from this tire pressure by 1.1 %. The recovery factor is 0.640 which differs from NASA's value of 0.644 by 0.6%. Based on this value, the predicted hydroplaning speed of the 186.6 kPa tire pressure passenger car tire is found to be 87.0 km/h which differs from the NASA predicted hydroplaning speed by a mere 0.3%. This provides affirmative verification of the ability of the proposed model to accurately predict the onset of hydroplaning.

#### **4.5 Effect of Tire Pressure on Hydroplaning**

The NASA hydroplaning equation, shown in Equation (2.18), indicates that the tire pressure is the sole factor affecting the hydroplaning speed in flooded smooth plane pavement surfaces (Horne, 1962; Horne and Leland, 1963; Horne and Joyner, 1965). This section examines the relationship between the tire pressure and the predicted hydroplaning speed using the proposed model, assuming a fixed tire deformation profile, and compares the simulation results against the NASA hydroplaning equation.

#### 4.5.1 Modeling Methodology

The simulation is conducted by varying the velocities of the air, water and the pavement surface in the proposed 3-D model. A fixed tire deformation profile is assumed. The pavement surface is assumed to be plane and free from microtexture. A water film thickness of 7.62 mm (0.3 in.) is assumed.

Speeds ranging from 0 km/h to 300 km/h were tested. Based on the range of tire pressures covered by the NASA hydroplaning equation, tire pressures ranging from 0 kPa to 2000 kPa were analyzed. This range of tire pressure encompasses those of passenger car tires and aircraft tires. A typical private car tire has a tire pressure of less than 200 kPa while an aircraft tire has a tire pressure of more than 1200 kPa (Yoder and Witczak, 1997). The desired parameter from the simulation output is the predicted ground hydrodynamic pressure under the wheel. The corresponding speed would be the hydroplaning speed for the given tire pressure.

#### 4.5.2 Results and Analysis

Figure 4.16 shows the relationship between the tire pressure and the hydroplaning speed obtained from the simulations. It is shown that the model could accurately predict hydroplaning speeds close to that predicted by the NASA hydroplaning equation. Experimental data by (Horne and Joyner, 1965) for different types of tires are also plotted in the same figure. It is seen that the model's predicted hydroplaning relationship matches very well with the experimental data.

Table 4.6 shows the uplift and friction forces experienced by the wheel and the corresponding coefficient of friction experienced by the wheel during hydroplaning. The lift force indicated in the table should be equal to the weight of the vehicle acting on each tire. In the model, the friction forces can be obtained by performing an integral of the horizontal component of the hydrodynamic pressure acting on the front and the bottom of the wheel (i.e. the hydroplaning region). The coefficient of friction can be obtained by dividing the sum of the horizontal forces (i.e. frictional forces in the horizontal direction) by the uplift force. It can be

observed that the coefficient of friction is in the range of 0.09 to 0.10 for a 7.62 mm (0.3 in.) thick of water film.

Table 4.7 shows the average ground hydrodynamic pressure and the recovery factor  $P/(0.5\rho U^2)$  for various hydroplaning speeds. It can be seen that the recovery factor differs from that predicted by the NASA hydroplaning equation by at most 4.2%. Typically, for highways where the speeds of vehicles are not expected to be higher than 150 km/h, the NASA hydroplaning equation is effectively modeled, with the predicted model's hydroplaning speed being different from the NASA predicted values by at most 2.6%. This demonstrates the close fit the proposed model has with the NASA hydroplaning equation.

The close fit between the proposed model and the NASA hydroplaning equation shows that the model can effectively model hydroplaning for an assumed water thickness of 7.62 mm (0.3 in.). More importantly, this offers a convenient platform in assessing how different factors can affect hydroplaning for a given water film thickness. A pavement engineer would be interested to know if microtexture and pavement grooving could affect the onset of hydroplaning. The proposed model can serve as a useful tool to study these effects.

#### **4.6 Effect of Microtexture on Hydroplaning**

This section examines the effects of pavement surface microtexture on hydroplaning using the proposed model.

Microtexture refers to the deviation of the pavement surface from the true planar surface with characteristic dimensions of wavelength and amplitude less than 0.5 mm. Peak-to-peak amplitudes usually vary in the range of 0.001 to 0.5 mm (ISO/CD 13473, 1994). Studies conducted by Horne and Dreher (1963) noted that “a rough or open textured surface required a greater depth of fluid for hydroplaning to occur because of more paths for the trapped water to escape”. In this case, no differentiation was made between macrotexture and microtexture. Horne (1977) stated that pavement with a good microtexture is a major mean to combat viscous hydroplaning and pavement with good macrotexture can delay hydroplaning. Perlolli (1977) stated that based on five different types of surfaces tested, microtexture affects the

relationship of friction coefficient and the water depth. However, there is no definite quantification on the microtexture depth and its effect on the coefficient of friction. Therefore, although observations had indicated that pavement microtexture helps to reduce the likelihood of hydroplaning, research so far has not established quantitatively the effects of microtexture on hydroplaning.

#### 4.6.1 Theoretical Aspects on Incorporating Roughness

Surface roughness could affect the drag, heating and transport of heat, mass and sediments. Unfortunately studies in these fields primarily rely on empirical framework and a limited data range, both of which are established from observations and experiments in pipes and flat-plate boundary layers. Progress in the research in rough-wall studies has been slow, primarily due to the intrinsic difficulties in measuring flow near the roughness elements (Piquet, 1999). In the present research, it is desired to understand the effect of microtexture on the onset of hydroplaning. As such, the effect of roughness is studied through the use of the law of the wall modified for roughness (Fluent Inc., 2005) as described in the following paragraphs.

Experiments in roughened pipes and channels indicate that the near-velocity distribution near the wall, when plotted in the logarithmic scale has the same slope ( $1/\kappa$ ) but different intercepts (an additive constant  $B$  in the log-law). Thus the law of the wall for the mean velocity modified for roughness has the form as shown in Equation (4.1).

$$\frac{u_p u^*}{\tau_w / \rho} = \frac{1}{\kappa} \ln \left( E \frac{\rho u^* y_p}{\eta} \right) - \Delta B \quad (4.1)$$

where  $u^* = C_\mu^{1/4} k^{1/2}$  and

$$\Delta B = \frac{1}{\kappa} \ln f_r \quad (4.2)$$

where  $f_r$  is the roughness function that quantifies the shift of the intercept due to roughness effects. In these equations,  $u_p$  is the velocity at point P;  $y_p$  is the distance of point P from the wall,  $\tau_w$  is the shear stress at the wall;  $k$  is the von Karman constant ( $= 0.42$ );  $E$  is an empirical

constant ( $= 9.793$ );  $\rho$  is the density of the fluid;  $\eta$  is the dynamic viscosity of the fluid;  $k$  is the turbulent kinetic energy;  $C_\mu$  is the unknown from the definition of the eddy viscosity in the standard  $k$ - $\varepsilon$  model as shown in Equation (3.12) and has the value of 0.09 from comprehensive data fitting (Launder and Spalding, 1974).

$\Delta B$  depends on the type and size of the roughness. There is no universal roughness function valid for all types of roughness. For sand grained roughness,  $\Delta B$  is found to be well-correlated with the non-dimensional roughness height,  $K_s^+ = \frac{\rho K_s u^*}{\eta}$  where  $K_s$  is the actual roughness height with respect to the true planar surface. Analyses of the experimental data show that the roughness function is not a single function of  $K_s^+$ , but takes different forms depending on the  $K_s^+$  values. It has been observed that there are three distinct regimes, namely the hydro-dynamically smooth regime ( $K_s^+ \leq 2.25$ ); the transitional ( $2.25 \leq K_s^+ \leq 90$ ); and the fully rough regime ( $K_s^+ \geq 90$ ). Roughness effects are negligible in the hydro-dynamically smooth regime, and become increasingly important in the transitional regime, and take full effect in the fully rough regime.

In FLUENT, the whole roughness regime is sub-divided into three regimes, and the formulas proposed by Cebeci and Bradshaw (1977), based on Nikuradse's (1933) data are adopted to compute  $\Delta B$  for each regime.

For the hydro-dynamically smooth regime ( $K_s^+ \leq 2.25$ ):

$$\Delta B = 0 \quad (4.3)$$

For the transitional regime ( $2.25 \leq K_s^+ \leq 90$ ):

$$\Delta B = \frac{1}{\kappa} \ln \left[ \frac{K_s^+ - 2.25}{87.75} + C_s K_s^+ \right] \times \sin \left[ 0.4258 (\ln K_s^+ - 0.811) \right] \quad (4.4)$$

For the fully rough regime ( $K_s^+ \geq 90$ ):

$$\Delta B = \frac{1}{\kappa} \ln (1 + C_s K_s^+) \quad (4.5)$$

where  $B$  is the additive constant in the log-law;  $K_S^+$  is the non-dimensional roughness height as defined earlier;  $C_S$  is the roughness constant and  $\kappa$  is the von Karman constant ( $= 0.42$ ).

In the solver, given a roughness parameter,  $\Delta B(K_S^+)$  is evaluated from the corresponding equations (Equations (4.3), (4.4) or (4.5)). The modified law-of-the-wall in Equation (4.2) is then used to evaluate shear stresses and other wall functions for the temperature and other turbulent quantities.

#### 4.6.2 Modeling Aspects on Incorporating Roughness

In the definition of microtexture, the peak-to-valley definition of roughness is employed. However, FLUENT employs the concept of roughness height  $K_S$  and roughness constant  $C_S$  (Fluent Inc., 2005). The term roughness height in this case refers to the average height of the surface roughness elements. This definition of roughness height used in FLUENT (2005) is the same as that defined by PIARC (1995). Typical roughness heights of various materials are shown in Table 4.9. It is noted that the roughness height of a glass surface is zero. The roughness constant  $C_S$  in Equations (4.4) and (4.5) is chosen to be 0.5 to reflect a roughness structure similar to that of uniform sand grain. This roughness constant is determined such that when used with the  $k$ - $\varepsilon$  turbulence models, reproduces Nikuradse's (1933) experimental data for pipes roughened with tightly packed, uniformly sized sand grained roughness (Fluent Inc., 2005). Thus, it can be assumed that the three-dimensional profile of the microtexture used in this study can be approximated by a profile exhibited by a closely-packed, uniformly sized sand grain roughness. Figure 4.17 shows a simplified representation of roughness assuming that the sand grain is modeled as a perfect sphere.

In the model, the tire-deformation profiles and the fluid flow models as proposed in the prior sections are used. As it has been shown that the profile could adequately model hydroplaning for plane smooth pavement surfaces, it is thus desired to determine how surface roughness in the range of 0 to 0.5 mm height (known as microtexture in the pavement engineering) could affect the onset of hydroplaning. One key consideration in this simulation is

the water film thickness. A pavement is said to be flooded when the tip of the microtexture is just covered with water, i.e. water layer thickness is considered to be zero. Since both the NASA hydroplaning equation and this study address the case of a flooded pavement, the actual thickness of the water layer does not include the height of the microtexture. Thus the model will need to consider the microtexture depth as shown in Figure. 4.18. In this study, the effect of roughness of the tire is ignored since the intention is to understand the effect of microtexture of the plane pavement surface on the ground hydrodynamic pressure and hence the onset of hydroplaning.

Microtexture depths ranging from 0 mm to 0.5 mm were tested. Simulations were first conducted using the NASA hydroplaning speed of 87.5 km/h (54.4 mph) for a passenger car tire with a tire pressure of 186.6 kPa. The average ground hydrodynamic pressure under the wheel would provide an indicator on the effect of microtexture on hydroplaning. Simulations were conducted to determine the predicted hydroplaning speed and the skid resistance (i.e. coefficient of friction) at the onset of hydroplaning.

#### **4.6.3 Results and Analysis**

Figure 4.19 shows the effect of microtexture on the average ground hydrodynamic pressure under the wheel at the test speed of 87.5 km/h (54.4 mph). This corresponds to the speed predicted by the NASA hydroplaning equation for a passenger car tire with a tire pressure of 186.6 kPa. It is shown that as the microtexture increases from 0 to 0.1 mm, the predicted average ground hydrodynamic pressure decreases from 184.6 kPa to 180.9 kPa. This indicates that an increase in microtexture in the range of 0 mm to 0.1 mm will cause a decrease in the average ground hydrodynamic pressure by about 2.5%. This decrease is insignificant and microtexture ranging from 0.01 mm to 0.1 mm has insignificant effect on the occurrence of hydroplaning.

The effect of microtexture on the average ground hydrodynamic pressure becomes more apparent when the microtexture increases beyond 0.1 mm as the average ground hydrodynamic pressure decreases practically in a linear fashion at an average rate of 14.03 kPa

per 0.1 mm of microtexture as the microtexture increases from 0.1 mm to 0.5 mm. This shows that the occurrence of hydroplaning could be delayed to a higher speed by increasing the pavement surface microtexture depth especially when the microtexture depth increases beyond 0.1 mm.

Figure 4.20 shows the effects of microtexture on the predicted hydroplaning speed and Figure 4.21 shows the effect of microtexture on the coefficient of friction at incipient hydroplaning. It is seen that the predicted hydroplaning speed increases marginally from 86.9 km/h for a smooth plane pavement surface to 87.9 km/h for a plane pavement surface of 0.1 mm microtexture. For a plane pavement surface with 0.2 mm microtexture, the predicted hydroplaning speed is 91.1 km/h which differs from that of the plane pavement surface by 4.8%. For microtexture in the range of 0.2 mm to 0.5 mm, the predicted hydroplaning speed increases from 91.1 km/h to 105.8 km/h. This reinforces the idea that hydroplaning can be delayed by increasing the depth of surface microtexture.

Figure 4.20 also shows that the NASA hydroplaning speed, which is based on a glass plane surface, is in fact a conservative solution, because it ignores the presence of microtexture. The proposed model shows that the NASA hydroplaning equation is adequate if the microtexture of the pavement surface is less than 0.1 mm. For pavement with microtexture greater than 0.1 mm or with macrotexture, the predicted hydroplaning speed based on the proposed model would deviate from the NASA hydroplaning speed.

A comparison of the friction coefficients during hydroplaning for the various microtextures reveals that the coefficient of friction increases marginally from 0.098 for a smooth plane pavement surface to 0.112 for a pavement surface with 0.3 mm microtexture and 0.132 for a pavement surface with 0.5 mm microtexture. Comparing these results with reported friction coefficients in studies done by Pelloli (1977), it is noted that the predicted range of friction coefficient of 0.125 during incipient hydroplaning by the proposed model for a pavement surface with microtexture depth of 0.45 mm and water depth of 7.62 mm is close to the experimental value of 0.12. This shows that the proposed model is able to estimate the coefficient of friction values close to those measured in experiments.



Figure 4.22 shows the relationship between tire inflation pressure and hydroplaning speed for different values of microtexture. The NASA hydroplaning equation, being essentially based on a glass surface (microtexture = 0 mm) provides a conservative estimate of the hydroplaning speed. For microtexture of 0.1 mm and below, the NASA hydroplaning equation can describe very well the hydroplaning phenomenon. For pavement microtexture greater than 0.1 mm, increasing deviations of the predicted hydroplaning speed from the corresponding NASA values are noted. This suggests that microtexture helps to delay the onset of hydroplaning. It is noted that when the microtexture reaches 0.5 mm, which could be considered as the lower limit of macrotexture, the hydroplaning curve deviates significantly from the NASA hydroplaning equation, indicating that NASA hydroplaning equation could not adequately describe the hydroplaning phenomenon under this scenario. An interesting point to note is that for typical passenger car with tire pressure less than 200 kPa, the improvement in hydroplaning speed with the introduction of microtexture is not readily apparent for drivers. However, for aircraft with tire pressure greater than 1200 kPa, the improvement in hydroplaning speed with the introduction of microtexture is apparent to pilots. This indicates the positive role microtexture plays in reducing hydroplaning occurrence on runways, besides the traditional approach of introducing macrotexture and pavement grooving.

To further validate the ability of the model to predict friction coefficient at incipient hydroplaning, experimental friction studies conducted by Pelloli (1977), Horne and Tanner (1969), Sugg (1969) and Horne (1969) on different flooded pavement surfaces are considered. The comparisons are summarized in Table 4.9. It is shown that with the exception of the concrete surface textured using longitudinal burlap drag, the proposed model provided a good prediction of the skid resistance for the rest of the textured surfaces for the various friction testers.

The results from the numerical simulations indicate that the effect of microtexture on hydroplaning is difficult to detect in practice, due to the relatively narrow range of microtexture encountered in normal pavement surfaces. On the other hand, the effects of macrotexture on hydroplaning can be readily detected as reported in past research (Horne and

Dreher, 1963; Horne and Joyner, 1965; Smith, 1977). This has led to the use of pavement macrotexture and pavement grooving to improve hydroplaning resistance of pavement surfaces.

#### 4.7 Summary

This chapter discusses the development of a three-dimensional hydroplaning model based on a passenger car tire and studies the effects of tire pressure and microtexture of the pavement surface on hydroplaning.

The first part of this chapter describes a three-dimensional finite-volume hydroplaning model. The assumed profile is based on a pneumatic tire with an inflation pressure of 186.6 kPa (27 psi) and sliding at a speed of 96.5 km/h (60 mph) on a flooded glass plane surface with a water film thickness of 7.62 mm (0.3 in.). The fluid model used is the same as that described in the previous chapter. It is found that the proposed 3-D model could adequately model hydroplaning and it gives a ratio of tire pressure to  $0.5\rho U^2$  of 0.640 which agrees well with the predicted NASA hydroplaning value of 0.644.

The second part of this chapter studies the effect of tire pressure on hydroplaning speed. It is shown that the model could accurately predict hydroplaning speeds close to that predicted by the NASA hydroplaning equation. Comparing with experimental results of hydroplaning speeds for different types of tires (Horne and Joyner, 1965), it is shown that the model's predicted hydroplaning relationship is relatively close to those obtained experimentally.

The third part of this chapter studies the effect of microtexture on the onset of hydroplaning. It is shown that hydroplaning speed increases with increasing microtexture depth, and the effect is most significant at 0.5 mm texture depth (by definition, the transition point from microtexture to macrotexture). The analysis highlighted that the improvement of pavement microtexture in the range from 0.2 mm to 0.5 mm did delay hydroplaning, though the improvement in braking ability might not be substantial. The study also shows that the NASA hydroplaning equation provides a conservative estimate of hydroplaning speed. The

under-estimation of hydroplaning speed by the NASA hydroplaning equation became more and more apparent as the microtexture of the pavement increases beyond 0.2 mm.

In summary, the analyses in this chapter show the suitability of the proposed three-dimensional finite-volume model in hydroplaning simulation. The computed tire pressure-hydroplaning speed relationship on a smooth plane surface closely follows that predicted by the simple NASA hydroplaning equation. However, the NASA equation is conservative. The hydroplaning speed predicted by the proposed model increases with the introduction of microtexture.

**Table 4.1: Summary of boundary conditions used in this study**

	Proposed numerical model in this study
Lead edge of footprint	Evaluated from Navier-Stokes equations based on boundary conditions of velocity inlet of velocity U for both air and water at pressure 0 kPa with a uniform velocity profile.
Side edge of footprint	Pressure outlet of 0 kPa.
Midline of footprint	Plane of symmetry.
Trailing edge of footprint	Pressure outlet of 0 kPa
Pavement surface	Moving wall of velocity U for experimental and numerical simulation, effects of gravity considered.
Tire Profile	Assumed tire deformation profile from experiments conducted by Horne and Joyner (1965)

**Table 4.2: Mass flow rate for air and water through various boundaries based on a turbulent flow model for the proposed 3-D model**

Boundary Conditions	Mass Flow Rate for Fluid (kg/s)	
	Air	Water
Velocity Inlet – Air	0.09007	-
Velocity Inlet – Water	-	12.9526
Pressure Outlet– Air	-0.02560	-
Pressure Outlet – Water	-	-0.2753
Top Pressure Outlet	-0.06426	-9.4549
Side Pressure Outlet	-0.00018	-3.2157
Sum (Percentage conserved)	-0.00003 (99.97%)	0.0067 (99.95%)

**Table 4.3: Effect of mesh quality on the various parameters under the wheel for the proposed 3D model**

Number of mesh elements in the smallest channel	Number of mesh elements in the model	$F_y$ (N)	$F_x$ (N)	Average ground hydrodynamic pressure (kPa)	% improved
5	290,530	3158.4	94.0	210.3	-
10	463,300	3172.4	94.8	228.5	7.96%
15	579,225	3176.6	95.7	228.8	0.13%
20	928,700	3173.9	96.0	228.9	0.04%

**Table 4.4: Summary of boundary conditions used in the study of the effect of boundary conditions for the 3D analysis**

Boundary condition locations	Model					
	A	B	C	D	E	F
Distance of velocity inlets from lead edge of footprint, X1 (mm)	100 (13 <i>t</i> )	100 (13 <i>t</i> )	500 (90 <i>t</i> )	100 (13 <i>t</i> )	100 (13 <i>t</i> )	100 (13 <i>t</i> )
Distance of pressure outlet from trailing edge of footprint, X2 (mm)	0 (0 <i>t</i> )	0 (0 <i>t</i> )	0 (0 <i>t</i> )	100 (13 <i>t</i> )	500 (90 <i>t</i> )	0 (0 <i>t</i> )
Distance of pressure outlet from top of tire model, X3 (mm)	25 (3.3 <i>t</i> )	50 (9 <i>t</i> )	50 (9 <i>t</i> )	50 (9 <i>t</i> )	50 (9 <i>t</i> )	25 (3.3 <i>t</i> )
Distance of pressure outlet from side of tire model, X4 (mm)	0 (0 <i>t</i> )	0 (0 <i>t</i> )	0 (0 <i>t</i> )	0 (0 <i>t</i> )	0 (0 <i>t</i> )	100 (13 <i>t</i> )

Note:  $t$  is the water film thickness used in the study and is equal to 7.62 mm (0.3 in.)

**Table 4.5: Effect of location of boundary conditions on the various parameters under the wheel for the 3D analyses**

Model	Number of mesh elements in model	$F_y$ (N)	$F_x$ on wheel (excluding the front portion) (N)	Average ground hydrodynamic pressure (kPa)
A	463,300	3172.4	94.8	228.5
B	544,100	3190.3	95.1	228.7
C	919,300	3146.8	94.2	225.6
D	579,225	3249.1	90.1	231.7
E	1,672,500	3293.2	95.3	232.8
F	754,980	3286.1	94.0	232.3

**Table 4.6: Friction forces and friction coefficient during hydroplaning**

Hydroplaning Speed (mph)	Hydroplaning Speed (km/h)	$F_y$ (N)	$F_x$ (N)	Friction coefficient
20	32.2	370.4	34.2	0.0923
30	48.3	814.8	76.3	0.0936
40	64.4	1,427.9	134.9	0.0945
54.4	87.5	2,575.1	244.5	0.0950
60	96.5	3,172.4	303.5	0.0957
70	112.6	4,289.3	410.0	0.0956
80	128.7	5,579.2	534.7	0.0958
90	144.8	7,036.4	675.9	0.0961
100	160.9	8,664.7	833.5	0.0962
110	177.0	10,463.8	1,007.6	0.0963
120	193.1	12,426.7	1,198.2	0.0964
130	209.2	14,560.1	1,405.4	0.0965
140	225.3	16,883.9	1,630.8	0.0966
150	241.4	19,352.3	1,870.9	0.0967
160	257.4	22,065.2	2,135.7	0.0968
170	273.5	24,756.1	2,398.5	0.0969
180	289.6	27,738.4	2,689.1	0.0969

**Table 4.7: Average ground hydrodynamic pressure and recovery factors for different hydroplaning speeds**

Hydroplaning Speed (mph)	Hydroplaning Speed (km/h)	$P_{av}$ (kPa)	$P_{av}/(0.5\rho U^2)$
20	32.2	26.6	0.670
30	48.3	58.4	0.655
40	64.4	102.4	0.645
54.4	87.5	184.6	0.640
60	96.5	228.5	0.637
70	112.6	307.1	0.632
80	128.7	399.3	0.629
90	144.8	503.4	0.627
100	160.9	619.9	0.625
110	177.0	748.3	0.623
120	193.1	888.5	0.622
130	209.2	1040.1	0.620
140	225.3	1207.0	0.621
150	241.4	1383.4	0.620
160	257.4	1570.1	0.618
170	273.5	1769.3	0.617
180	289.6	1982.3	0.617

**Table 4.8: Equivalent Roughness for New Pipes (Moody, 1944; Colebrook, 1955)**

Pipe	Equivalent roughness (mm)
Riveted steel	0.9-9.0
Concrete	0.3-3.0
Wood stave	0.18-0.9
Cast iron	0.26
Galvanised iron	0.15
Commercial Steel or wrought iron	0.045
Drawn tubing	0.0015
Plastic, glass	0.0 (smooth)

**Table 4.9: Comparison between Predicted and Experimental Friction Coefficients (Pelloli, 1977; Horne and Tanner, 1969; Sugg, 1969; and Horne, 1969)**

Type of Surface	Micro-texture depth (mm)	Friction Tester Used	Predicted Hydroplaning Speed (km/h)	Predicted Friction Coefficient	Experimental Measurement	
					Measured Friction Coefficient at Predicted Hydroplaning Speed	Source of Test Data
Coarse Graded Asphalt	0.45	Skiddometer	81.6	0.125	0.12	Pelloli, 1977
Fine-textured Concrete	0.12	GM Braking Trailer	83.3	0.099	0.10	Horne and Tanner, 1969
Textured Concrete (using longitudinal burlap drag)	0.20	GM Braking Trailer	85.6	0.103	0.12	Horne and Tanner, 1969
Gripstop	0.14	GM Braking Trailer	84.0	0.100	0.10	Horne and Tanner, 1969
Textured Asphalt	0.32	GM Braking Trailer	90.9	0.114	0.12	Horne and Tanner, 1969
Fine-textured Concrete	0.12	Mu-Tester	65.3	0.099	0.10	Sugg, 1969
Textured Concrete (using longitudinal burlap drag)	0.20	Mu-Tester	67.6	0.103	0.31	Sugg, 1969
Smooth Textured Asphalt	0.19	Mu-Tester	67.6	0.103	0.10	Sugg, 1969
Textured Asphalt	0.32	Mu-Tester	71.8	0.114	0.11	Sugg, 1969
Gripstop	0.14	Mu-Tester	66.3	0.100	0.07	Sugg, 1969
Fine-textured Concrete	0.12	NASA Diagonal Braking Car	83.3	0.099	0.11	Horne, 1969
Textured Concrete (using longitudinal burlap drag)	0.20	NASA Diagonal Braking Car	85.8	0.103	0.14	Horne, 1969

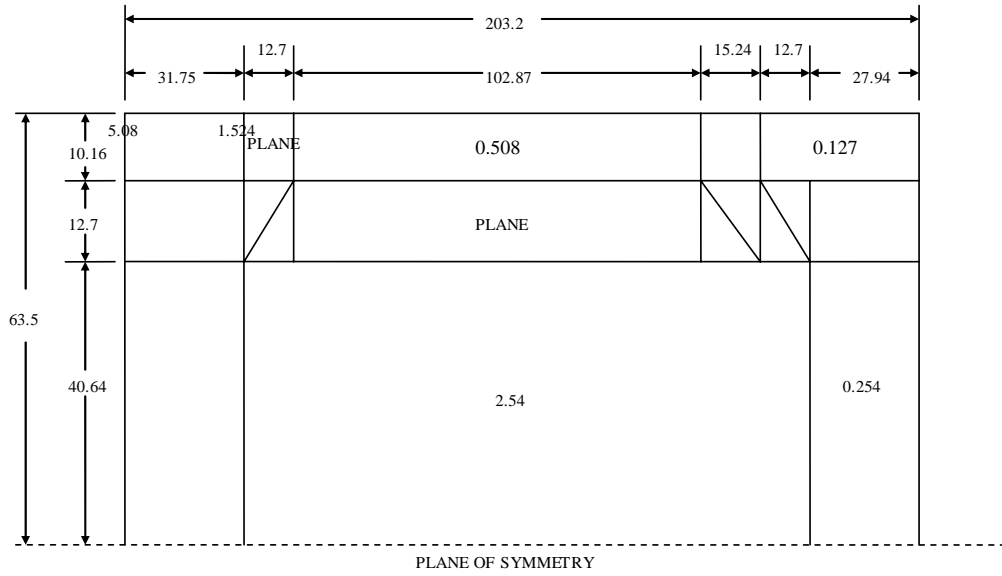


Figure 4.1: Tire deformation profile of a hydroplaning passenger car pneumatic tire at tire pressure of 186.6 kPa (Browne, 1971) (Dimensions are shown in mm.)

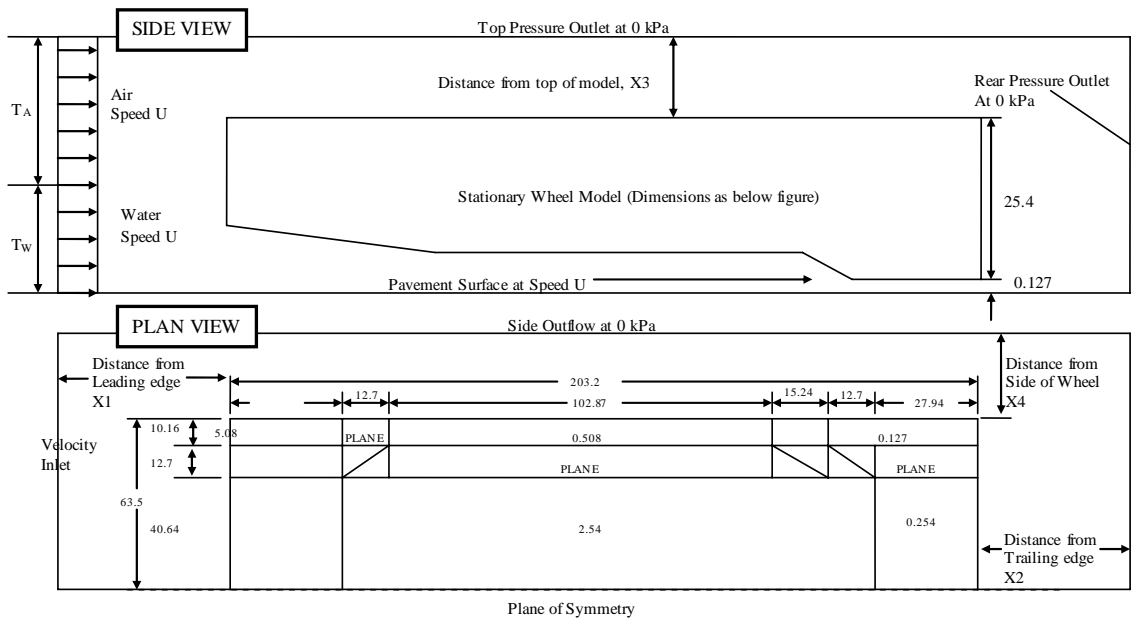


Figure 4.2: Geometry of the proposed 3D hydroplaning model (Dimensions are in mm.)



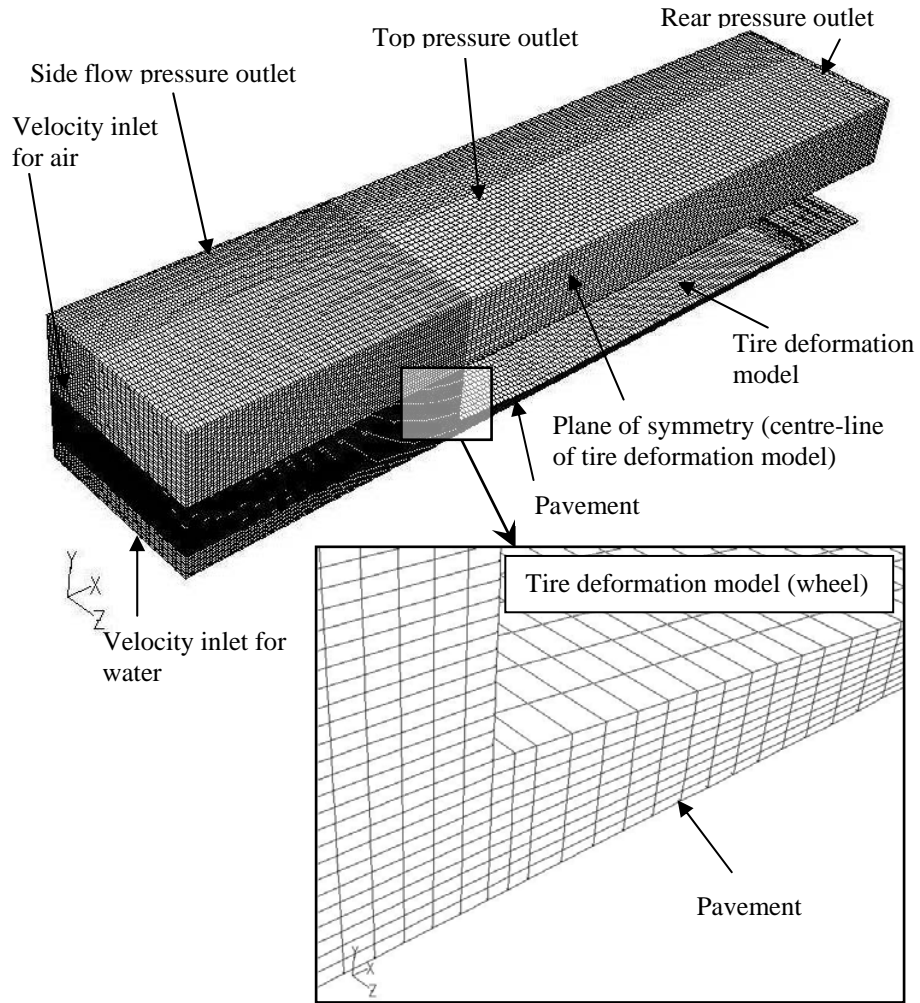


Figure 4.3: Mesh design of the three-dimensional model (Insert: Close-up of mesh design in the hydroplaning region under the wheel)

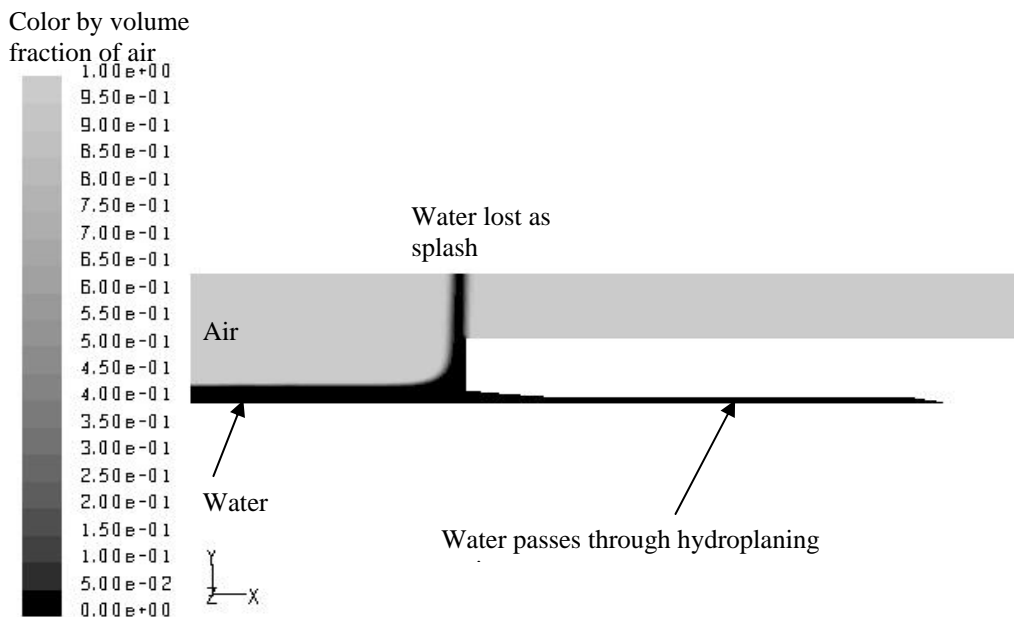
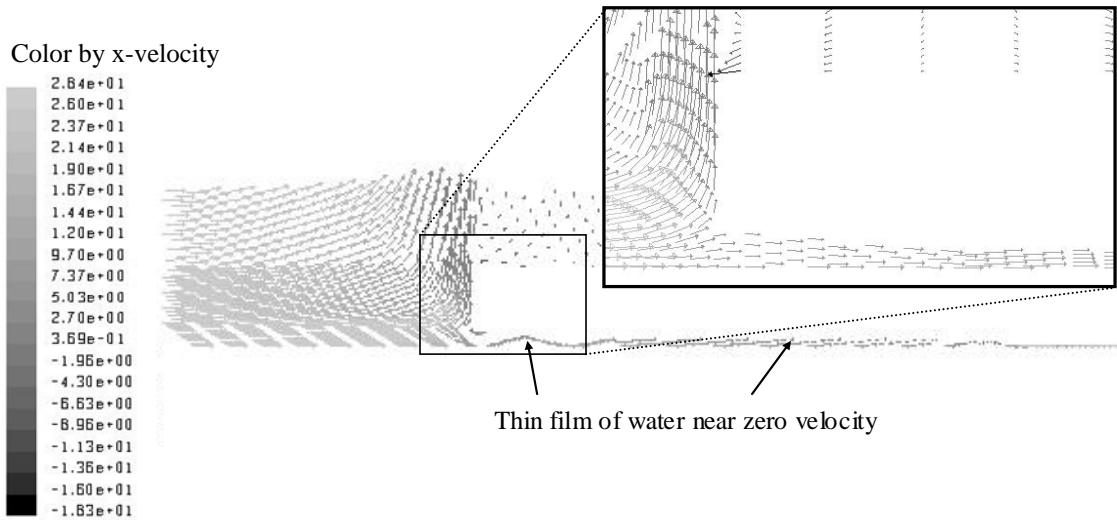
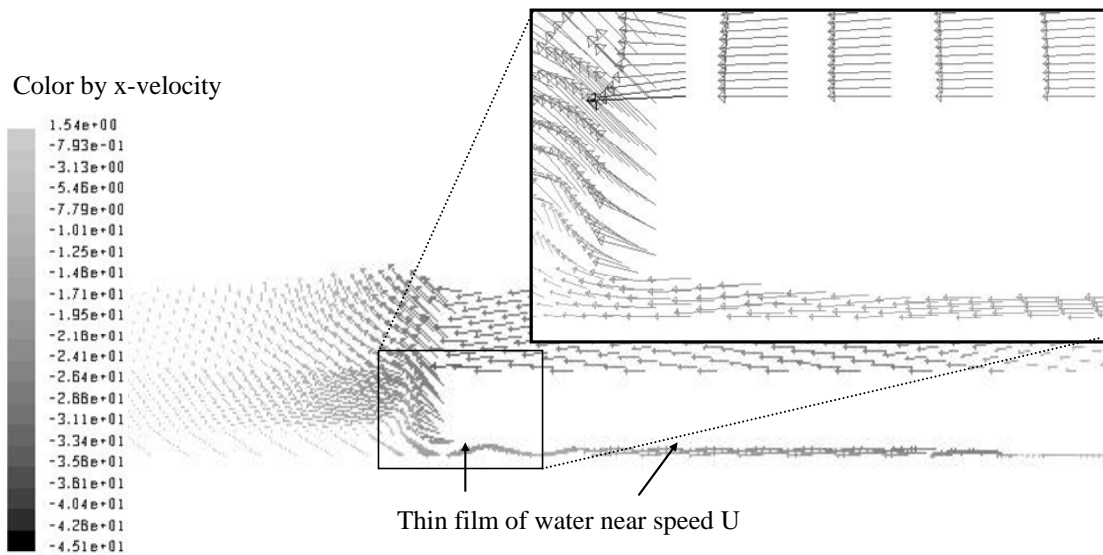


Figure 4.4: Steady state volume fraction plot along plane of symmetry (centerline of model) for the proposed 3D model



(a) Moving wheel reference frame



(b) Stationary observer reference frame

Figure 4.5: Zoom-in view of the velocity vector plot near the wheel along plane of symmetry for the proposed 3D model

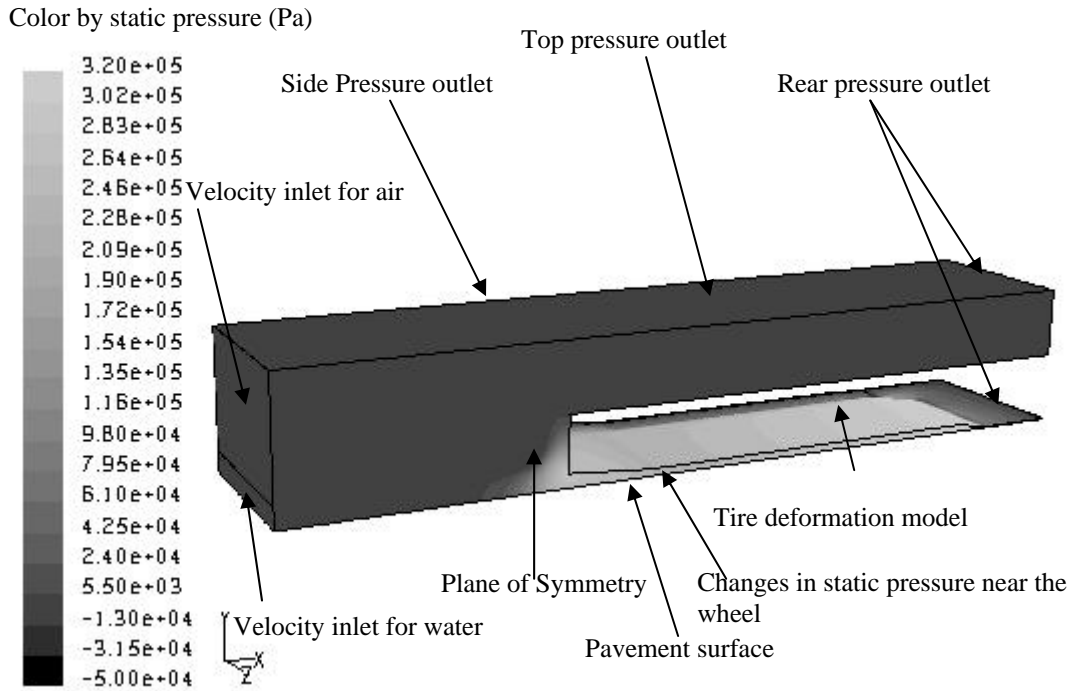


**Figure 4.6: Static pressure contour plot of the 3D model under the moving wheel reference frame**

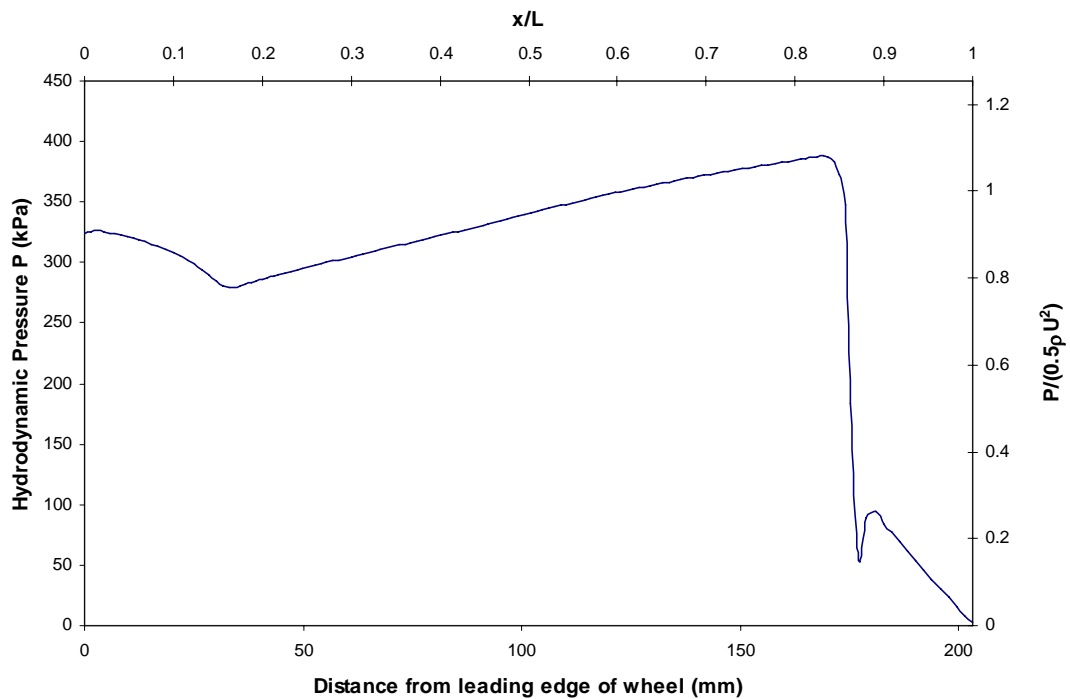


**Figure 4.7: Ground hydrodynamic pressure distribution along the centre-line under wheel for the proposed 3D model**

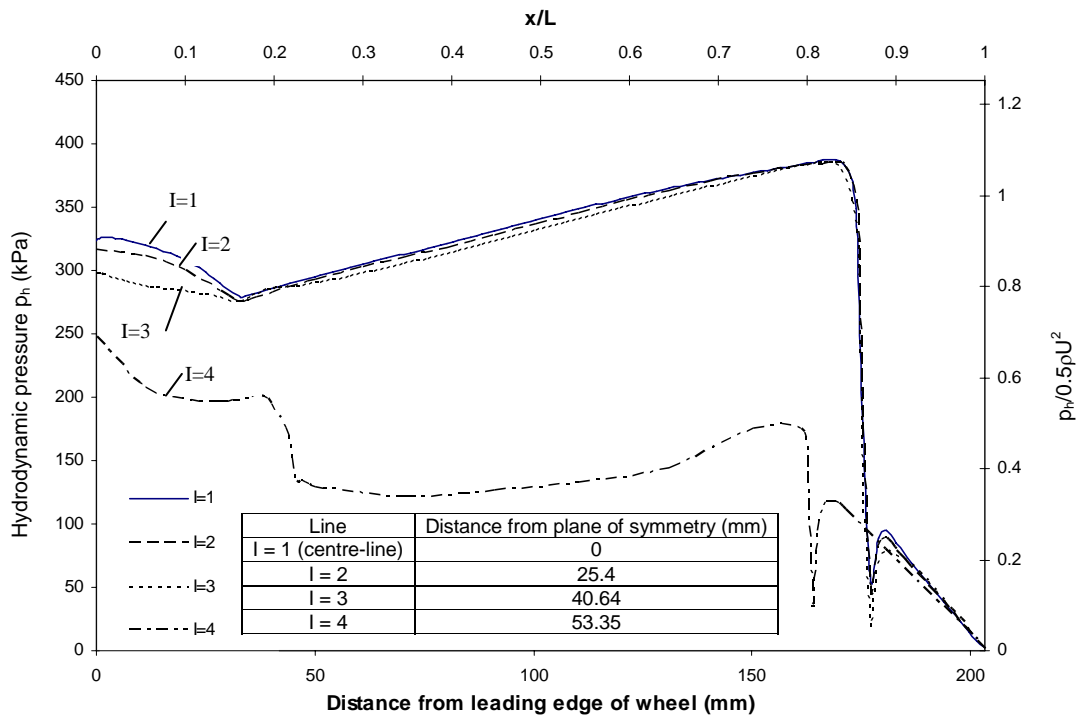


Figure 4.8: Ground hydrodynamic pressure distribution along lines under wheel for the proposed 3D model

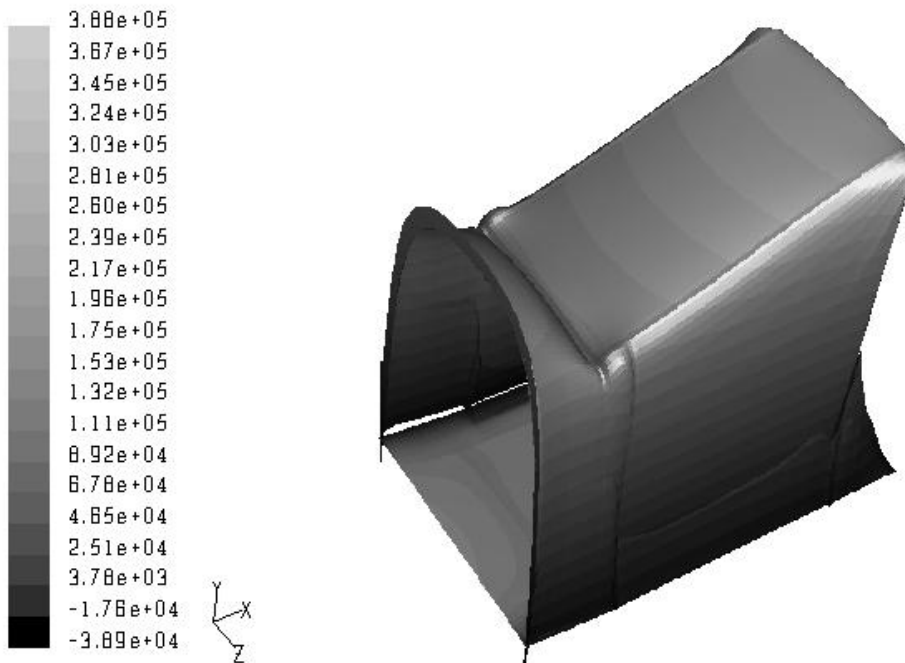
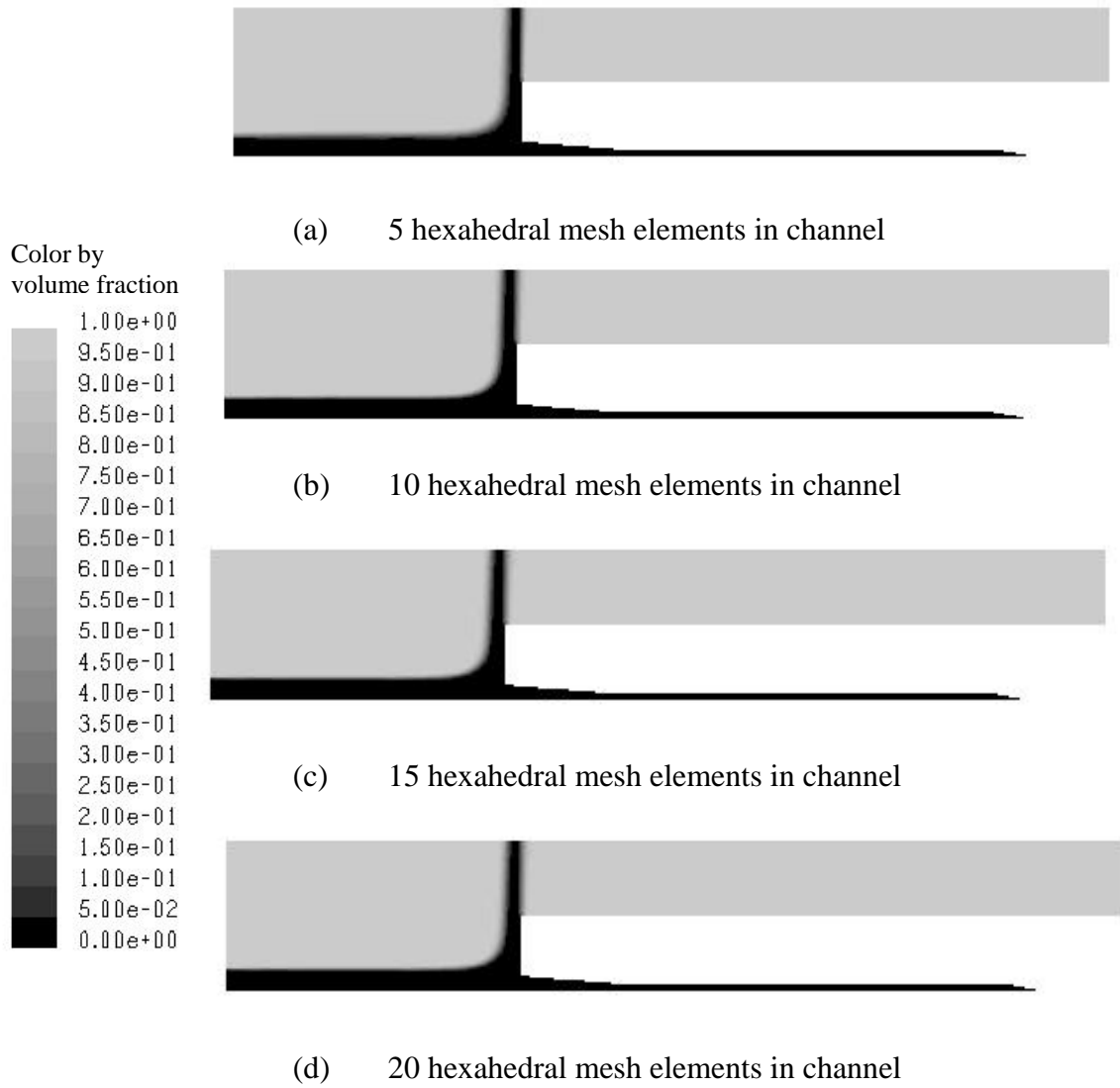


Figure 4.9: Ground hydrodynamic pressure distribution under wheel for the proposed 3D model



**Figure 4.10: Steady state volume fraction plots for the study of the effect of mesh size in the proposed 3D model**

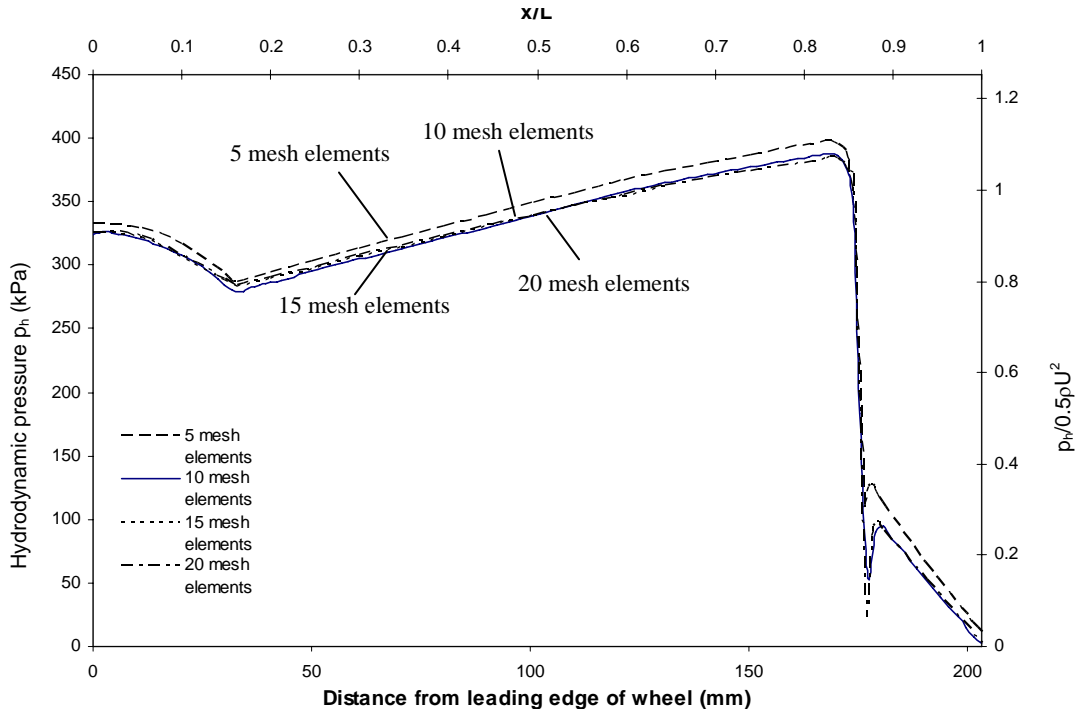


Figure 4.11: Ground hydrodynamic pressure distribution under the centre-line of the wheel for the study of the effect of mesh size in the proposed 3D model

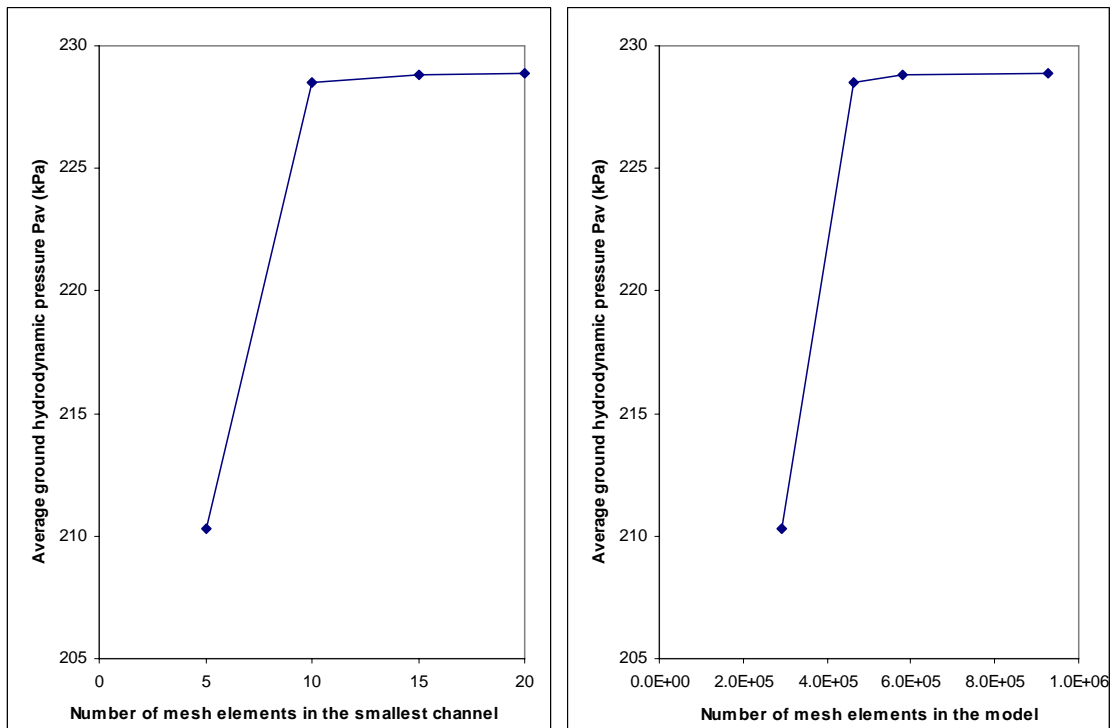


Figure 4.12: Effect of mesh quality on the average ground hydrodynamic pressure under the wheel in the proposed 3D model (left: in terms of number of elements in channel, right: in terms of number of elements in model)

Colors by volume fraction

1.00e+00
9.50e-01
9.00e-01
8.50e-01
8.00e-01
7.50e-01
7.00e-01
6.50e-01
6.00e-01
5.50e-01
5.00e-01
4.50e-01
4.00e-01
3.50e-01
3.00e-01
2.50e-01
2.00e-01
1.50e-01
1.00e-01
5.00e-02
0.00e+00

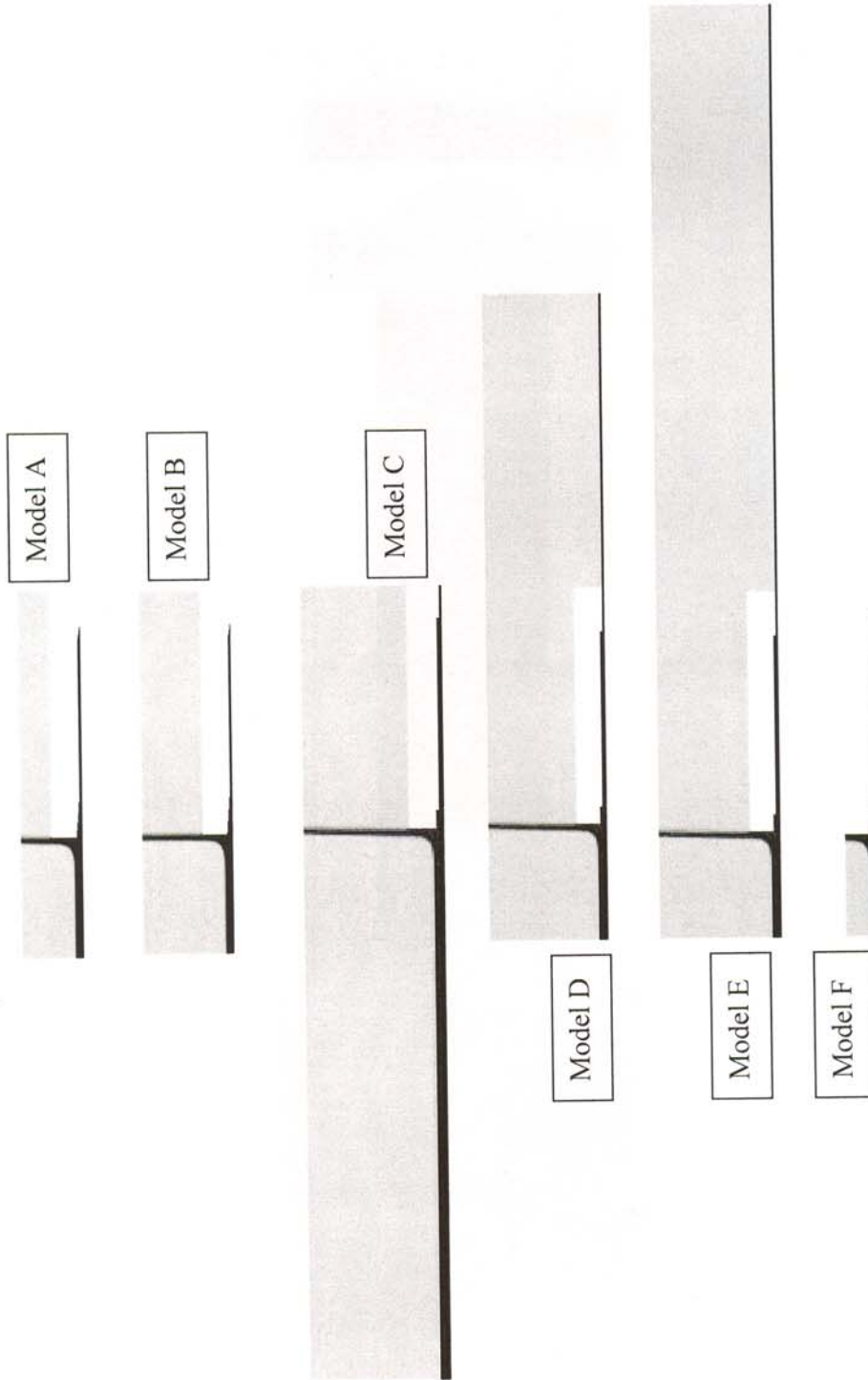


Figure 4.13: Steady state volume fraction plots along the plane of symmetry for the study of the effect of location of boundary conditions in the proposed 3D model

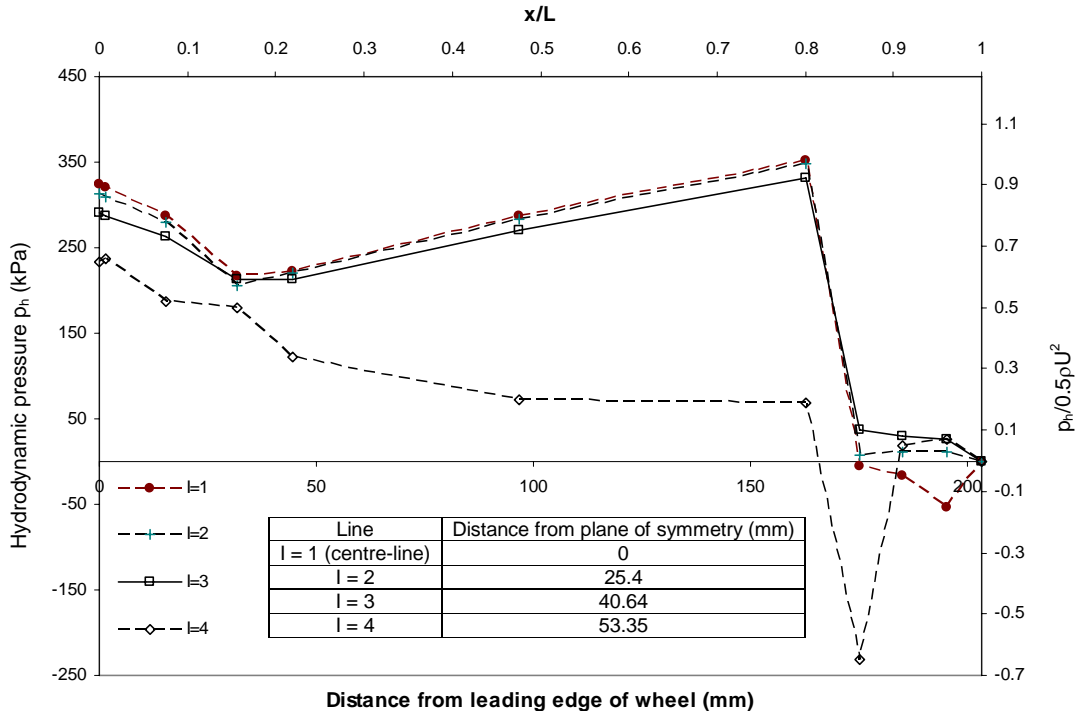


Figure 4.14: Ground hydrodynamic pressure distribution along lines under wheel in Browne's research (1971)

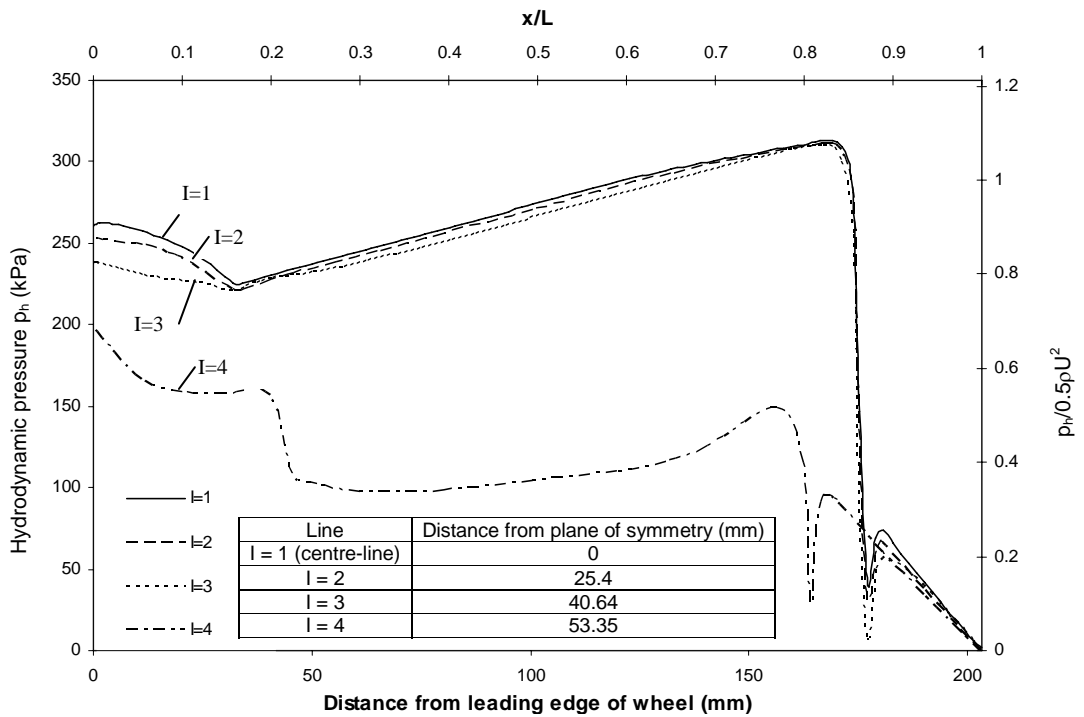


Figure 4.15: Ground hydrodynamic pressure distribution along lines under wheel for the proposed 3D model at test speed of 86.7 km/h (54.4 mph)



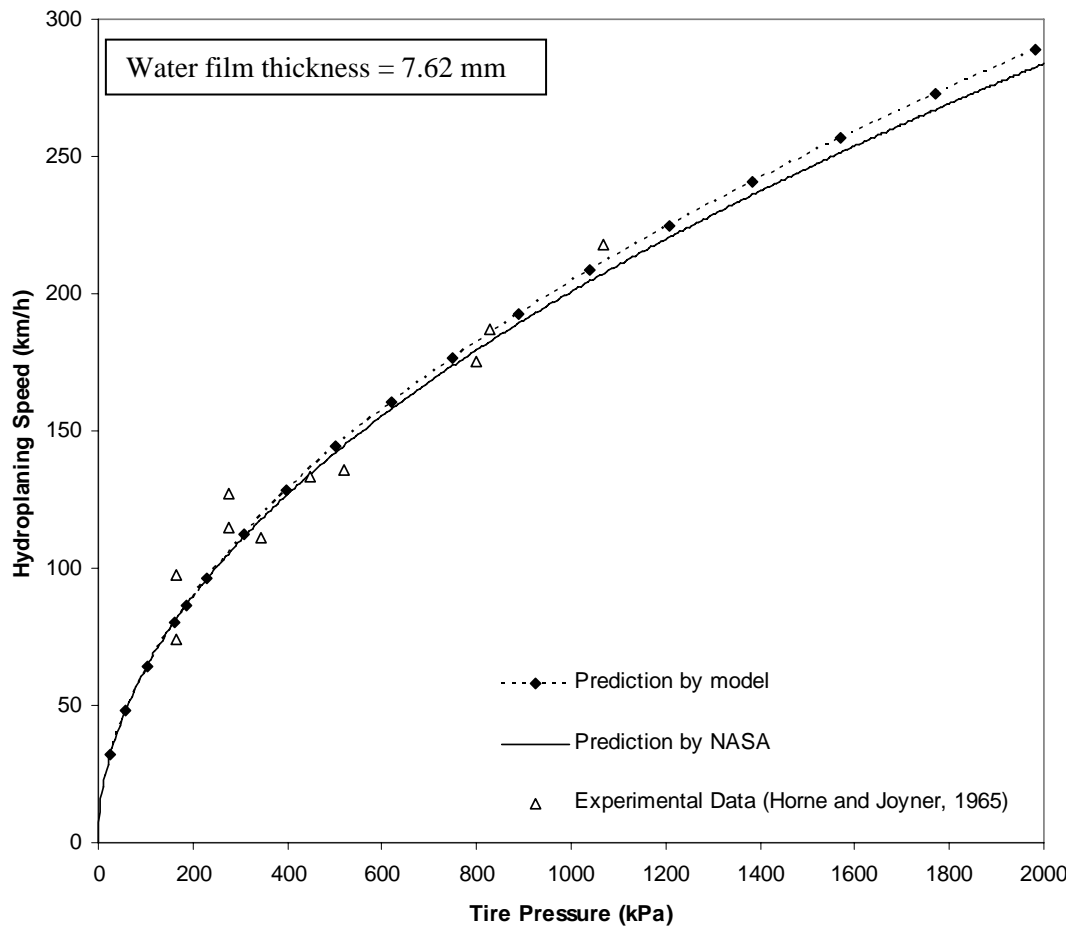


Figure 4.16: Relationship between tire pressure and hydroplaning speed

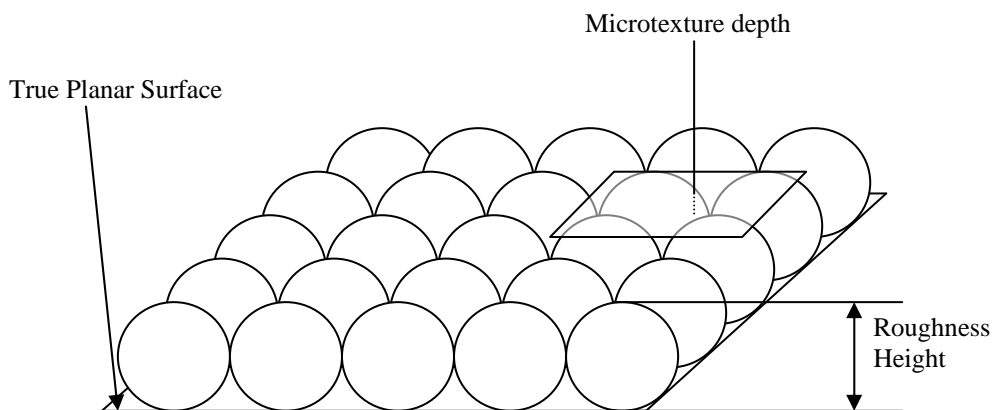
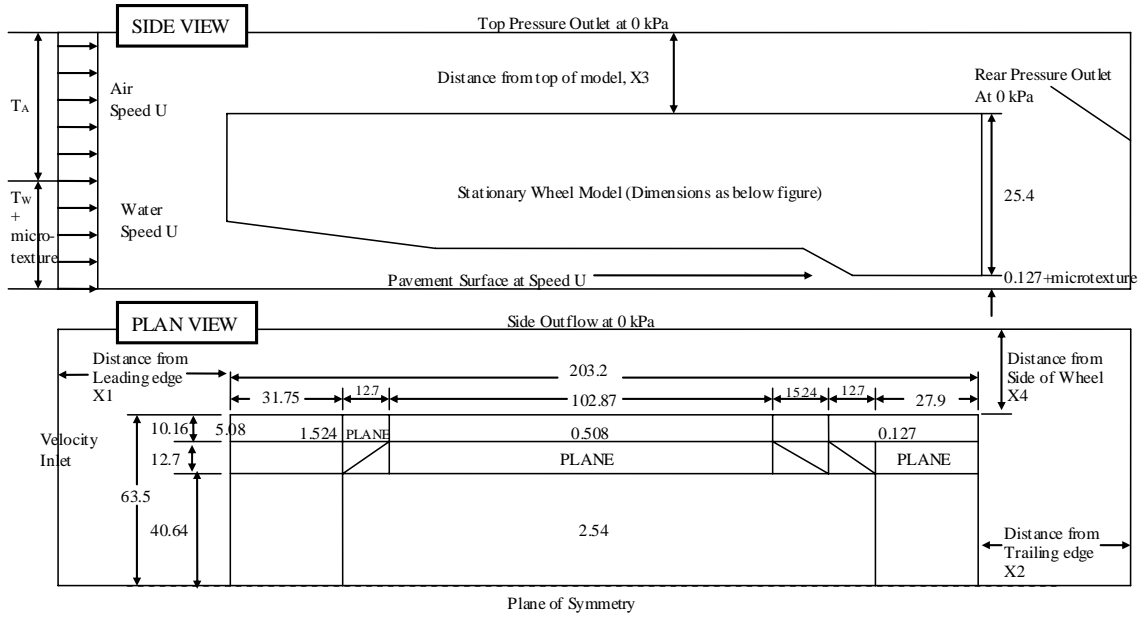
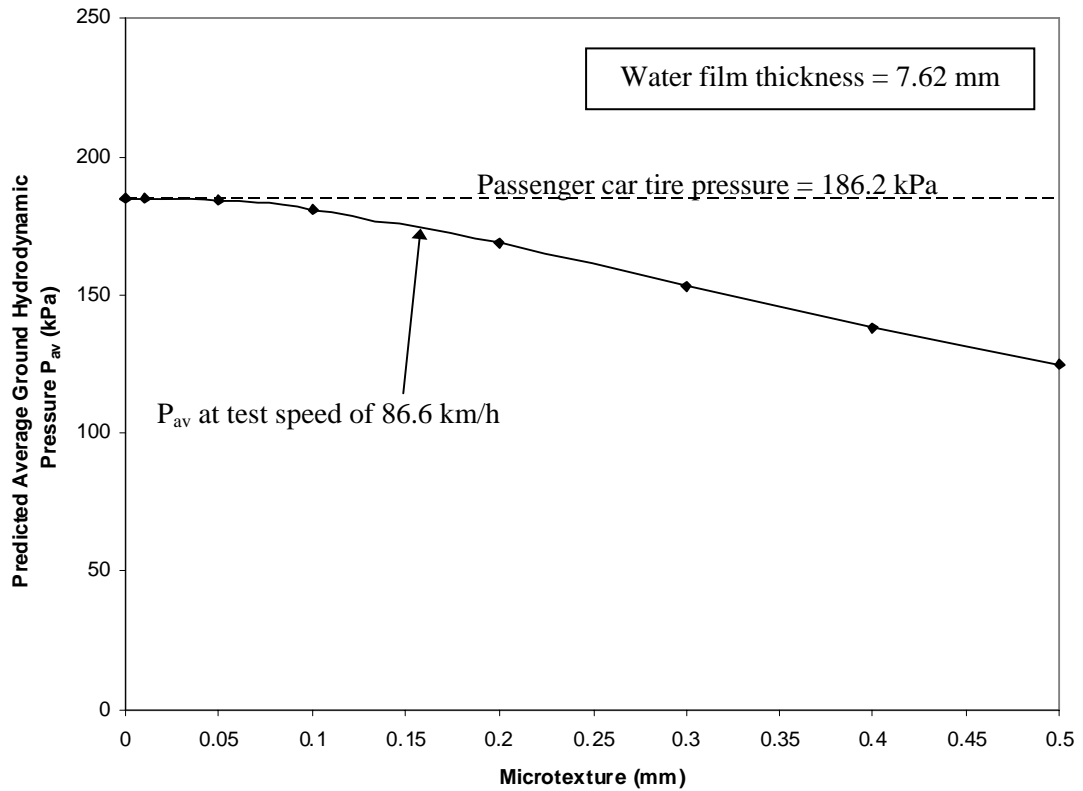


Figure 4.17: Simplified representation of roughness assuming that sand grain is a perfect sphere



**Figure 4.18: Geometry of the proposed 3D hydroplaning model to account for microtexture (Dimensions are in mm.)**



**Figure 4.19: Effect of microtexture on the predicted ground hydrodynamic pressure at the NASA hydroplaning speed of 87.5 km/h**

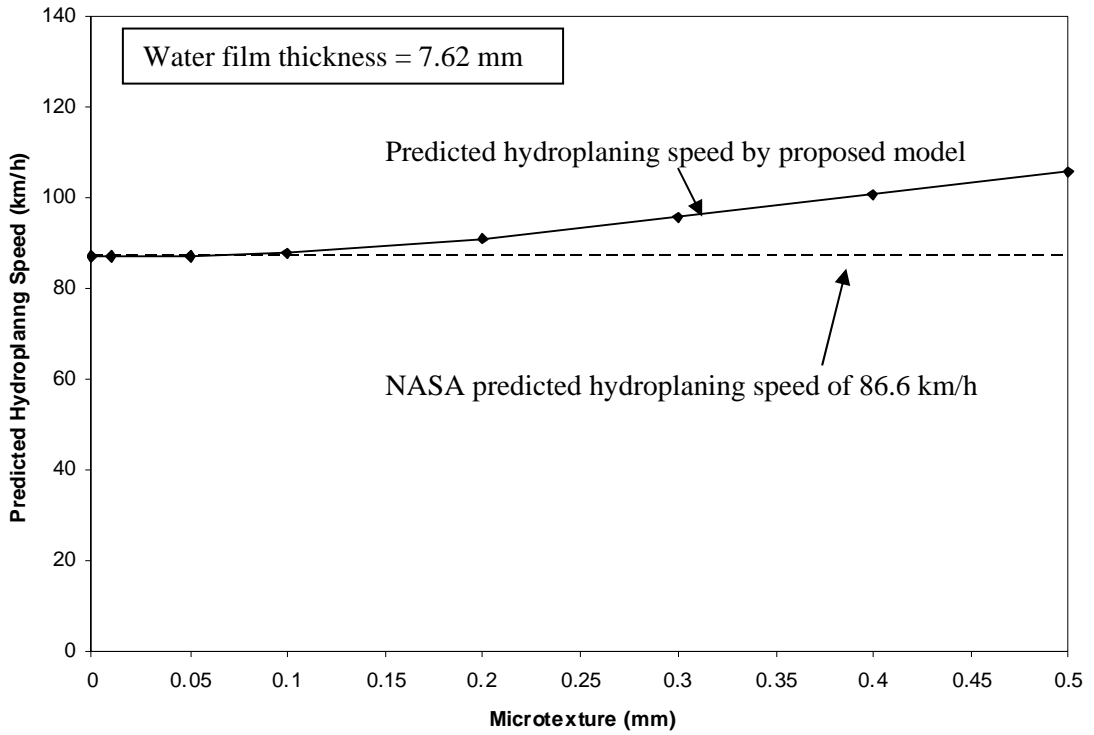


Figure 4.20: Effect of microtexture on the predicted hydroplaning speed

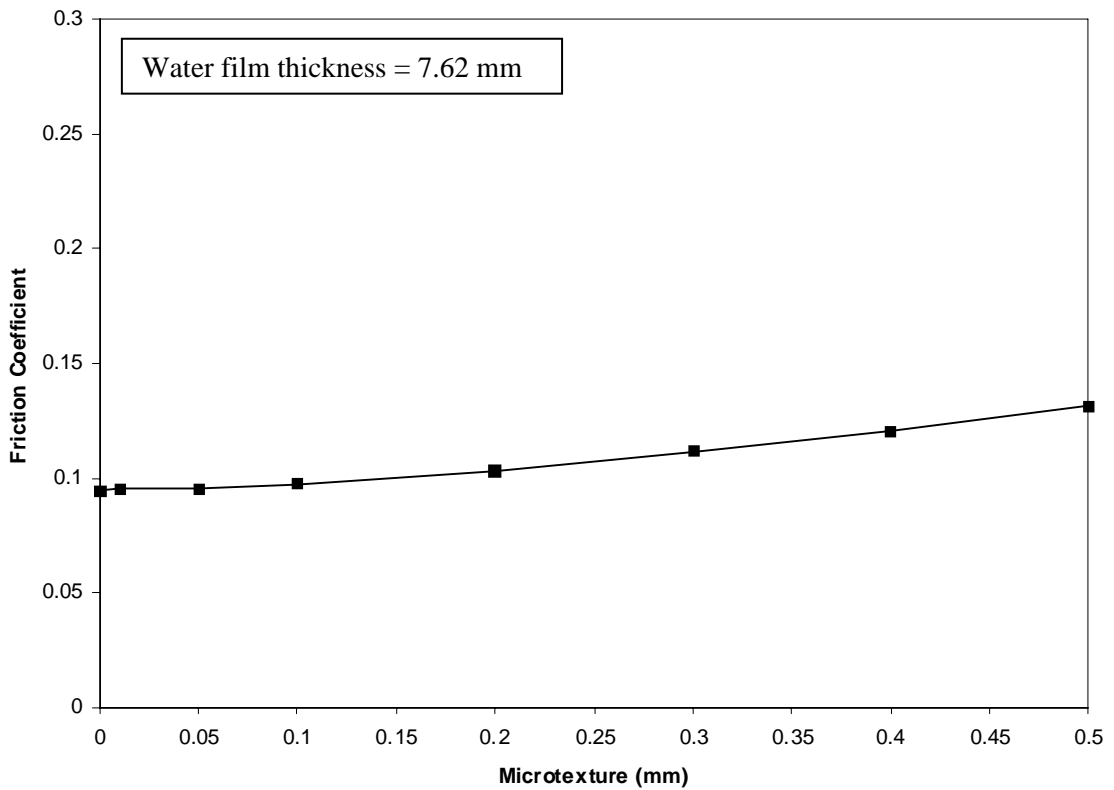


Figure 4.21: Effect of microtexture on the predicted coefficient of friction

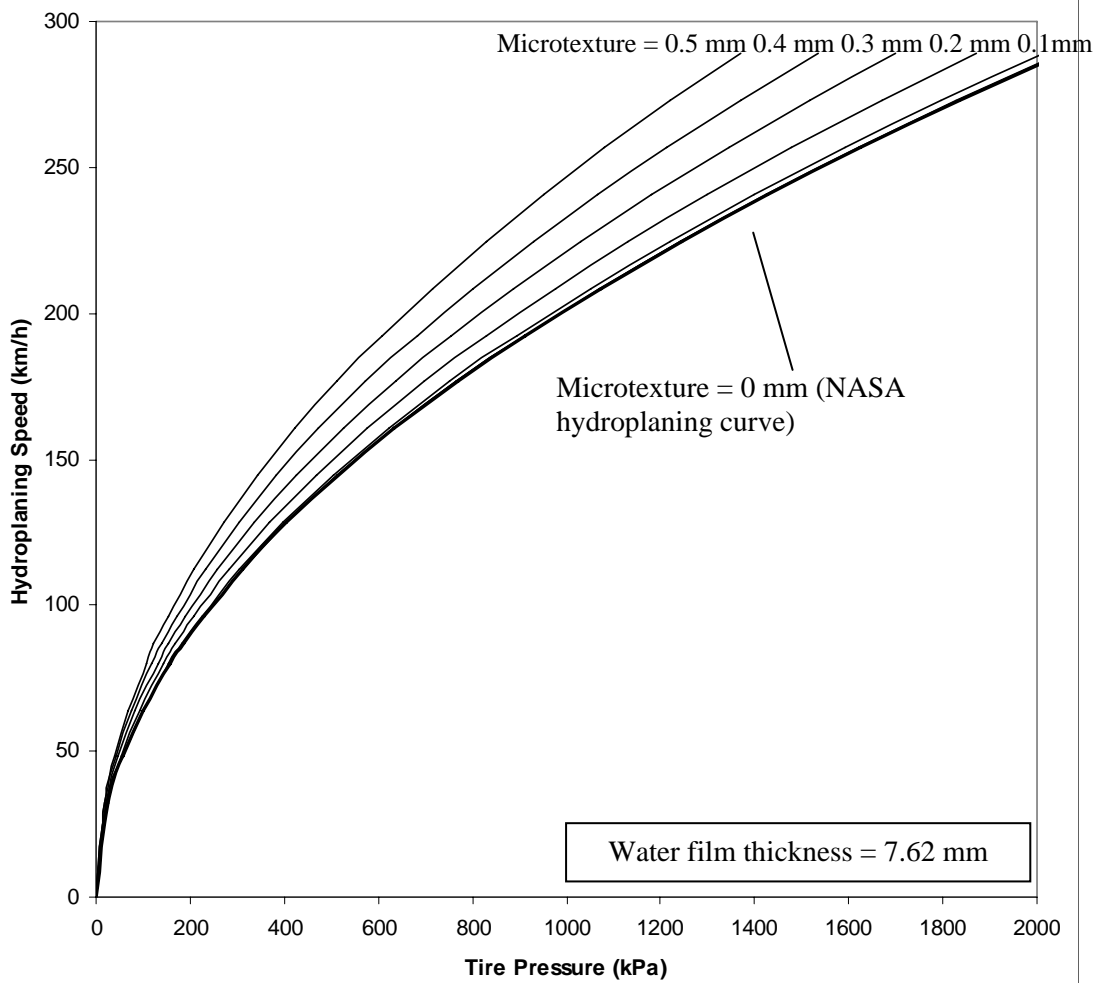


Figure 4.22: Effect of microtexture on the hydroplaning curves

## **CHAPTER 5      HYDROPLANING      ON      PAVEMENT      WITH GROOVING**

### **5.1      Introduction**

The previous chapters have discussed the modeling of hydroplaning on plane pavement surfaces. It is noted that plane pavement surfaces with only microtexture (which is typical for concrete pavements without any surface-texturing treatments) has typically low hydroplaning speeds and friction coefficients at incipient hydroplaning. Researchers have proposed the use of pavement grooving (Mosher, 1969) and air-jets (Horne and Joyner, 1965) to reduce the occurrence of hydroplaning. It was shown experimentally that transverse pavement grooving can substantially increase the water depth required for a vehicle traveling at a given speed to hydroplane, thereby delaying the occurrence or reducing the risk of hydroplaning. Tests conducted by Yager (1969) on aircraft tires showed that transverse runway grooves provide (1) substantially increased aircraft braking capability and directional control, (2) improved runway surface water drainage, and (3) more rapid wheel spin-up rates. They also reduce the susceptibility to dynamic hydroplaning and reverted rubber hydroplaning. These findings are consistent with other research on aircraft hydroplaning and runway skid resistance (Shilling, 1969; Pelloli, 1977) and led to the use of transverse grooving in runways as a measure to combat hydroplaning (FAA, 1997).

While transverse grooving has been found to significantly improve traction control and reduce hydroplaning occurrences on runways, the use of longitudinal grooving often showed little or no improvement in traction even though there was a reduction in hydroplaning occurrences (Horne, 1969; FHWA, 1980; ACI, 1988). On the other hand, longitudinal grooving tends to be favored by highway agencies as only one lane at a time needs to be closed during maintenance, unlike transverse grooving where the whole road section have to be closed (Highway Research Board, 1972; Pennsylvania Transportation Institute, 1988; ACPA, 2000). No detailed study to date has been conducted to offer an insight into the effectiveness

of longitudinal pavement grooving against hydroplaning. Thus it is of interest to pavement engineers to understand how transverse and longitudinal pavement grooving can affect the potential of hydroplaning occurrences.

This chapter presents the use of the simulation model described in Chapter 3 to study the effects of transverse and longitudinal grooving on hydroplaning. As described in Figure 2.15 in Chapter 2, this chapter first conducts a study on how different transverse and longitudinal grooving designs can affect hydroplaning. Next, it is sought to understand how the transverse and longitudinal pavement groove dimensions can affect hydroplaning. Through a systematic numerical study, a comparison between the effectiveness of transverse and longitudinal pavement grooving against hydroplaning can be made. The significance of the transverse and longitudinal pavement grooving in hydroplaning prevention is then discussed and the current guidelines on longitudinal and transverse groove dimensions are evaluated.

## **5.2 Verification of Simulation Model for Pavement with Pavement Grooving**

Chapter 4 has described the development and the use of numerical simulations to model hydroplaning on plane pavement surfaces with or without microtexture. The proposed model can also be applied to analyze the effects of pavement grooving on hydroplaning. This section shall discuss the verification of the model for simulating hydroplaning on transverse and longitudinal pavement grooving.

### **5.2.1 Verification against Experimental Data for Transverse Pavement Grooving**

Verification of the simulation model in predicting the hydroplaning speed for transverse pavement grooving can be performed by comparing against experimental data reported by Horne and Tanner (1969). Four different pavement surfaces with transverse groove dimensions of 6 mm width by 6 mm depth by 25 mm spacing are tested and are shown in Table 5.1. They employed ASTM E-524 standard smooth tire of 165.5 kPa (24 psi) inflation pressure, and experiments were conducted on test surfaces flooded with water depth of 5.08 mm (0.2 in.) to 7.62 mm (0.3 in.). In the simulation model, pavement microtexture is

represented using the roughness function which is available in FLUENT (Fluent Inc., 2005). The predicted hydroplaning speeds and the friction factor at incipient hydroplaning calculated by the proposed model are plotted in Figure 5.1 together with the measured data by Horne and Tanner (1969). Next, the exponential friction-to-speed relationship proposed by Meyer (21) is applied to fit the data points. Meyer's relationship is given in Equations (5.1) and (5.2).

$$SN_v = SN_0 e^{-(PNG/100)v} \quad (5.1)$$

$$PNG = 100 \left( \frac{d(SN_v)/dv}{SN_v} \right) \quad (5.2)$$

where  $SN_v$  is the skid number at vehicle speed  $v$ ,  $SN_0$  is a fictitious skid number at zero vehicle speed, and PNG is the percentage normalized gradient of the  $SN$  against  $v$  curve. Very high values of statistical coefficient of determination  $R^2$  of 0.938 and above are obtained for the four cases as shown in Figure 5.1. This confirms that the friction factors derived by the proposed simulation model are closely consistent with the experimentally measured data.

### 5.2.2 Verification against Experimental Data for Longitudinal Pavement Grooving

For longitudinal pavement grooving, verification can be made by comparing against experimental data conducted by Horne (1969). The ASTM E-524 standard smooth tire of 165.5 kPa (24 psi) inflation pressure is used and experiments were conducted on longitudinally grooved surfaces with 6 mm width, 6 mm depth and 19 mm spacing. The pavement is flooded with water depth of 5.08 mm (0.2 in.) to 7.62 mm (0.3 in.). Figure 5.2 shows the comparison between the simulation results of the predicted hydroplaning speed and the friction coefficient at incipient hydroplaning and the experimental data points. Similar to the previous sub-section, the exponential friction-to-speed relationship can be developed and a very high value of statistical coefficient of determination  $R^2$  of 0.959 are obtained. This confirms that the proposed simulation model can predict friction factors that are close to the experimentally measured data.

### **5.3 Simulation of Hydroplaning on Pavement with Pavement Grooving**

As experimental studies on hydroplaning are often large in scale, costly to conduct and risky to personnel carrying out the experiments, the numerical approach proposed could be an efficient and cost effective mean to study the hydroplaning phenomenon and the effectiveness of pavement grooving designs. The previous sub-section has already verified the model for hydroplaning speed prediction on longitudinal and transverse pavement grooving. This section shall discuss on the use of the simulation model to study the effectiveness of longitudinal and transverse pavement grooving on hydroplaning control. Three particular designs are studied to understand how longitudinal and transverse pavement grooving can affect hydroplaning, as shown in Table 5.2.

#### **5.3.1 Simulation Results for Transverse Pavement Grooving Designs**

The ground hydrodynamic pressure distributions along selected profiles under a wheel of tire inflation pressure 186.2 kPa and sliding at a speed of 86.6 km/h for grooved pavement Designs A, B and C are shown in Figure 5.3. The average ground hydrodynamic pressure under the hydroplaning wheel is found to be 35.1 kPa for Design A, 57.3 kPa for Design B and 90.2 kPa for Design C. Therefore, hydroplaning does not occur at the NASA hydroplaning speed meant for the plane surface.

The model is next applied for speeds ranging from 0 km/h to 300 km/h to derive a tire pressure-hydroplaning speed relationship and to compare it with the NASA hydroplaning equation. It is found that recovery factors of 0.1190, 0.1981 and 0.3128 are obtained for Designs A, B and C respectively. The corresponding hydroplaning speeds are 199.5 km/h, 156.10 km/h and 124.4 km/h for a passenger car tire with tire inflation pressure of 186.2 kPa, against the predicted NASA hydroplaning speed of 86.9 km/h respectively. These significant increases in hydroplaning speed clearly demonstrate the benefits of applying transverse pavement grooving to reduce the occurrences of hydroplaning. The friction factors experienced by the wheel for a passenger car tire of inflation pressure of 186.2 kPa at incipient hydroplaning are found to be 0.442, 0.294 and 0.192 for Designs A, B and C respectively.



Figure 5.4 shows the relationship between hydroplaning speed and tire-pressure for a smooth surface (i.e. NASA hydroplaning relationship) and the three transverse grooving designs. It can be observed that the use of transverse pavement grooving increases the hydroplaning speed for a given tire inflation pressure and among the three grooving designs, Design A is most effective in guarding against hydroplaning.

### 5.3.2 Simulation Results for Longitudinal Pavement Grooving Designs

The ground hydrodynamic pressure distributions along selected profiles under a wheel of tire inflation pressure 186.2 kPa and sliding at a speed of 86.6 km/h for grooved pavement Designs A, B and C are shown in Figure 5.5. The average ground hydrodynamic pressure under the hydroplaning wheel is found to be 151.1 for Design A, 168.8 kPa for Design B and 173.6 kPa for Design C. Therefore, hydroplaning does not occur at the hydroplaning speed meant for the plane surface. Applying the model over speeds ranging from 0 km/h to 300 km/h, it is found that recovery factors of 0.4630, 0.5849 and 0.6014 are obtained for Designs B and C respectively. The corresponding hydroplaning speeds are 102.2 km/h, 90.9 km/h and 89.6 km/h for a passenger car tire with tire inflation pressure of 186.2 kPa, against the predicted NASA hydroplaning speed of 86.9 km/h, which correspond to a 17.6%, 4.6 % and a 3.1 % increase respectively. The increase in hydroplaning speed is small but nevertheless it shows that longitudinal pavement grooving does reduce the occurrences of hydroplaning. The friction factors experienced by the wheel for a passenger car tire of inflation pressure of 186.2 kPa at incipient hydroplaning are found to be 0.125, 0.111 and 0.108 for Designs A, B and C respectively. These are marginally higher than the friction coefficient of 0.0962 for the plane pavement surface, indicating that longitudinal pavement grooving of Design A, B and C offer little improvement in friction coefficient at incipient hydroplaning.

Figure 5.6 shows the relationship between hydroplaning speed and tire-pressure for a smooth surface (i.e. NASA hydroplaning relationship) and the three longitudinal grooving designs. It can be observed that the use of longitudinal pavement grooving increases the hydroplaning speed for a given tire inflation pressure and among the three grooving designs,

similar to the case of the transverse pavement grooving, Design A is the most effective pavement grooving design in combating hydroplaning.

### **5.3.3 Comparison between Transverse and Longitudinal Pavement Grooving for Designs A, B and C**

Table 5.3 summarizes the simulation results for the three transverse and three longitudinal pavement grooving designs. It can be observed that consistently, the transverse pavement grooving of the three tested designs give a higher hydroplaning speed and a higher friction coefficient at incipient hydroplaning, compared to longitudinal pavement grooving of the same design. The numerical values of the friction coefficients at incipient hydroplaning for longitudinal pavement grooving are close to that of the plane pavement surface and the improvement in friction control is nearly negligible. However, somewhat more noticeable increases in hydroplaning speed are noted.

## **5.4 Effect of Transverse Groove Dimensions on Hydroplaning**

The simulations performed in the previous section highlighted the different effects that different transverse grooving designs have in reducing hydroplaning risk and enhancing braking control at incipient hydroplaning. As experimental studies of this nature are often large in scale, costly to conduct and risky to personnel carrying out the experiments, the numerical approach proposed could be an efficient and cost-effective means to study the hydroplaning phenomenon and the effectiveness of pavement grooving designs. This section presents an analytical approach to evaluate the effects of transverse pavement groove dimensions (groove width, depth and spacing) on hydroplaning.

### **5.4.1 Model Parameters Used in Study**

In the analysis of the effects of groove dimensions, five different centre-to-centre groove spacings (5 mm, 10 mm, 15 mm, 20 mm and 25 mm), six different groove depths (1 mm, 2 mm, 4 mm, 6 mm, 8 mm and 10 mm) and groove widths varying from 2 to 10 mm were

considered, as summarized in Table 5.4. These are selected to cover the typical ranges of acceptable groove dimensions of 12.7 mm to 19.1 mm in spacing, 3.2 mm to 4.8 mm in depth and 2.0 mm to 3.2 mm in width (Wu and Nagi, 1995; ACPA, 2005).

The hydroplaning phenomenon of a locked wheel sliding over a transversely grooved pavement surface covered with a film of water is studied. A constant water film thickness of 0.3 in. (7.62 mm) is adopted for the analysis. Hydroplaning is assumed to occur when the average ground hydrodynamic pressure is equal to the tire pressure of the wheel, i.e. when the hydrodynamic lift force is equal to the wheel load. The deformed profile at the onset of hydroplaning of a pneumatic tire is obtained from the well-known NASA experimental study reported by Horne and Dreher (1963). In this section, to analyze the effect of pavement grooving, which is a form of macrotexture, the microtexture depth of the pavement surface material is assumed to be zero. The applied boundary conditions and mesh design are similar to the model described in Chapter 4 and shown in Figure 4.2.

For each pavement grooving design, the computer simulation model is applied for cases of hydroplaning speeds ranging from 0 km/h to 300 km/h in steps of 15 km/h, and the corresponding tire inflation pressure for each case is obtained. The relationship between the hydroplaning speed and tire inflation pressure for a particular pavement grooving design can be established.

## **5.4.2 Results and Analysis**

The effects of groove depth, width and spacing respectively on hydroplaning are analyzed by means of the computer simulation model based on the 132 groove designs of Table 5.4. The results of analyses are presented in Table 5.5 for a passenger car tire with 186.2 kPa inflation pressure.

### **5.4.2.1 Effect of Groove Depth on Hydroplaning**

For easy presentation, the discussion is focused on transverse groove designs with groove spacing of 15 mm. The computed results, extracted from Table 5.5, for different

groove depths are summarized in Table 5.6. For the case of 2 mm groove width, the predicted hydroplaning speeds range from 108.1 km/h for a 1 mm groove depth to 142.6 km/h for a 10 mm groove depth. The friction coefficients experienced by the wheel at incipient hydroplaning are found to vary from 0.1568 to 0.2439 as groove depth changes from 1 mm to 10 mm. These correspond to a range of percentage increases in hydroplaning speed of 25.0% to 64.8%, compared to the NASA predicted hydroplaning speed of 86.5 km/h for a smooth plane pavement; and a range of percentage increases in friction coefficient of 62.5% to 152.8%, as compared to the associated friction coefficient of 0.0965 during incipient hydroplaning for the smooth plane pavement surface. The higher friction coefficient and hydroplaning speed associated with a larger groove depth indicates the benefit gained in reducing hydroplaning risk and the loss of braking control at incipient hydroplaning.

As can be seen from Table 5.6, similar trends of changes in hydroplaning speed and friction coefficient respectively with groove depth are also found for designs with other groove widths. It is noted that the percentage increases in hydroplaning speed and friction coefficient with groove depth are larger for groove designs having a larger groove width. It is also noted that the hydroplaning speeds obtained from the simulation are larger than 300 km/h for (a) groove depths greater than 6 mm at 6 mm groove width and 15 mm spacing, (b) groove depths greater than 2 mm at 8 mm groove width and 15 mm spacing, and (c) all groove depths at 10 mm groove width and 15 mm spacing. This indicates hydroplaning could not occur with these groove designs within the normal operating range of vehicles.

Figure 5.7 shows the relationships between hydroplaning speed and tire-pressure for different groove depths, for the case of 15 mm groove spacing with 4 different groove widths. Similar patterns of relationships to those shown in Figure 5.7 are also found for groove spacings of 5 mm, 10 mm, 20 mm and 25 mm respectively. It can be observed that for any given tire pressure, a larger groove depth for a given groove spacing and width would lead to a higher hydroplaning speed.

#### 5.4.2.2 Effect of Groove Width on Hydroplaning

For easy presentation, the discussion is again focused on transverse groove designs with groove spacing of 15 mm. The computed results, extracted from Table 5.6, for different groove depths are summarized in Table 5.7. Consider the cases of groove design with a 2 mm groove depth, the predicted hydroplaning speeds range from 110.1 km/h for a 2 mm groove width to 249.6 km/h for 6 mm groove width. The friction coefficients experienced by the wheel for a passenger car tire of tire inflation pressure of 186.2 kPa at incipient hydroplaning are found to vary from 0.1607 to 0.6760 as groove width changes from 2 mm to 6 mm. These correspond to a range of percentage increases in hydroplaning speed of 27.3% to 188.5% compared to the NASA predicted hydroplaning speed of 86.5 km/h, and a percentage increase in friction coefficient of 66.6% to 600.5% as compared to the friction coefficient of 0.0965 at incipient hydroplaning for the smooth plane pavement surface.

As can be seen from Table 5.7, similar trends of changes in hydroplaning speed and friction coefficient respectively with groove width are also found for designs with other groove widths. The results show that the percentage increases in hydroplaning speed and friction coefficient with groove width are higher for a larger groove depth. It is also noted that the hydroplaning speeds obtained from the simulation are larger than 300 km/h for (a) groove width of 10 mm at 1 mm groove depth and 15 mm spacing, (b) groove widths greater than 8 mm at 2 or 4 mm groove depth and 15 mm spacing, and (c) groove widths greater than 6 mm for 6 mm to 10 mm groove depth and 15 mm spacing. This indicates that hydroplaning would not occur with these groove designs within the operating speed range of vehicles.

Similar to the case of groove depth, the effect of groove width on hydroplaning can be studied for the 132 transverse pavement grooving designs analyzed. Figure 5.8 shows the relationship between hydroplaning speed and tire-pressure for different groove widths, for the case of 15 mm groove spacing with 4 different groove depths. Similar patterns of relationships are also found for groove spacings of 5 mm, 10 mm, 20 mm and 25 mm respectively. It can be observed from Figure 5.8 that for any given tire pressure and given groove depth and spacing,

a larger groove width would produce a higher hydroplaning speed. This is possibly because a larger groove width allows more outflow of water through the sides of the wheel.

### 5.4.2.3 Effect of Groove Spacing on Hydroplaning

For easy presentation, the discussion is focused on groove designs with 2 mm groove width. The computed results, extracted from Table 5.6, for different center-to-center groove spacing are summarized in Table 5.8. For the cases with groove depth of 6 mm, the predicted hydroplaning speeds range from 260.4 km/h for 5 mm groove spacing to 108.3 km/h for 25 mm groove spacing. The friction coefficients experienced by the wheel for a passenger car tire of tire inflation pressure of 186.2 kPa during incipient hydroplaning are found to vary from 0.1544 to 0.9140 when groove spacing decreases from 25 mm to 5 mm. These correspond to a range of percentages increase in hydroplaning speed of 201.0% to 25.2% and a range of percentage increases in friction coefficient of 847.2% to 60.0% with a decrease of groove spacing from 25 mm to 5 mm, with respect to the NASA predicted hydroplaning speed and its associated friction coefficient for the smooth plane pavement surface. The higher friction coefficient and hydroplaning speed associated with a smaller center-to-center groove spacing indicates the benefit gained in reducing hydroplaning risk and the loss of braking control at incipient hydroplaning.

As can be seen from Table 5.8, similar trends of changes in hydroplaning speed and friction coefficient respectively with groove spacing are also found for designs with other groove depths. The magnitude of percentage increase in hydroplaning speed and friction coefficient with groove spacing are higher for a larger groove depth.

Figure 5.9 shows the relationships between hydroplaning speed and tire-pressure for different groove spacings, for the case of 2 mm groove width with 4 different groove depths. Similar patterns of relationships are also found for groove widths of 4 mm, 6 mm, 8 mm and 10 mm respectively. It can be seen from Figure 5.9 that a smaller spacing produces a larger deviation from the NASA hydroplaning curve for the plane surface. In general, a larger groove

spacing leads to a lower hydroplaning speed since there is now less number of grooves in the tire imprint region, resulting in less outflow of water through the sides of the wheel.

#### **5.4.2.4 Relative Effects of Groove Depth, Width and Spacing**

The preceding sub-sections have discussed the effects of groove depth, width and spacing on the hydroplaning speed and friction coefficient at incipient hydroplaning. It is noted that in general, a larger groove width, groove depth and a smaller groove spacing would result in a larger hydroplaning speed and a higher friction coefficient at incipient hydroplaning. For a practical range of transverse grooving designs having groove width ranging from 2 mm to 4 mm, groove depth ranging from 2 mm to 6 mm and groove spacing ranging from 10 mm to 25 mm as shown in Table 5.9 (ACPA, 2005), the hydroplaning speed is found to vary from 100.8 km/h to 280.1 km/h and the friction coefficient at incipient hydroplaning varies between 0.1365 and 0.9307 for a passenger car with 186.2 kPa tire inflation pressure. Such a large range in hydroplaning speeds and friction coefficients respectively suggest that there is a need to study the relative effects of the groove dimensions of transverse pavement grooving in hydroplaning prevention.

To make a comparison between the relative effects of groove width, depth and spacing on hydroplaning, an effectiveness index can be defined in terms of the magnitude of change in hydroplaning speed for each unit change of a particular groove dimension. This effectiveness index with the unit of km/h/mm can be calculated for the 132 cases of groove design analyzed in this study, as given in Table 5.10, for the three different tire pressures (100 kPa, 200 kPa and 300kPa). A total of 199 data points of the effectiveness index for groove depth can be computed out of the 396 data considered for the different cases as shown in Figure 5.10(a). There are also 167 data points of the effectiveness index for groove width as shown in Figure 5.10(b) and 174 data points of the effectiveness index for groove spacing as shown in Figure 5.10(c).

It is seen that with the given range of practical groove dimensions, for each mm increase in groove depth, the raise in hydroplaning speed that can be achieved falls within the

range of 0 to 70 km/h with a mean of 9.37 km/h/mm. More than 80% of the cases give increases in hydroplaning speed in the range of 0 to 10 km/h for each mm increase in groove depth. For each mm increase in groove width, the raise in hydroplaning speed falls within the range of 0 to 105 km/h with a mean of 28.34 km/h/mm. More than 80% of the cases give increases in hydroplaning speed in the range of 15 to 35 km/h for each mm increase in groove width. For each mm decrease in groove spacing, the raise in hydroplaning speed falls within the range of 0 to 35 km/h with a mean of 7.37 km/h/mm. More than 80% of the cases give an increase in hydroplaning speed in the range of 0 to 12 km/h for each mm reduction in groove spacing.

It can be observed that groove width provides the largest effectiveness indices compared to groove depth and spacing. This indicates that groove width is an important factor in reducing hydroplaning occurrences and could be a primary factor in groove design. Groove depth is perhaps the next important factor followed by the groove spacing by comparing the frequency distribution plots and the mean effective index. However, one point to note is that unlike groove width and depth, the range of spacing adopted in practice is typically much larger than that for the groove width or depth. This means that in practice, spacing could be a more convenient measure in combating hydroplaning.

## **5.5 Effect of Longitudinal Groove Dimensions on Hydroplaning**

### **5.5.1 Model Parameters Used in Study**

As shown in Table 5.4, the range of pavement groove dimensions was studied: groove widths from 2 mm to 10 mm, groove depths from 1 mm to 10 mm, and groove center-to-center spacing from 5 mm to 25 mm. The total number of groove designs analyzed was also 132. These ranges of dimensions are selected based on common longitudinal groove dimensions reported in the literature (ACPA, 2005; Caltrans, 1999; International Groove and Grinding Association, 2005). The same numerical model as described in Section 5.3.1 with the boundary conditions as shown in Chapter 4 and Figure 4.2 is used in the simulation model.



## 5.5.2 Simulation Results

The main results of the simulation analysis are the expected hydroplaning speeds and the friction coefficient at the onset of hydroplaning. The computed hydroplaning speeds and friction coefficients of all the 132 designs of groove dimensions are presented in Table 5.11 for the case of a passenger car with 186.2 kPa tire inflation pressure. The respective effects of varying groove depth, groove width and groove spacing are analyzed in the following sub-sections. A raise in the hydroplaning speed means that the risk of hydroplaning will be reduced, while an increase in friction coefficient implies that the traction will be improved.

### 5.5.2.1 Effect of Groove Depth on Hydroplaning

For easy presentation, the discussion is focused on transverse groove designs with groove spacing of 20 mm. The computed results, extracted from Table 5.11, for different groove depths are summarized in Table 5.12. For the case of 2 mm groove width, the predicted hydroplaning speeds range from 87.2 km/h for a 1 mm groove depth to 95.6 km/h for a 10 mm groove depth. The friction coefficients experienced by the wheel at incipient hydroplaning are found to vary from 0.0978 to 0.1174 as groove depth changes from 1 mm to 10 mm. These correspond to a percentage increase in hydroplaning speed of 0.8% to 10.5%, compared to the NASA predicted hydroplaning speed of 86.5 km/h for a smooth plane pavement and a percentage increase in friction coefficient of 1.4% to 21.7%, as compared to the associated friction coefficient of 0.0965 during incipient hydroplaning for the smooth plane pavement surface. The higher friction coefficient and hydroplaning speed associated with a larger groove depth indicates the benefit gained in reducing hydroplaning risk and the loss of braking control at incipient hydroplaning.

As can be seen from Table 5.12, similar trends of changes in hydroplaning speed and friction coefficient respectively with groove depth are also found for designs with other groove widths. It is noted that the percentage increases in hydroplaning speed and friction coefficient with groove depth are larger for groove designs having a larger groove width.

Figure 5.11 shows the relationships between hydroplaning speed and tire-pressure for different groove depths, for the case of 20 mm groove spacing with 5 different groove widths. Similar patterns of relationships to those shown in Figure 2 are also found for groove spacing of 5 mm, 10 mm, 15 mm and 25 mm respectively. It can be observed that for any given tire pressure, a larger groove depth for a given groove spacing and width would lead to a higher hydroplaning speed. This is within expectation because of the fact that there would be larger outlet space along the grooves that allow water to escape from the tire imprint region. These plots also reveal that the impact of increasing groove depth on the hydroplaning speed increases with the magnitude of the tire pressure.

#### **5.5.2.2 Effect of Groove Width on Hydroplaning**

For easy presentation, the discussion is again focused on groove designs with groove spacing of 20 mm. The computed results, extracted from Table 5.11, for different groove depths are summarized in Table 5.13. Consider the cases of groove design with a 6 mm groove depth, the predicted hydroplaning speeds range from 92.25 km/h for a 2 mm groove width to 115.55 km/h for a 10 mm groove width. The friction coefficients experienced by the wheel for a passenger car tire of tire inflation pressure of 186.2 kPa during incipient hydroplaning are found to vary from 0.1090 to 0.1631 as groove width changes from 2 mm to 10 mm. These correspond to a percentage increase in hydroplaning speed of 6.65% to 33.58% compared to the NASA predicted hydroplaning speed of 86.5 km/h, and a percentage increase in friction coefficient of 12.95% to 69.02% as compared to the associated friction coefficient of 0.0965 during incipient hydroplaning for the smooth plane pavement surface.

As can be seen from Table 5.13, similar trends of changes in hydroplaning speed and friction coefficient respectively with groove width are also found for designs with other groove widths. The results show that the percentage increases in hydroplaning speed and friction coefficient with groove width are higher for a larger groove depth.

Figure 5.12 shows the relationship between hydroplaning speed and tire-pressure for different groove widths, for the case of 20 mm groove spacing with 4 different groove depths.

Similar patterns of relationships are also found for groove spacing of 5 mm, 10 mm, 15 mm and 25 mm respectively. It can be observed from Figure 5.12 that for any given tire pressure and given groove depth and spacing, a larger groove width would produce a higher hydroplaning speed. These plots also reveal that the impact of increasing groove depth on the hydroplaning speed increases with the magnitude of the tire pressure.

### 5.5.2.3 Effect of Groove Spacing on Hydroplaning

For easy presentation, the discussion is focused on groove designs with of 2 mm groove width. The computed results, extracted from Table 5.11, for different center-to-center groove spacing are summarized in Table 5.14. For the cases with groove depth of 6 mm, the predicted hydroplaning speeds range from 105.01 km/h for 5 mm groove spacing to 91.53 km/h for 25 mm groove spacing. The friction coefficients experienced by the wheel for a passenger car tire of tire inflation pressure of 186.2 kPa during incipient hydroplaning are found to vary from 0.1072 to 0.1410 when groove spacing decreases from 25 mm to 5 mm. These correspond to a percentage increase in hydroplaning speed of 21.40% to 5.82% and a percentage increase in friction coefficient of 11.09% to 46.11% with a decrease of groove spacing from 25 mm to 5 mm, with respect to the NASA predicted hydroplaning speed and its associated friction coefficient for the smooth plane pavement surface. The higher friction coefficient and hydroplaning speed associated with a smaller center-to-center groove spacing indicates the benefit gained in reducing hydroplaning risk and the loss of braking control at incipient hydroplaning.

As can be seen from Table 5.14, similar trends of changes in hydroplaning speed and friction coefficient respectively with groove spacing are also found for designs with other groove depths. The magnitude of percentage increase in hydroplaning speed and friction coefficient with groove spacing are higher for a larger groove depth.

Figure 5.13 shows the relationships between hydroplaning speed and tire-pressure for different groove spacing, for the case of 2 mm groove width with 4 different groove depths. Similar patterns of relationships are also found for groove widths of 4 mm, 6 mm, 8 mm and

10 mm respectively. It can be observed from Figure 5.13 that for any given tire pressure and given groove depth and width, a smaller groove spacing would produce a higher hydroplaning speed. These plots also reveal that the impact of decreasing groove spacing on the hydroplaning speed increases with the magnitude of the tire pressure.

#### **5.5.2.4. Relative Effects of Groove Depth, Width and Spacing**

The preceding sub-sections have discussed the effects of groove depth, width and spacing on the hydroplaning speed and friction coefficient at incipient hydroplaning. It is noted that in general, a larger groove width, a larger groove depth and a smaller groove spacing would result in a larger hydroplaning speed and a higher friction coefficient at incipient hydroplaning. For a practical range of longitudinal grooving designs having groove width ranging from 2 mm to 6 mm, groove depth ranging from 2 mm to 8 mm and groove spacing ranging from 10 mm to 20 mm, the hydroplaning speed is found to vary from 88.74 km/h to 124.16 km/h and the friction coefficient during incipient hydroplaning varies between 0.1010 and 0.2056. This corresponds to percentage increases of the hydroplaning speed over the NASA hydroplaning speed by 2.58% to 43.54%, and the corresponding increase in friction coefficient by 4.66% to 113.11%. Such a large range and magnitude in percentage increases in hydroplaning speeds and friction coefficients respectively suggest that it is important to select appropriate groove dimensions through analysis of their effects in order to achieve the desired outcomes of installing longitudinal grooves.

To make a comparison between the relative effects of groove width, depth and spacing on hydroplaning, an effectiveness index can be defined in terms of the magnitude of change in hydroplaning speed for each unit change of a particular groove dimension. This effectiveness index with the unit of km/h/mm can be calculated for the 132 cases of groove design analyzed in this study, as given in Table 5.15, for the three different tire pressures (100 kPa, 200 kPa and 300kPa). A total of 330 data points of the effectiveness index for groove depth can be computed out of the 396 data considered for the different cases as shown in Figure 5.14(a). There are also 300 data points of the effectiveness index for groove width as shown in Figure

5.14(b) and 288 data points of the effectiveness index for groove spacing as shown in Figure 5.14(c).

It is seen that with the given range of practical groove dimensions studied in this paper, for each mm increase in groove depth, the raise in hydroplaning speed that can be achieved falls within the range of 0 to 9 km/h with a mean of 2.799 km/h/mm. For each mm increase in groove width, the raise in hydroplaning speed falls within the range of 0 to 16 km/h with a mean of 3.558 km/h/mm. For each mm decrease in groove spacing, the raise in hydroplaning speed falls within the range of 0 to 5.25 km/h with a mean of 1.057 km/h/mm. It can be observed that groove width provides the largest effectiveness indices compared to groove depth and spacing. This indicates that groove width is an important factor in reducing hydroplaning occurrences and could be a primary factor in groove design. Groove depth is perhaps the next important factor followed by the groove spacing by comparing the frequency distribution plots and the mean effective index. However, one point to note is that unlike groove width and depth, the range of spacing adopted in practice is typically much larger than that for the groove width or depth. This means that in practice, spacing could be a more convenient measure in combating hydroplaning.

## **5.6 Comparison between Transverse and Longitudinal Pavement Grooving in Hydroplaning Prevention**

Based on the data presented in the previous sections, a comparison of the effectiveness of transverse and longitudinal pavement grooving in combating hydroplaning can be made. For the same pavement groove design, it is noted from Tables 5.10 and 5.15 that transverse pavement grooving consistently gives a higher hydroplaning speed. This reinforces the argument made in Section 5.2.5 where three different pavement grooving designs were tested. A reason for the better performance is the hydrodynamic pressure developed under the wheel on transversely-grooved pavements as compared to the longitudinally-grooved pavements, as observed in Figures 5.3 and 5.5. It is noted that the hydroplaning speeds obtained for the different transversely-grooved pavements tested are typically larger than 99.3 km/h as shown

in Table 5.5 compared to 87.0 km/h for longitudinal pavement grooving as shown in Table 5.11. This again highlights the more significant benefits transverse pavement grooving has on hydroplaning control.

However, this does not mean that longitudinal pavement grooving is not effective against hydroplaning. Noting the hydroplaning speeds shown in Table 5.11, it is observed that the range of hydroplaning speed for a 186.2 kPa tire inflation pressure can vary between 87.0 km/h to 145.3 km/h for the different longitudinal groove designs analyzed. This indicates that some of the longitudinal groove designs are more effective in hydroplaning control compared to others, considering the practical traffic speeds on highways. This means that there is a need to better analyze and design the longitudinal and transverse groove designs with respect to traffic speeds against hydroplaning as shall be discussed in Chapter 6.

In terms of the friction coefficient at incipient hydroplaning, it is noted that the magnitudes of the friction coefficient at incipient hydroplaning are at least 0.1361 for transversely-grooved pavements while those of longitudinally-grooved pavements are at least 0.0966. This indicates the marked improvement in friction coefficient at incipient hydroplaning for the transverse pavement grooving from the simulations as shown in Table 5.16. This is in line with the findings in the literature where the transverse pavement grooving give consistently better skid numbers in friction testing experiments (Horne, 1969; Sugg, 1969; FHWA, 1980; ACI, 1988). For the longitudinal pavement grooving, the improvement in friction coefficient is not obvious since the groove dimensions now play a critical role. This is highlighted in Table 5.11 where the friction coefficient ranges from 0.0966 to 0.2420. Certain groove designs would result in a noticeable improvement in friction coefficient at incipient hydroplaning while others may not, as shown in Section 5.2.5. This is probably the reason why different sources in the literature as shown in Table 5.16 (Horne, 1969; Sugg, 1969; FHWA, 1980; ACI, 1988) present conflicting argument on how longitudinal pavement grooving can improve skid number and hydroplaning potential since the groove dimensions used in their studies have an effect in their final assessment.

For example, Sugg (1969) suggested that the 1- by  $\frac{1}{4}$ - by  $\frac{1}{4}$ -inch (6 mm width by 6 mm depth by 25 mm spacing) transverse pavement grooving at least doubled the friction coefficient of the surface. It was noted that that longitudinal grooving was less effective than transverse grooving, and reducing the pitch of the grooves from 1 inch (25 mm) to  $\frac{3}{4}$  inch (19 mm) appeared to make little difference. With the simulation model, it can be found that the transverse pavement grooving of this particular design has a hydroplaning speed of 194.5 km/h and friction coefficient at incipient hydroplaning of 0.4685, which is twice and four times larger than the hydroplaning speed and friction coefficient at incipient hydroplaning of the plane surface respectively. For the longitudinal pavement grooving, it is noted that the hydroplaning speed is 99.3 km/h and the friction coefficient at incipient hydroplaning is 0.1278 for a 25 mm spacing while the hydroplaning speed is 101.1 km/h and the friction coefficient at incipient hydroplaning is 0.1329 for a 20 mm spacing. This actually quantifies and verifies the observations made in his studies. It also indicates that research in the literature only covers a limited number of designs and does not have the capability of the simulation model to cover a more extensive range to have a more complete understanding of the implications of groove dimensions on hydroplaning.

## **5.7 Summary**

This chapter has described the use of the developed hydroplaning simulation models from the previous two chapters in the study of transverse and longitudinal pavement grooving against hydroplaning, as shown in Figure 2.15 of Chapter 2. The chapter first studies how the transverse and longitudinal orientations of the pavement grooving can affect hydroplaning for three groove designs. Verification of the simulation results have been made against past experimental data and it is shown that the friction factors derived by the proposed simulation model agree with the experimentally measured data. It is also observed that the transverse pavement grooving of the three tested designs give higher hydroplaning speeds and higher friction coefficients at incipient hydroplaning, compared to longitudinal pavement grooving of the similar dimensions, which is similar to major conclusions found in past research. The

numerical values of the friction coefficients at incipient hydroplaning on longitudinally grooved pavement are marginally larger than that of the plane pavement surface and the improvement in friction control is relatively insignificant.

The second part of the chapter sought to evaluate the effects of pavement grooving dimensions on hydroplaning for both the transverse and longitudinal pavement grooving. It is noted that in general, a larger groove width, a larger groove depth and a smaller groove spacing would result in a larger hydroplaning speed and a higher friction coefficient at incipient hydroplaning for both transverse and longitudinal pavement grooving. It is also observed that groove width provides the largest effectiveness indices compared to groove depth and spacing. This indicates that groove width is an important factor in reducing hydroplaning occurrences and could be a primary factor in groove design. Groove depth is the next important factor followed by groove spacing. However, one point to note is that unlike groove width and depth, the range of spacing adopted in practice is typically much larger than that for groove width or depth. This means that in practice, spacing could be a more convenient measure in combating hydroplaning.

For the same pavement groove design, it is noted that transverse pavement grooving consistently gives a higher hydroplaning speed and friction coefficient at incipient hydroplaning as compared to longitudinal pavement grooving. However, it does not mean that longitudinal pavement grooving is not effective in hydroplaning prevention. It is found that certain longitudinal groove design would allow a noticeable improvement in traction control while others may not. This is probably why different sources in the literature have presented conflicting arguments on whether longitudinal pavement grooving can improve skid number and hydroplaning potential, since their conclusions were dependent on the groove dimensions used in their studies. Therefore, the approach of performing numerical simulation is an effective and efficient way to analyze different pavement groove designs in hydroplaning analysis.



**Table 5.1: Description of Various Transversely Grooved Pavement Surfaces tested by Horne and Tanner (1969)**

Pavement Surface	Description	Transverse Pavement Grooving Dimensions			Micro-texture (mm)
		Width (mm)	Depth (mm)	Spacing (mm)	
I	Canvas belt concrete	6.35	6.35	25.4	0.12
II	Burlap drag concrete	6.35	6.35	25.4	0.20
III	Small aggregate concrete (9.53 mm diameter or less)	6.35	6.35	25.4	0.14
IV	Large aggregate concrete (19.05 mm diameter or less)	6.35	6.35	25.4	0.19

**Table 5.2: Pavement Grooving Designs Analyzed**

Grooving Design	Groove Dimensions		
	Width $w$ (mm)	Depth $d$ (mm)	Spacing $s$ (mm)
A	6.35	6.35	25.4
B	3	3	10
C	5	5	45

**Table 5.3: Summary of Simulation Results for Grooving Designs Tested**

Parameter	Transverse Pavement Grooving			Longitudinal Pavement Grooving			Plane Pavement Surface
	Design A	Design B	Design C	Design A	Design B	Design C	
Hydroplaning Speed (km/h)	199.5	156.1	124.4	102.2	90.9	89.6	86.9
Friction Coefficient at Incipient Hydroplaning	0.442	0.294	0.192	0.125	0.111	0.108	0.095
Recovery Factor	0.1190	0.1891	0.3128	0.4630	0.5849	0.6014	0.6440

**Table 5.4: Groove Dimensions Tested**

Centre-to-centre spacing tested (mm)	Groove width tested (mm)	Groove depth tested (mm)
5	2	1, 2, 4, 6, 8, 10
	3	1, 2, 4, 6, 8, 10
	4	1, 2, 4, 6, 8, 10
10	2	1, 2, 4, 6, 8, 10
	4	1, 2, 4, 6, 8, 10
	6	1, 2, 4, 6, 8, 10
	8	1, 2, 4, 6, 8, 10
15	2	1, 2, 4, 6, 8, 10
	4	1, 2, 4, 6, 8, 10
	6	1, 2, 4, 6, 8, 10
	8	1, 2, 4, 6, 8, 10
	10	1, 2, 4, 6, 8, 10
20	2	1, 2, 4, 6, 8, 10
	4	1, 2, 4, 6, 8, 10
	6	1, 2, 4, 6, 8, 10
	8	1, 2, 4, 6, 8, 10
	10	1, 2, 4, 6, 8, 10
25	2	1, 2, 4, 6, 8, 10
	4	1, 2, 4, 6, 8, 10
	6	1, 2, 4, 6, 8, 10
	8	1, 2, 4, 6, 8, 10
	10	1, 2, 4, 6, 8, 10

**Table 5.5: Hydroplaning Speeds and Friction Coefficients of Pavements having Different Transverse Groove Dimensions for Passenger Cars with 186.2 kPa Tire Pressure**

s	w	d	$v_p$	$f$	s	w	d	$v_p$	$f$	s	w	d	$v_p$	$f$
5	2	1	192.43	0.4242	15	2	4	116.32	0.1735	20	6	8	243.87	0.7149
5	2	2	197.45	0.4668	15	2	6	124.09	0.1922	20	6	10	263.00	0.8153
5	2	4	247.64	0.7383	15	2	8	133.41	0.2173	20	8	1	196.00	0.4194
5	2	6	260.35	0.9140	15	2	10	142.57	0.2439	20	8	2	235.84	0.6572
5	2	8	273.61	1.0536	15	4	1	166.88	0.3235	20	8	4	272.29	0.9622
5	2	10	285.84	0.9664	15	4	2	170.99	0.3505	20	8	6	> 300	N.A.
5	3	1	258.50	0.6397	15	4	4	188.05	0.4316	20	8	8	> 300	N.A.
5	3	2	>300	N.A.	15	4	6	206.20	0.5162	20	8	10	> 300	N.A.
5	3	4	>300	N.A.	15	4	8	225.09	0.6099	20	10	1	> 300	N.A.
5	3	6	>300	N.A.	15	4	10	242.67	0.7043	20	10	2	> 300	N.A.
5	3	8	>300	N.A.	15	6	1	206.55	0.4662	20	10	4	> 300	N.A.
5	3	10	>300	N.A.	15	6	2	249.58	0.6760	20	10	6	> 300	N.A.
5	4	1	>300	N.A.	15	6	4	278.64	0.8761	20	10	8	> 300	N.A.
5	4	2	>300	N.A.	15	6	6	> 300	N.A.	20	10	10	> 300	N.A.
5	4	4	>300	N.A.	15	6	8	> 300	N.A.	25	2	1	99.35	0.1361
5	4	6	>300	N.A.	15	6	10	> 300	N.A.	25	2	2	100.76	0.1365
5	4	8	>300	N.A.	15	8	1	251.07	0.6168	25	2	4	103.38	0.1412
5	4	10	>300	N.A.	15	8	2	> 300	N.A.	25	2	6	108.33	0.1544
10	2	1	140.50	0.2394	15	8	4	> 300	N.A.	25	2	8	113.05	0.1672
10	2	2	142.40	0.2489	15	8	6	> 300	N.A.	25	2	10	118.46	0.1751
10	2	4	156.61	0.2985	15	8	8	> 300	N.A.	25	4	1	127.11	0.1978
10	2	6	170.82	0.3528	15	8	10	> 300	N.A.	25	4	2	129.44	0.2101
10	2	8	180.98	0.3919	15	10	1	> 300	N.A.	25	4	4	131.74	0.2254
10	2	10	196.71	0.4549	15	10	2	> 300	N.A.	25	4	6	140.02	0.2501
10	4	1	208.60	0.4609	15	10	4	> 300	N.A.	25	4	8	151.19	0.2843
10	4	2	230.96	0.5953	15	10	6	> 300	N.A.	25	4	10	164.29	0.3298
10	4	4	256.04	0.7667	15	10	8	> 300	N.A.	25	6	1	157.93	0.3073
10	4	6	280.08	0.9307	15	10	10	> 300	N.A.	25	6	2	168.50	0.3443
10	4	8	>300	N.A.	20	2	1	106.37	0.1499	25	6	4	181.35	0.4043
10	4	10	>300	N.A.	20	2	2	108.00	0.1555	25	6	6	194.54	0.4685
10	6	1	270.10	N.A.	20	2	4	111.82	0.1624	25	6	8	203.70	0.5095
10	6	2	>300	0.6915	20	2	6	119.36	0.1798	25	6	10	210.03	0.5376
10	6	4	>300	N.A.	20	2	8	123.38	0.1870	25	8	1	186.01	0.4043
10	6	6	>300	N.A.	20	2	10	141.03	0.2418	25	8	2	208.16	0.5045
10	6	8	>300	N.A.	20	4	1	146.70	0.2609	25	8	4	244.69	0.7117
10	6	10	>300	N.A.	20	4	2	149.44	0.2752	25	8	6	251.72	0.7604
10	8	1	>300	N.A.	20	4	4	156.93	0.3056	25	8	8	253.21	0.7757
10	8	2	>300	N.A.	20	4	6	168.68	0.3491	25	8	10	255.21	0.7866
10	8	4	>300	N.A.	20	4	8	184.02	0.4103	25	10	1	197.99	0.4292
10	8	6	>300	N.A.	20	4	10	196.24	0.4642	25	10	2	262.81	0.7321
10	8	8	>300	N.A.	20	6	1	176.29	0.3638	25	10	4	> 300	N.A.
10	8	10	>300	N.A.	20	6	2	197.34	0.4477	25	10	6	> 300	N.A.
15	2	1	108.08	0.1568	20	6	4	209.66	0.5783	25	10	8	> 300	N.A.
15	2	2	110.12	0.1607	20	6	6	230.57	0.6386	25	10	10	> 300	N.A.

Note: s refers to groove spacing in mm, w refers to groove width in mm, d refers to groove depth in mm,  $v_p$  refers to hydroplaning speed in km/h and  $f$  refers to the friction coefficient at incipient hydroplaning.

**Table 5.6: Effects of Transverse Groove Depth on Hydroplaning Speed and Friction Coefficient****(a) Groove designs of 2 mm groove width and 15 mm center-to-center spacing**

Groove depth (mm)	Predicted hydroplaning speed for 186.2 kPa tire pressure (km/h)	Percent increase over NASA hydroplaning speed for smooth pavement surface	Friction coefficient	Percent increase over friction coefficient at NASA hydroplaning speed
1	108.1	24.95%	0.1568	62.46%
2	110.1	27.30%	0.1607	66.56%
4	116.3	34.48%	0.1735	79.84%
6	124.1	43.46%	0.1922	99.18%
8	133.4	54.23%	0.2173	125.15%
10	142.6	64.82%	0.2439	152.76%

**(b) Groove designs of 4 mm groove width and 15 mm center-to-center spacing**

Groove depth (mm)	Predicted hydroplaning speed for 186.2 kPa tire pressure (km/h)	Percent increase over NASA hydroplaning speed for smooth pavement surface	Friction coefficient	Percent increase over friction coefficient at NASA hydroplaning speed
1	166.9	92.92%	0.3235	235.20%
2	171.0	97.67%	0.3505	263.17%
4	188.1	117.40%	0.4316	347.27%
6	206.2	138.38%	0.5162	434.89%
8	225.1	160.21%	0.6099	532.02%
10	242.7	180.54%	0.7043	629.86%

**(c) Groove designs of 6 mm groove width and 15 mm center-to-center spacing**

Groove depth (mm)	Predicted hydroplaning speed for 186.2 kPa tire pressure (km/h)	Percent increase over NASA hydroplaning speed for smooth pavement surface	Friction coefficient	Percent increase over friction coefficient at NASA hydroplaning speed
1	206.5	138.78%	0.4662	383.09%
2	249.6	188.53%	0.6760	600.49%
4	278.6	222.12%	0.8761	807.92%
6	> 300	N.A.	N.A.	N.A.
8	> 300	N.A.	N.A.	N.A.
10	> 300	N.A.	N.A.	N.A.

**(d) Groove designs of 8 mm groove width and 15 mm center-to-center spacing**

Groove depth (mm)	Predicted hydroplaning speed for 186.2 kPa tire pressure (km/h)	Percent increase over NASA hydroplaning speed for smooth pavement surface	Friction coefficient	Percent increase over friction coefficient at NASA hydroplaning speed
1	251.1	190.25%	0.6168	539.14%
2	> 300	N.A.	N.A.	N.A.
4	> 300	N.A.	N.A.	N.A.
6	> 300	N.A.	N.A.	N.A.
8	> 300	N.A.	N.A.	N.A.
10	> 300	N.A.	N.A.	N.A.

**(e) Groove designs of 10 mm groove width and 15 mm center-to-center spacing**

Groove depth (mm)	Predicted hydroplaning speed for 186.2 kPa tire pressure (km/h)	Percent increase over NASA hydroplaning speed for smooth pavement surface	Friction coefficient	Percent increase over friction coefficient at NASA hydroplaning speed
1	> 300	N.A.	N.A.	N.A.
2	> 300	N.A.	N.A.	N.A.
4	> 300	N.A.	N.A.	N.A.
6	> 300	N.A.	N.A.	N.A.
8	> 300	N.A.	N.A.	N.A.
10	> 300	N.A.	N.A.	N.A.

**Table 5.7: Effects of Transverse Groove Width on Hydroplaning Speed and Friction Coefficient**

<b>(a) Groove designs of 1 mm groove depth and 15 mm center-to-center spacing</b>				
Groove width (mm)	Predicted hydroplaning speed for 186.2 kPa tire pressure (km/h)	Percent increase over NASA hydroplaning speed for smooth pavement surface	Friction coefficient	Percent increase over friction coefficient at NASA hydroplaning speed
2	108.1	24.95%	0.1568	62.46%
4	166.9	92.92%	0.3235	235.20%
6	206.5	138.78%	0.4662	383.09%
8	251.1	190.25%	0.6168	539.14%
10	> 300	N.A.	N.A.	N.A.

<b>(b) Groove designs of 2 mm groove depth and 15 mm center-to-center spacing</b>				
Groove width (mm)	Predicted hydroplaning speed for 186.2 kPa tire pressure (km/h)	Percent increase over NASA hydroplaning speed for smooth pavement surface	Friction coefficient	Percent increase over friction coefficient at NASA hydroplaning speed
2	110.1	27.30%	0.1607	66.56%
4	171.0	97.67%	0.3505	263.17%
6	249.6	188.53%	0.6760	600.49%
8	> 300	N.A.	N.A.	N.A.
10	> 300	N.A.	N.A.	N.A.

<b>(c) Groove designs of 4 mm groove depth and 15 mm center-to-center spacing</b>				
Groove width (mm)	Predicted hydroplaning speed for 186.2 kPa tire pressure (km/h)	Percent increase over NASA hydroplaning speed for smooth pavement surface	Friction coefficient	Percent increase over friction coefficient at NASA hydroplaning speed
2	116.3	34.48%	0.1735	79.84%
4	188.1	117.40%	0.4316	347.27%
6	278.6	222.12%	0.8761	807.92%
8	> 300	N.A.	N.A.	N.A.
10	> 300	N.A.	N.A.	N.A.

<b>(d) Groove designs of 6 mm groove depth and 15 mm center-to-center spacing</b>				
Groove width (mm)	Predicted hydroplaning speed for 186.2 kPa tire pressure (km/h)	Percent increase over NASA hydroplaning speed for smooth pavement surface	Friction coefficient	Percent increase over friction coefficient at NASA hydroplaning speed
2	124.1	43.46%	0.1922	99.18%
4	206.2	138.38%	0.5162	434.89%
6	> 300	N.A.	N.A.	N.A.
8	> 300	N.A.	N.A.	N.A.
10	> 300	N.A.	N.A.	N.A.

<b>(e) Groove designs of 8 mm groove depth and 15 mm center-to-center spacing</b>				
Groove width (mm)	Predicted hydroplaning speed for 186.2 kPa tire pressure (km/h)	Percent increase over NASA hydroplaning speed for smooth pavement surface	Friction coefficient	Percent increase over friction coefficient at NASA hydroplaning speed
2	133.4	54.23%	0.2173	125.15%
4	225.1	160.21%	0.6099	532.02%
6	> 300	N.A.	N.A.	N.A.
8	> 300	N.A.	N.A.	N.A.
10	> 300	N.A.	N.A.	N.A.

<b>(f) Groove designs of 10 mm groove depth and 15 mm center-to-center spacing</b>				
Groove width (mm)	Predicted hydroplaning speed for 186.2 kPa tire pressure (km/h)	Percent increase over NASA hydroplaning speed for smooth pavement surface	Friction coefficient	Percent increase over friction coefficient at NASA hydroplaning speed
2	142.6	64.82%	0.2439	152.76%
4	242.7	180.54%	0.7043	629.86%
6	> 300	N.A.	N.A.	N.A.
8	> 300	N.A.	N.A.	N.A.
10	> 300	N.A.	N.A.	N.A.

**Table 5.8: Effects of Transverse Groove Spacing on Hydroplaning Speed and Friction Coefficient****(a) Groove designs of 2 mm groove width and 1 mm groove depth**

Groove spacing (mm)	Predicted hydroplaning speed for 186.2 kPa tire pressure (km/h)	Percent increase over NASA hydroplaning speed for smooth pavement surface	Friction coefficient	Percent increase over friction coefficient at NASA hydroplaning speed
5	192.4	122.47%	0.4242	339.61%
10	140.5	62.43%	0.2394	148.04%
15	108.1	24.95%	0.1568	62.46%
20	106.4	22.97%	0.1499	55.31%
25	99.3	14.85%	0.1361	41.08%

**(b) Groove designs of 2 mm groove width and 2 mm groove depth**

Groove spacing (mm)	Predicted hydroplaning speed for 186.2 kPa tire pressure (km/h)	Percent increase over NASA hydroplaning speed for smooth pavement surface	Friction coefficient	Percent increase over friction coefficient at NASA hydroplaning speed
5	197.5	128.27%	0.4668	383.70%
10	142.4	64.63%	0.2489	157.91%
15	110.1	27.30%	0.1607	66.56%
20	108.0	24.86%	0.1555	61.19%
25	100.8	16.49%	0.1365	41.42%

**(c) Groove designs of 2 mm groove width and 4 mm groove depth**

Groove spacing (mm)	Predicted hydroplaning speed for 186.2 kPa tire pressure (km/h)	Percent increase over NASA hydroplaning speed for smooth pavement surface	Friction coefficient	Percent increase over friction coefficient at NASA hydroplaning speed
5	247.6	186.29%	0.7383	665.10%
10	156.6	81.05%	0.2985	209.31%
15	116.3	34.48%	0.1735	79.84%
20	111.8	29.27%	0.1624	68.33%
25	103.4	19.51%	0.1412	46.32%

**(d) Groove designs of 2 mm groove width and 6 mm groove depth**

Groove spacing (mm)	Predicted hydroplaning speed for 186.2 kPa tire pressure (km/h)	Percent increase over NASA hydroplaning speed for smooth pavement surface	Friction coefficient	Percent increase over friction coefficient at NASA hydroplaning speed
5	260.4	200.99%	0.9140	847.16%
10	170.8	97.48%	0.3528	265.62%
15	124.1	43.46%	0.1922	99.18%
20	119.4	37.99%	0.1798	86.29%
25	108.3	25.23%	0.1544	60.02%

**(e) Groove designs of 2 mm groove width and 8 mm groove depth**

Groove spacing (mm)	Predicted hydroplaning speed for 186.2 kPa tire pressure (km/h)	Percent increase over NASA hydroplaning speed for smooth pavement surface	Friction coefficient	Percent increase over friction coefficient at NASA hydroplaning speed
5	273.6	216.31%	0.9436	877.82%
10	181.0	109.22%	0.3919	306.15%
15	133.4	54.23%	0.2173	125.15%
20	123.4	42.63%	0.1870	93.83%
25	113.1	30.69%	0.1672	73.24%

**(f) Groove designs of 2 mm groove width and 10 mm groove depth**

Groove spacing (mm)	Predicted hydroplaning speed for 186.2 kPa tire pressure (km/h)	Percent increase over NASA hydroplaning speed for smooth pavement surface	Friction coefficient	Percent increase over friction coefficient at NASA hydroplaning speed
5	285.8	230.46%	0.9664	901.48%
10	196.7	127.41%	0.4549	371.43%
15	142.6	64.82%	0.2439	152.76%
20	141.0	63.04%	0.2418	150.61%
25	118.5	36.95%	0.1751	81.40%

**Table 5.9: Recommended Transverse Tine Dimensions of Various States in U.S.A. (ACPA, 2005)**

State	Min Tine Width	Max Tine Width	Min Tine Depth	Max Tine Depth	Min Tine Spacing	Max Tine Spacing	Random Spacing
AZ	1.60	3.18	2.38	5.56	12.70	25.40	Yes
AR	3.18	3.18	3.18	4.76	12.70	19.05	No
CO	2.38	3.18	3.18	4.76	19.05	19.05	No
CT	2.03	2.03	3.18	6.35	12.70	12.70	No
DE	2.38	4.76	3.18	4.76	12.70	12.70	No
FL	2.03	3.05	2.54	3.81	12.70	12.70	No
GA	2.03	2.03	0.89	0.89	12.70	12.70	No
HI	2.39	2.39	3.96	3.96	19.05	19.05	No
ID	3.18	3.18	3.18	3.18	19.05	25.40	Yes
IL	1.91	1.91	3.18	3.18	19.05	19.05	No
IN	2.29	3.30	3.05	4.83	12.70	31.75	No
IA	3.18	3.18	3.18	4.76	N.A.	N.A.	Yes
KS	4.76	4.76	3.18	3.18	19.05	19.05	No
KY	2.00	3.00	3.00	4.50	7.50	25.00	Yes
LA	3.18	3.18	4.76	4.76	12.70	12.70	No
MI	3.18	3.18	6.35	6.35	12.70	12.70	Yes
MN	3.18	3.18	3.18	3.18	15.88	25.40	Yes
MS	N.A.	N.A.	2.38	3.96	12.70	12.70	No
MO	2.54	3.18	3.18	3.18	12.70	12.70	No
MT	2.03	2.03	3.18	4.76	19.05	19.05	No
NE	3.18	3.18	3.18	3.18	10.16	20.32	No
NV	2.39	3.18	3.18	6.35	30.48	30.48	No
NY	4.76	4.76	6.35	6.35	N.A.	N.A.	Yes
NC	2.03	3.05	3.81	6.35	12.70	19.05	Yes
ND	3.18	3.18	3.18	3.18	25.40	25.40	Yes
OK	2.03	3.18	3.18	6.35	12.70	25.40	No
OR	3.18	3.18	3.18	6.35	12.70	31.75	Yes
PA	2.38	4.76	3.18	4.76	9.53	19.05	No
PR	3.18	3.18	4.76	4.76	19.05	19.05	No
SC	2.54	2.54	3.18	3.18	12.70	12.70	No
TN	0.25	0.76	3.05	4.83	7.62	25.40	Yes
TX	2.11	2.11	4.76	4.76	N.A.	N.A.	Yes
UT	1.59	2.22	2.38	3.97	12.70	25.40	Yes
VA	3.18	3.18	8.38	8.38	19.05	19.05	No
WA	1.27	1.27	5.08	5.08	12.70	31.75	Yes
WI	3.18	3.18	6.35	6.35	9.53	38.10	Yes
WY	3.18	3.18	4.76	4.76	19.05	25.40	Yes

**Table 5.10: Hydroplaning Speeds for Different Transverse Groove Dimensions and Tire Pressures**

s	w	d	$P_t$	$v_p$	s	w	d	$P_t$	$v_p$	s	w	d	$p_t$	$v_p$
5	2	2	100	144.70	15	4	2	100	125.31	20	8	2	100	172.83
5	2	2	200	204.64	15	4	2	200	177.21	20	8	2	200	244.42
5	2	2	300	250.63	15	4	2	300	217.03	20	8	2	300	299.35
5	2	4	100	181.48	15	4	4	100	137.81	20	8	4	100	261.58
5	2	4	200	256.66	15	4	4	200	194.89	20	8	4	200	> 300
5	2	4	300	> 300	15	4	4	300	238.70	20	8	4	300	> 300
5	2	6	100	190.80	15	4	6	100	151.11	20	8	6	100	> 300
5	2	6	200	269.83	15	4	6	200	213.70	20	10	6	200	> 300
5	2	6	300	> 300	15	4	6	300	261.73	20	10	6	300	> 300
5	4	2	100	283.24	15	6	2	100	182.90	20	10	2	100	237.51
5	4	2	200	> 300	15	6	2	200	258.66	20	10	2	200	> 300
5	4	2	300	> 300	15	6	2	300	316.79	20	10	2	300	> 300
5	4	4	100	> 300	15	6	4	100	204.20	20	10	4	100	> 300
5	4	4	200	> 300	15	6	4	200	288.78	20	10	4	200	> 300
5	4	4	300	> 300	15	6	4	300	> 300	20	10	4	300	> 300
5	4	6	100	> 300	15	6	6	100	223.17	20	10	6	100	> 300
5	4	6	200	> 300	15	6	6	200	> 300	20	8	6	200	> 300
5	4	6	300	> 300	15	6	6	300	> 300	20	8	6	300	> 300
10	2	2	100	104.36	15	8	2	100	245.92	25	2	2	100	73.84
10	2	2	200	147.59	15	8	2	200	> 300	25	2	2	200	104.43
10	2	2	300	180.76	15	8	2	300	> 300	25	2	2	300	127.90
10	2	4	100	114.77	15	8	4	100	291.76	25	2	4	100	75.76
10	2	4	200	162.31	15	8	4	200	> 300	25	2	4	200	107.14
10	2	4	300	198.78	15	8	4	300	> 300	25	2	4	300	131.22
10	2	6	100	125.18	15	8	6	100	291.81	25	2	6	100	79.39
10	2	6	200	177.03	15	8	6	200	> 300	25	2	6	200	112.27
10	2	6	300	216.82	15	8	6	300	> 300	25	2	6	300	137.50
10	4	2	100	169.26	15	10	2	100	> 300	25	4	2	100	94.86
10	4	2	200	239.37	15	10	2	200	> 300	25	4	2	200	134.15
10	4	2	300	293.16	15	10	2	300	> 300	25	4	2	300	164.30
10	4	4	100	187.63	15	10	4	100	> 300	25	4	4	100	96.55
10	4	4	200	265.35	15	10	4	200	> 300	25	4	4	200	136.54
10	4	4	300	> 300	15	10	4	300	> 300	25	4	4	300	167.22
10	4	6	100	205.26	15	10	6	100	> 300	25	4	6	100	102.61
10	4	6	200	290.28	15	10	6	200	> 300	25	4	6	200	145.11
10	4	6	300	> 300	15	10	6	300	> 300	25	4	6	300	177.73
10	6	2	100	265.46	20	2	2	100	79.15	25	6	2	100	123.49
10	6	2	200	> 300	20	2	2	200	111.93	25	6	2	200	174.64
10	6	2	300	> 300	20	2	2	300	137.09	25	6	2	300	213.89
10	6	4	100	293.81	20	2	4	100	81.94	25	6	4	100	132.90
10	6	4	200	> 300	20	2	4	200	115.89	25	6	4	200	187.95
10	6	4	300	> 300	20	2	4	300	141.93	25	6	4	300	230.19
10	6	6	100	> 300	20	2	6	100	87.47	25	6	6	100	142.57
10	6	6	200	> 300	20	2	6	200	123.71	25	6	6	200	201.62
10	6	6	300	> 300	20	2	6	300	151.51	25	6	6	300	246.93
10	8	2	100	> 300	20	4	2	100	109.51	25	8	2	100	152.55
10	8	2	200	> 300	20	4	2	200	154.88	25	8	2	200	215.74
10	8	2	300	> 300	20	4	2	300	189.68	25	8	2	300	264.23
10	8	4	100	> 300	20	4	4	100	115.00	25	8	4	100	179.32
10	8	4	200	> 300	20	4	4	200	162.64	25	8	4	200	253.60
10	8	4	300	> 300	20	4	4	300	199.19	25	8	4	300	> 300
10	8	6	100	> 300	20	4	6	100	123.61	25	8	6	100	184.47
10	8	6	200	> 300	20	4	6	200	174.82	25	8	6	200	260.88
10	8	6	300	> 300	20	4	6	300	214.11	25	8	6	300	> 300
15	2	2	100	83.64	20	6	2	100	144.62	25	10	2	100	192.60
15	2	2	200	118.29	20	6	2	200	204.52	25	10	2	200	272.37
15	2	2	300	144.88	20	6	2	300	250.48	25	10	2	300	> 300
15	2	4	100	93.42	20	6	4	100	153.65	25	10	4	100	220.13
15	2	4	200	132.12	20	6	4	200	217.29	25	10	4	200	> 300
15	2	4	300	161.82	20	6	4	300	266.13	25	10	4	300	> 300
15	2	6	100	100.22	20	6	6	100	168.97	25	10	6	100	236.04
15	2	6	200	141.73	20	6	6	200	238.96	25	10	6	200	> 300
15	2	6	300	173.58	20	6	6	300	292.67	25	10	6	300	> 300

Note: s refers to groove spacing in mm, w refers to groove width in mm, d refers to groove depth in mm,  $p_t$  refers to tire pressure in kPa,  $v_p$  refers to hydroplaning speed in km/h.



**TABLE 5.11: Hydroplaning Speeds and Friction Coefficients of Pavements having Different Longitudinal Groove Dimensions for Passenger Cars with 186.2 kPa Tire Pressure**

s	w	d	$v_p$	$f$	s	w	d	$v_p$	$f$	s	w	d	$v_p$	$f$
5	2	1	89.05	0.1014	15	2	4	91.55	0.1072	20	6	8	105.70	0.1464
5	2	2	91.94	0.1078	15	2	6	93.77	0.1094	20	6	10	109.33	0.1580
5	2	4	98.61	0.1242	15	2	8	95.93	0.1180	20	8	1	92.66	0.1041
5	2	6	105.01	0.1410	15	2	10	97.93	0.1233	20	8	2	97.44	0.1147
5	2	8	108.79	0.1522	15	4	1	87.43	0.0987	20	8	4	104.63	0.1330
5	2	10	114.51	0.1696	15	4	2	90.83	0.1058	20	8	6	109.94	0.1490
5	3	1	90.34	0.1043	15	4	4	95.57	0.1172	20	8	8	115.84	0.1663
5	3	2	95.77	0.1170	15	4	6	100.20	0.1294	20	8	10	120.54	0.1820
5	3	4	104.75	0.1413	15	4	8	104.29	0.1410	20	10	1	97.36	0.1144
5	3	6	113.62	0.1679	15	4	10	108.71	0.1541	20	10	2	103.03	0.1273
5	3	8	116.76	0.1790	15	6	1	90.43	0.1060	20	10	4	109.37	0.1442
5	3	10	119.74	0.1901	15	6	2	94.53	0.1152	20	10	6	115.55	0.1631
5	4	1	91.03	0.1064	15	6	4	99.12	0.1275	20	10	8	121.39	0.1826
5	4	2	98.20	0.1241	15	6	6	105.51	0.1458	20	10	10	130.45	0.2109
5	4	4	106.95	0.1496	15	6	8	111.41	0.1643	25	2	1	87.04	0.0966
5	4	6	117.71	0.1840	15	6	10	116.79	0.1825	25	2	2	87.17	0.0968
5	4	8	122.14	0.2012	15	8	1	96.88	0.1137	25	2	4	89.81	0.1031
5	4	10	129.06	0.2280	15	8	2	102.37	0.1267	25	2	6	91.53	0.1072
10	2	1	87.39	0.0981	15	8	4	109.52	0.1464	25	2	8	92.82	0.1105
10	2	2	90.34	0.1042	15	8	6	116.27	0.1683	25	2	10	94.13	0.1139
10	2	4	93.23	0.1109	15	8	8	123.33	0.1907	25	4	1	87.26	0.0973
10	2	6	96.68	0.1217	15	8	10	129.52	0.2135	25	4	2	88.25	0.0995
10	2	8	103.01	0.1351	15	10	1	102.81	0.1274	25	4	4	92.42	0.1096
10	2	10	103.40	0.1368	15	10	2	104.28	0.1314	25	4	6	95.24	0.1167
10	4	1	88.37	0.1009	15	10	4	115.22	0.1615	25	4	8	97.99	0.1239
10	4	2	92.55	0.1100	15	10	6	123.36	0.1880	25	4	10	100.54	0.1310
10	4	4	99.29	0.1269	15	10	8	131.23	0.2172	25	6	1	89.13	0.1022
10	4	6	105.91	0.1453	15	10	10	141.12	0.2531	25	6	2	91.07	0.1067
10	4	8	111.83	0.1634	20	2	1	87.23	0.0978	25	6	4	95.57	0.1172
10	4	10	117.38	0.1817	20	2	2	88.74	0.1010	25	6	6	99.29	0.1278
10	6	1	96.45	0.1204	20	2	4	90.65	0.1052	25	6	8	103.19	0.1386
10	6	2	100.14	0.1294	20	2	6	92.25	0.1090	25	6	10	107.04	0.1499
10	6	4	105.46	0.1448	20	2	8	93.57	0.1129	25	8	1	89.85	0.1055
10	6	6	114.46	0.1730	20	2	10	95.60	0.1174	25	8	2	91.77	0.1085
10	6	8	124.16	0.2056	20	4	1	87.28	0.0990	25	8	4	97.99	0.1235
10	6	10	129.83	0.2293	20	4	2	90.25	0.1047	25	8	6	103.67	0.1390
10	8	1	102.50	0.1297	20	4	4	93.13	0.1115	25	8	8	108.94	0.1544
10	8	2	105.99	0.1365	20	4	6	96.69	0.1204	25	8	10	113.21	0.1684
10	8	4	116.33	0.1675	20	4	8	99.60	0.1284	25	10	1	90.76	0.1078
10	8	6	127.31	0.2045	20	4	10	103.23	0.1387	25	10	2	93.61	0.1124
10	8	8	137.07	0.2420	20	6	1	89.88	0.1066	25	10	4	100.51	0.1300
10	8	10	145.30	0.2773	20	6	2	92.50	0.1107	25	10	6	107.96	0.1506
15	2	1	87.30	0.0979	20	6	4	96.16	0.1196	25	10	8	114.79	0.1711
15	2	2	88.89	0.1011	20	6	6	101.09	0.1329	25	10	10	119.30	0.1878

Note:  $s$  refers to groove spacing in mm,  $w$  refers to groove width in mm,  $d$  refers to groove depth in mm,  $v_p$  refers to hydroplaning speed in km/h and  $f$  refers to the friction coefficient at incipient hydroplaning.

**Table 5.12: Effects of Longitudinal Groove Depth on Hydroplaning Speed and Friction Coefficient****(a) Groove designs of 2 mm groove width and 20 mm center-to-center spacing**

Groove depth (mm)	Predicted hydroplaning speed for 186.2 kPa tire pressure (km/h)	Percent increase over NASA hydroplaning speed for smooth pavement surface	Friction coefficient	Percent increase over friction coefficient at NASA hydroplaning speed
1	87.23	0.84%	0.0978	1.35%
2	88.74	2.59%	0.1010	4.66%
4	90.65	4.80%	0.1052	9.02%
6	92.25	6.65%	0.1090	12.95%
8	93.57	8.17%	0.1129	16.99%
10	95.60	10.52%	0.1174	21.66%

**(b) Groove designs of 4 mm groove width and 20 mm center-to-center spacing**

Groove depth (mm)	Predicted hydroplaning speed for 186.2 kPa tire pressure (km/h)	Percent increase over NASA hydroplaning speed for smooth pavement surface	Friction coefficient	Percent increase over friction coefficient at NASA hydroplaning speed
1	87.28	0.90%	0.0990	2.59%
2	90.25	4.34%	0.1047	8.50%
4	93.13	7.66%	0.1115	15.54%
6	96.69	11.78%	0.1204	24.77%
8	99.60	15.14%	0.1284	33.06%
10	103.23	19.34%	0.1387	43.73%

**(c) Groove designs of 6 mm groove width and 20 mm center-to-center spacing**

Groove depth (mm)	Predicted hydroplaning speed for 186.2 kPa tire pressure (km/h)	Percent increase over NASA hydroplaning speed for smooth pavement surface	Friction coefficient	Percent increase over friction coefficient at NASA hydroplaning speed
1	89.88	3.91%	0.1066	10.47%
2	92.50	6.94%	0.1107	14.72%
4	96.16	11.17%	0.1196	23.94%
6	101.09	16.87%	0.1329	37.72%
8	105.70	22.20%	0.1464	51.71%
10	109.33	26.39%	0.1580	63.73%

**(d) Groove designs of 8 mm groove width and 20 mm center-to-center spacing**

Groove depth (mm)	Predicted hydroplaning speed for 186.2 kPa tire pressure (km/h)	Percent increase over NASA hydroplaning speed for smooth pavement surface	Friction coefficient	Percent increase over friction coefficient at NASA hydroplaning speed
1	92.66	7.12%	0.1041	7.88%
2	97.44	12.65%	0.1147	18.86%
4	104.63	20.96%	0.1330	37.82%
6	109.94	27.10%	0.1490	54.40%
8	115.84	33.92%	0.1663	72.33%
10	120.54	39.35%	0.1820	88.60%

**(e) Groove designs of 10 mm groove width and 20 mm center-to-center spacing**

Groove depth (mm)	Predicted hydroplaning speed for 186.2 kPa tire pressure (km/h)	Percent increase over NASA hydroplaning speed for smooth pavement surface	Friction coefficient	Percent increase over friction coefficient at NASA hydroplaning speed
1	97.36	12.55%	0.1144	18.55%
2	103.03	19.11%	0.1273	31.92%
4	109.37	26.44%	0.1442	49.43%
6	115.55	33.58%	0.1631	69.02%
8	121.39	40.34%	0.1826	89.22%
10	130.45	50.81%	0.2109	118.55%

**Table 5.13: Effects of Longitudinal Groove Width on Hydroplaning Speed and Friction Coefficient****(a) Groove designs of 1 mm groove depth and 20 mm center-to-center spacing**

Groove width (mm)	Predicted hydroplaning speed for 186.2 kPa tire pressure (km/h)	Percent increase over NASA hydroplaning speed for smooth pavement surface	Friction coefficient	Percent increase over friction coefficient at NASA hydroplaning speed
2	87.23	0.84%	0.0978	1.35%
4	87.28	0.90%	0.0990	2.59%
6	89.88	3.91%	0.1066	10.47%
8	92.66	7.12%	0.1041	7.88%
10	97.36	12.55%	0.1144	18.55%

**(b) Groove designs of 2 mm groove depth and 20 mm center-to-center spacing**

Groove width (mm)	Predicted hydroplaning speed for 186.2 kPa tire pressure (km/h)	Percent increase over NASA hydroplaning speed for smooth pavement surface	Friction coefficient	Percent increase over friction coefficient at NASA hydroplaning speed
2	88.74	2.59%	0.1010	4.66%
4	90.25	4.34%	0.1047	8.50%
6	92.50	6.94%	0.1107	14.72%
8	97.44	12.65%	0.1147	18.86%
10	103.03	19.11%	0.1273	31.92%

**(c) Groove designs of 4 mm groove depth and 20 mm center-to-center spacing**

Groove width (mm)	Predicted hydroplaning speed for 186.2 kPa tire pressure (km/h)	Percent increase over NASA hydroplaning speed for smooth pavement surface	Friction coefficient	Percent increase over friction coefficient at NASA hydroplaning speed
2	90.65	4.80%	0.1052	9.02%
4	93.13	7.66%	0.1115	15.54%
6	96.16	11.17%	0.1196	23.94%
8	104.63	20.96%	0.1330	37.82%
10	109.37	26.44%	0.1442	49.43%

**(d) Groove designs of 6 mm groove depth and 20 mm center-to-center spacing**

Groove width (mm)	Predicted hydroplaning speed for 186.2 kPa tire pressure (km/h)	Percent increase over NASA hydroplaning speed for smooth pavement surface	Friction coefficient	Percent increase over friction coefficient at NASA hydroplaning speed
2	92.25	6.65%	0.1090	12.95%
4	96.69	11.78%	0.1204	24.77%
6	101.09	16.87%	0.1329	37.72%
8	109.94	27.10%	0.1490	54.40%
10	115.55	33.58%	0.1631	69.02%

**(e) Groove designs of 8 mm groove depth and 20 mm center-to-center spacing**

Groove width (mm)	Predicted hydroplaning speed for 186.2 kPa tire pressure (km/h)	Percent increase over NASA hydroplaning speed for smooth pavement surface	Friction coefficient	Percent increase over friction coefficient at NASA hydroplaning speed
2	93.57	8.17%	0.1129	16.99%
4	99.60	15.14%	0.1284	33.06%
6	105.70	22.20%	0.1464	51.71%
8	115.84	33.92%	0.1663	72.33%
10	121.39	40.34%	0.1826	89.22%

**(f) Groove designs of 10 mm groove depth and 20 mm center-to-center spacing**

Groove width (mm)	Predicted hydroplaning speed for 186.2 kPa tire pressure (km/h)	Percent increase over NASA hydroplaning speed for smooth pavement surface	Friction coefficient	Percent increase over friction coefficient at NASA hydroplaning speed
2	95.60	10.52%	0.1174	21.66%
4	103.23	19.34%	0.1387	43.73%
6	109.33	26.39%	0.1580	63.73%
8	120.54	39.35%	0.1820	88.60%
10	130.45	50.81%	0.2109	118.55%

**Table 5.14: Effects of Longitudinal Groove Spacing on Hydroplaning Speed and Friction Coefficient**

<b>(a) Groove designs of 2 mm groove width and 1 mm groove depth</b>				
Groove spacing (mm)	Predicted hydroplaning speed for 186.2 kPa tire pressure (km/h)	Percent increase over NASA hydroplaning speed for smooth pavement surface	Friction coefficient	Percent increase over friction coefficient at NASA hydroplaning speed
5	89.05	2.95%	0.1014	5.08%
10	87.39	1.03%	0.0981	1.66%
15	87.30	0.92%	0.0979	1.45%
20	87.23	0.84%	0.0978	1.35%
25	87.04	0.62%	0.0966	0.10%

<b>(b) Groove designs of 2 mm groove width and 2 mm groove depth</b>				
Groove spacing (mm)	Predicted hydroplaning speed for 186.2 kPa tire pressure (km/h)	Percent increase over NASA hydroplaning speed for smooth pavement surface	Friction coefficient	Percent increase over friction coefficient at NASA hydroplaning speed
5	91.94	6.29%	0.1078	11.71%
10	90.34	4.44%	0.1042	7.98%
15	88.89	2.76%	0.1011	4.77%
20	88.74	2.59%	0.1010	4.66%
25	87.17	0.77%	0.0968	0.31%

<b>(c) Groove designs of 2 mm groove width and 4 mm groove depth</b>				
Groove spacing (mm)	Predicted hydroplaning speed for 186.2 kPa tire pressure (km/h)	Percent increase over NASA hydroplaning speed for smooth pavement surface	Friction coefficient	Percent increase over friction coefficient at NASA hydroplaning speed
5	98.61	14.00%	0.1242	28.70%
10	93.23	7.78%	0.1109	14.92%
15	91.55	5.84%	0.1072	11.09%
20	90.65	4.80%	0.1052	9.02%
25	89.81	3.83%	0.1031	6.84%

<b>(d) Groove designs of 2 mm groove width and 6 mm groove depth</b>				
Groove spacing (mm)	Predicted hydroplaning speed for 186.2 kPa tire pressure (km/h)	Percent increase over NASA hydroplaning speed for smooth pavement surface	Friction coefficient	Percent increase over friction coefficient at NASA hydroplaning speed
5	105.01	21.40%	0.1410	46.11%
10	96.69	11.78%	0.1217	26.11%
15	93.77	8.40%	0.1094	13.37%
20	92.25	6.65%	0.1090	12.95%
25	91.53	5.82%	0.1072	11.09%

<b>(e) Groove designs of 2 mm groove width and 8 mm groove depth</b>				
Groove spacing (mm)	Predicted hydroplaning speed for 186.2 kPa tire pressure (km/h)	Percent increase over NASA hydroplaning speed for smooth pavement surface	Friction coefficient	Percent increase over friction coefficient at NASA hydroplaning speed
5	108.79	25.77%	0.1522	57.72%
10	103.01	19.09%	0.1351	40.00%
15	95.93	10.90%	0.1180	22.28%
20	93.57	8.17%	0.1129	16.99%
25	92.82	7.31%	0.1105	14.51%

<b>(f) Groove designs of 2 mm groove width and 10 mm groove depth</b>				
Groove spacing (mm)	Predicted hydroplaning speed for 186.2 kPa tire pressure (km/h)	Percent increase over NASA hydroplaning speed for smooth pavement surface	Friction coefficient	Percent increase over friction coefficient at NASA hydroplaning speed
5	114.51	32.38%	0.1696	75.75%
10	103.40	19.54%	0.1368	41.76%
15	97.93	13.21%	0.1233	27.77%
20	95.60	10.52%	0.1174	21.66%
25	94.13	8.82%	0.1139	18.03%

**Table 5.15: Hydroplaning Speeds for Different Longitudinal Groove Dimensions and Tire Pressures**

s	w	d	$p_t$	$v_p$	s	w	d	$p_t$	$v_p$	s	w	d	$p_t$	$v_p$
5	2	2	100	67.39	15	4	2	100	66.58	20	8	2	100	71.43
5	2	2	200	95.31	15	4	2	200	94.16	20	8	2	200	101.01
5	2	2	300	116.73	15	4	2	300	115.33	20	8	2	300	123.71
5	2	4	100	72.28	15	4	4	100	70.06	20	8	4	100	76.70
5	2	4	200	102.22	15	4	4	200	99.08	20	8	4	200	108.46
5	2	4	300	125.20	15	4	4	300	121.34	20	8	4	300	132.84
5	2	6	100	76.98	15	4	6	100	73.45	20	8	6	100	80.59
5	2	6	200	108.87	15	4	6	200	103.88	20	10	6	200	113.97
5	2	6	300	133.33	15	4	6	300	127.22	20	10	6	300	139.58
5	4	2	100	71.98	15	6	2	100	69.29	20	10	2	100	75.52
5	4	2	200	101.80	15	6	2	200	97.99	20	10	2	200	106.81
5	4	2	300	124.68	15	6	2	300	120.02	20	10	2	300	130.81
5	4	4	100	78.40	15	6	4	100	72.66	20	10	4	100	80.17
5	4	4	200	110.87	15	6	4	200	102.76	20	10	4	200	113.38
5	4	4	300	135.79	15	6	4	300	125.85	20	10	4	300	138.86
5	4	6	100	86.28	15	6	6	100	77.34	20	10	6	100	84.70
5	4	6	200	122.02	15	6	6	200	109.38	20	8	6	200	119.79
5	4	6	300	149.45	15	6	6	300	133.97	20	8	6	300	146.71
10	2	2	100	66.22	15	8	2	100	75.04	25	2	2	100	63.90
10	2	2	200	93.65	15	8	2	200	106.12	25	2	2	200	90.36
10	2	2	300	114.70	15	8	2	300	129.97	25	2	2	300	110.67
10	2	4	100	68.34	15	8	4	100	80.28	25	2	4	100	65.83
10	2	4	200	96.65	15	8	4	200	113.54	25	2	4	200	93.10
10	2	4	300	118.37	15	8	4	300	139.05	25	2	4	300	114.02
10	2	6	100	70.87	15	8	6	100	85.23	25	2	6	100	67.09
10	2	6	200	100.23	15	8	6	200	120.54	25	2	6	200	94.88
10	2	6	300	122.76	15	8	6	300	147.63	25	2	6	300	116.21
10	4	2	100	66.58	15	10	2	100	76.44	25	4	2	100	64.69
10	4	2	200	94.16	15	10	2	200	108.11	25	4	2	200	91.49
10	4	2	300	115.33	15	10	2	300	132.40	25	4	2	300	112.05
10	4	4	100	72.79	15	10	4	100	84.46	25	4	4	100	67.75
10	4	4	200	102.93	15	10	4	200	119.45	25	4	4	200	95.81
10	4	4	300	126.07	15	10	4	300	146.29	25	4	4	300	117.34
10	4	6	100	77.63	15	10	6	100	90.43	25	4	6	100	69.82
10	4	6	200	109.79	15	10	6	200	127.89	25	4	6	200	98.73
10	4	6	300	134.46	15	10	6	300	156.63	25	4	6	300	120.92
10	6	2	100	73.40	20	2	2	100	65.05	25	6	2	100	66.76
10	6	2	200	103.81	20	2	2	200	91.99	25	6	2	200	94.41
10	6	2	300	127.14	20	2	2	300	112.66	25	6	2	300	115.63
10	6	4	100	77.30	20	2	4	100	66.45	25	6	4	100	70.06
10	6	4	200	109.32	20	2	4	200	93.97	25	6	4	200	99.08
10	6	4	300	133.89	20	2	4	300	115.09	25	6	4	300	121.35
10	6	6	100	83.90	20	2	6	100	67.62	25	6	6	100	72.78
10	6	6	200	118.66	20	2	6	200	95.63	25	6	6	200	102.93
10	6	6	300	145.33	20	2	6	300	117.12	25	6	6	300	126.06
10	8	2	100	77.69	20	4	2	100	66.16	25	8	2	100	67.27
10	8	2	200	109.87	20	4	2	200	93.56	25	8	2	200	95.14
10	8	2	300	134.57	20	4	2	300	114.59	25	8	2	300	116.52
10	8	4	100	85.28	20	4	4	100	68.27	25	8	4	100	71.83
10	8	4	200	120.60	20	4	4	200	96.54	25	8	4	200	101.58
10	8	4	300	147.71	20	4	4	300	118.24	25	8	4	300	124.42
10	8	6	100	93.33	20	4	6	100	70.87	25	8	6	100	76.00
10	8	6	200	131.98	20	4	6	200	100.23	25	8	6	200	107.48
10	8	6	300	161.64	20	4	6	300	122.76	25	8	6	300	131.63
15	2	2	100	65.16	20	6	2	100	67.81	25	10	2	100	68.62
15	2	2	200	92.15	20	6	2	200	95.90	25	10	2	200	97.04
15	2	2	300	112.86	20	6	2	300	117.45	25	10	2	300	118.85
15	2	4	100	67.11	20	6	4	100	70.49	25	10	4	100	73.68
15	2	4	200	94.91	20	6	4	200	99.69	25	10	4	200	104.20
15	2	4	300	116.24	20	6	4	300	122.09	25	10	4	300	127.62
15	2	6	100	68.74	20	6	6	100	74.10	25	10	6	100	79.14
15	2	6	200	97.21	20	6	6	200	104.80	25	10	6	200	111.92
15	2	6	300	119.06	20	6	6	300	128.35	25	10	6	300	137.07

Note: s refers to groove spacing in mm, w refers to groove width in mm, d refers to groove depth in mm,  $p_t$  refers to tire pressure in kPa,  $v_p$  refers to hydroplaning speed in km/h

**Table 5.16: Findings from Selected Past Research on Transverse and Longitudinal Pavement Grooving**

Literature Source	Main Findings
Yager (1969)	"...braking friction coefficient levels obtained on the (transverse-) grooved runway surfaces are substantially higher than those obtained on the similar ungrooved surfaces throughout the test speed range..."
Sugg (1969)	"... The Miles Trailer showed the transversely grooved concrete to be superior to longitudinal grooves (in terms of braking force coefficient)..." "...All three test vehicles demonstrated that the 1- by ¼- by ¼-inch grooving at least doubled the (effective) friction coefficient of the surfaces. Longitudinal grooving was less effective than lateral, and reducing the pitch of the grooves from 1 inch to ¾ inch appeared to make little difference..."
Horne (1969)	"Placing 1 x ¼ x ¼ inch transverse grooves in pavement raises the skid resistance of surfaces..." "... The results from highway (longitudinal) grooving (1 x ¼ x ¼ inch) in California have provided the researcher an exasperating paradox. On every highway where the grooves are installed, vehicle accident rates under wet pavement conditions fell dramatically. Yet skid resistance before and after grooving showed very little difference in friction coefficient..."
Mosher (1969)	"... Longitudinal pavement grooving is seen to be very effective in eliminating wet-weather accidents where before and after records are available, even though the coefficient of friction is not significantly increased by this process..." "...Transverse grooves in concrete highways are used primarily at intersections. They decrease the stopping distance on slippery pavement by improving drainage and increasing the coefficient of friction..."
Federal Highway Administration (1980)	"...Both longitudinal and transverse grooves has been used in the United States, but longitudinal grooves are more common...Grooving acts like other form of macrotexture in reducing the potential of hydroplaning. However, despite its proven accident reduction effectiveness, longitudinal grooving does not normally increase the skid number...There is some indication that transverse grooving may increase the skid number..."
America Concrete Institute (1988)	"...The results of testing with a standard skid-tester indicate that transverse texture produce higher friction number than longitudinal textures..." "...Transverse provides a path perpendicular to the direction of travel for the escape of water under the tire which is an important factor in reducing hydroplaning..."
Highway Research Board (1972)	"...Grooving is a technique of altering an existing pavement surface to greatly increase its texture, thereby facilitating the displacement of water by the tires. It is used most often at locations where hydroplaning or wet-skidding accidents at high speeds are a problem...Grooves are either cut transversely or longitudinally...Accident experience attests to the effectiveness of (longitudinal) grooves in pavements...The skid numbers, as measured by locked wheel testers with water applied at the rate prescribed by ASTM E-274, do not show a significant increase..."
Pennsylvania Transportation Institute (1988)	"...Longitudinal grooving reduces wet weather accidents; although the skid resistance as measured in the conventional manner does not increase significantly...The grooves provide an escape for water at the tire pavement interface, reducing hydroplaning..."
American Concrete Pavement Association (2000)	"...Surface channels or grooves allow water to escape from beneath the tire to reduce hydroplaning..." "...Diamond grooving provides deep channels to hold water and excellent lateral control...Pioneering work in Caltrans showed that a reduction in accident rates of 85% after grooving high accidents locations at 14 sites near Los Angeles..."

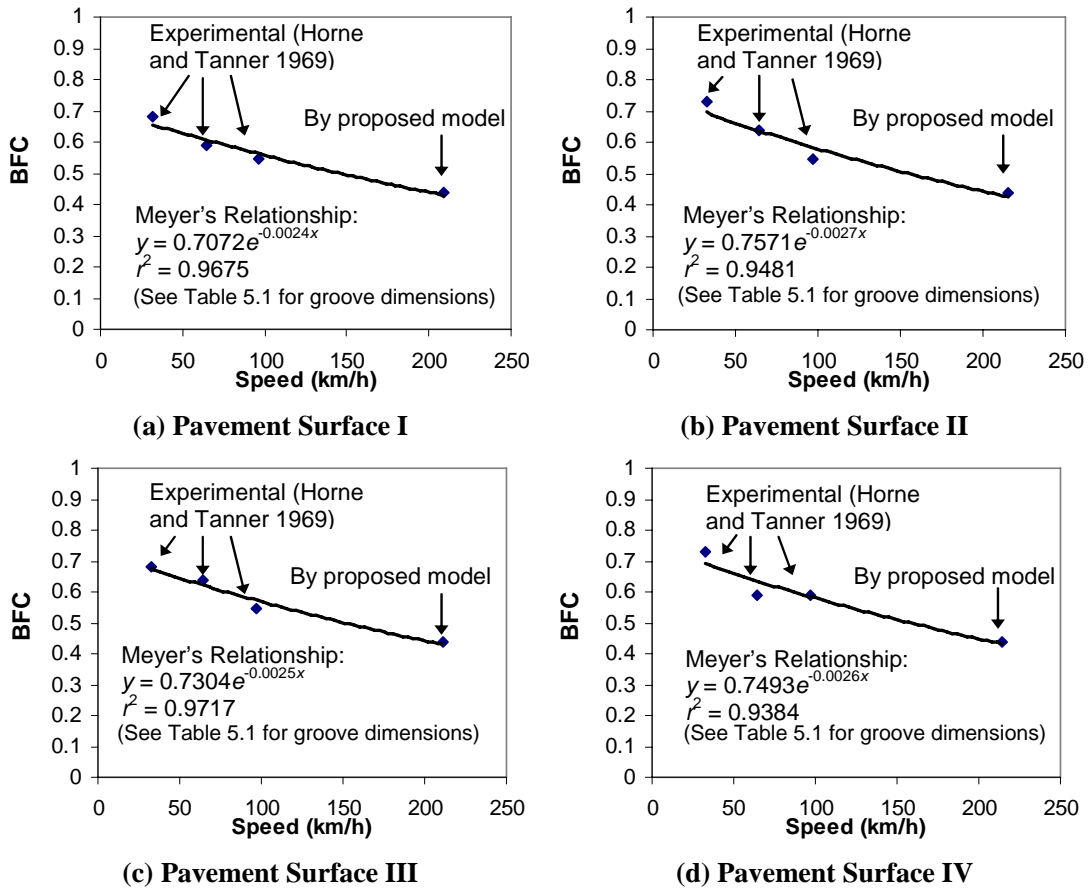


Figure 5.1: Meyer's relationship for experimentally measured data by Horne and Tanner (1969) and predicted points by proposed model

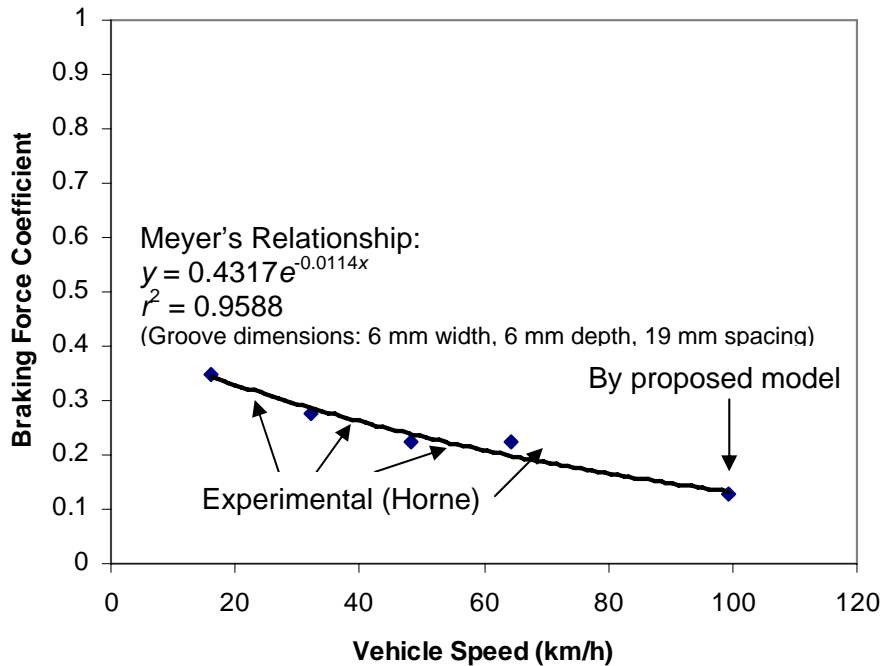
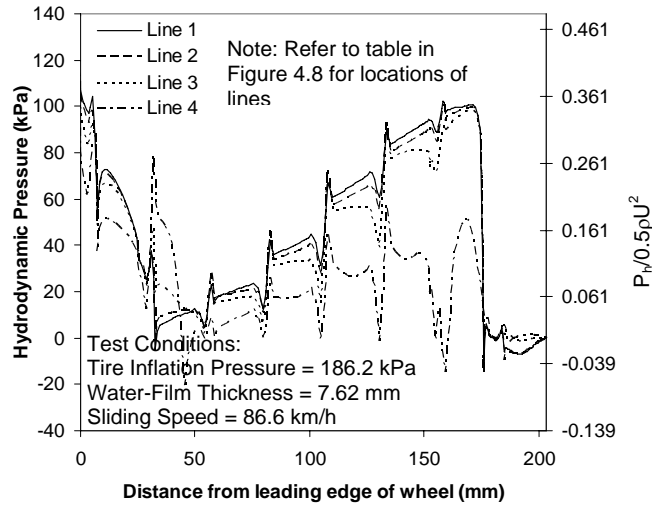
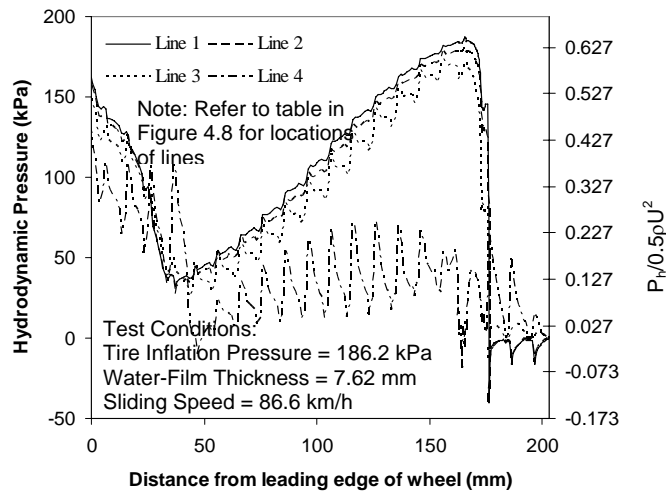


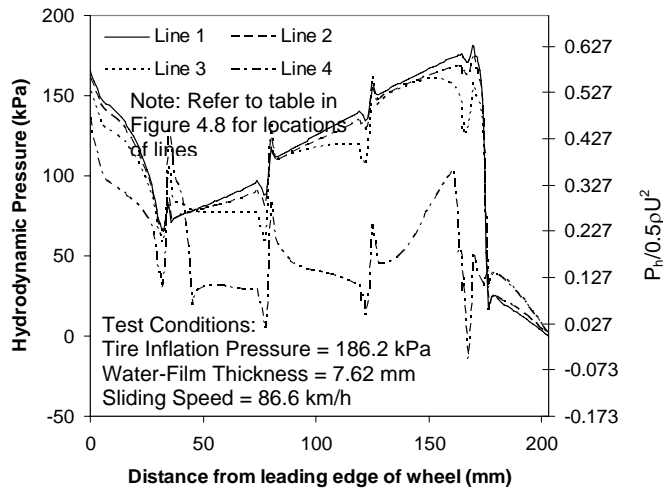
Figure 5.2: Meyer's relationship for experimentally measured data by Horne (1969) and predicted points by proposed model for longitudinal pavement grooving



(a) Design A



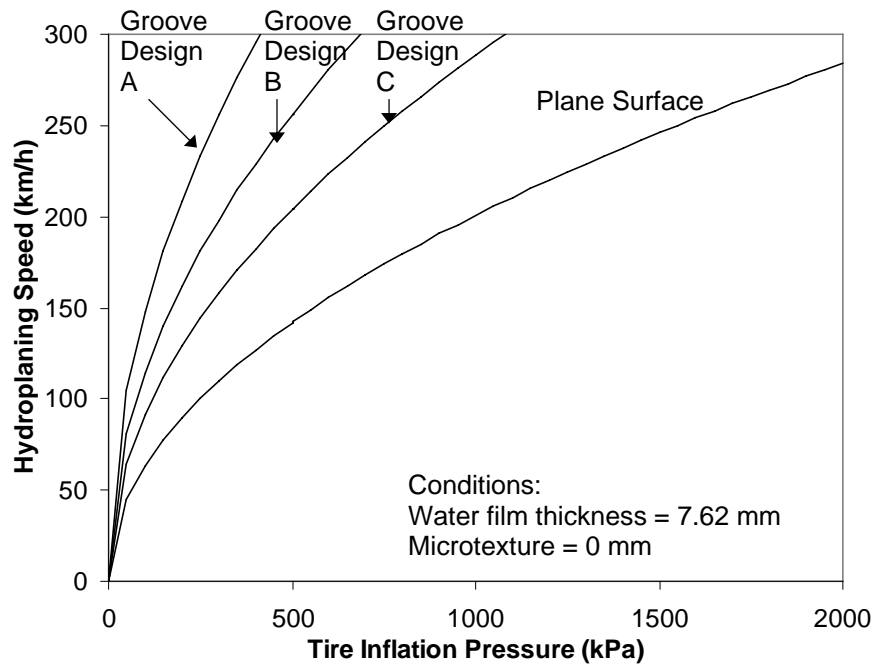
(b) Design B



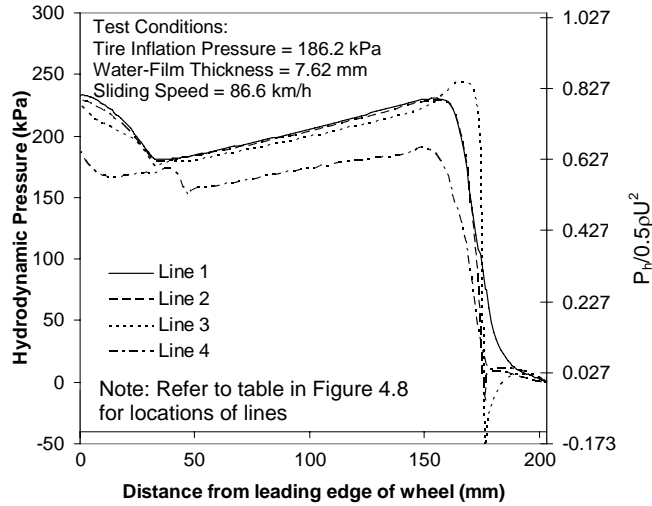
(c) Design C

Figure 5.3: Ground hydrodynamic pressure distribution under wheel for smooth transversely-grooved pavement of designs A, B and C

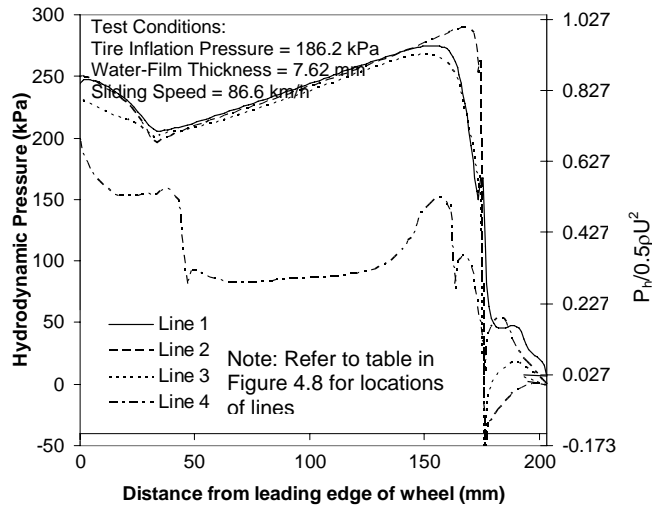




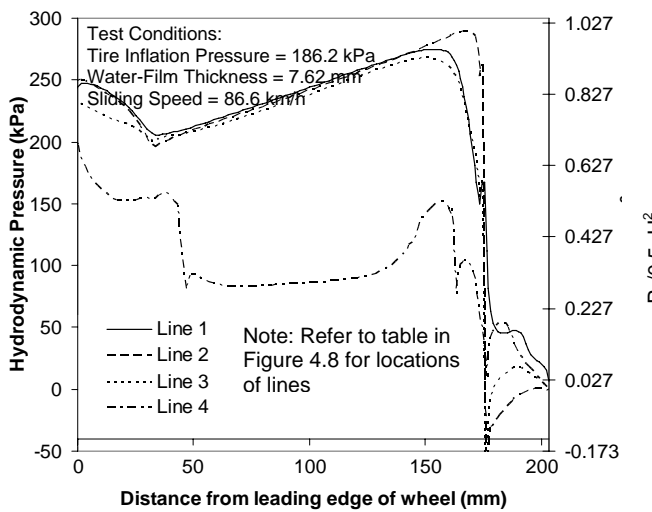
**Figure 5.4: Derived relationship between tire inflation pressure and hydroplaning speed for different transversely grooved pavement surfaces**



(a) Design A



(b) Design B



(a) Design C

Figure 5.5: Ground hydrodynamic pressure distribution under wheel for smooth transversely-grooved pavement of designs A, B and C

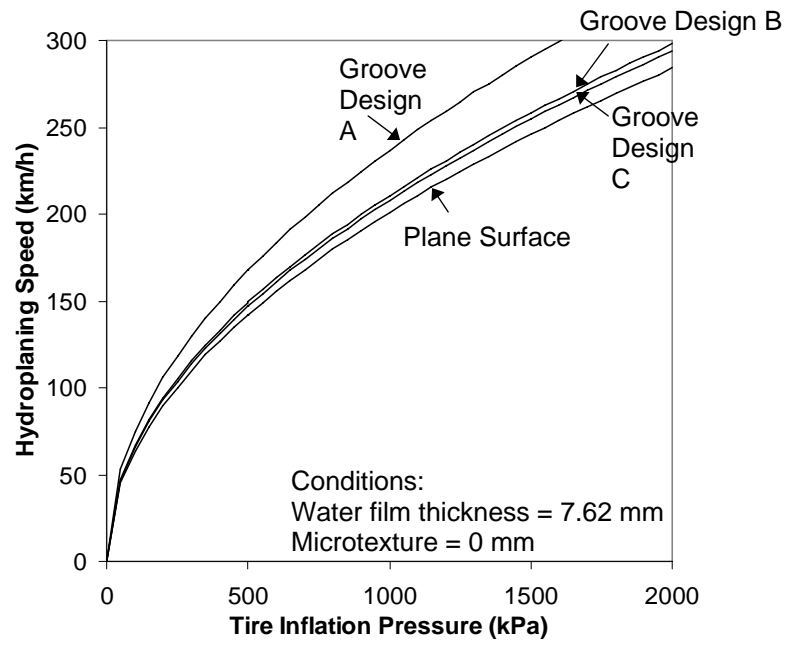
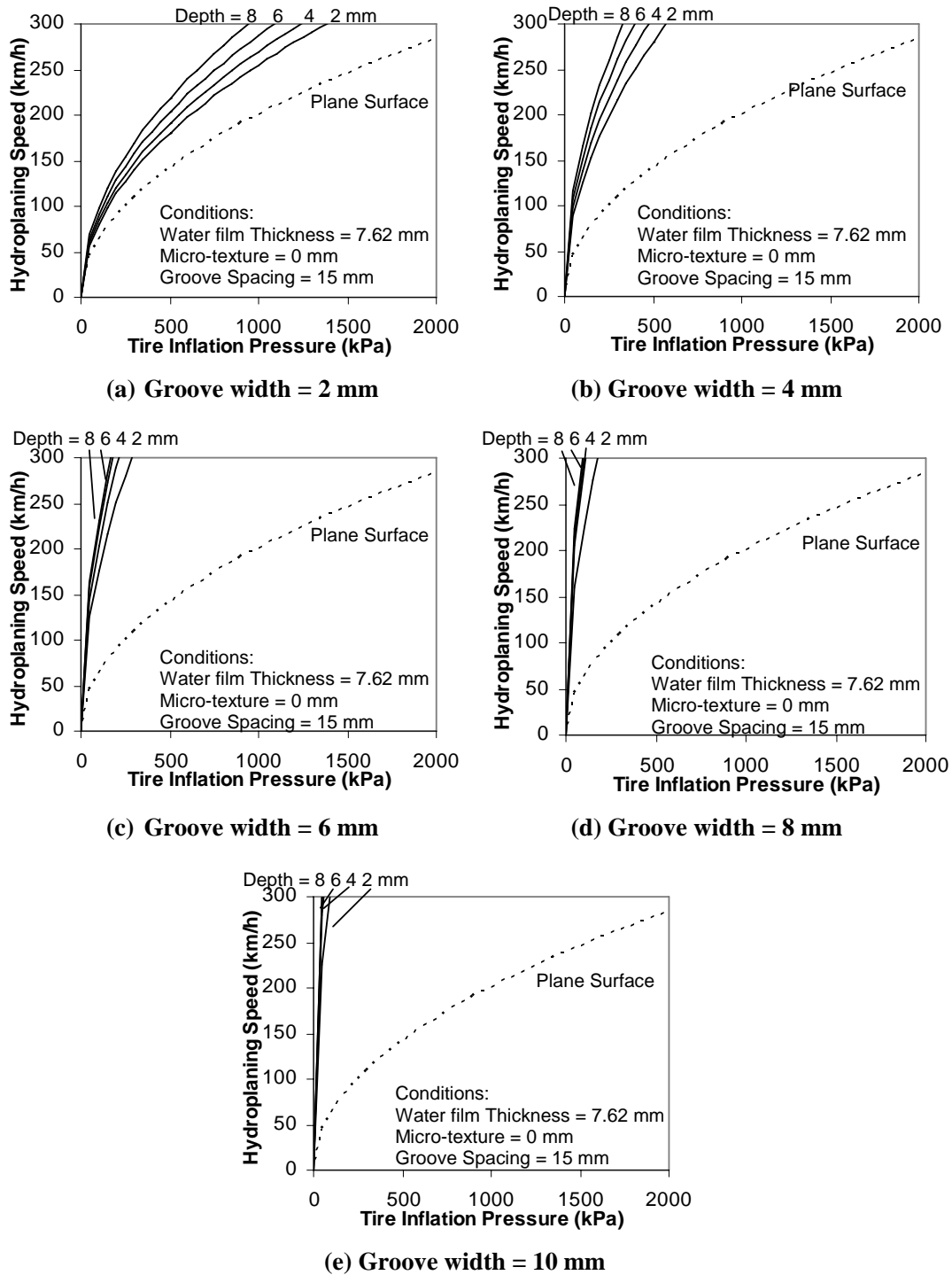


Figure 5.6: Derived relationship between tire inflation pressure and hydroplaning speed for different longitudinally grooved pavement surfaces



**Figure 5.7: Effect of transverse groove depth on hydroplaning as a function of tire pressure**

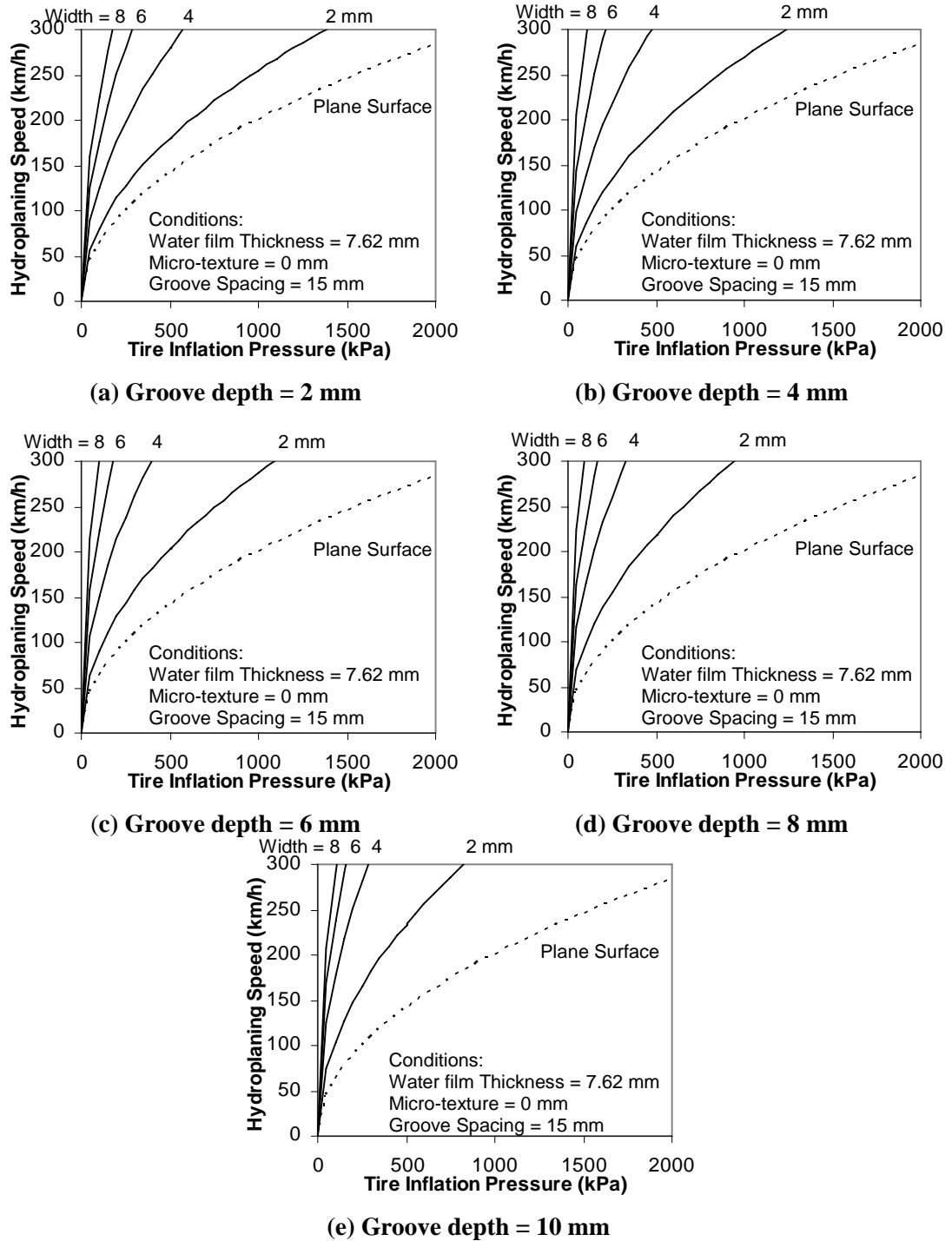


Figure 5.8: Effect of transverse groove width on hydroplaning curves for different depths at 15 mm spacing

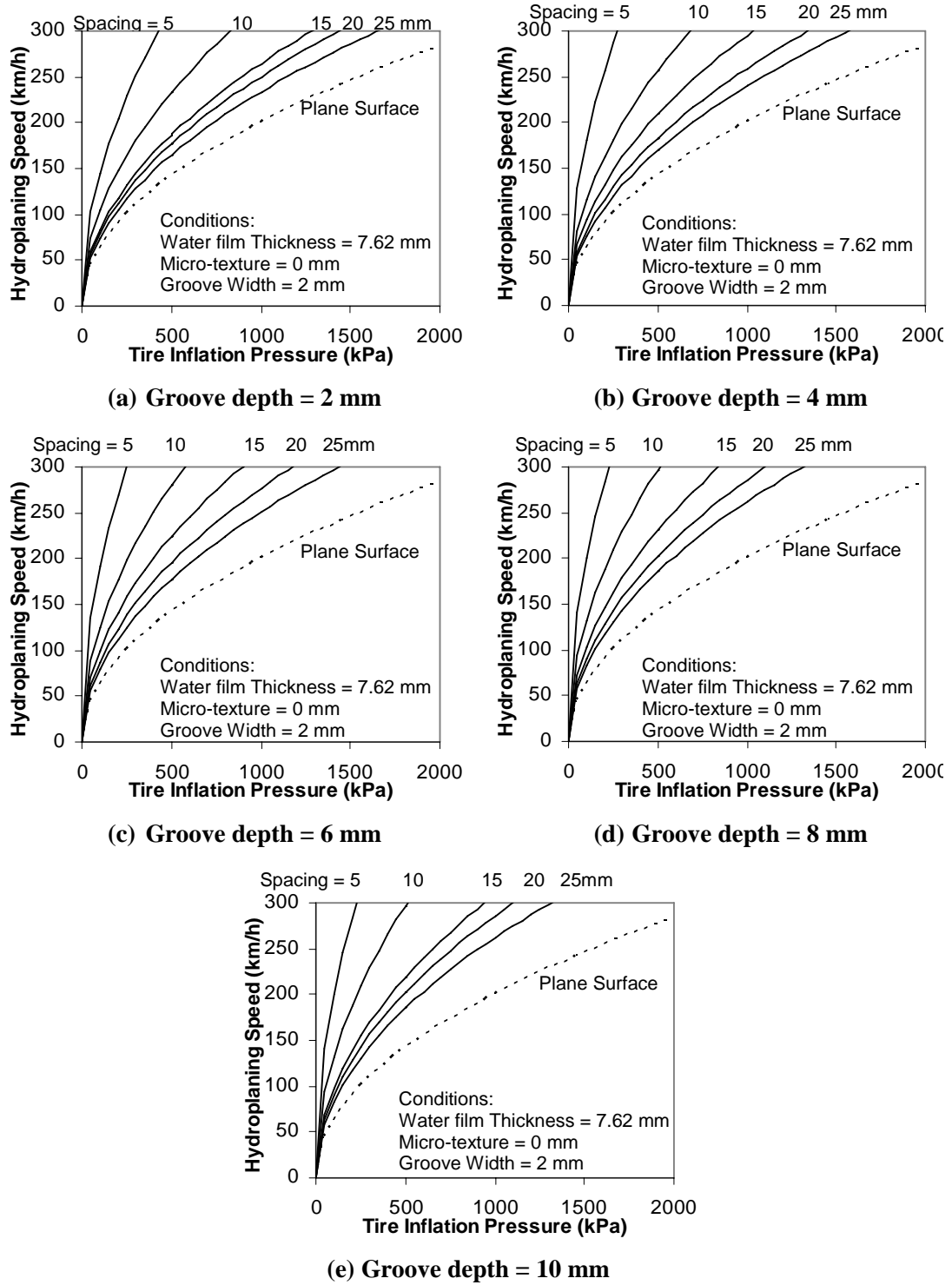
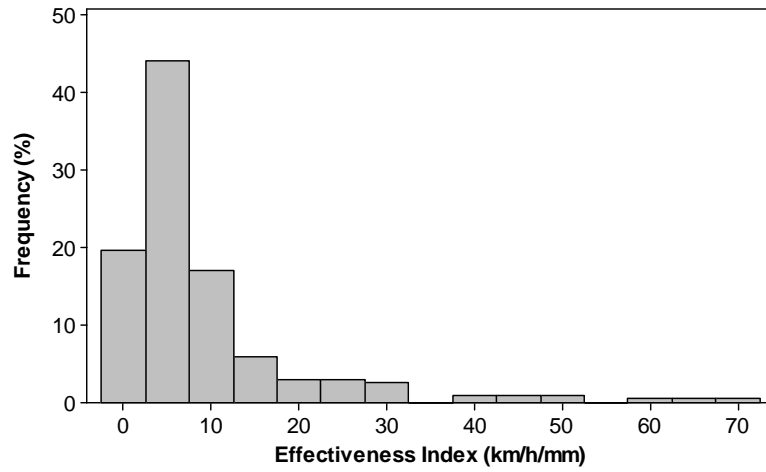
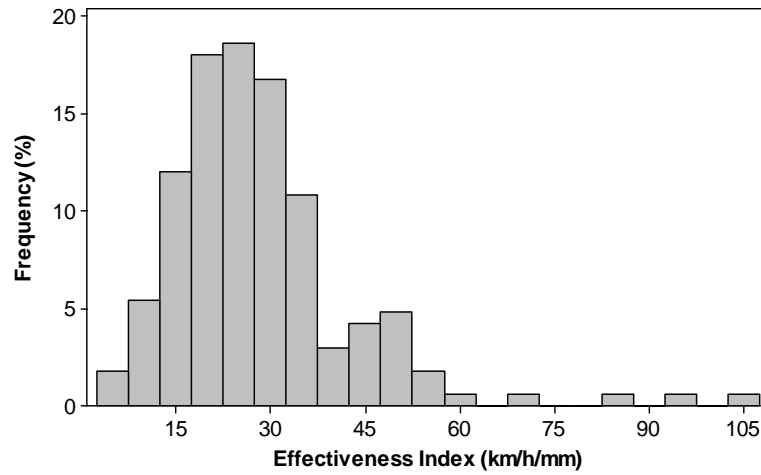


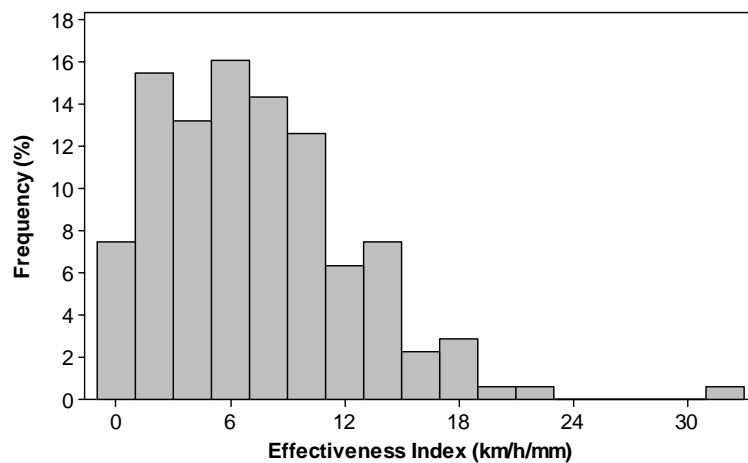
Figure 5.9: Effect of spacing between transverse grooves on hydroplaning curves for different groove depth for groove width of 2 mm



(a) Groove depth



(b) Groove width



(c) Groove spacing

Figure 5.10: Frequency distribution of effectiveness indices of different transverse groove dimensions

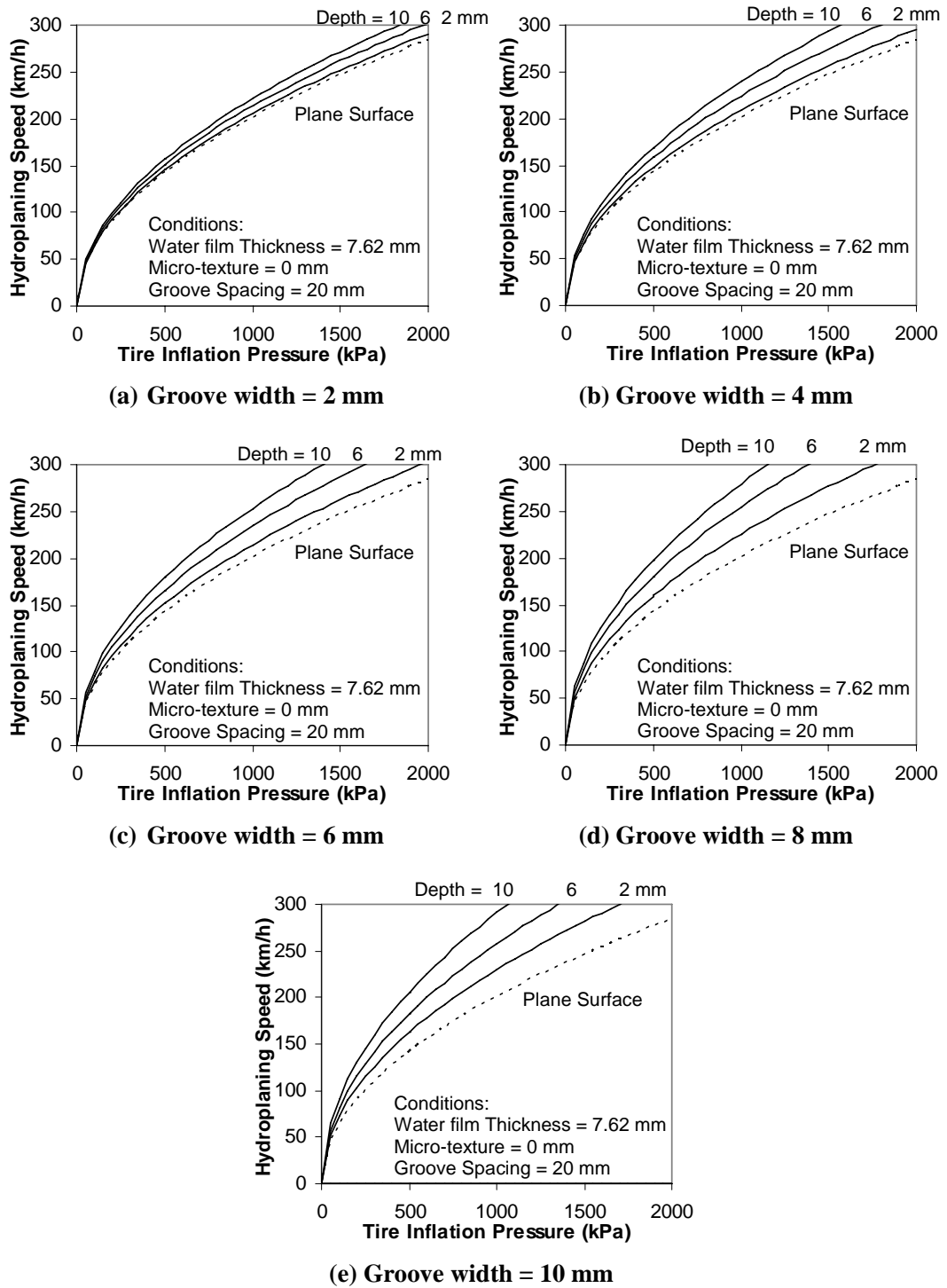


Figure 5.11: Effect of longitudinal groove depth on hydroplaning as a function of tire pressure



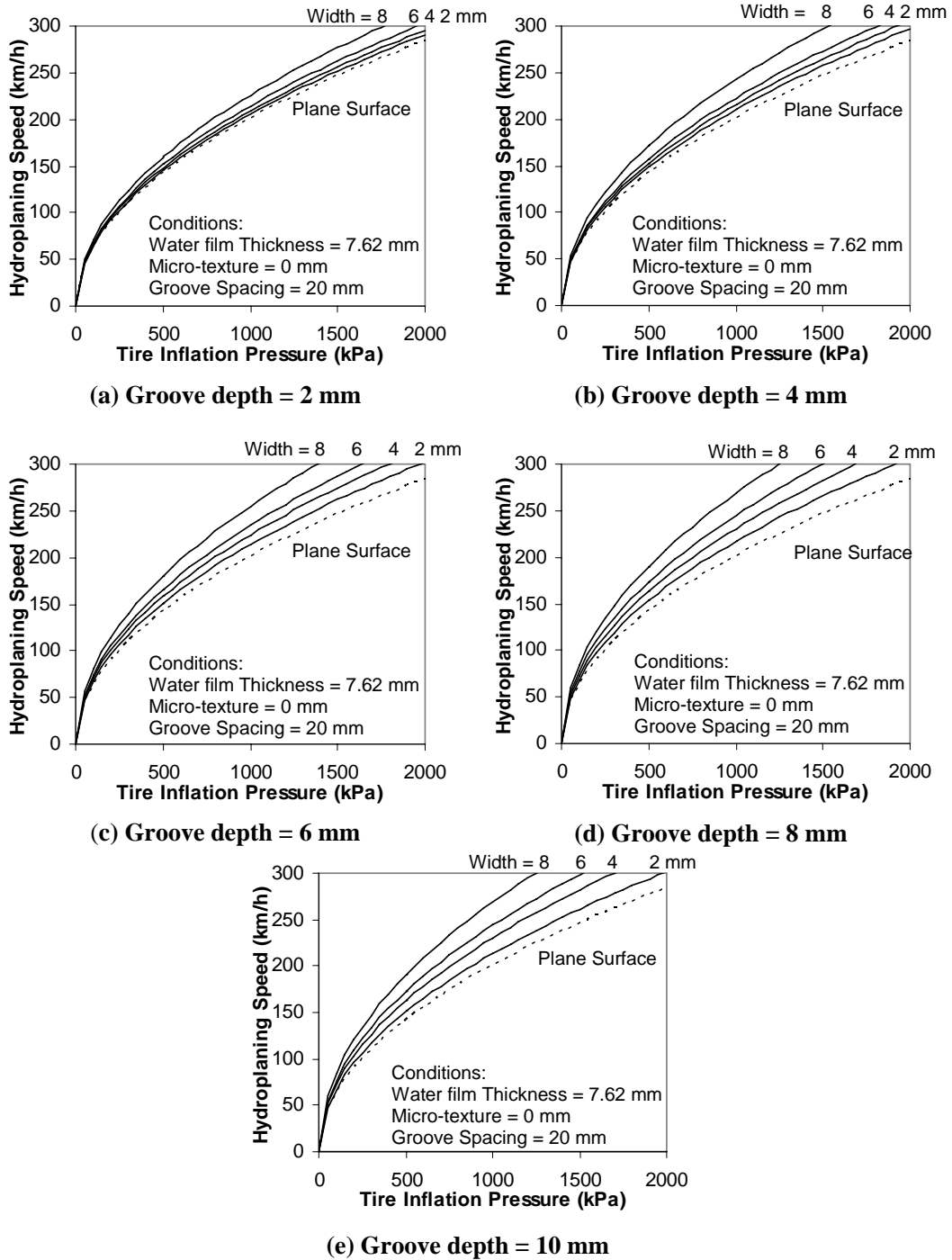
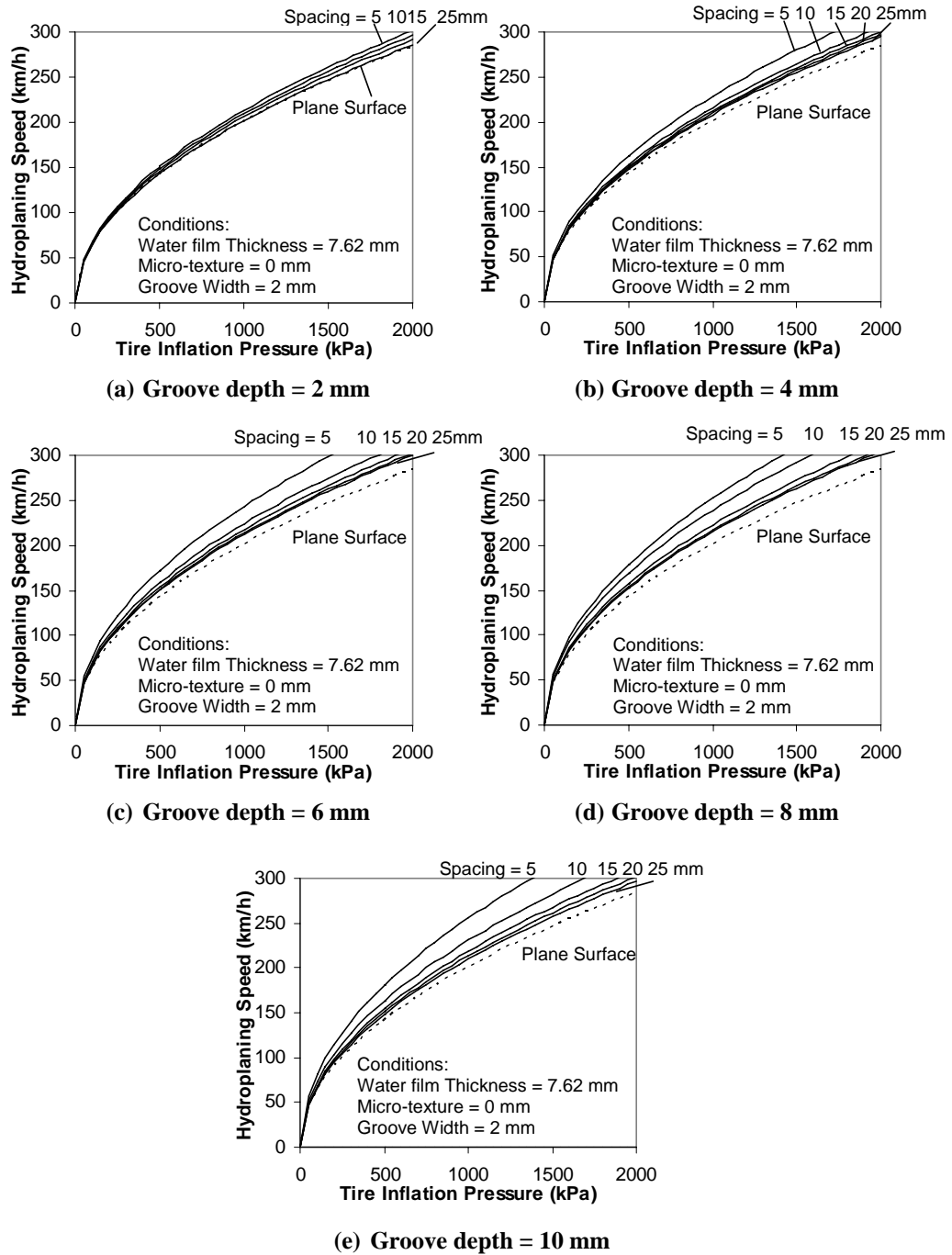
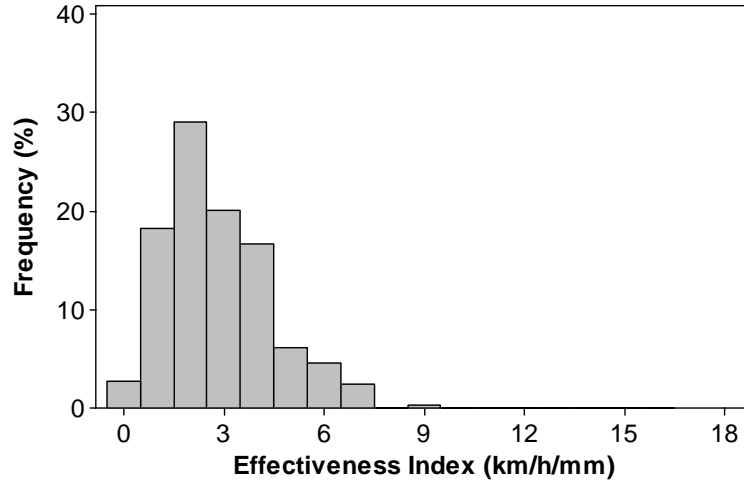


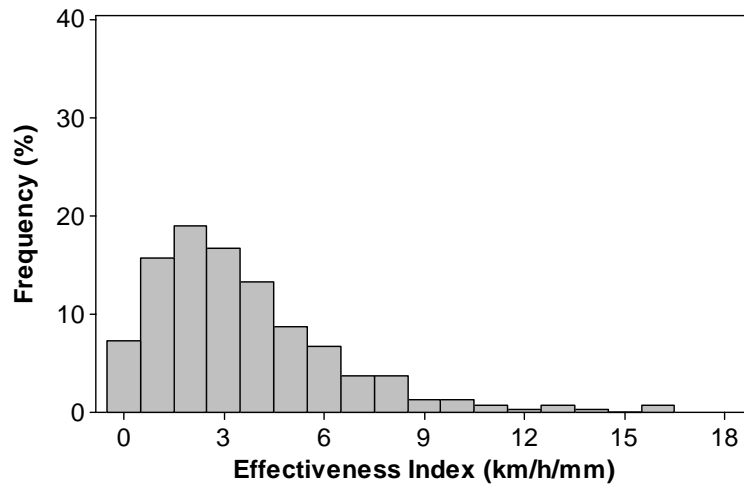
Figure 5.12: Effect of longitudinal groove width on hydroplaning as a function of tire pressure



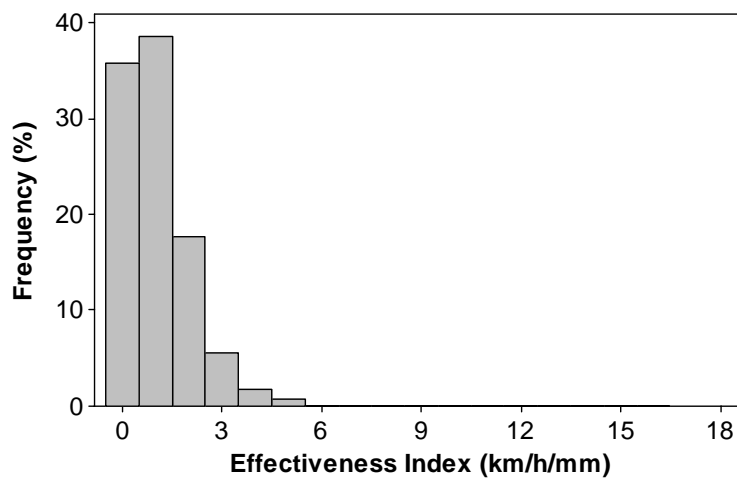
**Figure 5.13: Effect of longitudinal groove center-to-center spacing on hydroplaning as a function of tire pressure**



(a) Groove depth



(b) Groove width



(c) Groove spacing

Figure 5.14: Frequency distribution of effectiveness indices of different longitudinal groove dimensions

## **CHAPTER 6      DESIGN AND EVALUATION OF PAVEMENT GROOVES AGAINST HYDROPLANING**

### **6.1      Introduction**

It is observed in Chapter 5 that pavement groove dimensions play an important role in the reduction of hydroplaning potential (i.e. hydroplaning speed). However, current practices of pavement grooving design are based on either experience or past practice. Tables 5.9 and 6.1 show the summary of the recommended groove dimensions for transverse and longitudinal grooves respectively by various state highway agencies (ACPA, 2005). Most of the states provided a recommended range of groove width, depth and spacing respectively. Other agencies also have their own recommendations on the groove dimensions for skid resistance and noise control as described in Table 6.2 (Hoerner and Smith, 2002). However these guidelines could not offer pavement engineers information such as the safety factor or safety margin against hydroplaning, resulting in a lack of understanding of the effectiveness of the designed groove dimensions against hydroplaning. Since hydroplaning is a major safety consideration for pavement grooving design, it is of practical interest and desirable for pavement engineers or designers to be aware of the safety implications of a design. This chapter thus describes an evaluation procedure, based on the computer simulation model presented in Chapter 5 to determine the hydroplaning risk level of a given transverse pavement grooving design and a design procedure to determine the pavement groove dimensions based on a selected level of hydroplaning risk.

### **6.2      Concept of Hydroplaning Risk in Pavement Groove Dimension Design and Evaluation**

#### **6.2.1      Definition of Hydroplaning Risk**

The risk of hydroplaning can be defined as the probability of hydroplaning occurrence for the design vehicle type traveling at the design speed on the section of road concerned under

the given pavement conditions (i.e. pavement grooving design) and environmental conditions (such as water film thickness on the pavement surface). Assuming that the probability density function  $f(v)$  of the spot speeds of the design vehicle type is known, the design level of risk of hydroplaning  $\alpha$  can be computed as follows:

$$\alpha = P(V > V_p) = 1 - F(V_p) = 1 - \int_0^{V_p} f(v)dv \quad (6.1)$$

where  $V$  is the spot speed of the vehicle,  $V_p$  is the design hydroplaning speed,  $P(V > V_p)$  is the probability of a vehicle having a spot speed larger than the design hydroplaning speed, and  $F(V_p)$  is the cumulative probability of a vehicle with speeds smaller than the design hydroplaning speed. The wet-weather spot speed is of interest here and the spot speed distributions of the traffic stream traveling on the freeway can be determined using measurement methodologies stated by Lamm et al. (1990) and Roess et al. (2004).

### 6.2.2 Evaluation of Hydroplaning Risk for Given Pavement Groove Design

The hydroplaning risk associated with a particular pavement grooving design can be evaluated using the following steps:

- (1) Identify the pavement section and the dimensions (depth, width and spacing) of the groove design to be evaluated.
- (2) Select the design vehicle type (e.g. passenger cars, 40-footer container trucks or 40-seater buses) and the design thickness of water film on the pavement surface.
- (3) Determine the probability density function for the speed distribution of the selected design vehicle type.
- (4) Apply the computer simulation model for hydroplaning to the pavement section with the groove design to be evaluated and obtain the hydroplaning speed.
- (5) Apply Equation (6.1) to determine the hydroplaning risk  $\alpha$ . Alternatively, a plot of the function  $[1-F(V)]$  against speed  $V$  can be prepared, and  $V_p$  is entered

in the  $V$ -axis and the corresponding risk level can be read off from the axis  $\alpha = 1 - F(V)$ .

It must be highlighted that since hydroplaning is a wet-weather safety hazard, the vehicle speed distribution referred to in Step (3) above should accordingly be derived from wet-weather vehicle speed data. It is known that wet-weather vehicle speeds in general are significantly slower than normal dry-weather speeds. An example of using the proposed procedure to evaluate hydroplaning risk of transverse and longitudinal pavement grooving is illustrated in Sections 6.3.1 and 6.3.2 respectively.

### **6.2.3 Design of Pavement Groove Dimension based on Hydroplaning Risk**

In the planning of a new design of pavement grooving, it is appropriate to first select the required hydroplaning risk level. The following steps for the design of new pavement grooving are:

- (1) Select the design hydroplaning risk level.
- (2) Determine the design input parameters for computer simulation. These include water film thickness, tire inflation pressure, density and viscosity of the water film, temperature and surface microtexture etc.
- (3) Determine the design vehicle type and the design wet-weather vehicle speed distribution for the particular road section, and identify the design hydroplaning speed based on the selected design hydroplaning risk level.
- (4) Start with a pavement grooving design with trial groove dimensions of groove width, depth and spacing and perform the computer simulation.
- (5) If the computed hydroplaning speed is greater than the design hydroplaning speed, revise the groove dimensions by either (i) reducing the groove depth or width, or (ii) increasing the groove spacing. If the computed hydroplaning speed is smaller than the design hydroplaning speed, revise the groove dimensions by either (i) increasing the groove depth or width, or (ii) reducing the groove spacing.

- (6) Repeat step (4) until the computed hydroplaning speed matches with (or is sufficiently close to) the design hydroplaning speed.

The above trial-and-error procedure can be quite time-consuming. It is also noted from Chapter 5 that there exist more than one possible solution, each with a different combination of groove depth, width and spacing. The trial-and-error procedure is not designed to give all feasible solutions. In order to provide a fuller picture to the designer, instead of the iterative procedure of Steps (4) to (6), one could conduct in a systematic manner a series of computer simulation analyses to establish a hydroplaning risk table. Essentially this involves computer simulation analyses of the likely family of groove dimension designs and computes the hydroplaning risk level of each. These shall be further discussed in the Section 6.4.

### 6.3 Numerical Example on the Evaluation of Hydroplaning Risk for a given Pavement Groove Design

A numerical example is presented here to illustrate the evaluation procedure described in Section 6.2.2. The wet-weather speed distribution adopted for this example is obtained from the experimental data of Kyte et al. (2001) for a four-lane section of an interstate freeway. The posted speed limit was 105 km/h. A Weibull distribution as shown in Figure 6.1 is found to fit the experimental data well after performing a goodness of fit test at 95% level of confidence. The probability density function of the spot speeds for passenger cars (the assumed design vehicle) is shown in Equation (2).

$$f(v) = \frac{a(v-\theta)^{a-1}}{b^a} e^{-\left(\frac{v-\theta}{b}\right)^a} \quad \text{where } v > \theta, a > 0, b > 0 \quad (6.2)$$

and  $a = \text{shape parameter} = 6.13$

$b = \text{scale parameter} = 105.82$

$\theta = \text{threshold parameter} = 0$

with mean = 98.1 km/h and standard deviation = 19.1 km/h. This spot-speed distribution shall be used to illustrate how one can evaluate the hydroplaning risk associated with the transverse or longitudinal pavement grooving design.

### 6.3.1 Evaluating Hydroplaning Risks for Transverse Pavement Grooving

From Table 5.9 and other guidelines (Wu and Nagi, 1995; ACPA, 2005), it is noted that the dimensions of transverse pavement grooves typically fall within the following values: 2.0 mm – 3.2 mm groove width, 3.2 mm – 4.8 mm groove depth and 12.7 mm – 19.1 mm center-to-center spacing. As an illustration, for water film thickness of 7.62 mm, the range of hydroplaning risks for the recommended range of transverse groove dimensions can be evaluated for the wet-weather spot speed distribution shown in Figure 6.1, assuming that the design vehicle is a passenger car with 186.2 kPa tire inflation pressure.

Considering a design of 2.0 mm wide and 3.2 mm deep transverse grooves at 19.1 mm spacing, which is the worst case scenario of the typical range of acceptable transverse groove dimensions, the hydroplaning speed can be evaluated easily through the use of the hydroplaning table for the design vehicle shown in Table 5.5 in Chapter 5. The predicted hydroplaning speed is found to be 110.6 km/h. Substituting this value into Equation (6.2), a rather high hydroplaning risk of 28.4% is obtained for the design vehicle. Next, for the design of 3.2 mm wide and 4.8 mm deep transverse grooves at 12.7 mm spacing, which is the best scenario of common transverse groove dimensions, the hydroplaning speed obtained from Table 5.5 in Chapter 5 is 181.6 km/h and the corresponding computed hydroplaning risk is less than 0.001% for the design vehicle. Comparing against the hydroplaning risk of 74.3% associated with the plane pavement surface (where the hydroplaning speed is 86.6 km/h), there is a marked improvement in the reduction of the hydroplaning risk by providing transverse pavement grooving. This shows the effectiveness of the current transverse groove guidelines against hydroplaning. However, it is observed that the range in hydroplaning risks from 0.001% to 28.4% is extremely large and may not be acceptable from a practical point of view. This indicates the need for further refinement in the current technique of specifying pavement groove dimensions before construction.



### **6.3.2 Evaluating Hydroplaning Risks for Longitudinal Pavement Grooving**

From Tables 6.1 and 6.2, it is noted that the recommended longitudinal groove dimensions in practice are typically: 2.5 mm – 3.2 mm groove width, 3.2 mm – 6.9 mm groove depth and 12.7 mm – 19.1 mm center-to-center spacing. For a water film thickness of 7.62 mm, the range of hydroplaning risks for the recommended range of longitudinal groove dimensions can be evaluated for the wet-weather spot speed distribution shown in Figure 6.1. As in the previous sub-section, a passenger car with 186.2 kPa tire inflation pressure is assumed as the design vehicle for illustration.

The design of 2.5 mm wide and 3.2 mm deep longitudinal grooves at 19.1 mm spacing, which is the worst case scenario of the typical range of acceptable longitudinal groove dimensions, is considered. From Table 5.11 in Chapter 5, the predicted hydroplaning speed is found to be 91.1 km/h for the design vehicle. The simulation analysis by the computer model indicates a rather high hydroplaning risk of 67.1%. Similarly, the design of 3.2 mm wide and 6.9 mm deep longitudinal grooves at 12.7 mm spacing, which is the best scenario of common longitudinal groove dimensions, would give a hydroplaning speed of 101.5 km/h and the corresponding hydroplaning risk is 46.1%. Comparing against the hydroplaning risk of 74.3% associated with the plane pavement surface (where the hydroplaning speed is 86.6 km/h), there is some improvement in the reduction of the hydroplaning risk by providing longitudinal pavement grooving. However, the risk of hydroplaning for the recommendations is still rather high due to the large spacing between the grooves. Therefore it is imperative for pavement engineers to better refine the current recommended longitudinal groove dimensions used in practice in terms of hydroplaning control. This shall be further discussed in Section 6.4.

### **6.3.3 Comparison of Hydroplaning Risk in Transverse and Longitudinal Pavement Grooving**

Comparing the effectiveness of transverse and longitudinal pavement grooving, it can be easily observed that the risk of hydroplaning associated with transverse pavement grooving is much lower than that of longitudinal pavement grooving of the same design. This is

illustrated in Table 6.3 for the groove designs evaluated in Section 5.2 in Chapter 5 where the hydroplaning risks are evaluated using the method stated in Section 6.1.2. The design vehicle is assumed to be a passenger car with tire inflation pressure of 186.2 kPa and the wet-weather spot speed distribution described in Figure 6.1 is used. The water film thickness of 7.62 mm is assumed.

It is also noted that in terms of hydroplaning control, the provision of longitudinal pavement grooving could not reduce hydroplaning risk to an acceptably low level, although hydroplaning risk has been reduced. However, this risk evaluated is on the conservative side since it is assumed that there is zero microtexture and the pavement is excessively flooded. This risk can be further reduced by (i) providing good microtexture (as shown in Section 4.6 of Chapter 4), (ii) providing macrotexture that allow some form of transverse texture and (iii) reduce the water-film thickness on the pavement through the use of porous material or adequate surface drainage design (as shall be discussed in Chapter 7). Nevertheless, the technique described can still provide quantitative information of groove designs that will not be available from experiments.

#### **6.4 Numerical Example on Pavement Groove Dimension Design using Hydroplaning Risk Concept**

A numerical example is presented here to illustrate the procedure to design transverse and longitudinal groove dimensions as described in Section 6.2.3. Similar to the previous section, the wet-weather speed distribution adopted in this example is obtained from the experimental data of Kyte et al. (2001) for a four-lane section of an interstate freeway and is shown in Figure 6.1. The design vehicle in this section is assumed to be a passenger car with tire inflation pressure of 186.2 kPa and the assumed water film thickness is 7.62 mm.

##### **6.4.1 Design of Transverse Groove Dimensions**

It is also noted from the analysis presented in Table 5.5 and Figures 5.7, 5.8 and 5.9 of Chapter 5 that there exist more than one possible solution, each with a different combination of

groove depth, width and spacing. As explained in Section 6.2, the trial-and-error procedure is not designed to give all feasible solutions. In order to provide a fuller picture to the designer, one could conduct in a systematic manner a series of computer simulation analyses to establish a hydroplaning risk table. Essentially this involves computer simulation analyses of the likely family of groove dimension designs and computes the hydroplaning risk level of each. For example, for the numerical example analyzed in the preceding section, Table 6.4 shows the set of possible transverse pavement grooving designs and their respective hydroplaning risk levels.

A hydroplaning risk table such as the one shown in Table 6.4 is able to highlight to the designer all the transverse groove dimension designs that meet the required hydroplaning risk level. For instance, if the required hydroplaning risk is 0.001%, then the following groove designs from Table 6.4 are acceptable solutions:

- (a) Design with groove spacing of 25 mm – For groove depths of 8 mm or less, the groove width must be at least 6 mm. For a groove depth of 10 mm, the groove width must be 4 mm or more.
- (b) Design with groove spacing of 20 mm – For groove depths of 4 mm or less, the minimum groove width required is 6 mm. For a groove depth between 6 and 10 mm, the required groove width must be 4 mm or more.
- (c) Design with groove spacing of 15 mm – For groove depths up to 10 mm, the groove width required is at least 4 mm.
- (d) Design with groove spacing of 10 mm – For groove depths of up to 4 mm, the minimum groove width required is 4 mm. For a groove depth between 6 and 10 mm, a groove width of 2 mm or more is needed.
- (e) Design with groove spacing of 5 mm – For groove depths of up to 10 mm, all designs with a groove width of 2 mm or more will meet the requirement.

An advantage of working with the hydroplaning risk table is that it offers the designer flexibility to choose the appropriate design by incorporating other considerations. For example, cost of construction, ease of construction and maintenance, aesthetics and tire-pavement noise could be considered in selecting a design from the feasible solutions.

#### 6.4.2 Design of Longitudinal Groove Dimensions

The design procedures can be repeated for the design of longitudinal groove dimensions. A hydroplaning risk table such as the one shown in Table 6.5 is able to highlight to the designer all the longitudinal groove dimension designs that meet the required hydroplaning risk level. For the required hydroplaning risk of 10%, the following groove designs from Table 6.5 are acceptable solutions:

- (a) Design with groove spacing of 20 mm – For groove depths between 8 and 10 mm, the required groove width must be 10 mm.
- (b) Design with groove spacing of 15 mm – For a groove depth of 6 mm, the minimum groove width required is 10 mm. For groove depths between 8 and 10 mm, a groove width of 8 mm or more is needed.
- (c) Design with groove spacing of 10 mm – For a groove depth of 6 mm, the minimum groove width required is 8 mm. For groove depths between 8 and 10 mm, a groove width of 6 mm or more is needed.
- (d) Design with groove spacing of 5 mm – For groove depths between 8 and 10 mm, the required groove width is 4 mm.

From Table 6.5, the hydroplaning risk that can be achieved for longitudinal grooves is at most 0.1%, which is much larger than that for transverse grooves. This indicates that if the primary concern is to reduce hydroplaning occurrences on a particular site, the use of transverse groove on the site is a better option compared to longitudinal groove. Nevertheless, both are shown to be able to reduce hydroplaning occurrences by increasing the hydroplaning speed and reducing the hydroplaning risk, provided that the groove dimensions are appropriate.

#### 6.5 Summary

This chapter has discussed the use of the simulation models described in Chapters 4 and 5 in the design and evaluation of transverse and longitudinal pavement grooving. The concept of hydroplaning risk is introduced and is used as a means to quantify the effectiveness of pavement grooving against hydroplaning (for evaluation purpose) or as a safety margin (for

design purpose). An evaluation procedure to determine the hydroplaning risk of a given transverse or longitudinal pavement grooving design is discussed, and numerical examples on the evaluation of hydroplaning risk for transverse and longitudinal groove design are presented. This allows pavement engineers to evaluate the effectiveness of an existing grooved pavement in combating hydroplaning.

A trial-and-error procedure to design dimensions of transverse or longitudinal grooves is next proposed based on the concept of hydroplaning risk. As the trial-and-error procedure is time-consuming and there exist more than one possible groove designs that can satisfy the required hydroplaning risk level, the establishment of hydroplaning risk tables in the design of transverse or longitudinal groove dimensions is useful. A hydroplaning risk table would offer the designer flexibility in selecting a desirable design from a pool of feasible designs by incorporating other practical considerations.

**Table 6.1: Recommended Longitudinal Groove Dimensions of Various States in U.S.A. (ACPA, 2005)**

State	Min Groove Width	Max Groove Width	Min Groove Depth	Max Groove Depth	Min Groove Spacing	Max Groove Spacing	Random Spacing
CA	3.18	3.18	3.18	6.90	19.0	19.0	No
IA	3.18	3.18	3.18	4.76	N.A.	N.A.	Yes
MO	2.54	3.18	3.18	3.18	12.7	12.7	No

**Table 6.2: Recommended Guidelines on Surface Texturing Treatments (Hoerner and Smith, 2002)**

<b>Transverse Tining Recommendations</b>	
Tine spacing	Repeated random spacing of 10 to 76 mm (0.4 to 3 in.) Recommended when texturing conditions can be optimized (i.e. use of a specially constructed separate machine to provide more control over texturing timing, tine length and spacing and texture on tine.  OR Repeated random spacing of 10 to 51 mm (0.4 to 3 in.) Recommended when less than optimal finishing conditions are present (e.g. less control over tining procedure or hot and windy condition).
Tine depth	3 to 6 mm (0.125 to 0.25 in.)
Tine width	3 mm (0.125 in.)
<b>Longitudinal Tining Recommendations</b>	
Tine spacing	Uniform tine spacing of 19 mm (0.75 in.)
Tine depth	3 to 6 mm (0.125 to 0.25 in.)
Tine width	3 mm (0.125 in.)

**Table 6.3: Hydroplaning Risk for Pavement Grooving Designs A, B and C**

Groove Orientation	Design	Hydroplaning Risk
Transverse	A	< 0.001%
	B	0.002%
	C	6.75%
Longitudinal	A	44.58%
	B	67.44%
	C	69.72%
Plane Pavement Surface		74.16%

**Table 6.4: Family of Possible Transverse Pavement Grooving Designs based on Selected Level of Hydroplaning Risk**

s (mm)	d (mm)	w (mm)				
		2	4	6	8	10
25	1	>50%	10%	0.001%	0.001%	0.001%
	2	50%	5%			
	4		1%			
	6					
	8	25%	0.1%			
	10					
20	1	50%	0.1%	0.001%	0.001%	0.001%
	2	25%	0.01%			
	4					
	6					
	8	10%				
	10	1%				
15	1	50%	0.001%	0.001%	0.001%	0.001%
	2	25%				
	4					
	6					
	8	5%				
	10	1%				
10	1	0.1%	0.001%	0.001%	0.001%	0.001%
	2	0.01%				
	4					
	6					
	8					
	10					
5	1	0.001%	0.001%	0.001%	0.001%	0.001%
	2					
	4					
	6					
	8					
	10					

Note: s refers to groove spacing in mm, w refers to groove width in mm, d refers to groove depth in mm

**Table 6.5: Family of Possible Longitudinal Pavement Grooving Designs based on Selected Level of Hydroplaning Risk**

s (mm)	d (mm)	w (mm)				
		2	4	6	8	10
25	1	Risk >50%				
	2					
	4					
	6					
	8					
	10					
20	1	Risk >50%				
	2					
	4					
	6					
	8					
	10					
15	1	Risk >50%				
	2					
	4					
	6					
	8					
	10					
10	1	Risk >50%				
	2					
	4					
	6					
	8					
	10					
5	1	Risk >50%				
	2					
	4					
	6					
	8					
	10					

Note: s refers to groove spacing in mm, w refers to groove width in mm, d refers to groove depth in mm



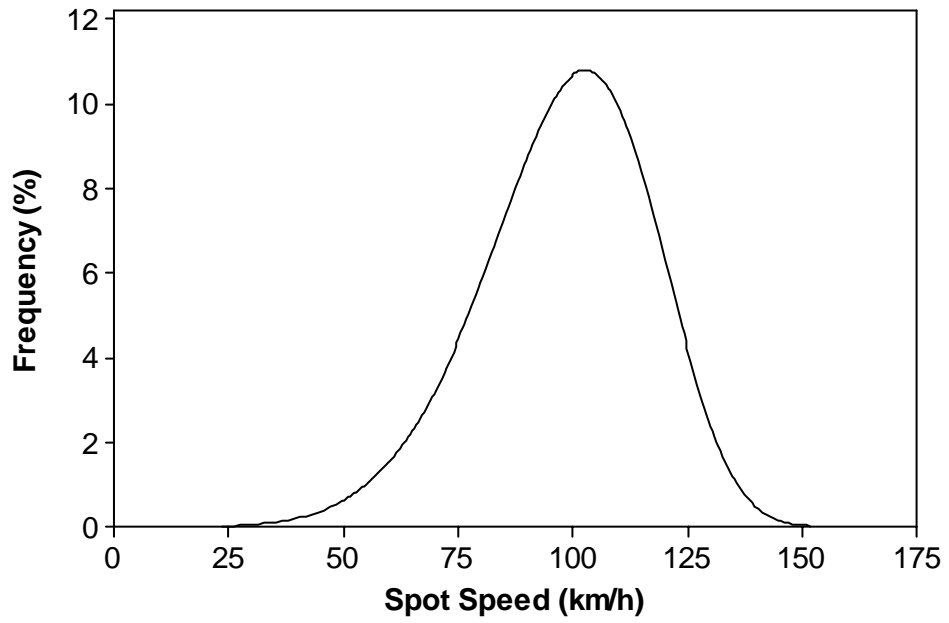


Figure 6.1: Wet-speed frequency distribution on a freeway

## CHAPTER 7 WET TIRE PAVEMENT INTERACTION AND HYDROPLANING MODELING

### 7.1 Introduction

The hydroplaning simulation model as described in Chapters 3 to 6 is able to describe hydroplaning on plane pavement surfaces with and without microtexture, and on pavement surfaces with longitudinal or transverse pavement grooving. However, this model has a major limitation: the need to have an assumed tire deformation profile at incipient hydroplaning. It considers tire-to-fluid (in the form of assumed tire deformation profile at hydroplaning) and fluid-to-pavement interactions, but not the interaction between the tire and the pavement surface. Ignoring tire-to-pavement interaction does not affect the simulation of hydroplaning because when hydroplaning occurs, the total fluid uplift force is equal to the tire load and there is no contact between the tire and the pavement surface. However, by not considering tire-to-pavement contact, the development of tire deformation in the transitional process leading to hydroplaning cannot be simulated. In other words, the earlier hydroplaning model requires the tire deformation profile at hydroplaning as input, and it could be used only when the tire deformation profile is known beforehand. This requirement of prior knowledge of the tire deformation profile has made the scope of potential applications of the model rather restrictive. Therefore the model could not be used to study the effect of water-film thickness, loading conditions on the predicted hydroplaning speed and more importantly, the modeling of wet-pavement skid resistance. Hence there is a need to drop this assumption in the next stage of this research as described in Figure 2.15 in Chapter 2.

This chapter therefore describes the further development of the analytical model that is capable of determining the hydroplaning speed as well as the available skid resistance on wet pavements for a locked wheel sliding on a flooded pavement surface. The improved simulation model could provide a more complete treatment of the tire-fluid-pavement problem by considering tire-to-fluid, fluid-to-pavement, as well as tire-to-pavement interactions. In

particular, this chapter shall deal with the different factors that can affect the hydroplaning speed which could not be modeled using the model developed in the earlier chapters.

## **7.2 Finite Element Modeling of Tire-Fluid-Pavement Interaction**

This section presents the development of an improved three-dimensional finite-element model to simulate the sliding of a locked wheel with a known tire inflation pressure and a known tire loading over a flooded plane pavement surface with a known water film thickness.

### **7.2.1 Overall Concept of Modeling Tire-Fluid-Pavement Interaction**

Similar to Chapter 3, the proposed three-dimensional finite-element model also makes use of a moving-wheel frame of reference as shown in Figure 7.1(a). The problem is modeled as a layer of water with a given thickness and a smooth plane pavement surface moving at a given speed towards the wheel. A steady-state analysis is adopted. Figures 7.1(a) and 7.1(b) depict the three main components of the model, namely the pneumatic tire sub-model, the pavement surface sub-model, and the fluid sub-model. The proposed model is formulated to simulate tire-pavement interaction, as well as the steady state flow on the pavement surface and around the tire.

At zero vehicle speed, the model computes the initial footprint of the tire created at the tire-pavement contact surface under the action of the wheel load. The wheel load is transmitted from the rim through the tire inflation pressure which acts on the tire wall. With this initial footprint, the sliding of the locked wheel is simulated by applying a pre-defined increment of sliding speed to the pavement surface, as well as an inlet velocity of the same increment to the fluid. The hydroplaning simulation analysis is conducted in two stages. First, from the speed of 0 km/h, a relatively large speed increment of 5 m/s (18 km/h) is applied, and a simulation run is executed, followed by another speed increment and a simulation run. The process is repeated until the fluid uplift force matches or exceeds the wheel load. This provides a rough estimate of the hydroplaning speed. Next, starting from a sliding speed slightly lower than the

rough hydroplaning speed estimated in the first stage, the sliding speed is increased at a small speed increment of 0.1 m/s (0.36 km/h) to determine the hydroplaning speed more accurately.

In the simulation analysis, there is a choice of the type of flow model to be used. The choice of whether a laminar flow model or a turbulence flow model should be used is dependent on the sliding wheel speed. This selection criterion is based on the Reynolds number (Re) of the flow which is defined as:

$$\text{Re} = \frac{V t_w}{\nu} \quad (7.1)$$

where V is the vehicle speed in m/s,  $t_w$  is the water film thickness in m, and  $\nu$  is the kinematic viscosity of fluid (i.e. water) on the pavement surface in  $\text{m}^2/\text{s}$ . The laminar flow model is appropriate for modeling a flow at low vehicle speeds with  $\text{Re} < 500$  while the turbulent flow model is needed to analyze a flow at high or near-hydroplaning speeds with  $\text{Re} > 2000$ . For  $500 < \text{Re} < 2000$ , the flow is transitional and may be either turbulent or laminar (Streeter et al. 1998).

For a given sliding speed, the solution to the tire-fluid-pavement interaction problem is arrived at by an iterative process. First the fluid stresses acting on the tire wall are calculated using the fluid model. The data of the computed stresses on the tire wall are next transferred to the solid model through a fluid-structure interaction interface, and the corresponding tire deformations are computed by the tire model. The computed tire deformation data are in turn transferred to the fluid model through the same fluid-structure interaction interface. The revised tire wall deformation input to the fluid model will result in changes in the fluid flow around the tire and hence the stresses acting on the tire wall are re-computed. This iterative computational process is repeated until the stress residuals and the displacement residuals of the tire wall satisfy a pre-defined convergence criterion. In this study, the same convergence criterion of 0.1% is applied for all residuals.

With each simulation run for a given sliding speed, the output includes the following useful information: tire deformation profile, the tire contact footprint, the pressure distribution over the tire-pavement contact area, the fluid flow pattern, the hydrodynamic pressure

distribution over the fluid-tire contact area, the normal contact force and the traction force at the tire-pavement interface, the fluid uplift force and the drag force at the tire-fluid interface.

Figure 7.2 summarizes the solution process described in the preceding paragraphs. In this study the finite element software package ADINA (ADINA R&D Inc. 2005a) is used to analyze the tire-fluid-pavement interaction problem. The software consists of three parts, namely, ADINA for tire and tire-pavement contact modeling, ADINA-F for fluid flow modeling, and ADINA FSI for tire-fluid interaction modeling.

### 7.2.2 Pneumatic Tire Modeling

A key component in the simulation of skid resistance and hydroplaning is the modeling of the tire. For easy presentation, the properties of the ASTM E524 standard smooth tire (ASTM 2005f) are used in this section to illustrate the modeling of a tire for skid resistance and hydroplaning simulation. A tire is modeled using 4-node isoparametric single-layer shell elements, known as the Mixed-Interpolation-of-Tensorial-Components (MITC4) elements in the ADINA software. Shell elements are adopted as they have been successfully used by other researchers in the modeling of tires in friction studies (Tanner, 1996; Johnson et al., 1999).

In the modeling of a pneumatic tire, three structural components are considered, namely tire rim, tire sidewalls and tire tread. The tire rim can be taken to be rigid, and is assumed to have an elastic modulus of 100 GPa, a Poisson's ratio of 0.3, and a density of  $2,700 \text{ kg/m}^3$ . The tire sidewalls are assumed to be of a homogeneous, isotropic elastic material with a composite elastic modulus of 20 MPa, a Poisson's ratio of 0.45 and a density of  $1200 \text{ kg/m}^3$ , based on data from past studies on textile-ply rubber of pneumatic tires (Tanner 1996, Zmindak and Grajciar 1997, Haney 2003). The choice of the elastic properties of the tire tread requires a careful calibration so that the simulated footprint would be as close as possible to the actual footprint of a stationary tire on a dry pavement under the same load.

In the calibration process, the elastic modulus of the tire tread is varied from 50 MPa to 250 MPa in intervals of 50 MPa. The Poisson's ratio and density of the rubber are kept as 0.45 and  $1200 \text{ kg/m}^3$  respectively. For a wheel load of 4,826 N, Table 7.1 shows the errors of

different trial simulation results of the contact footprint dimensions against the measured tire contact footprint data published by PIARC (1995). The analysis indicates that using the elastic modulus of 100 MPa for the tire tread rubber, the simulation would yield contact footprint dimensions with less than 3% error as compared to the experimental results. Figure 7.3 shows a comparison between a simulated contact footprint and that measured experimentally by PIARC (1995).

The simulation is repeated for three different loads and the computed footprints are compared against the measured footprint dimensions as shown in Table 7.2. It can be observed that the simulation results using the elastic modulus of 100 MPa compare very well with those obtained experimentally, indicating that the calibrated model is appropriate for the analysis carried out in the present study.

The boundary conditions that govern the modeling of the pneumatic tire are:

- Fluid-structure interface at the tread face of the tire,
- Wheel load acting on the rim of the tire, and
- Tire inflation pressure acting on the inner faces of the tire.

Figure 7.1(a) shows the tire model, together with the loads and boundary conditions. A convergence analysis for mesh design is performed and the results are as shown in Figure 7.4. It is found that using 5,100 shell elements in the tire model and 1,600 elements for the pavement surface would be sufficient to give relatively accurate results.

### **7.2.3 Pavement Surface Modeling**

Assuming that the deformations of the pavement surface are negligible in comparison with tire deformations, the plane pavement surface is represented as a rigid surface that does not deform under the action of the wheel load as shown in Figure 7.1(a). The pavement is assumed to have an elastic modulus of 30 GPa, a Poisson's ratio of 0.15, and a density of 2,200 kg/m<sup>3</sup>. The pavement surface is modeled using the 4-node isoparametric single-layer MITC4 shell elements in the ADINA software. This element type is suitable for use

to model both thin plates and shells (ADINA Inc. 2005a). The nodes on the pavement surface are fixed in translation and rotation for all directions to represent total fixity.

#### 7.2.4 Tire-Pavement Contact Modeling

An accurate modeling of the tire-pavement contact is important to closely simulate the skid resistance developed at the tire-pavement interface. The Coulomb concept of friction (Bathe 1996) is adopted for the simulation by defining a non-dimensional variable  $\tau$  as follows:

$$\tau = \frac{F_T}{\mu\lambda} \quad (7.2)$$

where  $F_T$  is the contactor segment tangential force,  $\mu$  is the coefficient of friction and  $\lambda$  is the contactor segment normal contact force.

The contact algorithm used in the simulation is the constraint function method. The pavement surface is assumed to be a contactor surface (also known as the master surface), while the tire tread face is treated to be a target surface (also known as the slave surface). The standard Coulomb friction condition can therefore be expressed as:

$$\begin{aligned} |\tau| &\leq 1 \\ \text{and } |\tau| < 1 &\text{ implies } \dot{u} = 0 \\ \text{while } |\tau| = 1 &\text{ implies } \text{sign}(\dot{u}) = \text{sign}(\tau) \end{aligned} \quad (7.3)$$

where  $\dot{u}$  is the sliding velocity. For the case of standard Coulomb friction,  $\mu$  is a constant given by the static coefficient of friction between the wet pavement surface and the tire tread rubber.  $\mu$  is a required input parameter to the skid resistance simulation analysis. It can be measured either in the laboratory or on site. However, it is not a required input parameter in the hydroplaning simulation analysis since it does not affect fluid flow and the development of the fluid uplift forces. It can also be deduced that the simulation model clearly differentiate between non-contact (the former part of Equation (7.3)) and contact (the latter part of Equation (7.3)) between the tire and pavement surface.

### 7.2.5 Fluid Flow Modeling

Fluid flow modeling can be achieved by modeling the behavior of fluid flow near the tire pavement contact patch using the complete set of Navier-Stokes equations as described in detail in Chapter 3. The Arbitrary-Lagrangian-Eulerian (ALE) formulation is used instead due to the need to consider fluid-structure interaction. In a general ALE coordinate system, it is convenient to express the governing equations in integral form in an arbitrary volume  $V$  bounded by its boundary  $\partial V$  (ADINA Inc. 2005b; Zhang et al. 2003).

$$\frac{\partial}{\partial t} \int_V \mathbf{U} dV + \oint_{\partial V} [(\mathbf{v} - \mathbf{w})\mathbf{U} - \mathbf{G}] \cdot d\mathbf{S} = \int_V \mathbf{R} dV \quad (7.4)$$

in which

$$\mathbf{U} = \begin{bmatrix} \rho \\ \rho \mathbf{v} \\ \rho E \\ \rho \varphi \\ 0 \end{bmatrix}, \quad \mathbf{G} = \begin{bmatrix} 0 \\ \boldsymbol{\tau} \\ \boldsymbol{\tau} \cdot \mathbf{v} + k \nabla \theta \\ d_\varphi \nabla \varphi \\ d_\psi \nabla \psi \end{bmatrix}, \quad \mathbf{R} = \begin{bmatrix} 0 \\ \mathbf{f}^B \\ \mathbf{f}^B \cdot \mathbf{v} + q^B \\ S_\varphi \\ 0 \end{bmatrix} \quad (7.5)$$

where  $\boldsymbol{\tau}$  is the stress tensor,  $\mathbf{e}$  is the strain tensor,  $\mathbf{v}$  is the velocity vector,  $\mathbf{w}$  is the moving mesh velocity vector,  $p$  is the fluid pressure,  $\rho$  is the density,  $E$  is the specific energy,  $e$  is the internal energy,  $\theta$  is the effective viscosity,  $\lambda$  is the second viscosity,  $\mathbf{f}^B$  is the specific rate of heat generation,  $\varphi$  represents any other variables governed by convective-diffusive equations with  $d_\varphi$  and  $S_\varphi$  being its diffusion coefficient and source term respectively, and  $\psi$  represents any other variables governed by the Laplace equations, with  $d_\psi$  being its diffusion coefficient. The variables that  $\varphi$  might represent are the turbulence kinetic energy  $K$  and the turbulence dissipation rate  $\varepsilon$  for the  $K$ - $\varepsilon$  turbulence model. The variables that  $\psi$  represents are the increments of fluid displacement  $\Delta \mathbf{d}_f$  for the moving boundary condition. The fluid body force  $\mathbf{f}^B$  in this case includes the gravitational forces. For incompressible flows, the density is assumed to be constant.



The findings in Chapter 3 have indicated that the  $K$ - $\varepsilon$  turbulence flow model can be used to model a flow at high or near-hydroplaning speeds. The  $K$ - $\varepsilon$  turbulence flow model can be described by Equations (7.6) and (7.7).

$$\frac{\partial(\rho K)}{\partial t} + \nabla \cdot \left[ \rho \mathbf{v} K - \left( \mu_0 + \frac{\mu_t}{\sigma_K} \right) \nabla K \right] = 2\mu_t D^2 - \rho \varepsilon + \left( \mu_0 + \frac{\mu_t}{\sigma_\theta} \right) \beta \mathbf{g} \cdot \nabla \theta \quad (7.6)$$

$$\frac{\partial(\rho \varepsilon)}{\partial t} + \nabla \cdot \left[ \rho \mathbf{v} \varepsilon - \left( \mu_0 + \frac{\mu_t}{\sigma_\varepsilon} \right) \nabla \varepsilon \right] = \frac{\varepsilon}{K} \left[ 2c_1 \mu_t D^2 - c_2 \rho \varepsilon + c_1 (1 - c_3) \left( \mu_0 + \frac{\mu_t}{\sigma_\theta} \right) \beta \mathbf{g} \cdot \nabla \theta \right] \quad (7.7)$$

where  $K$  is the kinetic energy,  $\varepsilon$  is the rate of dissipation of turbulence and  $\mu_t$  is the turbulent (eddy) viscosity. Here  $c_\mu$ ,  $c_1$ ,  $c_2$ ,  $c_3$ ,  $\sigma_k$ ,  $\sigma_\varepsilon$ ,  $\sigma_\theta$  are the model constants and have the values  $c_\mu = 0.09$ ,  $c_1 = 1.44$ ,  $c_2 = 1.92$ ,  $c_3 = 0.8$ ,  $\sigma_k = 1$ ,  $\sigma_\varepsilon = 1.3$ ,  $\sigma_\theta = 0.9$ . It is noted that Equations (7.4) to (7.7) are the same as the fluid flow equations introduced in Chapter 3.

The fluid domain is modeled using 4-node tetrahedral elements. This element type is known to be suitable for three-dimensional flows of both high and low Reynolds and Peclet numbers (ADINA R&D Inc. 2005b). In this study, water is used as the contaminant and the properties of water at 25°C are used in the simulation. The density, dynamic viscosity and kinematic viscosity of water at 25°C are 997.1 kg/m<sup>3</sup>, 0.894 x 10<sup>-3</sup> Ns/m<sup>3</sup> and 0.897 x 10<sup>-6</sup> m<sup>2</sup>/s respectively (Chemical Rubber Company 1988).

The boundary conditions of the fluid domain are:

- Velocity inlet at the front to simulate the vehicle speed under locked wheel conditions,
- Zero pressure (i.e. atmospheric pressure) at the side outflow,
- Pressure outlet at the front of the wheel to simulate the splash,
- Zero pressure at the contact surface between the tire and the pavement, and
- Fluid-structure interface at the tread face of the tire.

The finite-element mesh of the fluid flow model is shown in Figure 7.1(b), together with the loads and boundary conditions. A convergence analysis for mesh design is performed

and the results are shown in Figure 7.5. It is found that using 18,995 tetrahedral elements in the fluid model would give sufficiently accurate results.

### 7.2.6 Fluid-Structure Interaction (FSI) Modeling

The interaction between the pneumatic tire and the fluid, and that between the pavement surface and the fluid directly affect how the tire wall deforms as the sliding speed of the locked wheel increases. The interactions thus determine the changes in the tire footprint and the development of the fluid uplift forces. Since the pavement surface is modeled as a rigid surface, the interaction between the fluid and the pavement surface is comparatively straightforward. On the other hand, the interaction between the tire wall and the fluid requires a special numerical treatment known as “two-way coupling” which is an iterative process to couple the responses of the fluid model and the tire model.

In the coupling analysis, the fundamental conditions applied to the fluid-structure interface are the kinematic condition, or the displacement compatibility (Zhang and Bathe 2001):

$$\underline{\mathbf{d}}_f = \underline{\mathbf{d}}_s \quad (7.8)$$

and the dynamic condition (or traction equilibrium)

$$\mathbf{n} \bullet \underline{\boldsymbol{\tau}}_f = \mathbf{n} \bullet \underline{\boldsymbol{\tau}}_s \quad (7.9)$$

where  $\underline{\mathbf{d}}_f$  and  $\underline{\mathbf{d}}_s$  are, respectively, the fluid and solid (i.e. the tire wall) displacements and  $\underline{\boldsymbol{\tau}}_f$  and  $\underline{\boldsymbol{\tau}}_s$  are, respectively, the fluid and solid stresses. The underlining denotes that the values are defined on the fluid-structure interface only.

The stress and displacement criteria are used to check for the convergence of the iterations. The stress criterion is defined as:

$$r_\tau \equiv \frac{\|\underline{\boldsymbol{\tau}}_f^k - \underline{\boldsymbol{\tau}}_f^{k-1}\|}{\max\{\|\underline{\boldsymbol{\tau}}_f^k\|, \varepsilon_0\}} \leq \varepsilon_\tau \quad (7.10)$$

and the displacement criterion is defined as:

$$r_d \equiv \frac{\|\underline{\mathbf{d}}_s^k - \underline{\mathbf{d}}_s^{k-1}\|}{\max\{\|\underline{\mathbf{d}}_s^k\|, \varepsilon_0\}} \leq \varepsilon_d \quad (7.11)$$

where  $\varepsilon_\tau$  and  $\varepsilon_d$  are tolerances for stress and displacement convergence respectively and  $\varepsilon_0$  is a pre-determined constant for the purpose of overriding the stress and displacement tolerances in case they become too small to measure convergence. The tolerances are both set as 0.1%, and  $\varepsilon_0$  is given a value of  $10^{-8}$ .

### 7.3 Hydroplaning Analysis and Verification of Model

The measured hydroplaning speeds reported by Horne and Dreher (1963) in their widely cited experimental study were used for the verification of the proposed simulation model. The experimental data form the basis upon which the well-known NASA hydroplaning equation was developed. The experimental study employed an ASTM E-524 standard smooth tire with a tire inflation pressure of 165.5 kPa (ASTM 2005f). The applied wheel load was 4800 N, and the water film thickness was 7.62 mm.

Hydroplaning is considered to occur when the total fluid uplift force is equal to the vertical load applied on the wheel. Numerically, this is also the instant when the average ground hydrodynamic pressure developed in the fluid under the tire is equal to the tire inflation pressure. It is noted from the simulation that at this point, the normal contact force between the tire wall and the pavement surfaces drops to zero, and the contact area between the tire and pavement surface becomes zero.

The simulation analysis arrives at a hydroplaning speed of 82.1 km/h for the case studied. The experimentally derived NASA hydroplaning equation gives a hydroplaning speed of 81.8 km/h for a tire inflation pressure of 165.5 kPa (24 psi). The difference between the predicted and the NASA hydroplaning speeds is 0.4 %. To further check the validity of the proposed model against the NASA equation, which has tire pressure as the only variable, additional simulation runs are performed for tire inflation pressures ranging from 103.4 kPa (15 psi) to 248.2 kPa (36 psi), while keeping the load at 4800 N and the water-film thickness at

7.62 mm. Figure 7.6 shows the comparison between the hydroplaning speeds obtained from the simulation model and the NASA hydroplaning equation for the range of tire inflation pressures tested. It is noted that the results from the numerical simulation model fits closely with the experimentally derived NASA hydroplaning equation, confirming the ability of the proposed model to simulate the hydroplaning phenomenon. This indicates that the model can perform as well as that developed in Chapters 3 and 4 in terms of hydroplaning speed prediction.

#### 7.4 Effect of Footprint Aspect Ratio on Hydroplaning

It was found from experiments conducted in the Texas Transportation Institute and the NASA Langley Research Center by Horne et al. (1986) that hydroplaning speed is also dependent on the tire footprint aspect ratio as described by the following regression:

$$v_p = 51.80 - 17.15FAR + 0.72p \quad (7.12)$$

where  $FAR$  is the footprint aspect ratio (defined as the width of the footprint divided by its length) and  $p$  is the tire inflation pressure in psi. This equation is obtained based on experiments conducted on ASTM E501 (ribbed) tires (ASTM 2005d), ASTM E524 (smooth) tires (ASTM 2005f), and worn truck tires traveling on flooded pavement surface. This refinement to the 1963 NASA equation was based on additional experimental data using the ASTM E524 smooth tires. The revised experimentally derived hydroplaning speed equation offers a meaningful basis to verify the proposed simulation model by considering different tire footprint aspect ratios.

The proposed simulation model is applied to study the effect of loading varying from 2200 N to 5200 N as shown in Table 7.3. This loading range is selected based on the range of light to normal load expected of automotive tires (Horne et al. 1986). The corresponding footprint aspect ratios (defined as the width-to-length ratio of the footprint) for the ASTM smooth tire varies from 0.9 to 1.4.

In the simulation analysis, the water-film thickness on the pavement is fixed at 13 mm to be consistent with the experiments conducted by Horne et al. (1986). Table 7.4 shows the simulation results and the comparison with the hydroplaning speeds predicted using Equation (7.12) for the various footprint aspect ratios. The agreement between the simulation results and the experimentally derived values can be considered to be good, with the differences varying from 2 to 5%. It is observed that the computed hydroplaning speeds by the simulation model were consistently marginally lower than the experimentally derived values. This is possibly because the simulation model developed in this chapter could not model the effect of microtexture and the experiments were conducted on a fine-textured concrete pavement surface with some degree of surface roughness, which logically should have some beneficial drainage effect as compared with the perfectly smooth pavement surface assumed in the numerical simulation analysis. Comparing this range of differences with the simulation results presented in Section 4.6 of Chapter 4, it is noted that the effect of microtexture in the range of 0.1 to 0.2 mm would cause a deviation of approximately 2 to 5% for a tire inflation pressure of 165.5 kPa. This in fact is consistent with the error of the simulation model presented in this chapter.

Table 7.4 also lists the hydroplaning speed predicted by the original NASA equation. It clearly illustrates that by not considering the tire aspect ratio, the hydroplaning speed predicted by the original NASA equation may over- or under-estimates the actual hydroplaning speed. This indicates the need to consider the effect of footprint aspect ratio or at least the vehicle load on the hydroplaning speed.

### **7.5 Effect of Water-Film Thickness on Hydroplaning**

Numerous experimental studies (Gallaway et al. 1979, Henry and Meyer 1983, Huebner et al. 1986) have indicated that the thickness of water film on a pavement surface would also significantly affect the available wet pavement skid resistance and the hydroplaning speed. But both the NASA equation and the revised equation proposed by Horne et al. (1986) do not include the effect of water film thickness in the prediction of hydroplaning

speed. Unlike the hydroplaning simulation model presented in Chapters 3 and 4, the proposed model developed in this chapter does not have this limitation. The verification cases analyzed in the Sections 7.3 and 7.4 have demonstrated that correct hydroplaning speed predictions were obtained from the proposed model for different water depths. Hence this section aims to study in detail the effect of water-film thickness on hydroplaning.

The simulation model is applied to evaluate the hydroplaning speed under different water film thickness for the flooded plane pavement surface. Similar to the previous section, the simulation study employed an ASTM E-524 standard smooth tire with a tire inflation pressure of 165.5 kPa for ease of presentation. The applied wheel load is kept constant at 4800 N but the water film thickness is varied from 0.1 mm to 10 mm.

Figure 7.7 illustrates the relationship between the predicted hydroplaning speed from the simulation and the water-film thickness. It is observed that the predicted hydroplaning speed decreases with increasing water-film thickness. It is also noted that the rate of decrease of hydroplaning speed for the water-film thickness between 0.1 mm to 2 mm is much larger than that for water-film thickness between 2 mm to 10 mm. This is similar to findings made by past researchers (Agrawal and Henry, 1977; Gallaway et al., 1979).

Gallaway et al. (1979) developed Equation (7.13) to predict the hydroplaning speed of for rolling tires for water-film thickness greater than 2.4 mm.

$$v_p = (SD)^{0.04} (p_t)^{0.3} (TRD + 1)^{0.06} A \quad (r^2 = 0.72; N = 1038) \quad (7.13)$$

where  $A$  is the greater of  $\left[ \frac{10.409}{t_w^{0.06}} + 3.507 \right]$  or  $\left[ \frac{28.952}{t_w^{0.06}} - 7.817 \right] (MTD)^{0.14}$  and  $v_p$  is the hydroplaning speed in mph,  $SD$  is the spin-down in %,  $t_w$  is the water-film thickness in inch,  $MTD$  is the mean texture depth in inch,  $TRD$  is the tire tread depth in 1/32 inch.

For the case of 100% spin-down (i.e. the wheel stopped rotating) and a tire inflation pressure of 165.5 kPa (24 psi), smooth plane pavement surface (i.e. zero texture depth) and a smooth tire (i.e. zero tread depth), Equation (7.13) can be re-written as:

$$v_p = \frac{32.469}{t_w^{0.06}} + 10.940 \quad (7.14)$$

where  $v_p$  is the hydroplaning speed in mph, and  $t_w$  is the water film thickness in inch. It is noted that this model proposed by Gallaway et al. (1979) could not predict the NASA hydroplaning equation since the constants in Equation (7.13) are deliberately chosen to be conservative (Huebner et al., 1986).

Figure 7.7 also shows the comparison between the hydroplaning speeds predicted by the simulation model against the experimental regression equation from Gallaway et al. (1979) (Equation (7.14)) for the ASTM E-524 standard smooth tire with tire inflation pressure of 165.5 kPa and a tire load of 4800 N. It is found that the simulation results give a linear shift of Equation (7.14) as shown in Equation (7.15):

$$v_p = \frac{32.469}{t_w^{0.06}} + 15.597 \quad (7.15)$$

where  $v_p$  is the hydroplaning speed in mph, and  $t_w$  is the water film thickness in inch. The modified Equation (7.15) is now able to predict hydroplaning under locked wheel conditions for different water-film thickness from 0.1 mm to 10 mm. This shows that the simulation model has the capability to derive valuable relationships between water-film thickness and the hydroplaning speed.

## 7.6 Comparing Factors affecting Hydroplaning Speed

The simulation model can be used to study the effects of tire inflation pressure, wheel load, and the water-film thickness on hydroplaning speed. The ASTM E-524 tire is used for illustration. The ranges covered are as follows: 100 to 250 kPa for tire inflation pressure, 2400 N to 5280 N for wheel load, and 0.1 to 10 mm for water-film thickness. Table 7.5 shows the 560 different cases covered in this study.

Figure 7.8 shows the effects of the three parameters on hydroplaning speed. Figures 7.8(a) and 7.8(b) show the variation of hydroplaning speed with tire pressure for different loads and water-film thicknesses respectively. It is noted that hydroplaning speed increases with an increasing tire pressure, increasing load and decreasing water-film thickness. These trends are consistent with observations made from the experiments as described in Section 7.3.

Regression can be performed and the regression equations are shown in Table 7.6. It is noted from Tables 7.6(a) and 7.6(b) that the relationships between the hydroplaning speed and the tire inflation pressure for different loads and water-film thicknesses is similar in form to that of the NASA hydroplaning equation. The coefficients of the regression equation are found to be dependent on load and water-film thickness which are also noted from the formulation of the NASA hydroplaning equation proposed by Horne and Dreher (1963).

Compared to tire footprint aspect ratio, the information on the wheel load is more readily available in practice and it would be more convenient to use the wheel load as an independent parameter for the prediction of hydroplaning speed. Figure 7.9 shows the relationship between tire footprint aspect ratio and wheel load. It is observed that footprint aspect ratio and wheel load obey a linear relationship with a very high regression coefficient of 0.993. Referring back to Equation (7.12), it can be deduced that the hydroplaning speed should also be linearly related to the wheel load for any given tire inflation pressure. Figures 7.8(c) and 7.8(d) show the variation of hydroplaning speed with wheel load for different tire inflation pressures and water-film thicknesses respectively. It is noted that hydroplaning speed increases with increasing tire pressure, increasing load and decreasing water-film thickness. The trends shown in these figures are consistent with observations made from the experiments as described in Section 7.4. Regression can be performed and the regression equations are shown in Tables 7.6(c) and 7.6(d). It is noted that the linear relationships obtained are similar to that shown in Equation (7.12), which is derived from experiments conducted by Horne et al. (1986).

Figures 7.8(e) and 7.8(f) show the variation of hydroplaning speed with water-film thickness for different wheel loads and tire inflation pressures respectively. It is observed that the predicted hydroplaning speed decreases with increasing water-film thickness. It is also noted that hydroplaning speed decreases rapidly for water-film thickness between 0.1 mm to 2 and tends to level off for larger water-film thickness. This trend is observed for different wheel loads and tire inflation pressures respectively. Regressions are performed and the regression equations are shown in Table 7.6. It is noted from Table 7.6(e) and 7.6(f) that the relationships between the hydroplaning speed and the water-film thickness for different loads and water-



film thicknesses can be described in a form similar to that in Equation (7.14) which is experimentally derived.

It is noted that the experimentally-derived regression relationships involving hydroplaning speed against tire inflation pressure, wheel load and the water-film thickness respectively can be obtained from numerical simulations. It is also observed that these relationships are actually special cases, as the loading and environmental conditions play a critical role in the determination of the hydroplaning speed. From Figure 7.8, it can be observed that tire inflation pressure is the dominant factor affecting hydroplaning where an increase in tire inflation pressure from 100 kPa to 250 kPa would cause an increase in hydroplaning speed by about 40 km/h. The hydroplaning can be affected by the wheel load (or the footprint aspect ratio) where an increase in load from 2400 N to 5280N would cause an increase in hydroplaning speed by approximately 13 km/h. An increase in water-film thickness from 0.1 mm to 10 mm would cause a decrease in hydroplaning speed would cause a decrease in hydroplaning speed by about 15 km/h. Figure 7.10 shows the visual representation of the range of the hydroplaning speeds under the influence of these factors. It can be observed that tire inflation pressure is the primary factor that influences the hydroplaning speed, followed by water-film thickness and then wheel load. This is consistent with Horne and Dreher's (1965) findings that claimed that the tire inflation pressure is the dominant factor that can affect the hydroplaning speed and research by Gallaway et al. (1979) and Horne et al. (1986) that the water-film thickness and the wheel load can also affect the hydroplaning speed.

## 7.7 Summary

This chapter has presented the development of a computer simulation model that is capable of simulating tire-fluid-pavement interactions of a locked wheel sliding on a flooded plane pavement surface. The formulation and development of the three-dimensional finite element simulation model is based on theoretical considerations of solid mechanics, fluid dynamics, and fluid-structure interaction. The main components of the models consisting of the pneumatic tire model, the fluid flow model and the pavement surface model; and the two

interaction mechanisms, tire-pavement contact and tire-fluid interaction, are described in detail. This enables the proposed model to effectively study the variations in wet pavement skid resistance and hydroplaning speed due to changes in tire properties (such as tire elastic properties, and tire dimensions), changes in tire footprint aspect ratio caused by changes in the applied wheel load, and changes in the thickness of water film on the pavement surface. Such studies could not be performed using the hydroplaning simulation model developed in Chapters 3 and 4.

This chapter has also presented the validation of the proposed model based on hydroplaning speed prediction by checking against the well-known NASA equation, as well as other experimental data and experimentally derived relationships. It has also highlighted the importance of considering tire footprint aspect ratio in the prediction of hydroplaning speed. It is found that the hydroplaning speed increases with decreasing footprint aspect ratio of the ASTM E-524 tire (or increasing wheel load).

The respective effects of tire inflation pressure, wheel load and water-film thickness on hydroplaning speed are studied using the developed simulation model. It is found that the hydroplaning speed increases with increasing tire pressure, increasing load and decreasing water-film thickness. It is found that the experimentally-derived regression relationships involving hydroplaning speed as a function of tire inflation pressure, wheel load and water-film thickness can be obtained from the numerical simulations. These regression relationships are special cases applicable only to the test conditions of the respective studies. It is also observed that tire inflation pressure is the dominant factor affecting hydroplaning speed while wheel load and water-film thickness are the secondary factors. This illustrates the ability of the model in simulating hydroplaning and obtaining valuable relationships that are often difficult to obtain in practice unless large-scale experiments are conducted.

**Table 7.1: Contact Footprint Dimensions for Different Elastic Moduli of Tire Tread**

$E_{\text{tread}}$ (MPa)	Length of footprint (mm)	% error in length with PIARC (1995) data	Width of footprint (mm)	% error in width with PIARC (1995) data
50	212.47	37.07	151.02	-2.57
100	158.04	1.96	150.28	-3.04
150	158.10	2.00	119.87	-22.67
200	158.21	2.07	89.72	-42.11
250	158.29	2.12	59.73	-61.46

Note: Footprint length and width of 155 mm and 146 mm respectively are obtained from PIARC (1995) experiments of ASTM E524 tire with a tire inflation pressure 165.5 kPa, under a wheel load of 4,826N.

**Table 7.2: Comparison of Contact Footprint Dimensions with Experimental Data**

Test Load (N)	Footprint Dimensions obtained from Numerical Simulation			Footprint Dimensions obtained from Experiments			
	Length (mm)	Width (mm)	Footprint Aspect Ratio	Length (mm)	Width (mm)	Footprint Aspect Ratio	Source of Data
2200	106.7	145.3	1.36	107	150	1.40	Horne et al. (1986)
4826	158.0	150.3	0.95	155	146	0.94	PIARC (1995)
5200	166.1	150.3	0.90	174	150	0.86	Horne et al. (1986)

Note: Data are applicable for ASTM E524 smooth tire with a tire inflation pressure of 165.5 kPa.

**Table 7.3: Footprint Aspect Ratios for Different Loading Tested**

Load (N)	Footprint Dimensions		
	Length (mm)	Width (mm)	Footprint Aspect Ratio
2200	106.73	145.29	1.3613
2880	114.71	146.99	1.2814
3360	123.07	147.98	1.2024
3840	138.04	148.98	1.0793
4320	148.81	149.98	1.0079
4800	158.04	150.28	0.9509
5200	166.12	150.34	0.9050

Note: Data are applicable for ASTM E524 smooth tire with a tire inflation pressure of 165.5 kPa.

**Table 7.4: Hydroplaning Speeds for Different Footprint Aspect Ratios Tested**

Load (N)	Footprint Aspect Ratio	Hydroplaning Speeds (km/h)			
		Simulation Model	Experimental Model (Horne et al. 1986)	Difference between simulation and experimental model	NASA Hydroplaning Equation
2200	1.3613	71.1	73.6	-3.4%	81.8
2880	1.2814	73.8	75.8	-2.6%	81.8
3360	1.2024	74.6	78.0	-4.3%	81.8
3840	1.0793	78.2	81.4	-3.9%	81.8
4320	1.0079	79.2	83.3	-5.0%	81.8
4800	0.9509	81.3	84.9	-4.3%	81.8
5200	0.9050	83.6	86.2	-3.0%	81.8

**Table 7.5: Range of the different Parameters considered in this Study**

Parameter	Values studied
Tire Inflation Pressure $p_t$	100 kPa
	125 kPa
	150 kPa
	165.5 kPa
	175 kPa
	200 kPa
	225 kPa
	250 kPa
Wheel Load $P$	2400 N
	2880 N
	3360 N
	3840 N
	4320 N
	4800 N
	5280 N
Water-Film Thickness $t_w$	0.1 mm
	0.5 mm
	1.0 mm
	2.0 mm
	3.0 mm
	5.0 mm
	7.0 mm
	7.6 mm
	8.5 mm
	10.0 mm

**Table 7.6: Regression Relationships between Hydroplaning Speed and Different tested Parameters****(a) Hydroplaning Speed and Tire Inflation Pressure for Different Loads at 0.5 mm Water-Film Thickness**

Load	Regression Equation	$r^2$
$P = 5280 \text{ N}$	$v_p = 7.15\sqrt{p_t}$	0.998
$P = 4800 \text{ N}$	$v_p = 7.00\sqrt{p_t}$	0.999
$P = 3840 \text{ N}$	$v_p = 6.69\sqrt{p_t}$	0.999
$P = 2400 \text{ N}$	$v_p = 6.12\sqrt{p_t}$	0.997

**(b) Hydroplaning Speed and Tire Inflation Pressure for Different Water-Film Thicknesses at 4800 N Load**

Water-Film Thickness	Regression Equation	$r^2$
$t_w = 0.5 \text{ mm}$	$v_p = 7.00\sqrt{p_t}$	0.999
$t_w = 2 \text{ mm}$	$v_p = 6.72\sqrt{p_t}$	0.998
$t_w = 5 \text{ mm}$	$v_p = 6.44\sqrt{p_t}$	0.998
$t_w = 10 \text{ mm}$	$v_p = 6.24\sqrt{p_t}$	0.999

**(c) Hydroplaning Speed and Load for Different Tire Inflation Pressures at 0.5 mm Water-Film Thicknesses**

Tire Inflation Pressure	Regression Equation	$r^2$
$p_t = 100 \text{ kPa}$	$v_p = 53.3 + 0.00342P$	0.923
$p_t = 165.5 \text{ kPa}$	$v_p = 68.6 + 0.00440P$	0.939
$p_t = 200 \text{ kPa}$	$v_p = 75.4 + 0.00484P$	0.956
$p_t = 250 \text{ kPa}$	$v_p = 84.3 + 0.00541P$	0.945

**(d) Hydroplaning Speed and Load for Different Tire Inflation Pressures at 0.5 mm Water-Film Thicknesses**

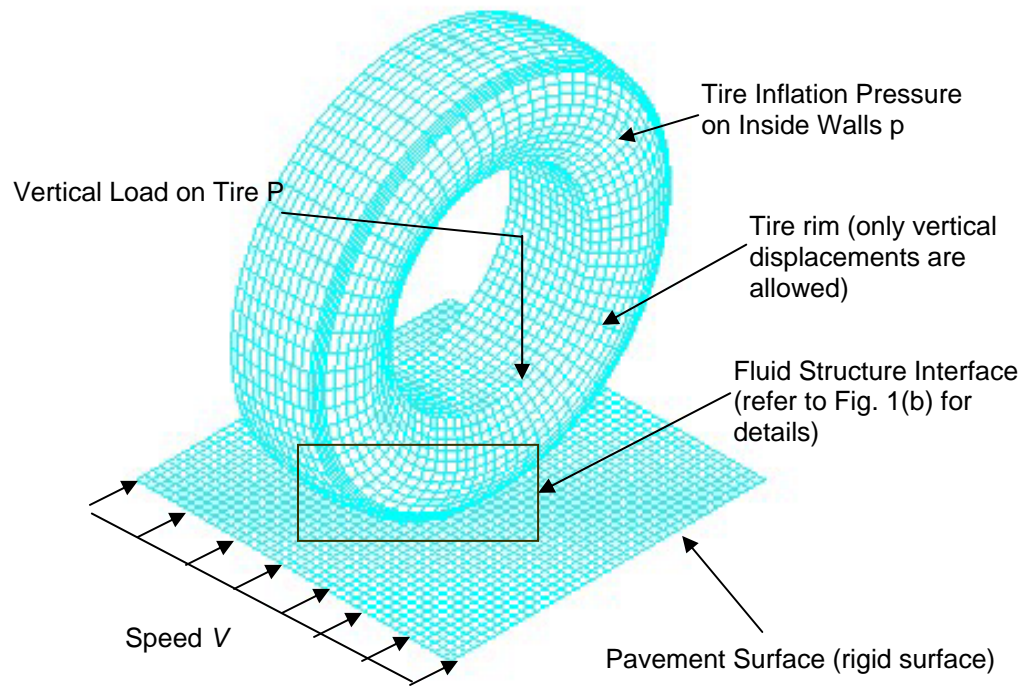
Water-Film Thickness	Regression Equation	$r^2$
$t_w = 0.5 \text{ mm}$	$v_p = 68.6 + 0.00440P$	0.939
$t_w = 2 \text{ mm}$	$v_p = 65.9 + 0.00422P$	0.927
$t_w = 5 \text{ mm}$	$v_p = 63.1 + 0.00405P$	0.932
$t_w = 10 \text{ mm}$	$v_p = 61.2 + 0.00393P$	0.954

**Table 7.6: Regression Relationships between Hydroplaning Speed and Different tested Parameters (cont'd)****(e) Hydroplaning Speed and Water-Film Thickness for Different Loads at 165.5 kPa Tire Inflation Pressure**

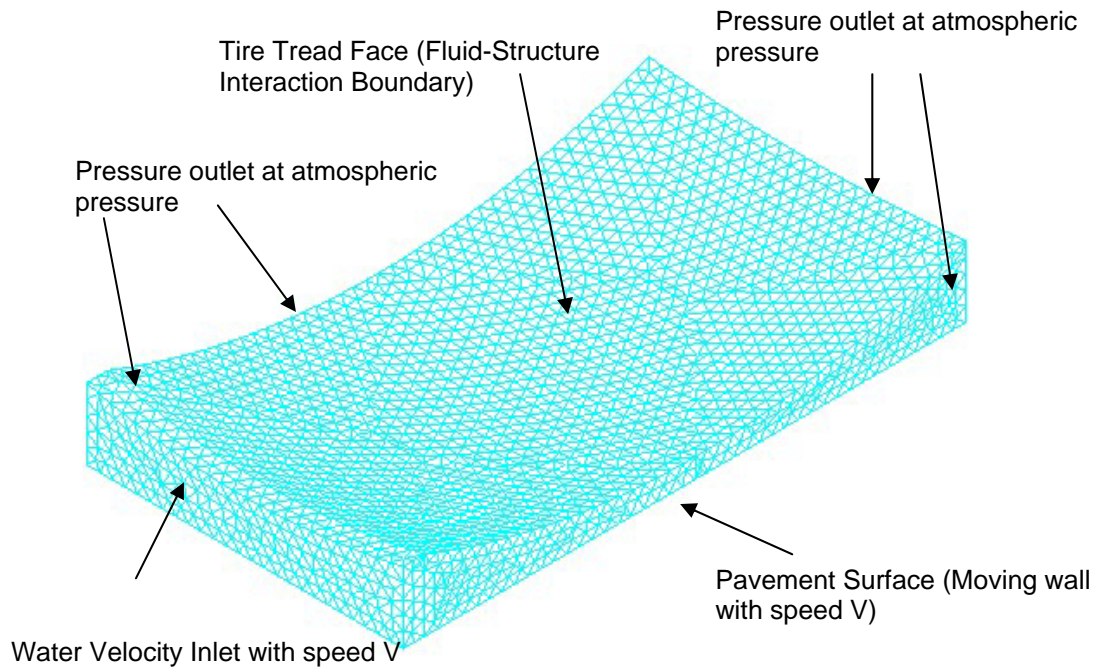
Load	Regression Equation	$r^2$
$P = 5280 \text{ N}$	$v_p = \frac{56.3}{t_w^{0.06}} + 33.8$	0.978
$P = 4800 \text{ N}$	$v_p = \frac{55.1}{t_w^{0.06}} + 33.0$	0.980
$P = 3840 \text{ N}$	$v_p = \frac{52.6}{t_w^{0.06}} + 31.6$	0.976
$P = 2400 \text{ N}$	$v_p = \frac{48.2}{t_w^{0.06}} + 28.9$	0.987

**(f) Hydroplaning Speed and Water-Film Thickness for Different Loads at 165.5 kPa Tire Inflation Pressure**

Tire Inflation Pressure	Regression Equation	$r^2$
$p_t = 100 \text{ kPa}$	$v_p = \frac{42.8}{t_w^{0.06}} + 25.7$	0.986
$p_t = 165.5 \text{ kPa}$	$v_p = \frac{55.1}{t_w^{0.06}} + 33.0$	0.980
$p_t = 200 \text{ kPa}$	$v_p = \frac{60.5}{t_w^{0.06}} + 36.3$	0.965
$p_t = 250 \text{ kPa}$	$v_p = \frac{67.7}{t_w^{0.06}} + 40.6$	0.972



(a) Pneumatic Tire Model



(b) Fluid model beneath the tire

Figure 7.1: Three-dimensional finite element model used in this study

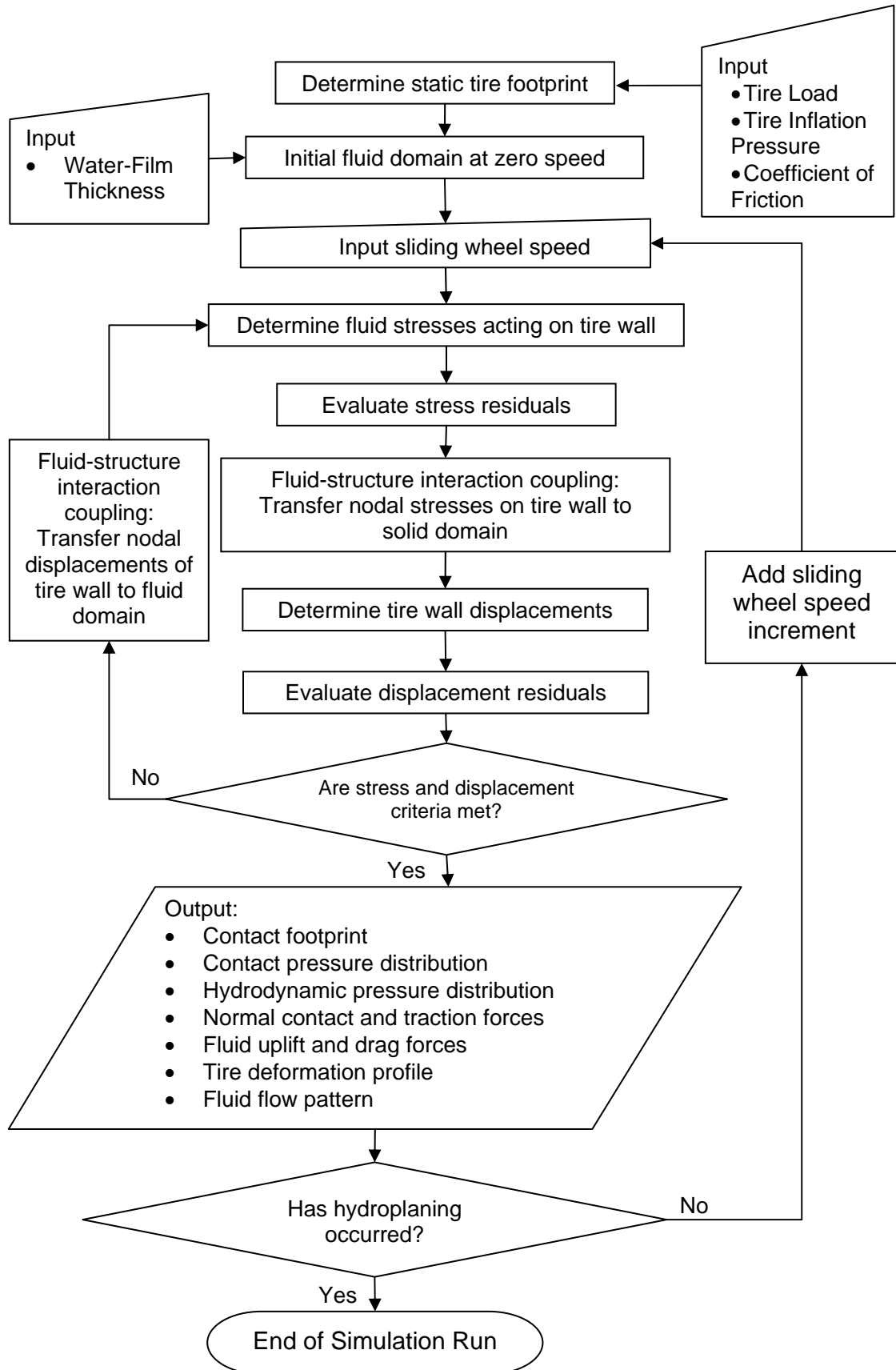


Figure 7.2: Overview of simulation procedure



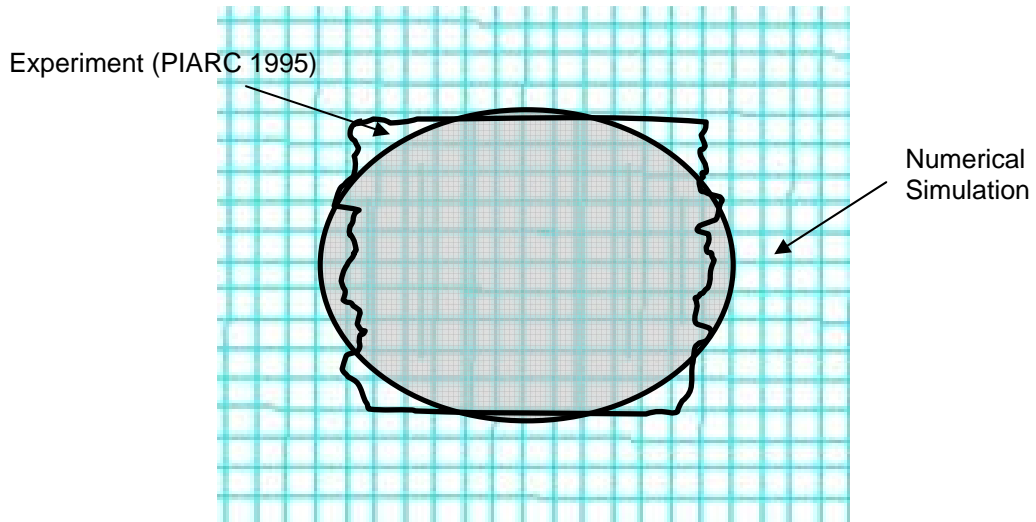


Figure 7.3: Tire contact footprints from simulation and experiment for ASTM E-524 tire at 165.5 kPa inflation pressure and 4826 N load

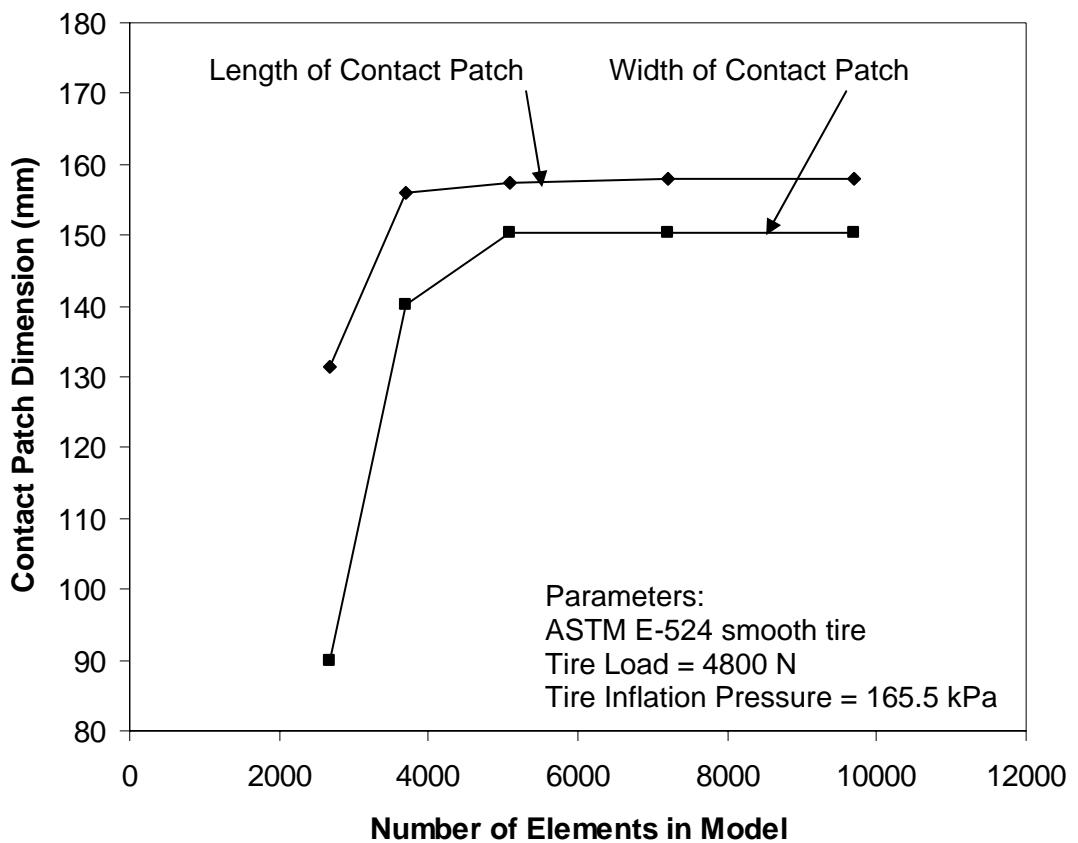


Figure 7.4: Convergence analysis of pneumatic tire model

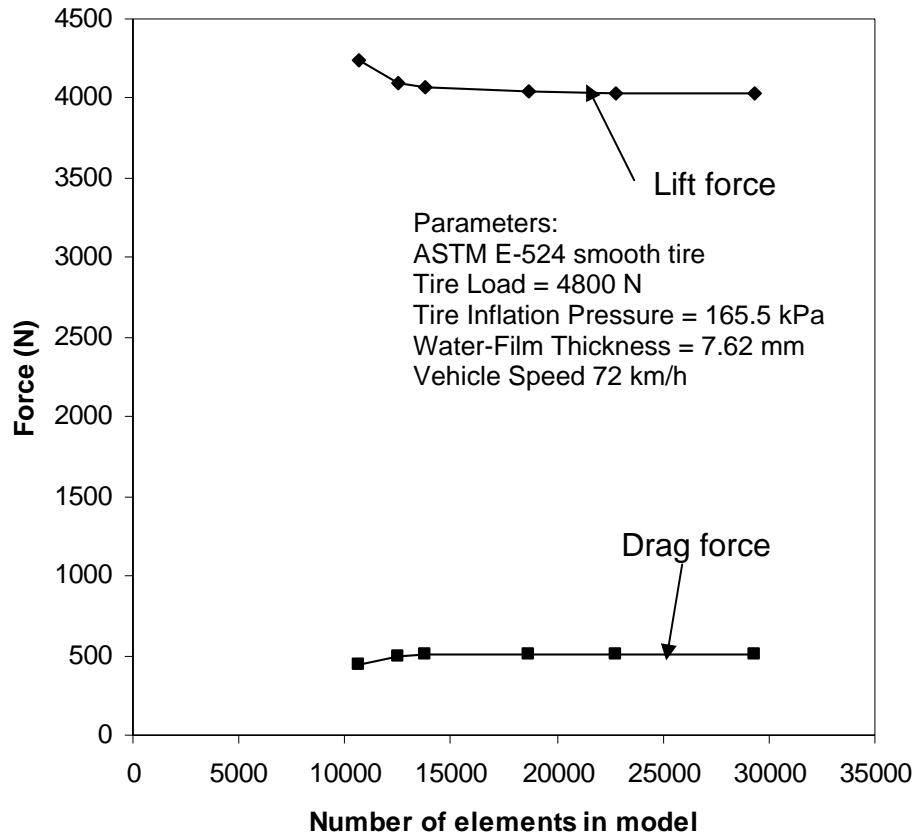


Figure 7.5: Convergence analysis of fluid model

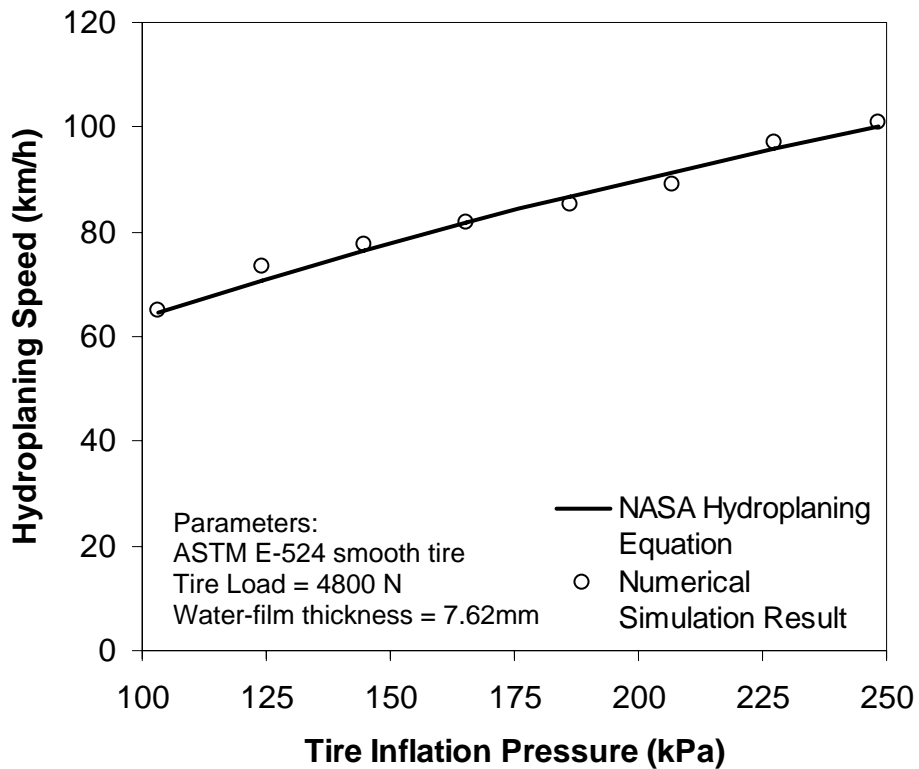


Figure 7.6: Effect of tire inflation pressure on hydroplaning speed

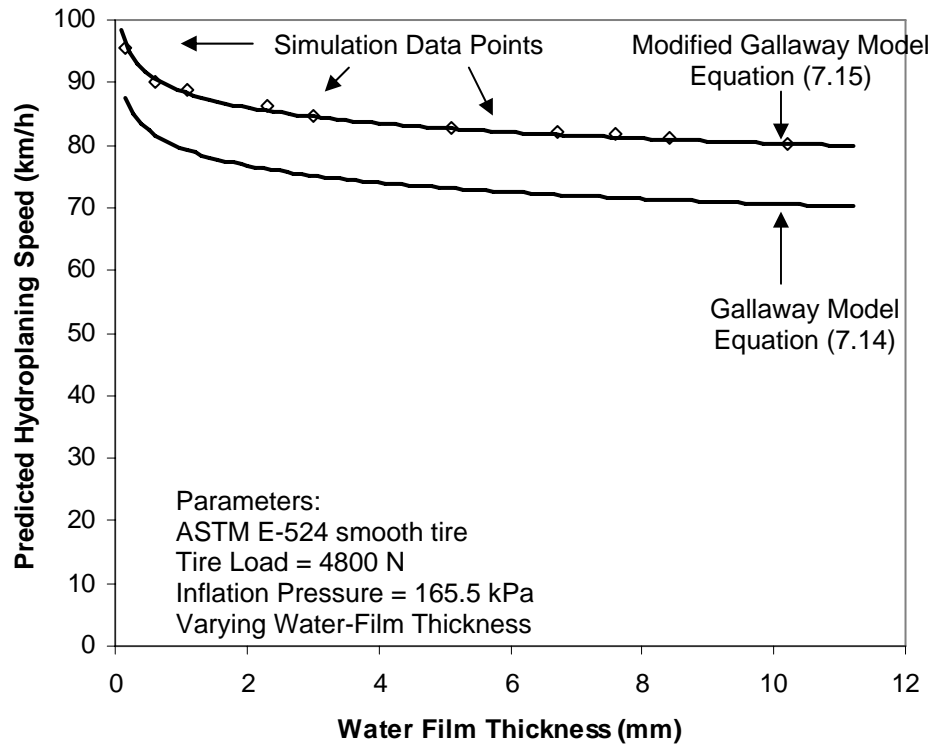
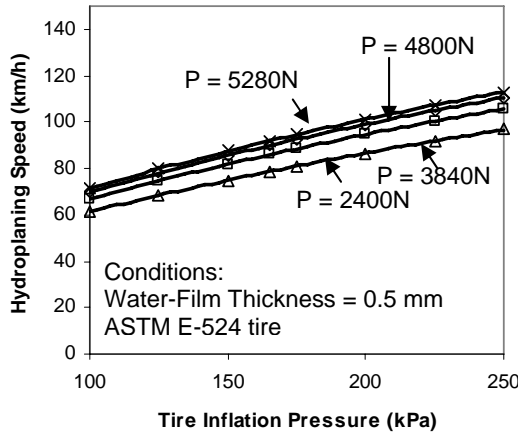
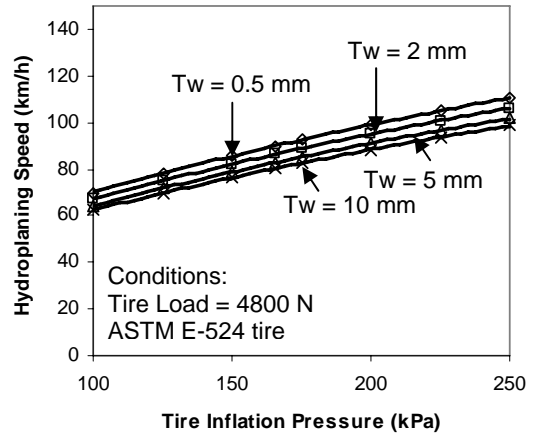


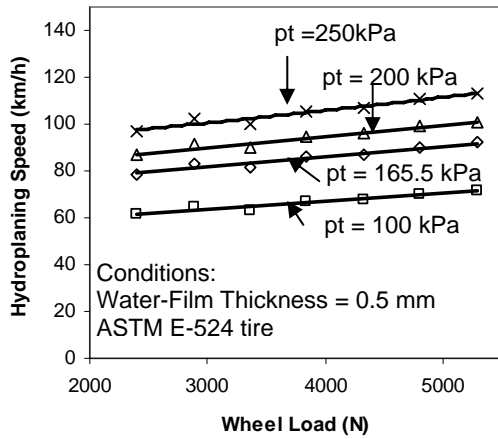
Figure 7.7: Comparison between simulation model and Gallaway model



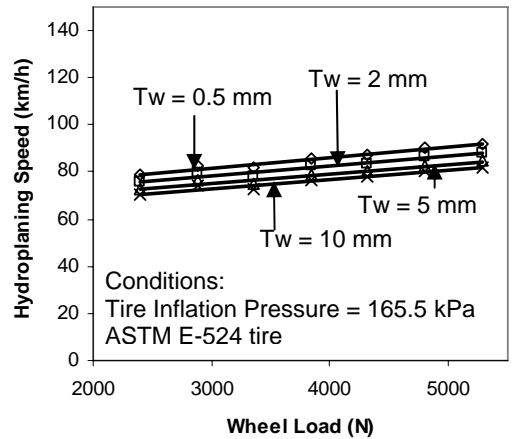
(a)



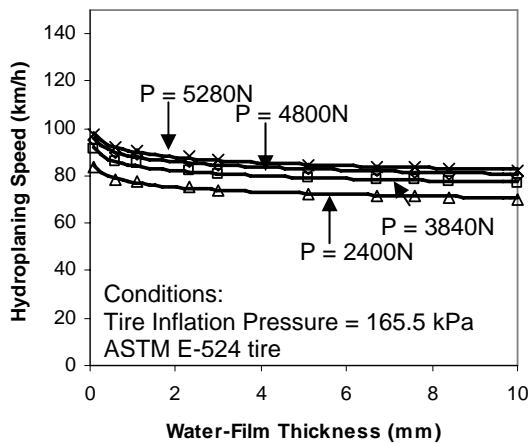
(b)



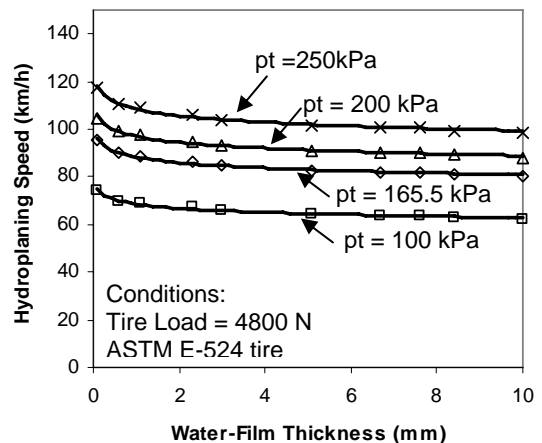
(c)



(d)



(e)



(f)

Figure 7.8: Effect of Tire Inflation Pressure, Wheel Load and Water-Film Thickness on Hydroplaning Speed

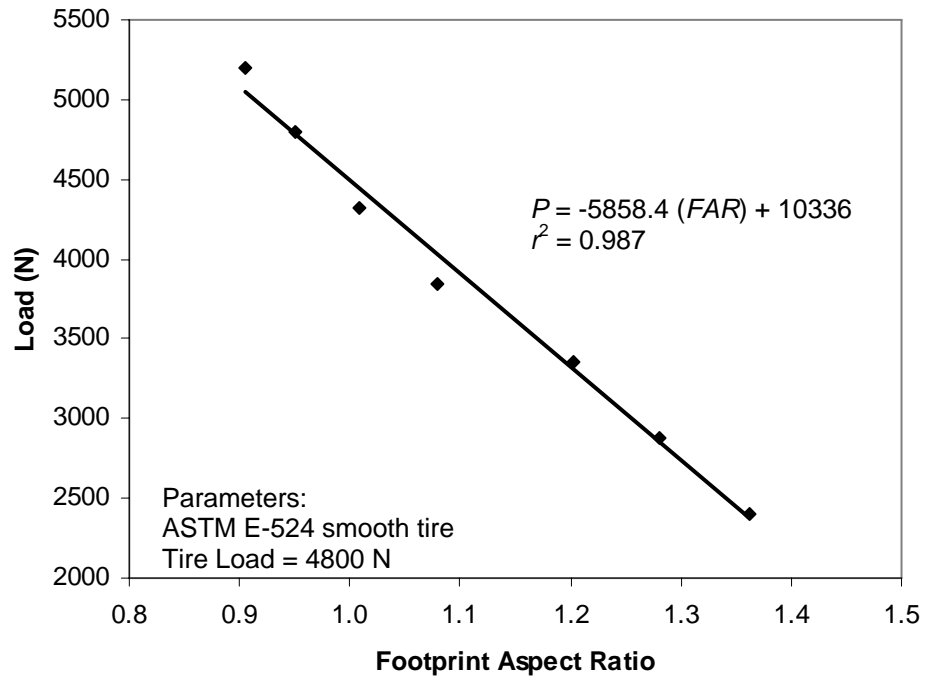


Figure 7.9: Relationship between footprint aspect ratio and wheel load

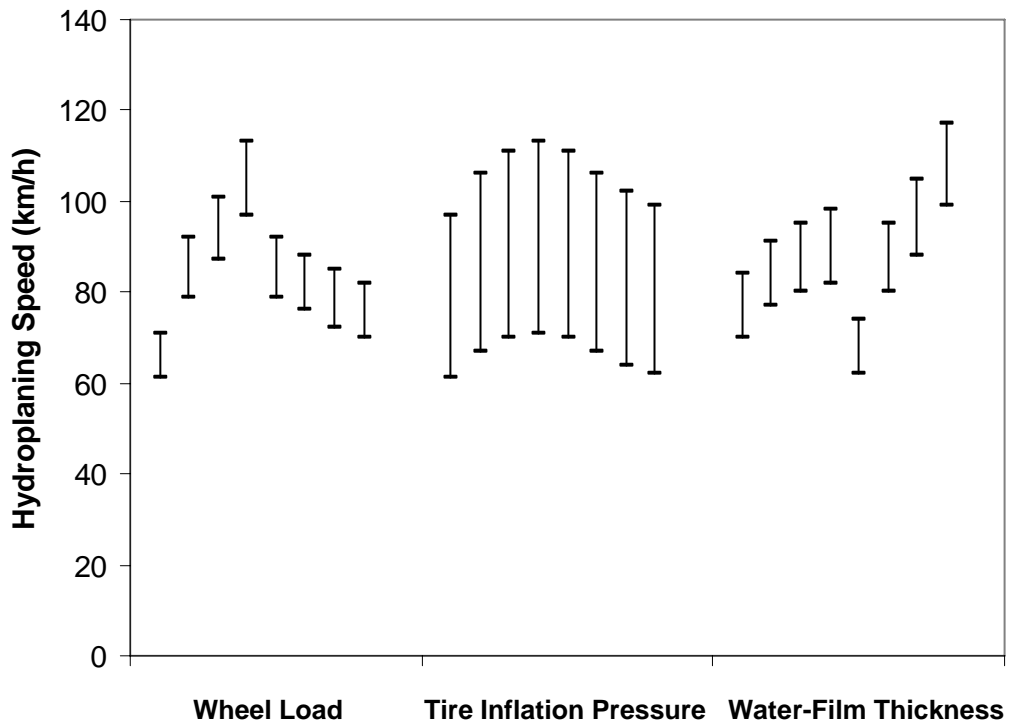


Figure 7.10: Comparison of various factors affecting hydroplaning speed

## **CHAPTER 8      NUMERICAL      MODELING      OF      WET PAVEMENT SKID RESISTANCE**

### **8.1      Introduction**

The improved simulation model developed in Chapter 7 is able to model hydroplaning under different magnitudes of wheel load and water-film thickness. These could not be studied previously using the hydroplaning simulation model developed in Chapters 3 and 4. Another limitation of the model developed in Chapters 3 and 4 is its inability to model skid resistance. The improved numerical simulation model developed in Chapter 7, which has been shown to be valid for hydroplaning simulation, could also simulate skid resistance. This is because it has considered tire-fluid interaction and tire-pavement contact in its formulation.

This chapter therefore describes the use of the improved simulation model to study skid resistance. The chapter shall first discuss the use of the simulation model in the evaluation of skid resistance of a sliding locked wheel on wet or flooded pavement. Next verification analyses against experimental skid resistance data are presented. The model is then applied to study the mechanisms of skid resistance and the effects of vehicle speed, water-film thickness, wheel loading and tire inflation pressure on skid resistance.

### **8.2      Wet-Pavement Skid Resistance Analysis by Proposed Model**

#### **8.2.1      Input Parameters**

The improved simulation model has the capability to simulate tire-fluid-pavement interactions for a locked wheel sliding on a flooded plane pavement surface, with the following input variables:

- (a) Tire dimensions – tire radius and width
- (b) Tire inflation pressure
- (c) Tire elastic properties – modulus of elasticity and Poisson's ratio of each of the following three components: tire rim, tire sidewalls, and tire tread.

- (d) Wheel load – magnitude of applied wheel load
- (e) Physical properties of water – temperature, density, dynamic viscosity, kinematic viscosity
- (f) Water film thickness on pavement surface
- (g) Sliding speed of locked wheel
- (h) Static frictional coefficient of pavement-tire contact for a wetted pavement surface

Items (a), (b), (d), (e), (f) and (g) of the input variables are relatively easy to determine.

The determination of items (c) and (h) requires some explanation. First, the tire rim can be taken to be perfectly rigid, as explained in Section 7.2.2, without much loss in computational accuracy. As for the tire sidewalls and tread, if their elastic properties are unavailable, a calibration of these properties can be conducted by means of a simple static loading test to measure the actual footprint. Next, the tire model can be used to determine the set of elastic properties that will produce a footprint matching the measured footprint.

Typically the modulus of elasticity of the tire sidewalls can vary within the range of 10 to 500 MPa, and that of the tire tread within the range of 50 to 250 MPa (Tanner, 1996). The matching of the computed and measured footprint can be evaluated based on the footprint area and its aspect ratio defined as the width-to-length ratio of the footprint. As tire footprint area and its aspect ratio change with the magnitude of wheel load, the calibration should cover the range of wheel loads expected in the skid resistance analysis. The calibration analysis for the elastic moduli of the tire sidewalls and tire tread of the standard ASTM E524 smooth tire has been described in Section 7.2.2.

The static friction coefficient,  $\mu$ , between two solid surfaces is defined as the ratio of the tangential force,  $F$ , required to produce sliding divided by the normal force,  $N$ , between the surfaces,

$$\mu = F/N \tag{8.1}$$

The static frictional coefficient of the pavement-tire contact between a tire and the wetted pavement surface can be determined in several ways. Experimentally, it can be determined in a laboratory measuring the horizontal force required to move a known mass of

tire rubber on a flat wetted surface of the pavement material of interest. Alternatively, the wetted flat surface of the pavement material could be tilted and the angle of tilt is increased until the rubber mass begins to slide down. The tangent of this angle gives the static coefficient of friction. Another method is to make a field measurement of a skid resistance value at a given sliding speed, and back-calculate the static frictional coefficient using the proposed simulation model. A detailed illustration of this back-calculation method is given in a latter section of this paper.

### 8.2.2 Computation of Skid Resistance

The detailed steps involved in the simulation analysis of the proposed model to determine the hydroplaning speed have been described in Section 7.2.1. The simulation begins with a wheel sliding speed of zero and the static tire footprint. The sliding speed is increased in a pre-defined increment until hydroplaning takes place when the fluid uplift force is equal to the wheel load. At any speed during the simulation, the following forces acting on the tire can be computed: the vertical fluid uplift and the horizontal drag forces due to tire-fluid interaction, and the vertical tire-pavement contact forces and the horizontal traction forces developed within the tire-pavement contact area.

The skid number  $SN$  at speed  $v$  (km/h) can be defined as:

$$SN_v = 100 \times \frac{F_x}{F_z} \quad (8.2)$$

where  $F_x$  is the horizontal resistance force to motion acting on the axle of the tire and  $F_z$  is the vertical loading acting on the tire. The horizontal resistance force  $F_x$  is equal to the traction forces developed at the tire-pavement contact and the fluid drag forces due to the tire-fluid interaction. The vertical loading  $F_z$  is an input parameter and remains constant throughout the simulation. It is also equal to the sum of the normal contact force and the fluid uplift forces.



### 8.3 Validation of Skid Resistance Prediction

#### 8.3.1 Experimental Data and Validation Approach

In view of the practical importance in understanding the various factors that affect the available wet-pavement skid resistance at different sliding speeds of a locked wheel, quite a number of experimental studies have been conducted in the past in accordance with the standard skid resistance test procedure using the ASTM E524 smooth tire (ASTM, 2005f). These experimental studies provide ready skid resistance data for the validation of the simulation model proposed in this paper. Only those tests conducted on plane pavement surfaces are considered. Table 8.1 lists the studies the experimental data of which are used for the validation analysis in this paper. It also summarizes the experimental test conditions of each study.

As all the tests listed in Table 8.1 used the ASTM standard E524 smooth tire (ASTM 2005f). The tire inflation pressure of 165.5 kPa is used in the simulation. The elastic moduli and Poisson's ratios for the tire rim, tire sidewalls and tire tread are taken to be 100 GPa and 0.3, 20 MPa and 0.45, and 100 MPa and 0.45 respectively. The density of the rim material is 2700 kg/m<sup>3</sup>, and that of the rubber material of the tire sidewalls and tire tread is 1200 kg/m<sup>3</sup>.

None of the studies reported the test temperature. This information is required for determining the properties of water. Fortunately, the very small changes in the properties of water within the normal range of temperatures between 15 to 35°C do not have any significant impact on the results of the simulation analysis. For all the cases simulated, the properties of water at 25°C are used. The density, dynamic viscosity and kinematic viscosity of water at 25°C are 997.1 kg/m<sup>3</sup>, 0.894 x 10<sup>-3</sup> Ns/m<sup>2</sup> and 0.897 x 10<sup>-6</sup> m<sup>2</sup>/s respectively (Chemical Rubber Company 1988).

Another unknown parameter is the static frictional coefficient which is a required input to the simulation analysis. Since all the tests in Table 8.1 measured pavement skid resistance in terms of SN<sub>v</sub>, the static frictional coefficient can be taken to be the skid number at a speed of zero, i.e. SN<sub>0</sub>. This required information of SN<sub>0</sub> is not available in any of the study cases listed

in Table 8.1. To overcome this problem, the following approach based on back-calculating of  $SN_0$  is adopted:

- (a) For each of the test studied in Table 8.1, a skid resistance measurement  $SN_i$  (i.e. skid resistance measured at speed  $i$ ) is randomly picked as the basis for back-calculating the value of  $SN_0$  using the proposed simulation model.
- (b) With the back-calculated value of  $SN_0$ , predict all other skid resistance values using the proposed simulation model and compare with the actual measured skid resistance in the test study.

The back-calculation of  $SN_0$  in step (a) is necessarily a trial and error process. For the selected skid resistance  $SN_i$ , a trial  $SN_0$  value is first assumed to run the simulation analysis to obtain an estimated  $SN_i$ . Based on the difference between the estimated and measured  $SN_i$ , a revised trial  $SN_0$  is assumed. This process is repeated until the estimated  $SN_i$  is sufficiently close to the measured  $SN_i$ . The back-calculated  $SN_0$  is next used as the input to predict the skid resistance values at other vehicle speeds.

### 8.3.2 Results of Validation

Table 8.2 summarizes the results of the validation analysis. It is observed that the numerical differences between the predicted and measured  $SN_v$  are at most 5.5. In fact, only 3 of the 32 test cases studied have a difference in SN larger than 3.0. In terms of percentage error, except for one case with 36.7% error, all the remaining 32 cases have errors of 16% or less. The results suggest that the simulation model is able to predict wet-pavement skid resistance at a given sliding locked wheel speed with satisfactory accuracy for practical applications.

Figure 8.1 shows the comparison between the predicted SN-v curves obtained from the numerical simulation and the corresponding measured SN values at different vehicle speeds. It is also noted the back-calculated  $SN_0$  values fall within the observed range of friction coefficients for rubber on wet concrete and wet asphalt pavements which are 0.35 to 0.75 and 0.40 to 0.75 respectively (Lee et al., 2005).

## 8.4 Analysis of Simulation Results on Mechanisms of Skid Resistance with Vehicle Speed

It is of theoretical interest to pavement researchers and practical importance to highway and airfield engineers to have a good understanding of the mechanisms responsible for the deterioration of wet-pavement skid resistance with increasing sliding speed of a locked wheel. The numerical simulation model, based on fundamental engineering concepts and theories, offers a practical and useful tool to gain an insight into the mechanisms through the detailed responses of the tire, the fluid and the pavement surface available from the simulation. The following sub-sections examine the simulation results in detail and attempt to offer some explanations on the roles of various factors that contribute to the progressive loss of wet-pavement skid resistance as the sliding speed of a locked wheel is raised.

### 8.4.1 Forces Contributing to Skid Resistance

By the definition of skid resistance given in Equation (8.2), it is clear that since the vertical loading  $F_z$  remains constant throughout the sliding process, the only variable that is responsible for the changes in the measured skid resistance is the horizontal resistance force  $F_x$ . The horizontal resistance force is the sum of the two forces: the traction force that develops at the tire-pavement contact interface to resist the sliding movement, and the fluid drag force due to the tire-fluid interaction caused by the fluid flow. The relative contributions of these components and their respective variations as the sliding speed changes will have direct influences on how the overall horizontal resistance force  $F_x$  changes in the process.

Based on the simulation results of a typical case analyzed, Figure 8.2(a) plots the changes in the horizontal traction force at the tire-pavement contact and the horizontal fluid drag force, respectively, with the sliding locked wheel speed. The traction force is a result of the Coulomb's friction action on the tire-pavement contact area, while the fluid drag force is a result of the fluid inertial forces. Initially at zero sliding speed of the locked wheel, there is no drag force and the total skid resistance is equal to that provided by the traction force. As the wheel sliding speed picks up, there is a gradual loss in the horizontal traction force up to about

a sliding speed of 20 km/h. Thereafter, there is a much faster rate of decrease in the traction force with the sliding speed, up to the point where hydroplaning occurs (82 km/h for the case shown in Figure 8.2(a)).

While the horizontal traction force decreases with the sliding wheel speed, the fluid drag force actually increases as the speed of fluid flow (in relation to the wheel or tire) rises. However, the magnitude of the increase of the drag force with speed is rather small compared with the corresponding loss of traction force at any given sliding speed. The increase in drag force is insufficient to compensate for the loss of traction force. As a result, there is a net loss in the total horizontal resistance force  $F_x$  as the locked-wheel sliding speed increases.

Figure 8.2(b) shows the relative percentage contributions of the two components of the horizontal resistance force at different sliding speeds. It is apparent that the traction force at the tire-pavement contact is the key contributor to wet-pavement skid resistance, being the dominating contributing component until a sliding speed close to the hydroplaning speed (i.e. until about 70 km/h for the case shown in Figure 8.2(b) with a hydroplaning speed of 82 km/h). It is noted that even when the drag force reaches its maximum at the point of hydroplaning, its magnitude of  $SN = 9.5$  is only 15.8% of the initial skid resistance  $SN_0 = 60$  available at zero or low sliding speed.

The above observation suggests that in practical design of highway or runway pavements, it makes sense to ignore the contribution of the drag force, and focus on selecting a pavement surface material that could offer a high static coefficient of friction, (i.e.  $SN_0$ ) so as to reduce the impact of skid resistance loss as the wheel sliding speed increases.

#### **8.4.2 Tire-Fluid-Pavement Interaction**

The increase in the fluid drag force with the wheel sliding speed can be attributed to the higher fluid inertial forces as the flow speed increases. On the other hand, the progressive loss of the traction force at the tire-pavement contact involves a more complex mechanism. It is due to the gradual reduction in the tire-pavement contact area (i.e. the size of tire footprint) as a result of tire-fluid-pavement interaction.

The changes in the area of the tire-pavement as the sliding speed increases are basically caused by the development of the fluid uplift force arising from the interaction between the fluid flow and the tire wall. Figure 8.3 shows the rising trend of the fluid uplift force as the wheel sliding speed, and hence the fluid flow speed relative to the wheel, becomes larger. Another direct result of the increased fluid uplift force is the reduction in tire-pavement contact area due to the upward deformation of the tire wall under the action of the increased fluid uplift force. This is apparent from the plot in Figure 8.4 that shows the reduction of the area of the tire-pavement contact zone (i.e. Zone B indicated in the figure). This reduction trend continues as higher and higher fluid uplift force is developed due to the higher fluid flow speed as a result of increasing sliding wheel speed, and diminishes to zero value when the uplift force becomes equal to the wheel load and causes hydroplaning to occur.

To sum up, the following sequence of events take place in the tire-fluid-pavement interaction process as the wheel sliding speed is raised. When the sliding speed is increased, the higher fluid flow speed causes a higher fluid uplift force to develop. This results in some upward deformation of the tire wall, thereby reducing the contact area (i.e. tire footprint) at the tire-pavement interface. With the reduced contact area, both the vertical normal force and the horizontal traction force at the tire-pavement interface are also reduced. This explains decreasing trend of the normal force in Figure 8.3, and the decreasing trend of the horizontal traction force in Figure 8.2(a).

#### **8.4.3 Variation of Tire-Pavement Contact Zone**

The tire-fluid-pavement interaction described in the preceding section is responsible for the reduction of the tire-pavement contact area as a higher wheel sliding speed is introduced. Figure 8.5 shows the stages of reduction of the tire-pavement contact zone as the sliding wheel speed increases. The boundary of the tire-pavement contact zone at each sliding wheel speed can be easily delineated from the nodal coordinates of the finite-element mesh at the tire-pavement interface, as depicted in the various sectional views “View X-X” shown in Figure 8.5.

Figure 8.5 indicates that as the wheel sliding speed is increased, part of the tire-pavement contact zone in the original tire footprint area is replaced by the so-called water-film zone. It can be observed that as the sliding wheel speed increases, the tire-pavement contact zone gradually retreats to the rear of the tire until the point of hydroplaning where there is a complete loss of the tire-pavement contact zone and the tire is sliding on a thin film of water. This process depicted in Figure 8.5 is similar to the conceptual skid resistance mechanism proposed by Veith (1983).

Based on the theories of fluid dynamics and solid mechanics adopted in the formulation of the simulation model, the fundamental principles involved in the tire-pavement contact zone and the water-film zone can be briefly described as follows.

- Water-film zone: In this zone, elasto-hydrodynamic lubrication forces dominate. The fluid forces acting on the tire wall is modeled using the Navier-Stokes equation with the consideration of turbulence in the simulation model. This in turn causes tire wall deformation which is modeled by solid mechanics theories. The friction contribution to skid resistance is governed by the fluid drag force in this zone, which is dependent on the fluid bulk properties and the sliding wheel speed.
- Tire-pavement contact zone: In this zone, the Coulomb friction law is applicable. The friction contribution to skid resistance is governed by the actual contact area and the skid number at zero speed,  $SN_0$ . In accordance with the Coulomb friction law, the reduction in the contact area leads to reduced values of the normal contact force and the horizontal traction force respectively.

#### **8.4.4 Characteristics of SN-Speed Curves**

An examination of the shapes of the SN-speed relationship curves in Figure 8.1, which are obtained from the simulation results of the proposed model, reveals that there is an initial phase of gentle change in the skid resistance with sliding wheel speed, followed by another phase of a relatively rapid rate of fall of the skid resistance. For the cases studied, as depicted in Figure 8.1, the transition point appears to take place at a sliding speed of about 20 km/h.

As can be seen from Figure 8.1, the rates of fall in skid resistance after the transition point vary among the 6 cases analyzed in this study. The rate of fall in each case is governed by the initial static coefficient of friction  $SN_0$  (representing approximately the skid resistance at the transition point), and the hydroplaning speed at which the hydroplaning occurs (representing the end point of the fall of skid resistance). The value of  $SN_0$  is purely a function of the surface characteristics of the tire and the pavement. A high  $SN_0$  can be achieved by selecting good quality paving materials which produce a high coefficient of friction between the tire and the wetted pavement surface.

The end point of the SN-speed curve is defined by the hydroplaning speed and the residual skid resistance available at hydroplaning. According to the proposed simulation model, there is no tire-pavement contact when hydroplaning occurs and the contribution to skid resistance from tire-pavement friction is zero. The residual skid resistance at hydroplaning is contributed totally by the fluid drag force (see Figure 8.2). However, improving the roughness texture of the pavement surface can affect the flow conditions and raise both the hydroplaning speed and the residual skid resistance. It can be achieved through an appropriate selection of the paving mix design (e.g. friction course mix) and the application of surface roughness treatment (e.g. grooving, or other means to improve either the microtexture or macrotexture of pavement surface). This has the overall effect of reducing the rate of fall of skid resistance with sliding wheel speed, and achieve a higher skid resistance at any given sliding wheel speed.

### **8.5 Comparing Factors Affecting Skid Resistance**

The simulation model can be used to study the effects of tire inflation pressure, wheel load, and water-film thickness on the skid resistance measured in terms of skid number SN. The ASTM E-524 tire is used for illustration. The ranges covered are as follows: 100 to 250 kPa for tire inflation pressure, 2400 N to 5280 N for wheel load, and 0.1 to 10 mm for water-film thickness. Table 8.3 shows the different cases covered in this study.

### 8.5.1 Effect of Wheel Load on Skid Resistance

The plots that present the effects of wheel load are found in Figures 8.6(a) and (b) for the analysis of skid resistance. The following observations of the effects of wheel load on skid resistance can be made:

- (i) In general, all other parameters being constant, wet-pavement skid resistance increases as wheel load becomes larger.
- (ii) Figure 8.6(a) shows that as the wheel load is increased from 2400 N to 5280 N, the gain in SN remains more or less constant with  $t_w$ , the thickness of water film. The total gain in skid resistance  $\Delta SN$  is about 10 for the water-film thickness  $t_w$  ranging between 0.5 mm to 10 mm.
- (iii) Figure 8.6(b) shows the variation of SN with sliding speed as the wheel load is increased from 2400 N to 5280 N. At a low speed of 20 km/h, SN remains more or less constant (i.e. not affected much by changes in wheel load). At wheel sliding speed of 40 and 60 km/h respectively, there are significant increases in skid resistance as the wheel load is raised. However, the rate of increase falls when the wheel sliding speed is increased to 80 km/h. This trend is similar to that exhibited in past research by Sacia (1976).

The mechanism that leads to the changes in the skid number SN is rather complex as can be seen from the following re-written form of Equation (8.3),

$$SN_v = 100 \times \frac{F_x}{F_z} = 100 \times \frac{\mu(F_z - Uplift) + Drag}{F_z} \quad (8.3)$$

$$\text{i.e. } SN_v = 100 \times \left[ \mu + \frac{Drag - \mu(Uplift)}{F_z} \right] \quad (8.4)$$

where  $\mu$  is the coefficient of friction between the tire and the pavement surface. All three variables  $F_z$ , drag and uplift forces will vary as the applied wheel load changes. Figure 8.7 shows an example of the computed variations of these variables with wheel load. It is noted that the three variables increase with increasing wheel loads for the same vehicle sliding speed of 64 km/h and tire inflation pressure of 165.5 kPa, but at different rates. The rate of increase is



the highest for  $F_z$ , followed by  $\mu$ (Uplift) and lastly the drag force. This means that the latter term in Equation (8.4) increases in magnitude with increasing load and hence  $SN_{64}$  increases with increasing wheel load.

### 8.5.2 Effect of Tire Inflation Pressure on Skid Resistance

The plots that present the effects of tire inflation pressure are found in Figures 8.6(c) and (d) for the analysis of skid resistance. The following observations of the effects of tire inflation pressure on skid resistance can be made:

- (i) In general, all other parameters being constant, wet-pavement skid resistance increases marginally as tire inflation pressure becomes larger.
- (ii) Figure 8.6(c) shows that as the tire inflation pressure increases from 100 kPa to 250 kPa, the SN remains marginally affected for the different wheel load levels.
- (iii) Figure 8.6(d) shows the variation of SN with sliding speed as the tire inflation pressure increases from 100 kPa to 250 kPa. It is noted that SN is not affected much for vehicle speeds up to 60 km/h. This trend is similar to that exhibited in past research by Sacia (1976).

### 8.5.3 Effect of Water-Film Thickness on Skid Resistance

The plots that present the effects of water-film thickness are found Figures 8.6(e) and (f) for the analysis of skid resistance. The following observations of the effects of water-film thickness on skid resistance can be made:

- (i) In general, all other parameters being constant, wet-pavement skid resistance decreases with increasing water-film thickness and tends to level off for water-film thickness larger than 6 mm.
- (ii) Figure 8.6(e) shows the variation in SN with wheel loads as the water-film thickness increases from 0.1 mm to 10 mm at a vehicle sliding speed of 60 km/h. It is observed that the loss in SN is 6 for wheel load  $P = 2400$  N and increases to 45 for  $P = 5280$  N.

- (iii) Figure 8.6(f) shows the variation of SN with sliding speed as the water-film thickness increases from 0.1 mm to 10 mm. At a low speed of 20 km/h, SN remains more or less constant. At wheel sliding speed of 40 and 60 km/h respectively, there are significant decreases in skid resistance with an increase in water-film thickness. However, the rate of decrease falls when the wheel sliding speed is increased to 80 km/h. This trend is similar to that exhibited in past research by Sacia (1976) and Rose and Gallaway (1977).

#### 8.5.4 Effect of Vehicle Speed on Skid Resistance

Figures 8.6(g) and (h) present the analysis of the effects of vehicle sliding speed on skid resistance. The following observations of the effects of water-film thickness on skid resistance can be made:

- (i) In general, all other parameters being constant, wet-pavement skid resistance decreases with increasing vehicle speed.
- (ii) Figure 8.6(g) shows the variation in SN with vehicle speed for different water-film thickness. It is observed that SN decreases from 60 at zero speed to 10 to 20 at hydroplaning (depending on the water-film thickness). At vehicle speeds below 20 km/h, SN remains more or less constant for the different water-film thickness. At higher vehicle sliding speeds, a lower SN is observed for a larger water-film thickness.
- (iii) Figure 8.6(h) shows the variation of SN with sliding speed as the wheel load increases from 2400 N to 5280 N. It is observed that SN decreases from 60 at zero speed to about 10 to 15 at hydroplaning (depending on the wheel load). At vehicle speeds below 20 km/h, SN remains more or less constant for the different water-film thickness. At higher vehicle sliding speeds, a lower SN is observed for a smaller wheel load. This behavior is similar to that exhibited in past experimental research (Sacia, 1976; Gallway et al., 1979).

### **8.5.5 Comparison of Factors affecting Skid Resistance**

Table 8.4 shows the comparison of the effects of wheel load, tire inflation pressure and water-film thickness on the range of predicted skid numbers. For easy presentation, Figure 8.8 shows the visual representation of the range of SN under the influence of these factors. It can be observed that vehicle speed is the primary factor that influences the skid number, followed by water-film thickness, wheel load and then tire inflation pressure. This is consistent with the experimental findings by Sacia (1976) which indicate that vehicle speed is a key factor in the reduction of skid resistance on wet and flooded pavements followed by water-film thickness, wheel load and tire inflation pressure.

### **8.6 Summary**

This chapter has discussed the use of the developed numerical model in the simulation of skid resistance of a locked wheel traveling on wet or flooded pavement surfaces. The application of the proposed skid resistance simulation model to study the decreasing trend of wet-pavement skid resistance with the sliding speed of a locked wheel has been illustrated in this chapter. The validity of the proposed model is verified by checking the predicted skid resistance values with the measured skid resistance data of experimental studies conducted by past researchers. Very good matching is found between the predicted values by the proposed numerical model and the measured data from different sources. The validation check has verified that the proposed simulation model could satisfactorily estimate the wet-pavement skid resistance at different locked-wheel sliding speeds for different water film thicknesses. The analytical model thus offers a useful tool to predict the magnitude of wet-pavement skid resistance at any given locked-wheel sliding speed.

The chapter has also demonstrated that the proposed simulation model, which is based on fundamental engineering concepts and theories, is able to provide detailed information on the behaviors and responses of the tire, the fluid and the pavement surface at different sliding speeds of the locked wheel. From the computed changes of the tire contact area, the normal contact force, and the fluid uplift force and drag force as the locked-wheel sliding speed is

increased, a good insight into the deterioration mechanism of wet-pavement skid resistance can be obtained.

The simulation model is then applied to evaluate the effects of the following four factors on skid resistance: wheel load, tire inflation pressure and water-film thickness, and vehicle sliding speed. The skid resistance is found to increase with wheel load and marginally with tire pressure, but decrease as the sliding wheel speed or the water-film thickness increases. Vehicle sliding speed was the most important factor affecting the magnitude of skid resistance, followed by water-film thickness, wheel load and tire inflation pressure. The analysis demonstrates that the analytical simulation model is a convenient tool for predicting wet-pavement skid resistance and hydroplaning speed as shown in Chapter 7, and is also an effective means to study the influences of various factors on hydroplaning and skid resistance without the need to conduct large-scale experiments

**Table 8.1: Test Conditions for Skid Numbers at Different Vehicle Speeds**

Source of Data	Pavement Surface Type	Tire Inflation Pressure (kPa)	Load (N)	Water-Film Thickness (mm)	Test Speed (km/h)
Rose and Gallaway (1977)	Concrete	165.5	4800	0.1	32
					64
					80
				5.0	32
					64
					80
	15.0	32			
		64			
		80			
	220.6	4800	5.0	32	
				64	
				80	
15.0			32		
			64		
			80		
Horne (1969)	Ungrooved Concrete	165.5	4800	5.08– 10.16 (7.62 mm used in simulation)	8
					16
					32
					48
					64
	80				
	Asphalt	165.5	4800	5.08– 10.16 (7.62 mm used in simulation)	48
					64
					80
	Horne and Tanner (1969)	Concrete	165.5	4800	5.08– 10.16 (7.62 mm used in simulation)
64					
80					
Small-aggregate Asphalt		165.5	4800	5.08– 10.16 (7.62 mm used in simulation)	32
					40
Agrawal and Henry (1977)	Smooth Concrete	165.5	2861	1.47	48
					64
					72
					80

**Table 8.2: Comparison between Experimental and Simulation Results for SN**

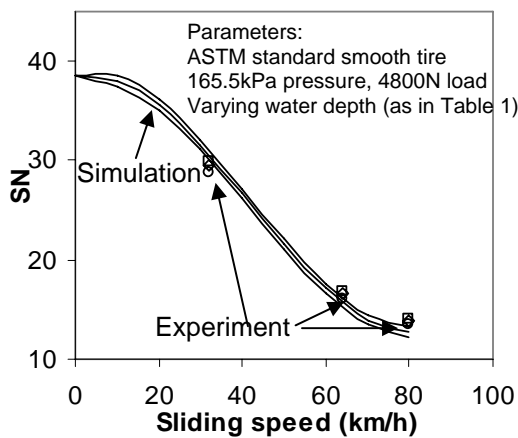
Source	Experimental Data		Predicted $SN_v$	Numerical Difference	Percentage error	Back-calculated $SN_0$
	Test Speed	Measured $SN_v$				
Rose and Galloway (1977)	32	30	32.1	-2.1	-7.0%	-
	64	17	16.0	1	5.9%	-
	80	14	13.3	0.7	5.0%	38.5
	32	29	31.6	-2.6	-9.0%	-
	64	16	15.5	0.5	3.1%	38.5
	80	14	12.8	1.2	8.6%	-
	32	29	31.1	-2.1	-7.2%	-
	64	16	15.0	1	6.3%	-
	80	13	12.3	0.7	5.4%	38.5
	32	43	42.4	-0.6	-1.4%	52.5
	64	26	25.5	-0.5	-1.9%	-
	80	22	24.0	2.0	9.0%	-
	32	46	45.6	-0.4	-0.8%	52.5
	64	26	25.5	-0.5	-1.9%	-
80	22	23.4	1.4	6.3%	-	
Horne (1969)	8	60	59.6	0.4	0.7%	60
	16	55	57.4	-2.4	-4.4%	-
	32	45	48.7	-3.7	-8.2%	-
	48	35	36.1	-1.1	-3.1%	-
	64	20	22.2	-2.2	-11.0%	-
	80	15	9.5	5.5	36.7%	-
	48	45	44.0	1.0	2.2%	72.5
	64	30	25.2	4.8	16.0%	-
80	10	11.5	-1.5	-15.0%	-	
Horne and Tanner (1969)	32	49	48.7	0.3	0.6%	60
	64	25	22.2	2.8	11.2%	-
	80	10	10.7	-0.7	-7.0%	-
	32	45	44.4	0.6	1.3%	55.0
	40	40	38.8	1.2	3.0%	-
Agrawal and Henry (1977)	48	30	29.3	0.7	2.3%	47.5
	64	20	19.2	0.8	3.9%	-
	72	15	14.6	0.4	2.7%	-
	80	12	10.6	1.4	11.7%	-

**Table 8.3: Factors considered in parametric study of skid resistance for the ASTM E524 tire on plane pavement surface**

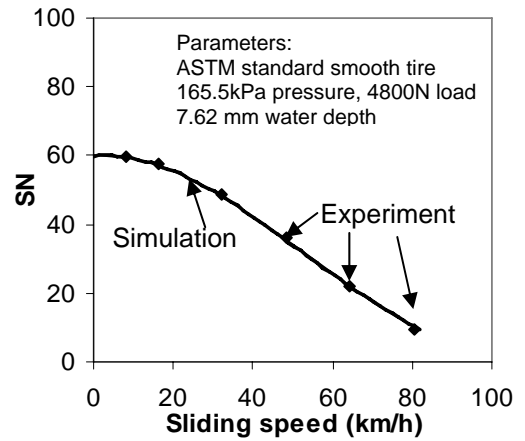
Factor	Range
Wheel load	2400 N to 5280 N
Tire inflation pressure	100 kPa to 250 kPa
Wheel sliding speed	0 km/h to hydroplaning speed
Water-film thickness	0.1 mm to 10 mm

**Table 8.4: Comparison of factors affecting skid resistance**

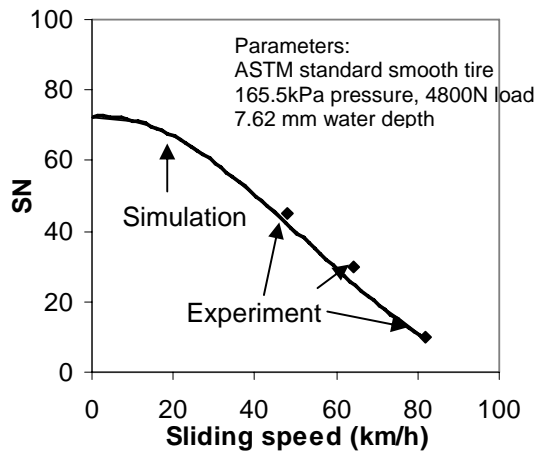
Factor	Range of Factor	Range of Predicted SN	Remarks
Wheel load P	2400 N – 5280 N	29 – 38 for $t_w = 0.5$ mm 26 – 36 for $t_w = 1.0$ mm 23 – 33 for $t_w = 2.0$ mm 21 – 30 for $t_w = 10.0$ mm	Tire pressure and wheel sliding speed are kept constant at 165.5 kPa and 64 km/h respectively.
		56 – 57 for $v = 20$ km/h 43 – 51 for $v = 40$ km/h 29 – 38 for $v = 60$ km/h 13 – 17 for $v = 80$ km/h	Tire pressure and water-film thickness are kept constant at 165.5 kPa and 0.5 mm respectively.
Tire inflation pressure $p_t$	100 kPa – 250 kPa	27 – 32 for $P = 2400$ N 30 – 33 for $P = 3840$ N 34 – 38 for $P = 4800$ N	Water-film thickness and wheel sliding speed are kept constant at 0.5 mm and 64 km/h respectively.
		57 – 58 for $v = 20$ km/h 49 – 50 for $v = 40$ km/h 34 – 36 for $v = 60$ km/h	Water-film thickness and wheel load are kept constant at 0.5 mm and 4800 N respectively.
Wheel sliding speed $v$	0 km/h – hydroplaning speed	60 – 11 for $t_w = 0.5$ mm 60 – 12 for $t_w = 1.0$ mm 60 – 13 for $t_w = 2.0$ mm 60 – 15 for $t_w = 10.0$ mm	Tire pressure and wheel load are kept constant at 165.5 kPa and 4800 N respectively.
		60 – 11 for $P = 2400$ N 60 – 11 for $P = 3840$ N 60 – 11 for $P = 4800$ N 60 – 13 for $P = 4800$ N	Tire pressure and water-film thickness are kept constant at 165.5 kPa and 0.5 mm respectively.
Water-film thickness $t_w$	0.1 mm – 10 mm	27 – 21 for $P = 2400$ N 34 – 25 for $P = 3840$ N 41 – 28 for $P = 4800$ N 45 – 30 for $P = 5280$ N	Tire pressure and wheel sliding speed are kept constant at 165.5 kPa and 64 km/h respectively.
		58 – 56 for $v = 20$ km/h 52 – 44 for $v = 40$ km/h 41 – 28 for $v = 60$ km/h 23 – 17 for $v = 80$ km/h	Tire pressure and wheel load are kept constant at 165.5 kPa and 4800 N respectively



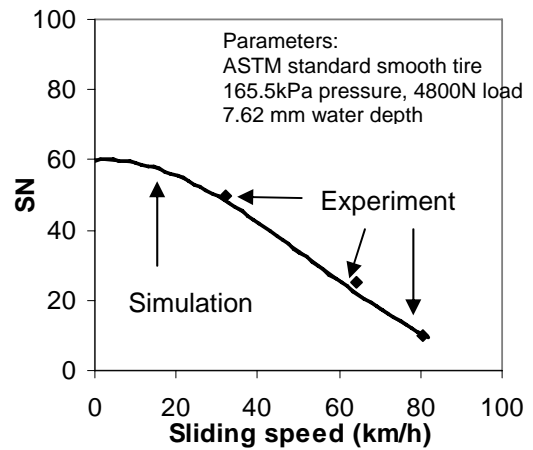
(a) Concrete (Rose and Gallaway 1977)



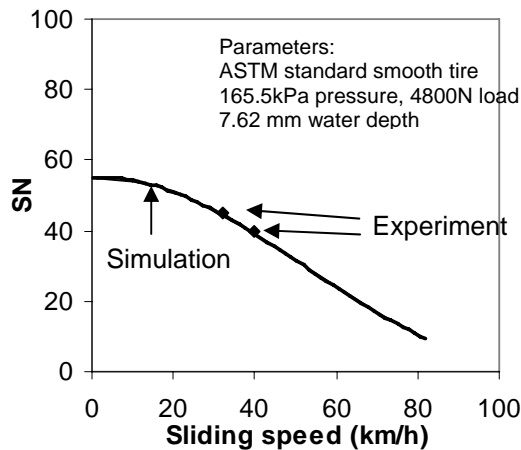
(b) Ungrooved concrete (Horne 1969)



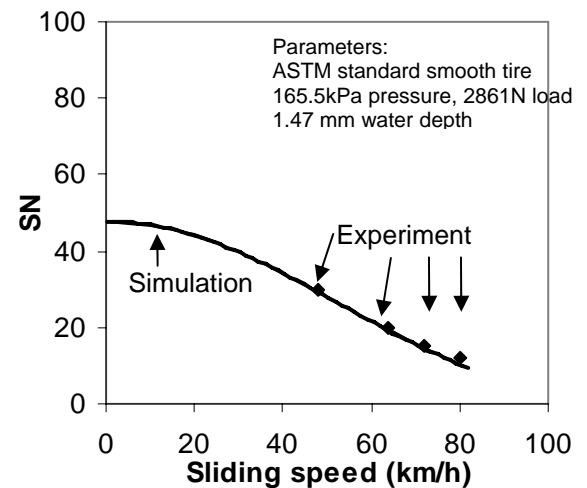
(c) Asphalt (Horne 1969)



(d) Concrete (Horne and Tanner 1969)



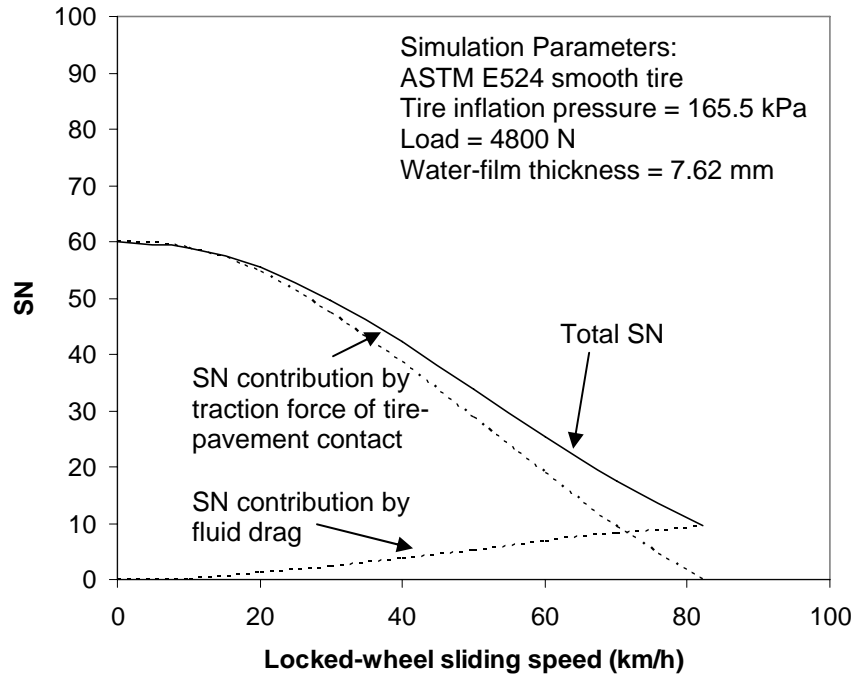
(f) Small-aggregate asphalt (Horne and Tanner 1969)



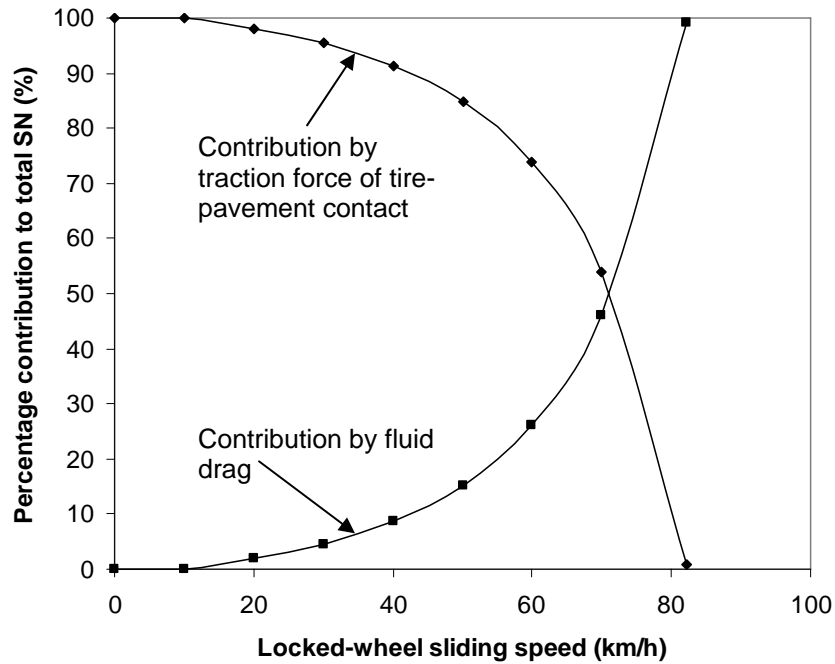
(h) Smooth concrete (Agrawal and Henry 1977)

Figure 8.1: Comparison of SN-v relationships between simulation and experiments





(a) Variations of traction force and fluid drag force



(b) Relative contributions of traction force and fluid drag force

Figure 8.2: Contributions of traction and fluid drag to skid resistance

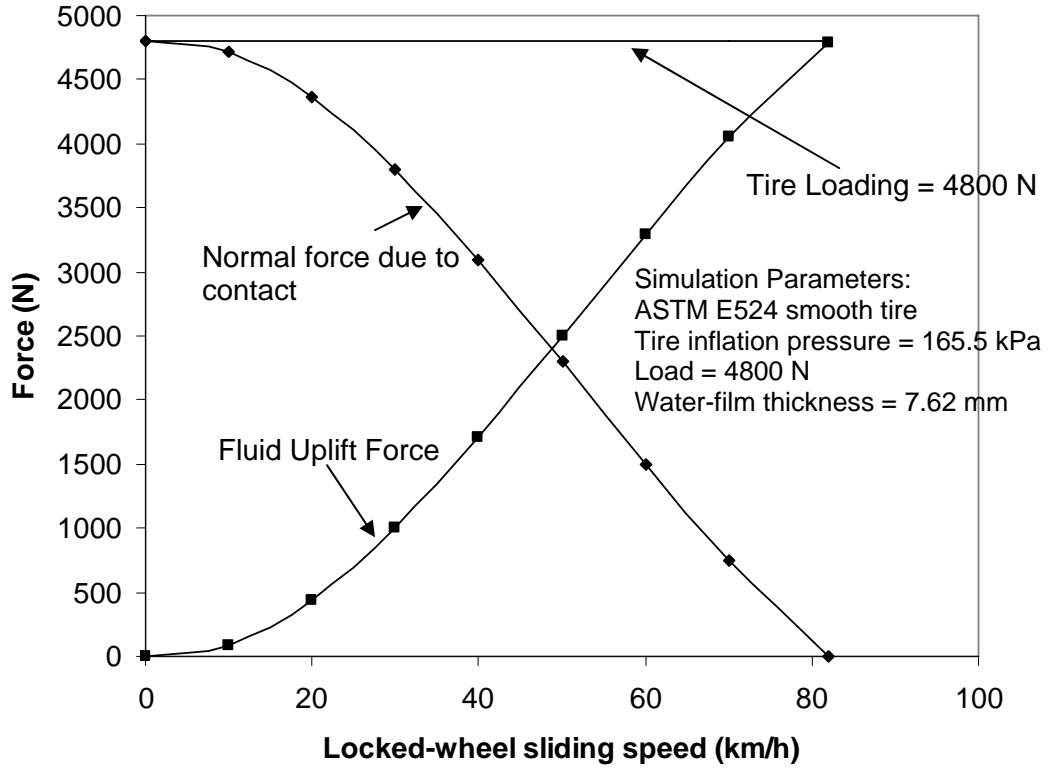


Figure 8.3: Variations of normal contact and fluid uplift forces with locked-wheel sliding speed

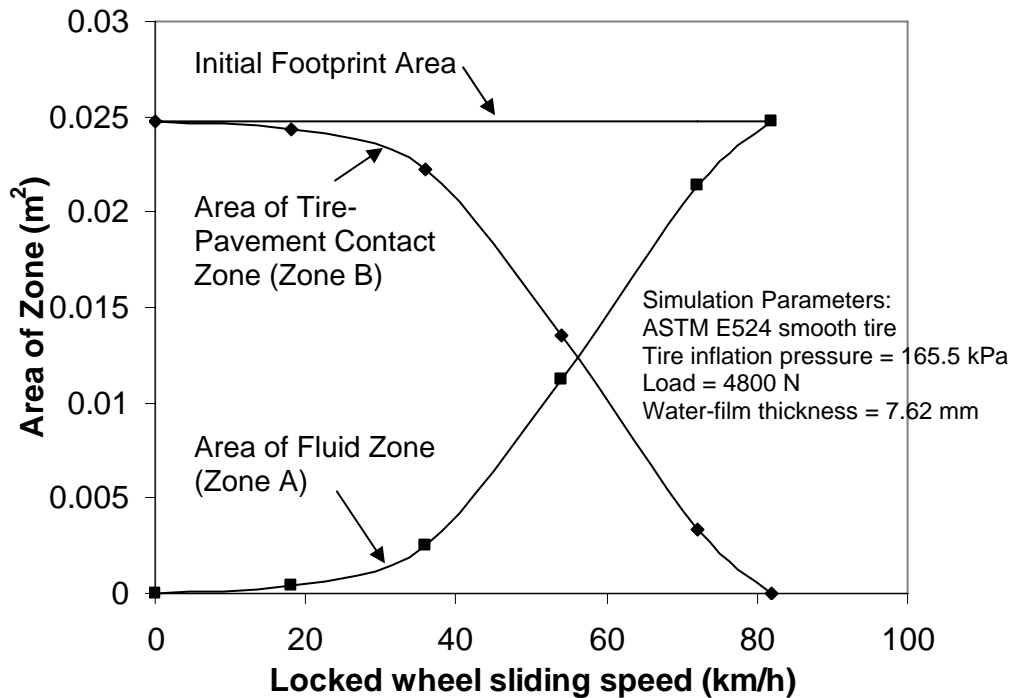
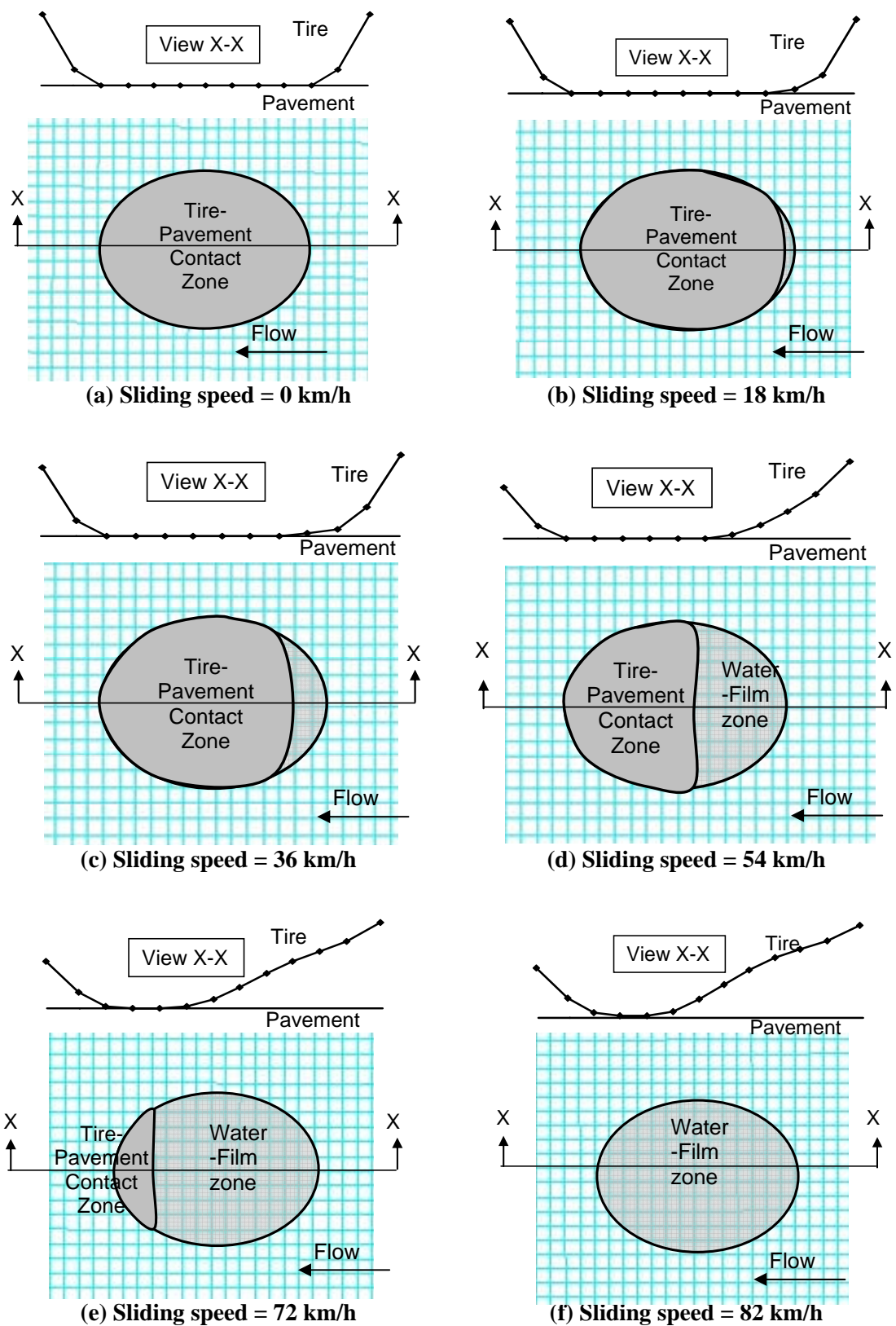


Figure 8.4: Changes in tire-pavement contact zone area with sliding wheel speed



Note: Vertical displacements of the nodes on the tire are scaled larger for easier viewing of tire deformation profile at different speeds

Figure 8.5: Variations of tire-pavement contact zone with sliding wheel speed

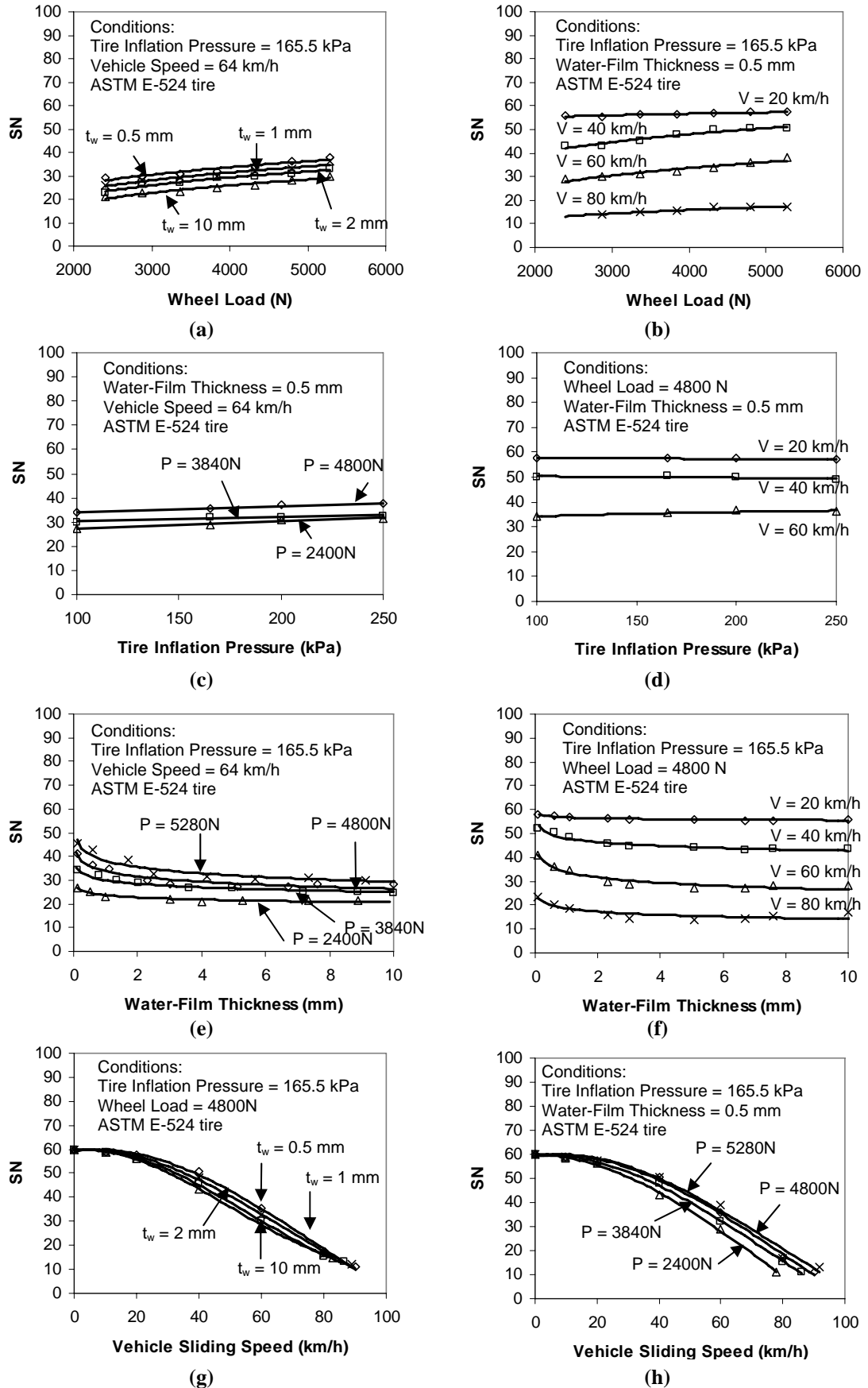


Figure 8.6: Effects of tire inflation pressure, wheel load, water-film thickness and vehicle sliding speed on skid number

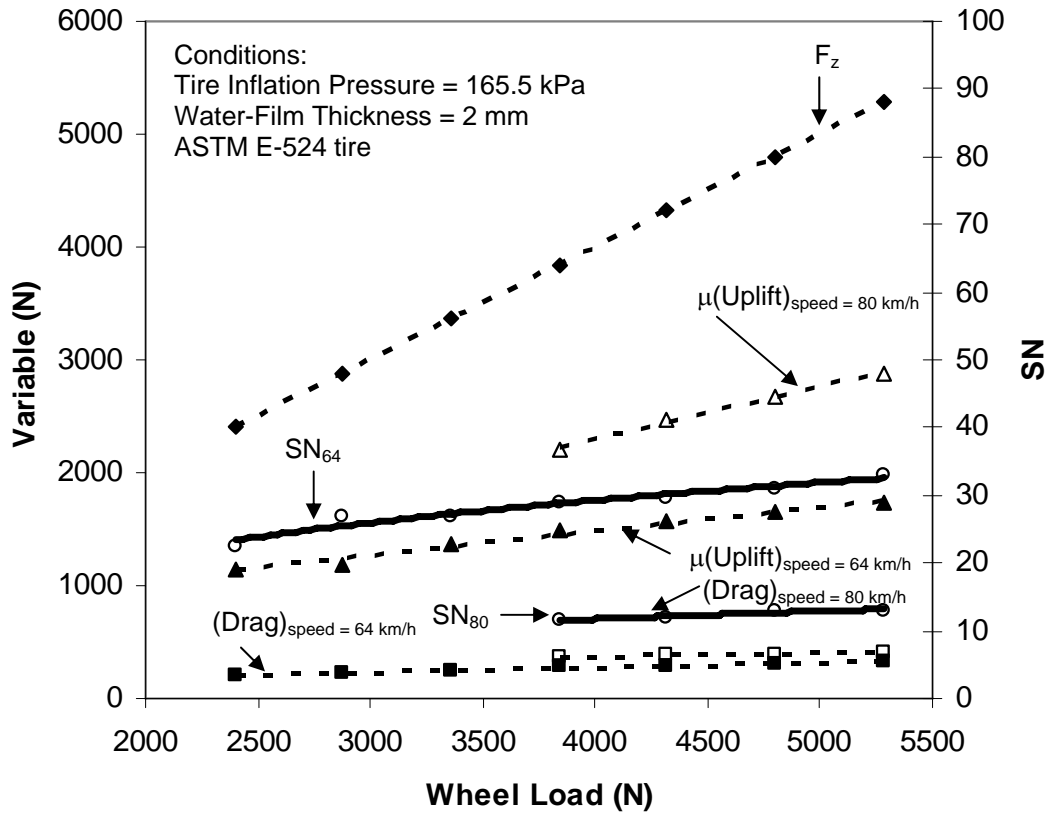


Figure 8.7: Variation of variables in Equation (8.4) with wheel load

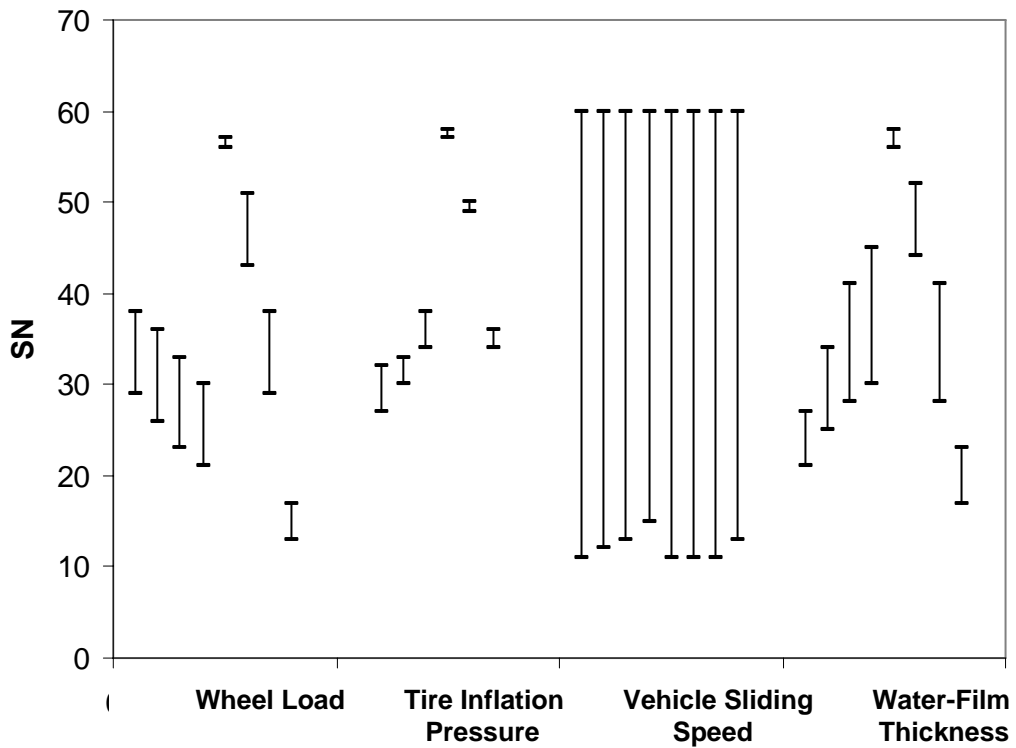


Figure 8.8: Comparison of various factors affecting skid number

## **CHAPTER 9      CONCLUSIONS AND RECOMMENDATIONS**

### **9.1      Conclusions of Research**

The objectives of this research, as stated in the beginning of this thesis, are (a) to develop a numerical model for simulating hydroplaning of a locked-wheel sliding over a smooth plane pavement using an assumed tire deformation profile, (b) to apply the proposed numerical model with the assumed tire deformation profile to study the effect of pavement grooving on hydroplaning, (c) to propose a design procedure for pavement groove dimensions in hydroplaning control, and (d) to propose an improved numerical model considering coupled tire-fluid-pavement interaction for estimating skid resistance and hydroplaning speed of a locked-wheel sliding over a smooth plane pavement. The research in this study have adopted a two-stage approach, the first involves developing numerical models to simulate hydroplaning using an assumed tire deformation profile on plane pavement surfaces or pavement with longitudinal and transverse pavement groovings, and the second involves developing improved models to simulate hydroplaning and wet pavement skid resistance with the consideration of tire-fluid-pavement interaction.

#### **9.1.1      Numerical Modeling of Hydroplaning using Assumed Hydroplaning Tire Profile**

The first stage of this research involves developing a numerical simulation model for simulating hydroplaning using the concept of computational fluid dynamics and using an assumed hydroplaning tire profile (i.e. the NASA hydroplaning tire profile). This part of the research arises from the current lack of appropriate hydroplaning simulation models that can simulate hydroplaning as described by the NASA hydroplaning equation. The key research findings are highlighted in the following sub-sections.

### **9.1.1.1 Development of Three-Dimensional Pneumatic Tire Hydroplaning Simulation Model**

The theoretical foundations for the hydroplaning simulation have been considered in the research. The hydroplaning phenomenon of a locked wheel over a flooded smooth pavement is studied. Three main models have to be considered, namely the fluid flow model, the tire deformation model and the pavement surface model. For the fluid flow model, the complete set of Navier-Stokes equations is applied with the consideration of turbulence. Turbulence is modeled using the standard k- $\epsilon$  model developed by Launder and Spalding (1974). For the hydroplaning tire deformation model, a hydroplaning profile used by Browne (1971) in his experiments and numerical modeling on hydroplaning of pneumatic tires is first considered. For the pavement surface model, it is assumed that the pavement surface is a smooth plane surface. Water is used as a contaminant. Hydroplaning is assumed to occur when the average ground hydrodynamic pressure is equal to the tire pressure of the wheel. The CFD package FLUENT (FLUENT Inc., 2005) is used to simulate the hydroplaning phenomenon by means of the finite volume method.

The possibility of two-dimensional or three-dimensional modeling of the hydroplaning phenomenon is considered. It is found that the proposed two-dimensional model using a turbulent flow model assumption is a poor model in simulating hydroplaning. This is because one important component of outflow, the in-plane and out-of-plane outflows are not modeled, thus resulting in an excessively high hydrodynamic pressure under the wheel and an extremely high percentage of splash. The two-dimensional model also results in an over-conservative prediction of hydroplaning speed which is very much lower than that predicted by the NASA hydroplaning equation. It is found that the proposed three-dimensional model could adequately model hydroplaning and it gives a recovery factor (defined as the ratio of tire pressure to  $0.5\rho U^2$  where  $\rho$  is the density of fluid and  $U$  is the vehicle speed) close to the predicted NASA value of 0.644. The shapes of the computed ground hydrodynamic profiles obtained from the numerical simulation are closely consistent with the experimental data reported by Horne and

Dreher (1963), Horne and Joyner (1965) and Browne (1971). Therefore, the proposed three-dimensional model is suitable for the simulation of hydroplaning.

#### **9.1.1.2 Hydroplaning Simulation on Plane Pavement Surfaces**

After determining the appropriateness of fluid flow models and the use of three-dimensional modeling, the research next set out to study the effect of tire inflation pressure on hydroplaning speed for plane pavement surfaces with zero microtexture. It is shown that the model could accurately predict hydroplaning speeds close to that predicted by the NASA hydroplaning equation for different tire pressures. This indicates that the simulation model is capable of simulating hydroplaning according to the NASA hydroplaning equation. The effect of microtexture at the onset of hydroplaning is also studied and it is shown that hydroplaning speed increases with increasing microtexture depth, and the effect is most significant at 0.5 mm texture depth (by definition, the transition point from microtexture to macrotexture). It is found that the improvement of pavement microtexture in the 0.2 mm to 0.5 mm range can delay hydroplaning, though the improvement in braking ability might not be substantial. The study also shows that the NASA hydroplaning equation provides a conservative estimate of hydroplaning speed. The under-estimation of hydroplaning speed by the NASA hydroplaning equation became more and more apparent as the microtexture of the pavement increases beyond 0.2 mm. This highlights the ability of the model in giving pavement engineers an understanding of the role microtexture plays in hydroplaning prevention.

#### **9.1.1.3 Hydroplaning on Pavement with Transverse or Longitudinal Pavement Grooving**

With the developed hydroplaning simulation model that can model the NASA hydroplaning equation, the research studies how transverse and longitudinal pavement grooving can affect hydroplaning. This is because studies on pavement grooving are experimental in nature and pavement researchers do not have a clear idea on the effects of transverse and longitudinal orientation of the pavement grooves and the effect of groove size on hydroplaning control. Thus numerical simulations have been performed on various



transverse and longitudinal groove designs used in past experimental research and verification of the simulation results has been made against the past experimental data. It has been shown that the friction factors derived by the proposed simulation model agree with the experimentally measured data for both transverse and longitudinal pavement grooving.

The effects of pavement grooving dimensions on hydroplaning for both the transverse and longitudinal pavement grooving are studied. It is noted that in general, a larger groove width, a larger groove depth and a smaller center-to-center groove spacing would result in a larger hydroplaning speed and a higher friction coefficient at incipient hydroplaning for both transverse and longitudinal pavement grooving. It is also found that groove width is an important factor in reducing hydroplaning occurrences and a primary factor in groove design. Groove depth is the next important factor followed by groove spacing. However, as the range of spacing adopted in practice is typically much larger than that for the groove width or depth, varying the groove spacing could be a more convenient measure in combating hydroplaning.

It is observed that transverse pavement grooving consistently gives a higher hydroplaning speed and friction coefficient at incipient hydroplaning as compared to longitudinal pavement grooving of the same groove design. However, it does not mean that longitudinal pavement grooving is not effective in hydroplaning prevention. It is found that certain longitudinal groove design would allow a noticeable improvement in traction control while others may not. The research also reconciles the conflicting arguments in past literature on whether longitudinal pavement grooving can improve skid number and hydroplaning potential. Through the use of numerical simulations, it is found that the conclusions in past experimental research were actually dependent on the groove dimensions used in the respective study. This shows that the use of the numerical hydroplaning simulation model is an effective and efficient way to analyze different pavement groove designs in hydroplaning analysis.

#### **9.1.1.4 Design and Evaluation of Pavement Grooves against Hydroplaning**

The design of pavement grooving has so far been based on experience and has been largely empirical in nature. Currently, most agencies provide guidelines on recommended groove dimensions. However these guidelines could not offer pavement engineers information such as the safety factor or safety margin against hydroplaning, resulting in a lack of understanding of the effectiveness of the designed groove dimensions against hydroplaning. Since hydroplaning is a major safety consideration for pavement grooving design, it is of practical interest and desirable for pavement engineers or designers to be aware of the safety implications of a design. With the capability of the numerical simulation model to model hydroplaning on pavement surfaces with pavement grooving, the research is now capable of performing a rational study on the design and evaluation of transverse and longitudinal pavement grooving based on the hydroplaning consideration.

The concept of hydroplaning risk is introduced and is used as a mean to quantify the effectiveness of the pavement grooving against hydroplaning (for evaluation purpose) or as a safety margin (for design purpose). An evaluation procedure to determine the hydroplaning risk of a given transverse and longitudinal pavement grooving design has been developed to allow pavement engineers to evaluate the effectiveness of the existing pavement grooves in combating hydroplaning. A trial-and-error design procedure is developed to allow pavement engineers to select appropriate transverse or longitudinal groove dimensions based on a selected level of hydroplaning risk. The trial-and-error procedure is time-consuming and can yield more than one possible groove design that can satisfy the required hydroplaning risk level. Hence the use of hydroplaning risk tables in the design of transverse or longitudinal groove dimensions is advocated. A hydroplaning risk table would offer the designer flexibility in selecting a desirable design from the pool of feasible designs by incorporating other practical considerations.

### **9.1.2 Numerical Modeling of Hydroplaning and Skid Resistance considering Fluid-Structure-Interaction**

The hydroplaning simulation model developed in the first stage of this research have so far been able to describe hydroplaning on plane pavement surfaces with and without microtexture, and on pavement surface with longitudinal and transverse pavement grooving. However, this model has a major limitation: the need to have an assumed tire deformation profile at incipient hydroplaning. The requirement of prior knowledge of the tire deformation profile has made the scope of potential applications of the model rather restrictive. For example, the developed model could not provide solutions to issues concerning the effect of water-film thickness, loading conditions on the predicted hydroplaning speed and more importantly, the modeling of wet-pavement skid resistance. Hence the second stage of the research focuses on the relaxation of the assumption of the input tire deformation profile by considering the full tire-fluid-pavement interaction problem. The key research findings are summarized as follows.

#### **9.1.2.1 Development of Improved Simulation Model for Hydroplaning**

A three-dimensional finite-element simulation model that is capable of simulating tire-fluid-pavement interactions of a locked wheel sliding on a flooded plane pavement surface has been developed. The formulation and development of the three-dimensional finite element simulation model is based on theoretical considerations of solid mechanics, fluid dynamics, and fluid-structure interaction. There are three main components in the simulation model: the pneumatic tire model, the fluid flow model and the pavement surface model, and two interaction mechanisms: tire-pavement contact and tire-fluid interaction. This enables the simulation model to effectively study the variations in wet pavement skid resistance and hydroplaning speed due to changes in tire properties (such as tire elastic properties, and tire dimensions), changes in tire footprint aspect ratio caused by changes in the applied wheel load, and changes in the thickness of water film on the pavement surface.

The developed model has been validated by checking the predicted hydroplaning speed against the well-known NASA equation, as well as other experimental data and experimentally derived relationships. The studies found that it is important to consider the effect of tire footprint aspect ratio in the prediction of hydroplaning speed. The hydroplaning speed is found to increase with decreasing footprint aspect ratio (or increasing wheel load) of the ASTM E-524 standard smooth tire.

The effects of tire inflation pressure, wheel load and water-film thickness on hydroplaning speed are studied using the developed simulation model. It is found that the hydroplaning speed increases with increasing tire pressure, increasing load and decreasing water-film thickness. It is found that the experimentally-derived regression relationships involving hydroplaning speed against tire inflation pressure, wheel load and the water-film thickness can be obtained from the numerical simulations and they are actually special cases, since the loading and environmental conditions play a critical role in the determination of the hydroplaning speed. It is also observed that tire inflation pressure is the dominant factor affecting hydroplaning speed while the wheel load and the water-film thickness are the secondary factors. This shows the ability of the model in simulating hydroplaning and obtaining valuable relationships that are often difficult to obtain in practice unless large-scale experiments are conducted.

#### **9.1.2.2 Modeling of Wet-Pavement Skid Resistance**

The improved simulation is next used to simulate skid resistance of a locked wheel traveling on wet or flooded pavement surfaces. The validity of the improved model in skid resistance prediction has been verified by checking the predicted skid resistance values with the measured skid resistance data of experimental studies conducted by past researchers under different conditions (e.g. load, tire inflation pressure, water-film thickness and vehicle speed). Hence the analytical model could offer a useful tool to predict the magnitude of wet-pavement skid resistance at any given locked-wheel sliding speed.

The improved model, which is based on fundamental engineering concepts and theories, is also able to provide detailed information on the behaviors and responses of the tire, the fluid and the pavement surface at different sliding speeds of the locked wheel. From the computed changes of the tire contact area, the normal contact force, and the fluid uplift force and drag force as the locked-wheel sliding speed is increased, a good insight into the deterioration mechanism of wet-pavement skid resistance can be obtained and this complements the hypothesis proposed by past researchers such as Moore (1975) and Veith (1983) on the various mechanisms of wet-pavement skid resistance.

The effects of the wheel load, tire inflation pressure and water-film thickness, and vehicle sliding speed on skid resistance in terms of skid number is next studied. The skid resistance is found to increase with wheel load and marginally with tire pressure, but decrease as the sliding wheel speed or the water-film thickness increases. Vehicle sliding speed was the most important factor affecting the magnitude of skid resistance, followed by water-film thickness, wheel load and tire inflation pressure. These findings are consistent with the experimental findings from past research. This demonstrates that the developed improved simulation model is a convenient tool for predicting both wet-pavement skid resistance and hydroplaning speed, and is also an effective means to study the influences of various factors on hydroplaning and skid resistance without the need to conduct expensive large-scale experiments.

## **9.2 Recommendations for Further Research**

This research has identified some areas which are recommended for further research so as to gain a better understanding of wet-pavement skid resistance.

- (a) This research focuses primarily on modeling hydroplaning and skid resistance for locked wheels. It could be extended to rolling tires and it would be useful if one can model hydroplaning and skid resistance under different slip and yaw conditions.
- (b) This research uses the ASTM E524-88 smooth tire (ASTM, 2005d) as a basis of comparison to the NASA hydroplaning equation and results of friction testing

equipment. Further research can be done by performing hydroplaning and skid resistance simulations on ribbed tires such as the ASTM E501-94 standard ribbed tire (ASTM, 2005f), commercial truck tires, aircraft tires and other configurations of tires (such as dual tires).

- (c) One limitation of the improved model is its inability to model hysteresis due to the assumption of elastic behavior of the tire and the lack of consideration of pavement macrotexture. Therefore further work is needed to develop techniques to model the effects of macrotexture on hydroplaning and skid resistance with the consideration of the effect of hysteresis on the skid resistance (in terms of skid number).
- (d) This research considers a steady-state mode i.e. the vehicle speed is kept constant. This is to ensure that the simulation is consistent with the ASTM E274-97 testing method where the speed is kept constant (ASTM, 2005a). Further research can be done to consider the dynamic event of a braking tire similar to the stopping distance method as stated in ASTM E445-88 (ASTM, 2005c).

---

**REFERENCES**

1. ABAQUS Inc. (2003). ABAQUS 6.4 Analysis User's Manual, USA.
2. ADINA R&D Inc. (2005a). ADINA Theory and Modeling Guide Volume I: ADINA Solids and Structures, ADINA R&D Inc., Watertown, Massachusetts.
3. ADINA R&D Inc. (2005b). ADINA Theory and Modeling Guide Volume III: ADINA CFD and FSI, ADINA R&D Inc., Watertown, Massachusetts.
4. Agrawal S. K. and J. J. Henry. (1977). Technique for Evaluating Hydroplaning Potential of Pavements, Transportation Research Record, No. 633, pp. 1-7.
5. Aksenov, A. A. and A. A. Dyadkin. (1996). Numerical Methods for Industrial Aerodynamics Problems; Simulation of Car Tire Aquaplaning. In Proceedings of the International Scientific Conference, Numerical Method in Continuum Mechanics, ES VSDS, Zilina.
6. Albert, B. J. and J. C. Walker. (1966). Tire to Wet Road Friction at High Speeds, Proceedings of the Institution of Mechanical Engineers, Vol.10, Part 2A, No.4.
7. American Association of State Highway and Transportation Officials (AASHTO). (2004). A Policy on Geometric Design of Highways and Streets, 5<sup>th</sup> Ed., Washington D. C.
8. American Concrete Institute (ACI). (1988). Texturing Concrete Pavement. Reported by ACI Committee 325, Detroit, Michigan.
9. American Concrete Pavement Association. (2000) Special Report: Concrete Pavement Technology and Research, Special Report-902P, Stokie, Illinois.
10. American Concrete Pavement Association (ACPA). (2005). Database of the State DOT Concrete Pavement Practices –Timing Dimensions. Washington D.C.: American Concrete Paving Association. Website: <www.pavement.com> (Mar. 1, 2005).

11. American Society for Testing and Materials. (2005a). ASTM Standard E 274-97. Standard Test Method for Skid Resistance of Paved Surfaces Using a Full-Scale Tire. ASTM Standards Sources, CD-ROM, Philadelphia.
12. American Society for Testing and Materials. (2005b). ASTM Standard E 303-93. Standard Test Method for Measuring Surface Frictional Properties Using the British Pendulum Tester. ASTM Standards Sources, CD-ROM, Philadelphia.
13. American Society for Testing and Materials. (2005c). ASTM Standard E 445-88. Standard Test Method for Stopping Distance on Paved Surfaces Using a Passenger Vehicle Equipped With Full-Scale Tires. ASTM Standards Sources, CD-ROM, Philadelphia.
14. American Society for Testing and Materials. (2005d). ASTM Standard E 501-94. Standard Specification for Standard Rib Tire for Pavement Skid-Resistance Tests. ASTM Standards Sources, CD-ROM, Philadelphia.
15. American Society for Testing and Materials. (2005e). ASTM Standard E 503-88. Standard Test Methods for Measurement of Skid Resistance on Paved Surfaces Using a Passenger Vehicle Diagonal Braking Technique. ASTM Standards Sources, CD-ROM, Philadelphia.
16. American Society for Testing and Materials. (2005f). ASTM Standard E 524-88. Standard Specification for Standard Smooth Tire for Pavement Skid-Resistance Tests. ASTM Standards Sources, CD-ROM, Philadelphia.
17. American Society for Testing and Materials. (2005g). ASTM Standard E 867-02a. Terminology Relating to Vehicle-Pavement Systems. ASTM Standards Sources, CD-ROM, Philadelphia.
18. American Society for Testing and Materials. (2005h). ASTM Standard E 965-96. Standard Test Method for Measuring Pavement Macro-texture depth using a Volumetric Technique. ASTM Standards Sources, CD-ROM, Philadelphia.



19. American Society for Testing and Materials. (2005i). ASTM Standard E 1845-01. Standard Test Method for Calculating Pavement Macrotexture Mean Profile Depth. ASTM Standards Sources, CD-ROM, Philadelphia.
20. American Society for Testing and Materials. (2005j). ASTM Standard E 1859-97. Standard Test Method for Friction Coefficient Measurements between Tire and Pavement using a Variable Slip Technique. ASTM Standards Sources, CD-ROM, Philadelphia.
21. Amontons, G. (1699). De la resistance caus'ee dans les machines, Memoires de l'Academie Royale, A, pp. 257-282.
22. Anderson, D. A., R. S. Huebner, J. R. Reed, J. C. Warner and J. J. Henry. (1998). Improved Surface Drainage of Pavements: Final Report. National Cooperative Highway Research Program NCHRP Web Document 16, Pennsylvania State University.
23. Andren, P. and A. Jolkin. (2003). Elastohydrodynamic Aspect of the Tire-Pavement Contact Aquaplaning, VTI Report 483A, Linkoping, Sweden.
24. Balmer, G. G. and, B. M. Gallaway. (1983). Pavement Design and Controls for Minimizing Automotive Hydroplaning and Increasing Traction. In Frictional Interaction of Tire and Pavement, ASTM STP 793, ed. by W. E. Meyer and J. D. Walters, pp. 167-190, American Society for Testing and Materials, Philadelphia.
25. Bartenev, G. M. (1954). Theory of Dry Friction of Rubber, Dokl. Acad. Nauk., SSSR, 96, pp. 1161-1164.
26. Bathe, K. J. (1976). Static and Dynamic Geometric and Material Non-linear Analysis Using ADINA. MIT Report No. 82448-2, Engineering Department, Cambridge, Massachusetts.
27. Bathe, K. J. (1996). Finite Element Procedures. Prentice Hall, New Jersey.
28. Bathe, K. J. and E. L. Wilson. (1973). NONSAP-a General Finite Element Program for Nonlinear Dynamic Analysis of Complex Structures, Paper M3/1, In Proc. 2nd Int. Conf. Structural Mechanics in Reactor Technology, Berlin.

29. Benedetto, A. A (2002). Decision Support System for the Safety of Airport Runways: The Case of Heavy Rainstorms, *Transportation Research Part A*, Vol. 36, pp. 665-682.
30. Bhushan, B. (1999). *Principles and Applications of Tribology*, Wiley, New York.
31. Bhushan, B. (2002). *Introduction to Tribology*, John Wiley and Sons., New York.
32. Blevins, R. D. (1984). *Applied Fluid Dynamics Handbook*, Van Nostrand Reinhold Co. Inc., New York.
33. Bowden, F. P. and D. Tabor. (1964). *The Friction and Lubrication of Solids*, Clarendon Press, Oxford.
34. Brown, R. (1996). *Physical Testing of Rubber*, 3rd Ed., Chapman and Hall, London.
35. Browne, A. L. (1971). *Dynamic Hydroplaning of Pneumatic Tires*, PhD thesis, Northwestern University, USA.
36. Browne, A. L. (1975). *Mathematical Analysis for Pneumatic Tire Hydroplaning*. In *Surface Texture verses Skidding: Measurements, Frictional Aspects, and Safety Features of Tire-pavement Interaction*. ASTM STP 583, ed. by J. G. Rose, pp. 75-94, American Society for Testing and Materials, Philadelphia.
37. Browne, A. L. and D. Whicker. (1983). *An Interactive Tire-Fluid Model for Dynamic Hydroplaning*. In *Frictional Interaction of Tire and Pavement*, ASTM STP 793, ed. by W. E. Meyer and J. D. Walters, pp. 130-150, American Society for Testing and Materials, Philadelphia.
38. California Department of Transportation (Caltrans). (1978). *The Effect of Pavement Grooving on Skid Resistance*, Report No. CA-TL-78-19, California.
39. California Department of Transportation (Caltrans). (1999). *Section 42: Groove and Grind Pavement*. In *Standard Specifications, State of California Business, Transportation and Housing Agency*, Department of Transportation.
40. Cameron, A. (1976). *Basic Lubrication Theory*, 2nd Edition, Wiley, New York.
41. Cebeci, T. and P. Bradshaw. (1977). *Momentum Transfer in Boundary Layers*, Hemisphere Publishing Corporation, New York.

42. Chemical Rubber Company. (1988). Handbook of Chemistry and Physics, 69th Edition, CRC Press, Cleveland, Ohio.
43. Colebrook, C. F. (1939). Turbulent Flow in Pipes with Particular Reference to the Transition Between Smooth and Rough Pipe Laws, Journal of the Institute of Civil Engineers, London, Vol. 11.
44. Costello, B. S. (2000). In Search of Smooth Landings, ASTM Standardization News, Vol. 28, No. 5, pp. 26-33.
45. Coulomb, C. A. (1785). Theorie des machines simples, en ayant egard au frottement de leurs parties, et la roideur des ordages. Mem Math Phys Paris, x: 161-342.
46. Davis, P. A. (1997). Quasi-Static and Dynamic Response Characteristics of F-4 Bias-Ply and Radial-Belted Main Gear Tires, NASA Technical Paper 3586, National Aeronautics and Space Administration, Langley Research Center, Hampton, Virginia.
47. Desaguliers, J. T. (1734). A Course of Experimental Philosophy, London.
48. Dowson, D. (1969). Boundary Lubrication. American Society of Mechanical Engineers Special Publication.
49. Dreher, R. C. and W. B. Horne. (1966). Ground-Run Tests with a Bogie Landing Gear in Water and Slush, NASA Technical Note D-3515, National Aeronautics and Space Administration, Washington D.C.
50. Eshel, A. A (1967). Study of Tires on a Wet Runway, Report No. RR67-24, Ampex Corporation, Redwood City, California.
51. Federal Aviation Administration (FAA). (1997). Measurement, Construction and Maintenance of Skid-Resistant Airport Pavement Surfaces, FAA Advisory Circular 150/5320-12C, Washington D.C: US Department of Transportation.
52. Federal Highway Administration. (1978). Effectiveness of Alternative Skid Reduction Measures, Vol. IV, Criteria for Improvement of Pavement Surface Macrotecture, Final Report.
53. Federal Highway Administration. (1980). Pavement Macrotecture Review, FHWA RD80-505, Final Report.

54. Ferziger, J. H. and M. Peric. (2002). Computational Methods for Fluid Dynamics, 3rd Edition, Springer-Verlag, Germany.
55. Fluent Inc. (2004). Gambit 2.2 Modeling Guide. Lebanon, New Hampshire.
56. Fluent Inc. (2005). Fluent 6.2 User Guide. Lebanon, New Hampshire.
57. Forster, S. W. (1990). Pavement Micro-Texture and its Relation to Skid Resistance, Transportation Research Record, No. 1215, pp. 151-164.
58. Frene, J., D. Nicols, B. Degueerce, D. Berthe and M. Godet. (1997). Hydrodynamic Lubrication – Bearings and Thrusts Bearings, Elsevier, Amsterdam.
59. Gallaway, B. M., D. L. Ivey, G. G. Hayes, W. G. Ledbetter, R. M. Olson, D. L. Woods and R. E. Schiller. (1979). Pavement and Geometric Design Criteria for Minimizing Hydroplaning. Federal Highway Administration Report No. FHWA-RD-79-31.
60. Giles, C. G., B. E. Sabey and K. H. F. Cardew. (1964). Development and Performance of the Portable Skid Resistance Tester. Road Research Laboratory, Department of Scientific and Industrial Research, Road Research Technical Paper 66, Her Majesty's Stationery Office, London.
61. Gough, V. E. (1958a). Friction of Rubber, No.1, The Engineer, Oct. 31, pp. 701-704.
62. Gough, V. E. (1958b). Friction of Rubber, No.2, The Engineer, Nov. 7, pp. 741-743.
63. Gough, V. E. (1959). Discussion of Paper by D. Tabor. Revue Generale Du Caoutchouc, Vol.36, No. 10, pp.1409.
64. Greenwood, J. A. and D. Tabor. (1958). The Friction of Hard Slider and Lubricated Rubber: The Importance of Deformation Losses, Proceedings of the Physical Society, Vol. 71, No. 6, pp. 989-1001.
65. Groger, H. and M. Weis. (1996). Calculation of the Three-Dimensional Free Surface Flow Around an Automobile Tire, Tire Science and Technology, 24, pp. 39-49.
66. Gross, W. A., L. A. Matsch, V. Castelli., A. Eshel, J. H. Vohr and M. Wildmann. (1980). Fluid Film Lubrication, Wiley, New York.

67. Haisler, W. E. (1977). AGGIE I. a Finite Element Program for Non-Linear Structural Analysis. Technical Report No.3275-77-1, Texas A&M University, College Station, Texas.
68. Hamrock, B. J. (1994). Fundamentals of Fluid Film Lubrication, McGraw-Hill, New York.
69. Han, Y. H. (2003). Fatigue Life Prediction for Cord-Rubber Composite Tires Using a Global-Local Finite Element Method. PhD Thesis, University of Texas at Austin.
70. Haney, P. (2003). The Racing and High Performance Tire: Using the Tires to Tune for Grip and Balance. Society of Automotive Engineers, Springfield, Illinois.
71. Harlow, F. H. and J. E. Welsh. (1965). Numerical Calculation of Time Dependent Viscous Incompressible Flow with Free Surface, The Physics of Fluids, Vol. 8, pp. 2182-2189.
72. Harrin, E. N. (1958). Low Tire Friction and Cornering Forces on a Wet Surface, NACA Technical Note 4406.
73. Harrin, E. N. (1960). Investigation of Tandem-Wheel and Air-Jets Arrangements for Improving Braking Friction on Wet Surfaces. NASA Technical Note D-405.
74. Hegmon, R. R. (1969). The Contribution of Deformation Losses to Rubber Friction, Rubber Chemistry and Technology, Vol. 42, No. 4, pp. 1122-1135.
75. Henry, J. J. (1986). Tire Wet-Pavement Traction Measurement: A State-of-the-Art Review. In The Tire Pavement Interface, ASTM STP 929, ed. by Pottinger, M. G. and Yager, T. J., pp. 47-60, American Society of Testing and Materials, Philadelphia.
76. Henry, J. J. (2000). Evaluation of Pavement Friction Characteristics. NCHRP Synthesis 291, Transportation Research Board, Washington D.C.
77. Henry, J. J. and W. E. Meyer. (1983). The Simulation of Tire Traction on Wet Pavements. In Proceedings of the 18th International Automobile Technical Congress, Report 369, Hamburg, Germany, pp. 121-128.
78. Hersy, M. D. (1966). Theory and Research on Lubrication, Wiley, New York.

79. Highway Research Board. (1972). Skid Resistance. National Cooperative Highway Research Program Synthesis of Highway Practice, No. 14, Highway Research Board, Washington D. C.
80. Hinze, J. O. (1975). Turbulence, 2<sup>nd</sup> Edition, McGraw-Hill, New York.
81. Hirt, C. W. and B. D. Nicholls. (1981). Volume of Fluid (VOF) Method for Dynamics of Free Boundaries, Journal of Computational Physics, Vol. 39, pp.201-221.
82. Hoerner, T. E. and K. D. Smith. (2002). High Performance Concrete Pavement: Pavement Texturing and Tire-Pavement Noise. FHWA-IF-02-020. Federal Highway Administration, U.S. Department of Transportation.
83. Holla, L. and W. O. Yandell. (1969). Australian Road Research, Vol. 5, No. 2, pp.76.
84. Horne, W. B. (1969). Results from Studies of Highway Grooving and Texturing at NASA Wallops Station. In Pavement Grooving and Traction Studies, NASA SP-5073, pp. 425-464, National Aeronautic and Space Administration, Washington D.C., USA.
85. Horne, W. B. (1969). Results from Studies of Highway Grooving and Texturing at NASA Wallops Station. In Pavement Grooving and Traction Studies, NASA SP-5073, pp. 425-464, National Aeronautics and Space Administration, Washington D.C., USA.
86. Horne, W. B. (1977). Status of Runway Slipperiness Research, Transportation Research Record, No. 624, pp. 95-121.
87. Horne, W. B. and R. C. Dreher. (1963). Phenomena of Pneumatic Tire Hydroplaning, NASA Technical Note D-2056, National Aeronautics and Space Administration, Washington D.C.
88. Horne, W. B. and U. T. Joyner. (1965). Pneumatic Tire Hydroplaning and Some Effects on Vehicle Performance. In SAE International Automotive Engineering Congress, 11-15 Jan, Detroit, Michigan, USA.
89. Horne, W. B. and T. J. W. Leland. (1962). Influence of Tire Tread Pattern and Runway Surface Condition on Braking Friction and Rolling resistance of a Modern Aircraft Tire, NASA Technical Note D-1376, National Aeronautics and Space Administration, Washington D.C.

90. Horne, W. B. and Tanner, J. A. (1969). Joint NASA-British Ministry of Technology Skid Correlation Study: Results from American Vehicles. In Pavement Grooving and Traction Studies, NASA SP-5073, pp. 325-360, National Aeronautics and Space Administration, Washington D.C., USA.
91. Horne, W. B., J. L. McCarty and J. Tanner. (1976). A. Some Effects of Adverse Weather Conditions on Performance of Airplane Antiskid Braking Systems, NASA Technical Note D-8202, National Aeronautic and Space Administration, Washington D.C., USA.
92. Horne, W. B., T. J. Yager and D. L. Ivey. (1986). Recent Studies to Investigate Effects of Tire Footprint Aspect Ratio on Dynamic Hydroplaning Speed. In The Tire Pavement Interface, ASTM STP 929, ed. by M. G. Pottinger and M. G. Yager, pp. 26-46, American Society for Testing and Materials, Philadelphia.
93. Horne, W. B., T. J. Yager and G. R. Taylor. (1969). Review of Causes and Alleviation of Low Tire Traction on Wet Runway. NASA TN D-4406, National Aeronautic and Space Administration, Washington D.C., USA.
94. Hosking, J. R. (1987). Relationship between Skidding Accidents and Accident Frequency: Estimates Based on Seasonal Variation, TRRL Report, RR76, Department of Transport, Crowthorne, United Kingdom.
95. Hosking, J. R. and Woodford, G. C. (1976). Measurement of Skidding Resistance: Part I, Guide to Use of SCRIM; Part II, Factors Affecting Slipperiness of a Road Surface; Part III, Factors Adducting SCRIM Measurements, Department of Environment, TRRL Reports LR 737-739, United Kingdom.
96. Huebner, R. S., J. R. Reed and J. J. Henry. (1986). Criteria for Predicting Hydroplaning Potential, ASCE Journal of Transportation Engineering, Vol. 112, No. 5, pp. 549-553.
97. International Groove and Grinding Association (IGGA). (2005). State DOT Specifications. Website: <<http://www.igga.net/specs.html>>. (Apr. 1 2005).

98. ISO/CD 13473. (1994). Characterization of Pavement Textures Utilizing Surface Profile: Estimation of Mean Texture Depth, Committee Draft from ISO/TC 43/SC 1/WG 39.
99. Issa, R. I. (1986). Solution of Implicitly Discretized Fluid Flow Equations by Operator Splitting, *Journal of Computational Physics*, Vol. 62, pp. 364-374.
100. Johnson, A. R., J. A. Tanner and A. J. Mason. (1999). Quasi-Static Viscoelastic Finite Element Model of an Aircraft Tire, NASA/TM-1999-209141, National Aeronautics and Space Administration, Langley Research Center, Hampton, Virginia.
101. Keith, R. A. and A. Cunningham. (1998). Measurement of Energy Loss Profiles during Short Duration Sliding Contacts: A Computer-Compatible Instrument Based on the British Pendulum Skid Tester, *Measurement Science and Technology*, Vol. 9, pp. 1566-1570.
102. Kennedy, C. K., A. E. Young and I. C. Butler. (1990). Measurements of Skidding Resistance and Surface Texture and the Use of Results in the United Kingdom. Symposium: Surface Characteristic of Roadway, ASTM, Philadelphia, pp. 87-101.
103. Khonsari, M. M. and E. R. Booser. (2001). *Applied Tribology – Bearing Design and Lubrication*, Wiley, New York.
104. Kokkalis, A. G. and O. K. Panagouli. (1998). Fractal Evaluation of Pavement Skid Resistance Variations I: Surface Wetting, *Chaos, Solitons and Fractals*, Vol. 9, No. 11, pp. 1875-1890.
105. Kulakowski, B. T. and W. E. Meyer. (1989). Skid Resistance of Adjacent Tangent and Nontangent Sections of Roads, *Transportation Research Record*, No. 1215, pp. 132-136.
106. Kummer, H. W. (1966). Unified Theory of Rubber and Tire Friction, *Engineering Research Bulletin*, B-94, Pennsylvania State University.
107. Kummer, H. W. and W. E. Meyer. (1966). New Theory Permits Better Frictional Coupling Between Tire and Road. Paper B 11, 11th International FISITA Congress, Munich.



108. Kyte, M., Z. Khatib, P. Shannon and F. Kitchener. (2001). Effect of Weather on Free-Flow Speed, Transportation Research Record, No. 1776, pp. 60-68.
109. Lamm, R., E. M. Choueiri and T. Mailaender. (1990). Comparison of Operating Speeds on Dry and Wet Pavements of Two-Lanes Rural Highways, Transportation Research Record, No. 1280, pp. 199-207.
110. Lamm, R., B. Psarianos and T. Mailaender. (1999). Highway Design and Traffic Engineering Handbook, McGraw-Hill, New York.
111. Lander, F. T. and T. Williams. (1968). The Skidding Resistance of Wet Runway Surfaces, Ministry of Transport TRRL Report 184, United Kingdom.
112. Launder, B. E. and D. B. Spalding. (1974). The Numerical Computation of Turbulent Flows, Computational Methods in Applied Mechanics in Engineering, Vol. 3, pp. 269-289.
113. Lee, Y. P. K. (2004). Analyzing Laboratory Skid Resistance Test Using Finite Element Modeling. PhD Thesis, Department of Civil Engineering, National University of Singapore.
114. Lee, Y. P. K., Fwa, T. F., Liu, Y. R. and Choo Y. S. (2005). Prediction of Skid Resistance using Finite Element Modeling. In E-Proceedings of the 4th Asia Pacific Conference on Transportation and Environment (CD-ROM), Xi'an, People's Republic of China.
115. Liu, Y. (2004). Evaluation of British Pendulum Tester for Laboratory Pavement Skid Resistance Measurements. M Eng Thesis, Department of Civil Engineering, National University of Singapore.
116. Liu, Y. R., T. F. Fwa and Y. S. Choo. (2003). Finite Element Modeling of Skid Resistance Test, ASCE Journal of Transportation Engineering, Vol. 129, No. 3. pp. 316-321.
117. Lowne, R. W. (1970). The Effect of Road Surface Texture on Tire Wear, Wear, Vol. 15, pp. 57-70.

118. MacCurdy, E. (1938). *The Notebooks of Leonardo da Vinci*, Vols. 1 and 2, arranged and rendered into English, Jonathan Cape, London.
119. Martin, C. S. (1966). *Hydrodynamics of Tire Hydroplaning*, Final Report, Project B-608, Georgia Institute of Technology.
120. Maycock, G. (1965). *Studies of the Skidding Resistance of Passenger Car Tires on Wet Surfaces*, Proceedings of the Institute of Mechanical Engineers, Vol. 180, Pt. 2A, pp. 122-141.
121. Meyer, W. E. (1991). *Pavement Texture Significance and Measurement*, ASTM Standardization News, Vol. 19, No. 2, pp. 28-31.
122. Michelin. (2001). *The Tyre: Grip*, Societe de Technologie Michelin, France.
123. Moody, L. F. (1944). *Friction Factors for Pipe Flow*, Transactions of the ASME, Vol. 66.
124. Moore, D. F. (1966). *Prediction of Skid-resistance Gradient and Drainage Characteristics for Pavements*, Highway Research Record 131, pp.181-203.
125. Moore, D. F. (1967). *A Theory of Viscous Hydroplaning*, International Journal of Mechanical Science, Vol. 9, pp. 797-810.
126. Moore, D. F. (1969). *A History of Research on Surface Texture*, Wear, Vol. 13, Issue 6, pp. 381-412.
127. Moore, D. F. (1972). *The Friction and Lubrication of Elastomers*. Pergammon Press, New York.
128. Moore, D. F. (1975). *Principles and Applications of Tribology*, Wheaton and Co., Exeter, Great Britain.
129. Moore, D. F. and W. Geyer. (1974). *A Review of Hysteresis Theories for Elastomers*, Wear, 30, pp. 1-33.
130. Mosher, L. G. (1969). *Results from Studies of Highway Grooving and Texturing by Several State Highway Departments*. In *Pavement Traction and Grooving Studies*, NASA SP-5073, pp. 465-504, National Aeronautic and Space Administration, Washington D.C., USA.

131. MSC. Software Corporation. (2003a). MSC.Marc. Redwood City, California, USA.
132. MSC. Software Corporation. (2003b). MSC/NASTRAN. Santa Ana, California, USA.
133. Nikuradse, J. (1933). Laws for flow at rough pipes (Strömungswiderstand in rauhen Röhren), *Forschg. Arb. Ing.-Wes.* No. 361.
134. Okano, T. and M. Koishi. (2000). A New Computational Procedure to Predict Transient Hydroplaning on a Tire. Presented in The 19<sup>th</sup> Annual Meeting and Conference on Tire Science and Technology, Akron, Ohio, USA.
135. Organisation for Economic Cooperation and Development (OECD). (1984). Road Surface Characteristics: Their Interaction and Their Optimisation. Paris.
136. Pantakar, S. V. (1980). Numerical Heat and Fluid Flow, Hemisphere, Washington D.C.
137. Pelloli, R. (1977). Road Surface Characteristics and Hydroplaning, *Transportation Research Record*, No. 624, pp. 27-32.
138. Pennsylvania Transportation Institute. (1988). Skid Resistance Manual, Submitted to FHWA, Contract No. DTFH-61-88-C-00058.
139. Permanent International Association of Road Congresses (PIARC). (1987). Report of the Committee on Surface Characteristics, Proceedings of the 18th World Road Congress. Brussels, Belgium.
140. Permanent International Association of Road Congresses (PIARC). (1995). International PIARC Experiment to Compare and Harmonize Texture and Skid Resistance Measurements, Spain.
141. Persson, B. N. J. (1998). On the Theory of Rubber Friction, *Surface Science*, Vol. 401, Issue 3.
142. Pinkus, O. and B. Sterlicht. (1961). *Theory of Hydrodynamic Lubrication*, McGraw-Hill, New York.
143. Piquet, J. (1999). *Turbulent Flows: Models and Physics*, Springer-Verlag, Germany.
144. Priyantha, W. J. and L. G. Gary. (1995). Use of Skid Performance History as Basis for Aggregate Qualification for Seal Coats and Hot-Mix Asphalt Concrete Surface Courses, *Transportation Research Record*, No. 1501, pp. 31-38.

145. Reynolds, O. (1886). On the Theory of Lubrication and its Application to Mr Beauchamp Tower's Experiments Including an Experimental Determination of the Viscosity of Olive Oil in Phil. Trans., Roy. Soc. London, Vol. 177(i), pp. 157-23.
146. Reznikovskii, M. M. and G. I. Brodskii. (1967). Features of the Mechanism of Abrasion of Highly Elastic Materials. In Abrasion of Rubber, ed. by D. I. James, pp. 14-22, Maclaren and Sons Ltd., London.
147. Road Research Laboratory. (1960). Instruction for Using the Portable Skid Resistance Tester, Road Note No. 27. Britain.
148. Roess, R. P., E. S. Prassas and W. R. McShane. (2004). Traffic Engineering, 3<sup>rd</sup> Ed. Pearson Prentice Hall, Upper Saddle River, New Jersey.
149. Rose, J. G. and B. M. Gallaway. (1977). Water Depth Influence on Pavement Friction, ASCE Journal of Transportation Engineering, Vol. 103, No. 4, pp. 491-506.
150. Sabey, B. E. (1965). Road Surface Characteristics and Skidding Resistance. Journal of the British Granite and Whinstone Federation, Vol. 5, No. 2. pp. 7-18.
151. Sacia, S. R. (1976). The Effect of Operating Conditions on the Skid Performance of Tires, Transportation Research Record, No. 621, pp. 126-135.
152. Salt, G. F. (1977). Research on Skid Resistance at the Transport and Research Laboratory (1927-1977), Transportation Research Record, No. 622, pp. 26-38.
153. Savkoor, A. R. (1965). On the Friction of Rubber, Wear, 8, pp. 222-237.
154. Schlichting, H. (1960). Boundary Layer Theory, 4th Edition, McGraw-Hill, New York.
155. Shilling, B. (1969). R.A.E. Aircraft Tests on Grooved, Open Graded and Asphalt Runways in Great Britain. In Pavement Grooving and Traction Studies, NASA SP-5073, pp. 67-80. , National Aeronautic and Space Administration, Washington D.C., USA.
156. Shulze, K. H. and L. Beckman. (1965). Skid Resistance, ASTM STP 326, American Society for Testing and Materials, Philadelphia, pp. 42-49.
157. Smith, H. A. (1977). Pavement Contributions to Wet-Weather Skidding Accident Reduction, Transportation Research Record 622, pp. 51-59.

158. Sommers, D. E., J. F. Marcy, E. P. Klueg and D. W. Conley. (1962). Runway Slush Effects on the Takeoff of a Jet Transport, Final Report, Project No. 308-3X, Federal Aviation Administration, USA.
159. Stachowiak, G. W. and A. W. Batchelor. (2005). Engineering Tribology, 3rd Edition, Elsevier Butterworth-Heinemann, Boston.
160. Streeter, V. L., E. B. Wylie and K. W. Bedford. (1998). Fluid Mechanics, 9th Ed. McGraw Hill, Singapore.
161. Sugg, R. W. (1969). Joint NASA-British Ministry of Technology Skid correlation Studies – Results from British Vehicles. In Pavement Grooving and Traction Studies, NASA SP-5073, pp. 361-410, National Aeronautic and Space Administration, Washington D.C., USA.
162. Sugg, R. W. (1972). The Development and Testing of the Runway Friction Meter MK1 (Mu-Meter), Procurement Executive, Ministry of Defence, London, pp. 109.
163. Szeri, A. Z. (1998). Fluid Film Lubrication – Theory and Design, Cambridge University Press, Cambridge, UK.
164. Tannehill, J. C., D. A. Anderson. and R. H. Pletcher. (1997). Computational Fluid Mechanics and Heat Transfer, 2<sup>nd</sup> Edition, Taylor and Francis, U.S.A.
165. Tanner, J. A. (1996). Computational Methods for Frictional Contact With Applications to the Space Shuttle Orbiter Nose-Gear Tire, NASA Technical Paper 3573, National Aeronautics and Space Administration, Langley Research Center, Hampton, Virginia.
166. Tsakonas, S., C. J. Henry and W. R. Jacobs. (1968). Hydrodynamics of Aircraft Tire Hydroplaning, NASA CR-1125, National Aeronautics and Space Administration, Washington D. C.
167. Veith, A. G. (1983). Tires-Roads-Rainfall-Vehicles: The Traction Connection. In Frictional Interaction of Tire and Pavement, ASTM STP 793, ed. by W. E. Meyer and J. D. Walter, pp. 3-40, American Society for Testing and Materials, Philadelphia.

168. Veith, A. G. (1986). The Most Complex Tire-Pavement Interaction: Tire Wear, In The Tire Pavement Interface, ASTM STP 929, ed. by M. G. Pottinger and M. G. Yager, pp. 125-158, American Society for Testing and Materials, Philadelphia.
169. Wallace, K. B. (1964). Airfield Pavement Skidding Characteristics. University of Melbourne, Australia.
170. Wambold, J. C., J. J. Henry and R. R. Hegmon. (1986). Skid Resistance of Wet-Pavement Accidents Sites. In The Tire Pavement Interface, ASTM STP 929, ed. by M. G. Pottinger, and T. J. Yager, pp. 47-60, American Society of Testing and Materials, Philadelphia.
171. Williams, A. R. and M. S. Evans. (1983). Influence of Tread Wear Irregularity on Wet Friction Performance of Tires. In Frictional Interaction of Tire and Pavement, ASTM STP 793, ed. by W. E. Meyer and J. D. Walter, pp. 41-64, American Society for Testing and Materials, Philadelphia.
172. Williams, J. R. (1969). Aquaplaning: The British Ministry of Technology Programme. In Pavement Grooving and Traction Studies, NASA SP-5073, pp. 81-100, National Aeronautic and Space Administration, Washington D.C., USA.
173. Williams, M. L., R. F. Landel and J. D. Ferry. (1955). Temperature Dependence on Relaxation Mechanisms in Amorphous Polymers, Journal of American Chemical Society, Vol. 77, pp. 3701-3707.
174. Wolshon, B. (2004). Geometric Design of Streets and Highway. In Handbook of Transportation Engineering, ed. by M. Kutz, pp. 13.1-13.21, McGraw-Hill, New York.
175. Wu, C. L., and M. A. Nagi. (1995). Optimizing Surface Texture of Concrete Pavement, Research and Development Bulletin RD111T, Portland Cement Association, Skokie, Illinois.
176. Yager, T. J. (1969). Comparative Braking Performance of Various Aircraft on Grooved and Ungrooved Pavements at the Landing Research Runway, NASA Wallops Station. In Pavement Grooving and Traction Studies, NASA SP-5073, pp. 35-66, National Aeronautic and Space Administration, Washington D.C., USA.

- 
177. Yandell, W. O. (1971). A New Theory of Hysteric Sliding Friction, *Wear*, Vol. 17, No. 4, pp. 229-244.
  178. Yeager R. W. and J. L. Tuttle. (1972). Testing and Analysis of Tire Hydroplaning. In SAE National Automobile Engineering Meeting, Detroit, Michigan.
  179. Yoder, E. J. and M. W. Witzcak. (1997). *Principles of Pavement Design*, 2nd Ed, John Wiley and Sons, Canada.
  180. Zhang, H. and Bathe, K. J. (2001). Direct and Iterative Computing of Fluid Flows Coupled with Structures. In *Computational Fluid and Solid Mechanics: Proceedings of the First MIT Conference on Computational Fluid and Solid Mechanics*, K. J. Bathe, ed., Elsevier Science, New York, pp. 1440-1443.
  181. Zhang, H., Zhang X., Ji, S., Guo, Y., Ledezma, G., Elabbasi, N. and deCougny, H. (2003). Recent Development of Fluid-Structure Interaction Capabilities in the ADINA System, *Computers and Structures*, Vol. 81, pp. 1071-1085.
  182. Zmindak, M and I. Grajciar. (1997). Simulation of the Aquaplane Problem, *Computers and Structures*, Vol. 64, No. 5/6, pp. 1155-1164. 1997.
  183. Zoeppritz, H. P. (1977). An Overview of European Measuring Methods and Techniques, *Transportation Research Record*, No. 621, pp. 75-82.